A cumulative dissertation approved by the Department of Materials Science
in fulfillment of the requirements for the academic degree of
Doctor rerum naturalium (Dr. rer. nat.)

---

# Revealing the Domain Structure and the Relaxation Dynamics of BNT-Based Lead-Free Piezoceramics via Piezoresponse Force Microscopy


**M.Sc. Na Liu**

Born in Shenyang, Liaoning, China

Matrikel-Nr. 2474692


TECHNISCHE
UNIVERSITÄT
DARMSTADT

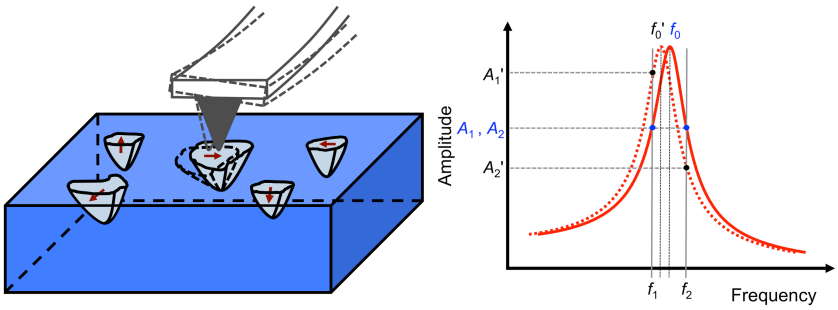

# Revealing the Domain Structure and the Relaxation Dynamics of BNT-Based Lead-Free Piezoceramics via Piezoresponse Force Microscopy

Referee: Prof. Dr. Robert Stark

Co-referee: Prof. Dr. Baixiang Xu

Fachbereich Material- und Geowissenschaften

Technische Universität Darmstadt

Date of submission: 13. 04. 2017

Date of oral examination: 13. 06. 2017

Darmstadt, 2017

D17

“When you drink the water, remember the spring.”

“饮水思源”

“If you can’t explain it simply, you don’t understand it well enough.”

— Albert Einstein

## Declaration

M.Sc. Na Liu
Nieder-Ramstädter-Str. 11,
64283 Darmstadt

### Declaration

The work described in this thesis was carried out in the group of Physics of Surfaces, Department of Materials Science, Technische Universität Darmstadt during the period from September 2012 to January 2017. I certify that the work in this thesis is the author's original work and no part of the thesis has been submitted for a degree at any other university or institute. Prior to the submission of this thesis, some work has been published as described in the relevant Chapters herein.

Eidesstattliche Erklärung

Hiermit erkläre ich an Eides statt, dass ich die vorliegende Dissertation selbstständig und nur mit den angegebenen Quellen und Hilfsmitteln angefertigt habe. Von mir wurde weder an der Technischen Universität Darmstadt noch an einer anderen Hochschule ein Promotionsversuch unternommen.

Darmstadt, den

(Na Liu)

The present cumulative dissertation summarizes the essential scientific findings published in the following peer-reviewed articles. The publications [1]−[3] are enclosed in the Chapter “cumulative publications of this thesis”.

[1] Na Liu, Robert Dittmer, Robert W. Stark and Christian Dietz, “Visualization of polar nanoregions in lead-free relaxors via piezoresponse force microscopy in torsional dual *ac* resonance tracking mode”, *Nanoscale*, **7**, 11787 (2015).

[2] Matias Acosta, Na Liu, Marco Deluca, Sabrina Heidt, Ines Ringl, Christian Dietz, Robert W. Stark and Wook Jo, “Tailoring ergodicity through selective A-site doping in the $Bi_{1/2}Na_{1/2}TiO_3$-$Bi_{1/2}K_{1/2}TiO_3$ system”, *Journal of Applied Physics*, **117**, 134106 (2015).

[3] Na Liu, Matias Acosta, Shuai Wang, Bai-Xiang Xu, Robert W. Stark and Christian Dietz, “Revealing the core-shell interactions of a giant strain relaxor ferroelectric $0.75Bi_{1/2}Na_{1/2}TiO_3$-$0.25SrTiO_3$”, *Scientific Reports*, **6**, 36910 (2016).

# Table of Contents

**Declaration** ..... **I**

**Table of Contents** ..... **III**

**List of Symbols and Abbreviations** ..... **V**

**1 Introduction** ..... **1**

**2 Fundamentals** ..... **4**

**2.1 Ferroelectrics** ..... **4**

2.1.1 Dielectricity ..... 4

2.1.2 Piezoelectricity ..... 7

2.1.3 Ferroelectricity ..... 8

**2.2 Relaxor Ferroelectrics** ..... **16**

2.2.1 Characteristics of Relaxor Ferroelelctrics ..... 16

2.2.2 Temperature-dependent Phase States in Relaxors ..... 23

2.2.3 Field-induced Transitions in Canonical Relaxors ..... 28

2.2.4 Bismuth Sodium Titanate $Bi_{1/2}Na_{1/2}TiO_3$-based Lead-free Relaxor Ferroelectric Ceramics ..... 30

**2.3 Piezoresponse Force Microscopy** ..... **32**

2.3.1 Operating Principle of the Atomic Force Microscope ..... 32

2.3.2 Principle of Piezoresponse Force Microscopy ..... 33

2.3.3 Modes of Piezoresponse Force Microscopy ..... 36

**3 Cumulative Part of the Present Thesis** ..... **40**

**3.1 Visualization of Polar Nanoregions in $(1-x)(Bi_{1/2}Na_{1/2}TiO_3\text{-}Bi_{1/2}K_{1/2}TiO_3)\text{-}x(BiMg_{1/2}Ti_{1/2}O_3)$ Relaxor Ferroelectrics via Piezoresponse Force Microscopy in Torsional Dual *AC* Resonance Tracking Mode** ..... **41**

3.1.1 Experimental and Method ..... 41

3.1.2 Results and Discussion ..... 48

3.1.3 Statement of Personal Contribution ..... 57

**3.2 Nanoinsight into Relaxation Behavior and Ergodicity Distribution in La-doped $Bi_{1/2}Na_{1/2}TiO_3$-$Bi_{1/2}K_{1/2}TiO_3$ Relaxors via Piezoresponse Force Microscopy** ..... **59**

3.2.1 Experimental and Method ..... 59

3.2.2 Results and Discussion ..... 65

3.2.3 Statement of Personal Contribution ..... 80

**3.3 Revealing the Core-shell Interactions in a Relaxor Piezoceramic $0.75Bi_{1/2}Na_{1/2}TiO_3\text{-}0.25SrTiO_3$ via Piezoresponse Force Microscopy** ..... **81**

3.3.1 Experimental and Method ..... 81

3.3.2 Results and Discussion ..... 84
3.3.3 Statement of Personal Contribution ..... 92

**4 Conclusions and Outlook ..... 93**
**4.1 Conclusions ..... 93**
**4.2 Outlook ..... 96**

**References ..... 98**

**Cumulative Publications ..... 112**

**Acknowledgements**

**List of Publications**

**Curriculum Vitae**

## List of Symbols and Abbreviations

| | |
|---|---|
| AC | Alternating current |
| AFM | Atomic force microscope |
| BMT | Bismuth magnesium titanate $Bi_{1/2}Mg_{1/2}TiO_3$ |
| BNT | Bismuth sodium titanate $Bi_{1/2}Na_{1/2}TiO_3$ |
| BNT-25ST | 0.75 mol fraction BNT-0.25 mol fraction $SrTiO_3$ |
| BKT | Bismuth potassium titanate $Bi_{1/2}K_{1/2}TiO_3$ |
| BT | Barium titanate $BaTiO_3$ |
| BZT | Barium zinc titanate $Bi(Zn_{1/2}Ti_{1/2})O_3$ |
| DART | Dual ac resonance tracking |
| DC | Direct current |
| DSHO | Damped simple harmonic oscillator |
| ER | Ergodic relaxor |
| FC | Field cooling |
| FE | Ferroelectric |
| KNN | Potassium sodium niobate $K_{1/2}Na_{1/2}NbO_3$ |
| LPFM | Lateral piezoresponse force microscopy |
| MPB | Morphotropic phase boundary |
| NR | Non-ergodic relaxor |
| PE | Paraelectric |
| PFM | Piezoresponse force microscopy |
| PLZT | Lead lanthanum zirconate titanate $Pb_{1-x}La_x(Zr_{1-y}Ti_y)_{1-x/4}O_3$ |
| PMN | Lead magnesium niobate $Pb(Mg_{1/3}Nb_{2/3})O_3$ |
| PNRs | Polar nanoregions |
| PZN | Lead zinc niobate $Pb(Zn_{1/3}Nb_{2/3})O_3$ |
| PZT | Lead zirconate titanate $Pb(Zr_{1-y}Ti_y)O_3$ |
| Relaxor(s) | Relaxor ferroelectric(s) |
| SF-PFM | Single frequency piezoresponse force microscopy |
| SNR | Signal-to-noise ratio |
| SPM | Scanning probe microscopy |
| SS-PFM | Scanning spectroscopy-piezoresponse force microscopy |

| | |
|---|---|
| STM | Scanning tunneling microscopy |
| ST | Strontium titanate ($SrTiO_3$) |
| STEM | Scanning transmission electron microscopy |
| TDART | Torsional dual ac resonance tracking |
| TEM | Transmission electron microscopy |
| VDF-TrFE | Vinylidene fluoridetrifluoroethilene |
| VPFM | Vertical piezoresponse force microscopy |
| XRD | X-ray diffraction |
| ZFC | Zero field cooling |
| $A_{ac}$ | First harmonic piezoresponse amplitude |
| $d_{33}$ | Piezoelectric coefficient measured along the poling direction |
| $d_{33}^{eff}$ | Effective piezoelectric coefficient |
| $Q$ | Quality factor |
| $\varphi$ | Phase shift with respect to the driving field |
| $E_a$ | Activation energy |
| $E_c$ | Coercive electric field |
| $E_{loc}$ | Local electric field |
| $f_D$ | Debye frequency |
| $\beta$ | Stretching exponent |
| $P_{max}$ | Maximum polarization |
| $P_s$ | Spontaneous polarization |
| $\rho$ | Dipole moment |
| $S_{max}$ | Maximum strain |
| $S_r$ | Remanent strain |
| $T_B$ | Burns temperature |
| $T_C$ | Curie temperature |
| $T_d$ | Depolarization temperature |
| $T_f$ | Freezing temperature |
| $T_m$ | Temperature at the maximum of the real part of the relative permittivity |
| $\tan(\delta)$ | Dielectric loss factor |
| $\tau$ | Characteristic relaxation time |
| $\xi$ | Correlation length |

| | |
|---|---|
| $\varepsilon$ | Dielectric permittivity |
| $f_0$ | Contact resonance frequency |
| $k$ | Spring constant |
| $k_B$ | Boltzmann constant |
| $V_{ac}$ | Driving voltage |
| $V_{dc}$ | Poling voltage |

# 1 Introduction

Piezoelectric ceramics are useful materials for the application in actuators, transducers, generators, multilayered capacitors, ultrasonic motors and sensors[1-4] because of their ability to convert electrical into mechanical energy and vice versa. The most commonly used piezoelectric materials are lead-containing materials with an estimated market share of billions of dollars worldwide,[5] particularly lead zirconate titanate $Pb(Zr_{1-x}Ti_x)O_3$ (PZT), which was reported first in the 1950s.[6] However, lead oxide is highly contaminating the environment and harmful for human and animal health in general because of its volatilization at high temperatures, *e.g.* during calcination and sintering.[7,8] Since the release of the regulations, Restriction of the use of certain Hazardous Substances in electrical and electronic equipment (RoHS) and the directives Waste Electrical and Electronic Equipment (WEEE),[9-11] many attempts have thus been made by researchers to develop lead-free piezoelectric alternatives.[7,12,13] However, there is still no single compound that is capable of replacing PZT across the entire range of applications. Three main solid solution-based systems have been recognized as most promising substitutions for PZT, including barium titanate $BaTiO_3$ (BT)-based, bismuth sodium $Bi_{1/2}Na_{1/2}TiO_3$/potassium titanate $Bi_{1/2}K_{1/2}TiO_3$ (BNT or BKT)-based, and potassium sodium niobate $(K_{1/2}Na_{1/2})NbO_3$ (KNN)-based materials. Among them, the BNT-based pseudo-binary or -ternary lead-free solid solutions have potential to exhibit outstanding electromechanical properties featuring a normalized strain value ($S_{max}/E_{max}$) above 500 pm/V, which is comparable to or even surpasses that of the lead-based counterparts.[7,14-16]

For actuator applications, a chemically disordered system characterized by a diffuse phase transition and a large dielectric permittivity observed in a broad temperature range can be formed through heterovalent substitutions on both A or B sites in $ABO_3$ perovskite ferroelectric crystals. This material modification can result in a giant strain response to relatively weak external stimuli. These relaxor ferroelectrics (relaxors) were discovered by Smolenskii *et al*.[17,18] The peculiarities of relaxors are related to the inhomogeneous distribution of the chemical order causing a polarization inhomogeneity on the nanoscale, so-called polar nanoregions (PNRs) that emerge below the Burns temperature $T_B$. For example, in a typical relaxor such as $Pb(Mg_{1/2}Nb_{2/3})O_3$ (PMN), PNRs with short-range order are claimed to appear at $T_B$.[19,20] Upon cooling, these PNRs grow from 2–3 nm in size to 10 nm below the freezing temperature $T_f$ (approximately 220 K for PMN).[21] This nanoscale domain formation is in contrast to the creation of long-range ordered macro domains in conventional ferroelectrics.

The presence of short-range ordered PNRs and their dynamics response to the external electric field are claimed to be the origin of the extraordinary electromechanical properties of relaxors, particularly of their large strain response.[22-26] The domain structure of PNRs that originates from the existence of the chemical disorder and the associated inherent random field induced by cation doping or replacement play a crucial role for the functionalities of lead-free relaxors.[27] In conventional relaxors, there are two different states depending on the temperature: the ergodic relaxor state transforms reversibly to the ferroelectric state and the non-ergodic relaxor state transforms irreversibly during electric field cycling.[28,29] Macroscopically, in the ergodic relaxor state (cooling down to Burns temperature, $T_B$), the PNRs are very small and their dipole moments are thermally

fluctuating between equivalent orientations. Upon cooling, the increased number of PNRs and enhancement of their interactions slow down the dynamics of the PNRs, which results in a broad distribution of the size of PNRs and randomness of their interactions. Hence, the broad relaxation time distribution and the resulting frequency-dependent broad peak of the dielectric permittivity *vs*. temperature $T_m$ are observed in relaxors. Cooling to freezing temperature, the relaxation time diverges and clusters of PNRs freeze to a glassy state, which is also called the non-ergodic relaxor state.[30,31] In both states, the average symmetry of the relaxor system remains cubic.[32,33] Because the domain structure and their dynamic response to applied electric fields mainly determine the macroscopic electromechanical behavior of ferroelectrics, the necessity to study the properties of PNRs of lead-free relaxors with respect to the size, morphology, and dynamic response and evolution to a static or dynamic external electric stimulus, is undisputed. PNRs can be studied by various experimental methods, *e.g.*, X-ray diffraction (XRD),[22] diffuse neutron scattering,[34,35] dielectric spectroscopy,[30,36] acoustic emission,[37,38] and high resolution transmission electron microscopy (TEM).[39] However, these techniques do not provide a direct observation or the local identification of the virgin state of PNRs.

Over the past two decades, the scanning probe microscope has revolutionized materials science, including the field of ferroelectricity, by providing high-resolution and nondestructive characterization of domain structures as well as observation of local polarization dynamics of ferroelectric materials.[40-42] Among the scanning probe microscopy (SPM) techniques, the most commonly used technique for the nanoscale characterization of ferroelectrics is piezoresponse force microscopy (PFM).[42] In 1992, PFM was first demonstrated by Güthner and Dransfeld who locally polarized a ferroelectric copolymer film using a biased-tip of the SPM and subsequently imaged the polarized regions applying an *ac* electric field.[43] Since then, PFM has been substantially developed and used to characterize ferroelectric thin films,[44-46] ceramics,[47] and single crystals[48,49] with a high spatial resolution to directly, nondestructively, and dynamically study the domain morphology, domain nucleation and growth subjected to an external electrical field, mechanical stress, temperature changes, and the mechanism of polarization reversal and relaxation on the nanoscale. The advantages of PFM over other techniques for studying conventional ferroelectrics include: 1) straightforward operation and easy implementation; 2) high spatial resolution (few tens of nanometers); 3) high sensitivity to the local polarization as a result of the direct tip-surface interaction; 4) non-destructive character; 5) effective manipulation of nanoscale domains and local spectroscopy capabilities, which makes this method also well suited for studying relaxors.[50-53]

In classical lead-containing relaxors, nanometer-sized domains with distinctive structures can be observed using PFM, *e.g.* labyrinthine-structured PNRs with the size of approximately 50 nm shown in La-doped lead zirconium titanate (PLZT) ceramic with a stoichiometric formula of $Pb_{0.9125}La_{0.0975}(Zr_{0.65}Ti_{0.35})_{0.976}O_3$,[54] nanodomains embedded in micrometer-sized domains in $0.8Pb(Mg_{1/2}Nb_{2/3})O_3$-$0.2PbTiO_3$ (PMN-PT) single crystal.[26] In lead-free relaxor piezoelectric ceramics, because of tiny size (approximately 1−10 nm) of PNRs in the ergodic state and the limited lateral resolution of the instrument, the virgin domain structure of PNRs are difficult to visualize by the conventional PFM.[23,25] However, by applying sufficient high electric field, these PNRs can be aligned and form the long-range ordered ferroelectric domain, which confirms the capability of the

polarization reversal.[55-58] Additionally, it was demonstrated that higher switching electric field is needed for the relaxor materials that are characterized by a higher degree of ergodictiy.[25] Thus, the local distribution of the ergodicity and the dynamics of PNRs in the lead-free relaxor systems can be revealed using PFM to locally switch the PNRs and study the subsequent relaxation behavior of the poled domains. However, the data acquisition rate is limited in the conventional PFM imaging (several minutes per frame or longer), which restricts its application to unravel the dynamic effects (< several seconds) of PNRs.[57] Recently, a high-speed version of PFM imaging was reported by Huey's group to facilitate the observation of the ferroelectric domain nucleation[59] and switching,[60,61] reaching considerably enhanced imaging rates (in the range of 1 frame per second and beyond) for the study of ferroelectric thin film capacitor. However, high-speed PFM on visualizing the relaxation behavior on lead-free relaxor ceramics was not reported. Because of the small size and high dynamics of PNRs in lead-free relaxor ceramics, the spatiotemporal resolution of conventional PFM techniques is not sufficient to thoroughly study this class of materials on the nanoscale. Thus, novel PFM techniques providing high spatial and temporal resolution have to be developed.

The aim of this thesis is to gain an insight into the fundamental physical mechanisms with respect to the distribution of the ergodicity and PNRs dynamics in different kinds of BNT-based lead-free relaxor ferroelectrics with peculiar macroscopic properties, *e.g.* a large electromechanical response, using PFM. Existing PFM modes that are restricted in spatial and temporal resolution were further developed and improved to enhance the visualization of the PNRs structure and observe the relaxation behavior of electric field-induced ferroelectric domains. The distribution of local degree of ergodicity associated with the dynamics of PNRs, and the interfacial interactions of ergodic and non-ergodic quantities were studied. The fundamental microscopic-structure–macroscopic-properties relationship of lead-free relaxors was elucidated.

# 2 Fundamentals

In this Chapter, the basic principles of conventional ferroelectrics and relaxor ferroelectrics, as well as the scanning probe microscope to study the electromechanical properties of these materials, are introduced. A brief introduction to the properties and the polarization mechanisms of dielectrics, piezoelectrics and ferroelectrics, is provided. A description of relaxors that are the main subject of this thesis is provided, and the family of BNT-based lead-free relaxors is introduced. Additionally, the fundamental of the SPM mode PFM, which allows the study of the domain distribution, evolution and relaxation of ferroelectrics on the nanoscale is discussed.

## 2.1 Ferroelectrics

In this Chapter, the basics of dielectrics and their polarization mechanisms and an introduction into the subgroups piezoelectrics, ferroelectrics, and relaxor ferroelectrics is provided.[62]

### 2.1.1 Dielectricity

All dielectrics are electrically insulating crystalline or non-crystalline materials, where polarization can be induced by applying an external electric field $\boldsymbol{E}$.[63] In dielectrics, the total polarization $\boldsymbol{P}$ induced by an external electric field $\boldsymbol{E}$ can be described as in the following equations:

$$\boldsymbol{P} = \varepsilon_0 \cdot \chi \cdot \boldsymbol{E} = \varepsilon_0 \cdot (\varepsilon_r - 1) \cdot \boldsymbol{E} = \varepsilon_0 \cdot \varepsilon_r \cdot \boldsymbol{E} - \varepsilon_0 \boldsymbol{E} = \boldsymbol{D} - \varepsilon_0 \cdot \boldsymbol{E} \tag{2.1}$$

where $\boldsymbol{D}$ is the macroscopic dielectric displacement, $\varepsilon_0$ is the permittivity of the vacuum, $\chi$ is the electric susceptibility that is related to the strength of the polarizability in response to the electric field, and $\varepsilon_r$ is the relative dielectric permittivity (dielectric constant). Note: $\boldsymbol{D}$ and $\boldsymbol{E}$ are first-rank tensors or vectors.

The macroscopic polarization in crystalline dielectrics is an overall effect of distinct local polarization components under the applied electrical field. There are four types of polarization, which are schematically described in Fig. 2.1:[63-65]

- Electronic polarization, which occurs in all dielectrics, is deformation of the symmetrical distribution of the electron clouds relative to the inner positive nucleus of atoms.
- Ionic polarization is observed in ionic crystals. It is displacement of the sub-lattices of the positively charged cations and negatively charged anions relative to each other.
- Orientation or dipolar polarization can be observed in dipolar materials consisting of asymmetrically structured molecules or particles with a permanent dipole moment exhibiting a statistical distribution of the dipole moment directions in the absence of an electric field, *e.g.* water.
- Space charge polarization occurs in dielectrics with spatial heterogeneities of charge carrier (electrons, holes or ions) densities. This interfacial polarization is often observed in materials with heterogeneous grain boundaries, where the field could trap the charges at the interface.

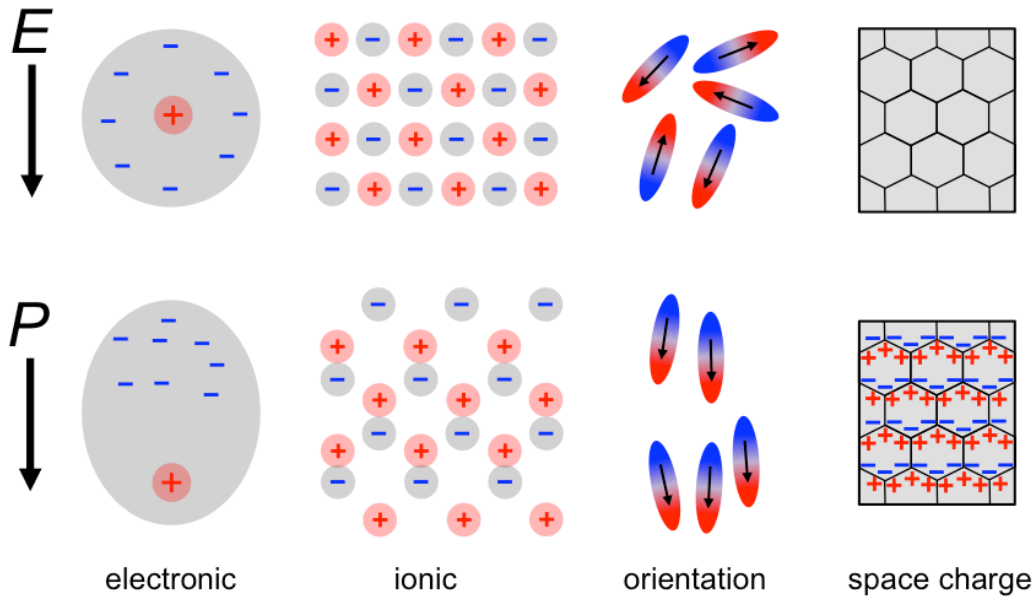


Figure 2.1 Origins of electric polarization in dielectrics.

Thus, the macroscopic polarization $\boldsymbol{P}$ in crystalline dielectrics is quantitatively expressed as the sum of the individual dipole moments $\boldsymbol{p}_n$ with a density of $N_n$, $\boldsymbol{P} = \sum_n N_n \boldsymbol{p}_n$, where $n$ represents each type of polarization.[63] Each individual dipole moment $\boldsymbol{p}_n$ is induced by a local electric field $\boldsymbol{E}_{n,\mathrm{loc}}$ applied at the position of the particular dipole with a polarizability of $\alpha_n$.

$$\boldsymbol{p}_n = \alpha_n \boldsymbol{E}_{n,\mathrm{loc}}. \tag{2.2}$$

In dielectrics, because of the very high electrostatic interactions between the dipoles, the local field $\boldsymbol{E}_{n,\mathrm{loc}}$ is given by the superposition of the applied external electric field $\boldsymbol{E}$ and the sum of electric field $\boldsymbol{E}'$ induced by all other dipoles.

**Dielectric Dispersion and Dielectric Relaxation**

Polarization in dielectrics is the process of the local charge movement responding to an electric field, which requires different times to perform, and thus different frequency components are apparent in a Fourier transform. As seen from the dispersion of the dielectric permittivity shown in Fig. 2.2, microscopic polarizations can be distinguished by characteristic frequencies (different relaxation times).[63] Electronic and ionic polarizations are intrinsic contributions that only originate from the lattice itself, exhibiting resonance processes, whereas the contributions such as the space charge and orientation polarizations are extrinsic because of the strong influence of the neighbor dipoles, presenting relaxation processes. The dielectric dispersion of each polarization causes the dielectric loss of the material, and thus the total permittivity of a dielectric can be mathematically expressed by a complex equation:

$$\varepsilon = \varepsilon' + i\varepsilon'', \tag{2.3}$$

where $\varepsilon$ is the complex permittivity, $\varepsilon'$ is the real part of complex permittivity and $\varepsilon''$ is the imaginary part of the complex permittivity. The $\tan(\delta)$ is designated as the dielectric loss factor, and is expressed as:

$$\tan(\delta) = \frac{\varepsilon''}{\varepsilon'}. \tag{2.4}$$

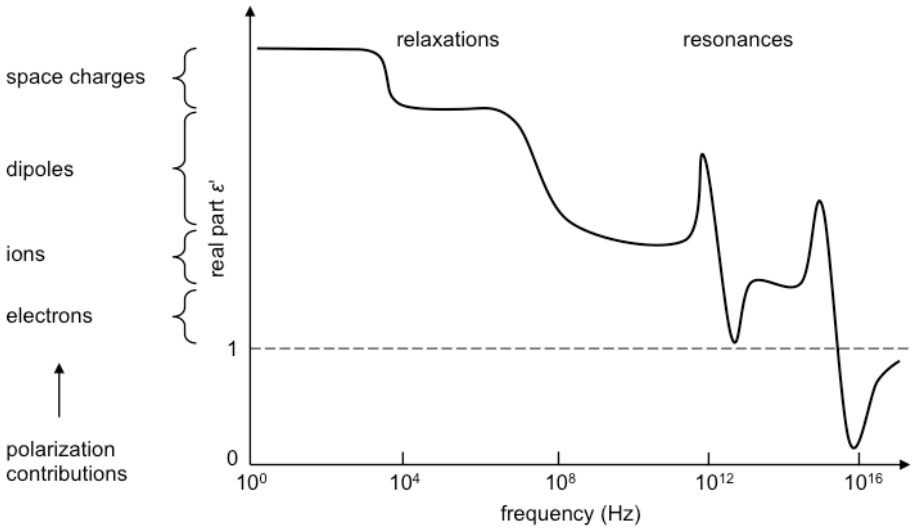


Figure 2.2 Schematic of the frequency dependence of the real part of the dielectric permittivity (from Ref. [63]).

**Electrostriction**

Electrostriction is a property of all dielectric materials regardless of the symmetry, which can result in an overall strain of the dielectric under an applied electric field. There is a quadratic coupling between the strain and electric field, or between the strain and polarization, which can be expressed as:[66,67]

$$S_{ij} = M_{ijkl} E_k E_l \tag{2.5}$$

or

$$S_{ij} = Q_{ijkl} P_k P_l \tag{2.6}$$

with the induced second-rank tensor strain $S_{ij}$, the electric field $E_k$ and $E_l$, the polarization $P_k$ and $P_l$, and the electric field-related fourth-rank tensor $M_{ijkl}$, and the polarization-related electrostrictive tensor $Q_{ijkl}$. As shown in Equations (2.5) and (2.6), the strain depends on $E^2$, and therefore is independent of the polarity of the electric field.

Among the 32 crystallographic point groups describing all crystalline materials based on their symmetry operations and polarity, the classification of dielectrics and their respective physical properties are depicted in Fig. 2.3.[62,67]

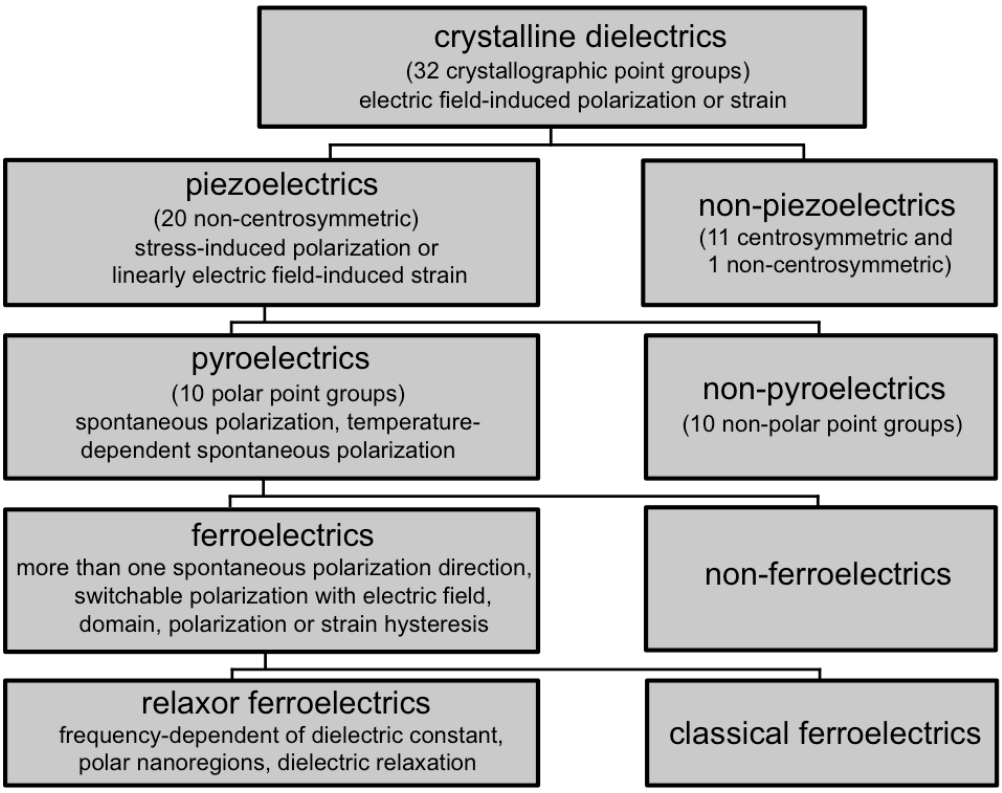


Figure 2.3 Classification of crystalline dielectrics and their respective physical properties.

### 2.1.2 Piezoelectricity

One of the subgroups of dielectrics, as depicted in Fig. 2.3, is piezoelectric, which exhibits the physical phenomenon of interconversion between electrical (input/output) and mechanical (output/input) energy, and thus, these materials can be widely applied as sensors, transducers, ultrasonic motors, generators, and actuators.[6,68] Piezoelectricity was first discovered by Pierre and Jacques Curie in 1880 in certain crystals such as quartz, tourmaline, zinc blends, and Rochelle salt.[69] The requisite condition for the occurrence of piezoelectricity is the lack of a symmetric center in the piezoelectric crystals. Out of 32 symmetry point groups, 21 classes are non-centrosymmetric, but the piezoelectricity cannot be presented in point group 432.[67] When a piezoelectric crystal is subject to an external mechanical stress $\sigma_{jk}$, surface charges on the crystal can be generated. This is the direct piezoelectric effect, which can be expressed as:

$$D_i = d_{ijk}\sigma_{jk}, \tag{2.7}$$

where the direct piezoelectric coefficient $d_{ijk}$ is a third-rank tensor, and the stress $\sigma_{jk}$ is a second-rank tensor. When a piezoelectric crystal is subject to an external electric field $E_k$, strain can be induced. This defines the converse piezoelectric effect in piezoelectric materials, which can be described by:

$$S_{ij} = d_{ijk}E_k, \tag{2.8}$$

where $d_{ijk}$ is the indirect piezoelectric coefficient that is numerically the same as the direct piezoelectric coefficient. This equality is based on the thermodynamics in which $S_{ik} = S_{ki}$ and $d_{ijk}$ is symmetrical in $j$ and $k$. The Voigt notation in the matrix can be simplified as follows: $i = 1, 2, 3$ represents the indices $ii = 11, 22, 33$ and $i = 4, 5, 6$ represents $ij = 23$ or $32$, $13$ or $31$, $12$ or $21$.[70] For piezoelectrics, the most important constant is the longitudinal piezoelectric coefficient, which is referred to as $d_{33}$. The strain is linearly proportional to the electric field in piezoelectric crystals (Equation (2.8)), which is different from the electrostrictive effect that follows a non-linear strain-field relationship. The characterization of strain versus electric field in ferroelectrics is shown in Chapter 2.1.3.

Among the 20 piezoelectric classes, 10 point groups are pyroelectrics that possess a unique polar axis, which causes a built-in polarization that is called spontaneous polarization (see Fig. 2.3).[6] In the absence of the applied electric field, the polarization can be changed by varying the temperature. If the direction of the spontaneous polarization can be switched by applying a sufficiently high external electric field, the materials are called ferroelectrics, which are a subgroup of the pyroelectrics. Detailed information about the phase transition, domain formation, and switching will be provided in the following sections.

### 2.1.3 Ferroelectricity

Ferroelectrics are a subgroup of piezoelectrics and pyroelectrics shown in Fig. 2.3. Ferroelectrics are crystals that have a unique polar axis and a switchable macroscopic spontaneous polarization $\boldsymbol{P}_\mathrm{S}$ by an external electric field.[71] At equilibrium, a ferroelectric crystal exhibits a noncentrosymmetric structure, so that the spontaneous polarization remains by symmetry. In ferroelectric crystals, there are at least two discrete stable or metastable equilibrium states of non-zero spontaneous polarization $P_\mathrm{S}$ with different orientations in the absence of an applied electric field. By applying the required external electric field at a certain temperature to the ferroelectric crystal, which is stronger than the coercive field, the spontaneous polarization vector can be switched between these orientations ($\boldsymbol{P}_\mathrm{S}$ to $-\boldsymbol{P}_\mathrm{S}$), which is called polarization reversal. The switching process between these states changes the energy of the states through coupling between the electric field and polarization. Ferroelectricity occurs in ferroelectric crystals at temperatures below a critical point, called the Curie temperature $T_\mathrm{C}$, where the material undergoes a structural phase transition from the paraelectric phase that is characterized by a normal dielectric behavior above $T_\mathrm{C}$ to the ferroelectric phase that is characterized by a reversible spontaneous polarization below $T_\mathrm{C}$.[6] In general, the peculiarities of ferroelectric materials such as piezoelectricity, high non-linear optical activity, pyroelectricity, switchable polarization, and non-linear dielectric behavior facilitate a wide range of functional applications in electronic devices such as microactuators, microwave phase filters, sensors, infrared detectors, and non-volatile memories.[72,73]

The phenomenon of ferroelectricity was discovered in 1921 in the Rochelle salt single crystal.[74] Since the discovery of ferroelectricity in the perovskite type material $BaTiO_3$ in 1949,[75] many $ABO_3$ perovskite type

compounds have been developed and extensively reviewed for ferroelectric properties. In the following section, the perovskite structure and important physical properties are introduced.

**Ferroelectric Perovskite Crystal**

The generalized construction of the unit cell that has an $ABO_3$ perovskite structure is based on a cubic close-packed assembly of $AO_3$ with the A ions coordinated with 12 oxygen ions, and the B ions in the $BO_6$ octahedral interstices. Typically, cation A (*e.g.*, $Ba^{2+}$ or $Pb^{2+}$) has the valence from +1 to +3 and B cation (*e.g.*, $Ti^{4+}$) has the valence from +3 to +6. For many compounds that have the $ABO_3$ structure, because of small variations in the sizes of A and B ions, the deviation from an ideal cubic structure can be measured through the Goldschmidt's tolerance factor $R$ based on the filling of a unit cell by ions with radii $r$, expressed as follows:[71,76]

$$R = \frac{r_A + r_O}{\sqrt{2}(r_B + r_O)}. \tag{2.9}$$

A typical tolerance factor is in the range of $0.95 < R < 1.06$. When $R < 1$, the A atom is small compared with the cavity between $BO_6$, *i.e.* the A ion is not capable of effectively bonding with all 12 neighboring oxygen ions. If $R$ is smaller but very close to one, rotation and tilting of the $BO_6$ is favored, such as for $SrTiO_3$ and $CaTiO_3$. The smaller $R$ is, the stronger the lattice is distorted and the more the 6-fold coordination of A ions is favored, *e.g.* as for $LiNbO_3$. When $R > 1$, the structure is dominated by the A-O distance and the B ion is very small for the $BO_6$ leading to a small polar distortion developing in the structure, *e.g.* as for $BaTiO_3$.

Taking $BaTiO_3$ as an example (Fig. 2.4), at high-temperature and in the paraelectric phase, the single crystal has a centrosymmetric cubic structure, meaning that the center of positive charges ($Ba^{2+}$ and $Ti^{4+}$) coincides with the center of negative charges ($O^{2-}$), which leads to a zero spontaneous polarization $P_S$. Cooling down to Curie temperature (for $BaTiO_3$, $T_C \approx 128$ ℃), the cubic symmetry in the paraelectric phase can be broken during the phase transformation to a tetragonal distortion leading to a change in the shape of the unit cell, which is associated with the creation of a spontaneous polarization. The off-center shift of $Ti^{4+}$ and $O^{2-}$ relative to $Ba^{2+}$ is shown in Fig. 2.4, and it illustrates the spontaneous polarization along the *c*-axis. Six enantiomorphism $P_S$ in the tetragonal phase are originated from the six equivalent directions (positive and negative orientations) along their *a*-axis of the cubic cell.

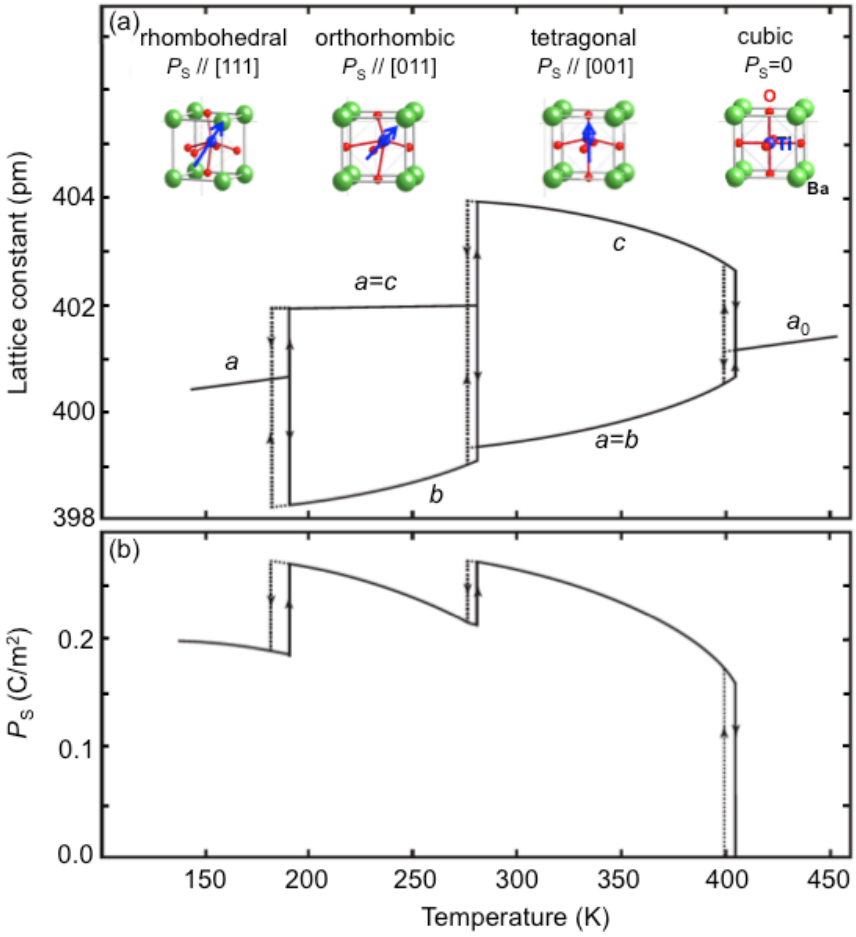


Figure 2.4 Temperature-dependency of the lattice constant (**a**) and spontaneous polarization (**b**) of the corresponding $ABO_3$ perovskite crystal structures of $BaTiO_3$ (adapted from Ref. [77]).

**Temperature-dependent Phase Transition of the Ferroelectric Crystal**

Thermodynamically, the transition from the high-temperature paraelectric phase into the low-temperature ferroelectric phase involves a change in entropy that is accompanied by the changes in the lattice constants, dielectric permittivity $\varepsilon$, and polarization $P$. This relationship can be described by the Landau-Devonshire theory based on the analysis of equilibrium behavior near a phase transition, which uses an order parameter such as characterization (*i.e.* polarization $P$) changing from a zero value for high symmetry (paraelectric phase) to a finite value for lower symmetry (ferroelectric phase).[71,78] This theory is appropriate for bulk systems with spatially uniform polarization, *i.e.* the local fluctuation in the order parameter is small.

Phase transitions can be described using Gibbs free energy $G$, which can be expanded near the transition as a power series of the order parameter, polarization $P$. Taking only one polar axis, this energy can be described as:

$$G(P) = G_0 + \frac{1}{2}\alpha P^2 + \frac{1}{4}\beta P^4 + \frac{1}{6}\gamma P^6 - E \cdot P, \tag{2.10}$$

where $\alpha$, $\beta$ and $\gamma$ are the Landau coefficients. The initial energy for the unpolarized, unstrained crystal $G_0$ should be zero. The equilibrium configuration of the system can be determined by the minimum of the free

energy $G(P)$. The first partial derivative provide the necessary condition for this minimum, which is described as followed:

$$\frac{\partial G}{\partial P} = \alpha P + \beta P^3 + \gamma P^5 - E = 0, \tag{2.11}$$

then the electric field $E$ can be expressed as:

$$E = \alpha P + \beta P^3 + \gamma P^5. \tag{2.12}$$

By differentiating the Equation (2.12) with respect to *P*, the linear dielectric susceptibility $\chi$ in the paraelectric state ($P = 0$) can be written as:

$$\frac{1}{\chi} = \frac{\partial E}{\partial P} = \alpha. \tag{2.13}$$

It is assumed that around the Curie point ($T \sim T_0$),

$$\alpha = \alpha_0(T - T_0) \tag{2.14}$$

Combining Equations (2.13) and (2.14), the relationship between the dielectric permittivity and the temperature obeys the Curie-Weiss law in the high-temperature paraelectric phase ($T > T_0$)

$$\chi = \frac{C}{T - T_0}, \tag{2.15}$$

where $C = \alpha_0^{-1}$ is the Curie constant, $T_0$ is the Curie-Weiss temperature that is the intersection point obtained by extrapolating the $\chi^{-1}$ to the *x*-axis, and $T$ is the absolute temperature.

Thus, Equation (2.10) can be modified as follows:

$$G(P) = \frac{1}{2}\alpha_0(T - T_0)P^2 + \frac{1}{4}\beta P^4 + \frac{1}{2}\gamma P^6 - E \cdot P. \tag{2.16}$$

Generally, two kinds of transitions may occur in ferroelectrics, which is determined by the sign of $\beta$, as follows: when $\beta < 0$, the first order transition occurs, corresponding to discontinuous changes of $P_S$; when $\beta > 0$, the second order transition occurs, referring to continuous changes of $P_S$.[6,79]

Figure 2.5 shows the temperature-dependent free energy (a,d), spontaneous polarization (b,e) and susceptibility (c,f) in its first order (a,b,c) and second order (d,e,f) paraelectric-ferroelectric transition. In the first order transition, at $T = T_C$, the free energy has three equal states (Fig. 2.5(a)) corresponding to the discontinuous change of the spontaneous polarization $P_S$ and the dielectric susceptibility $\chi$ at $T_C$ (Fig. 2.5(b) and (c)).[71,80] A thermal hysteresis can be observed in the first order transition, *e.g.* $BaTiO_3$, as shown in Fig. 2.4(b). In the second order phase transition, at $T \geq T_0$, the free energy has one potential well, which changes to two potential wells (Fig. 2.5(d)). A spontaneous polarization $P_S$ emerges below $T_0$, and further continuously increases with decreasing temperature. Thus, the order parameter, *i.e.* spontaneous polarization $P_S$, transforms continuously as

a function of temperature, as shown in Fig. 2.5(e). At $T_0$, the dielectric susceptibility $\chi$ diverges, and the slope of $\chi^{-1}$ versus the temperature curve is two times larger below $T_0$ than that above $T_0$, as shown in Fig. 2.5(f). $LiNbO_3$ is the second-order phase transition ferroelectric representative.

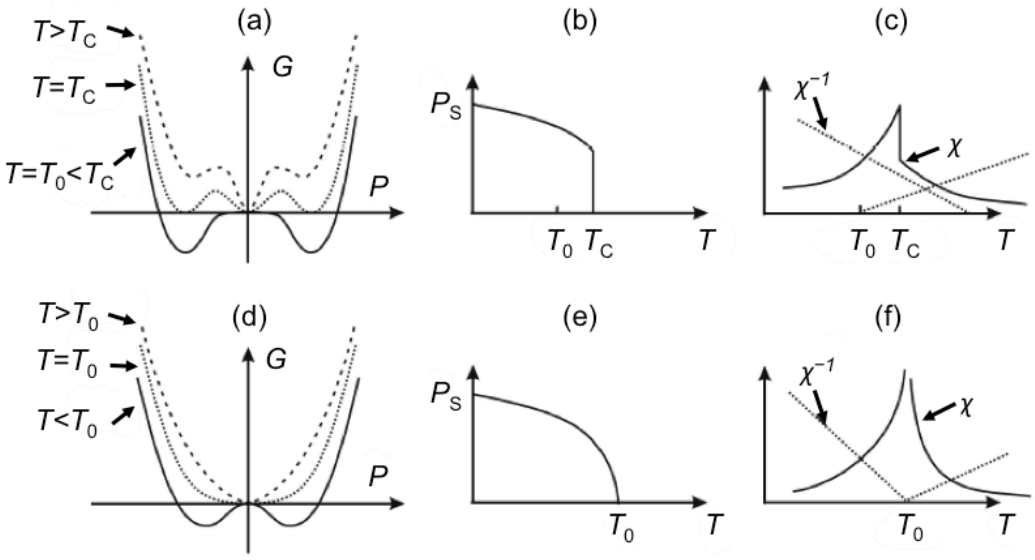


Figure 2.5 Schematic diagrams illustrating (**a**,**d**) temperature-dependent free energy $G(P)$ as a function of the polarization, (**b**,**e**) temperature-dependent spontaneous polarization $P_S$, and (**c**,**f**) temperature-dependent susceptibility $\chi$ and its inverse $\chi^{-1}$, for a first order (**a**,**b**,**c**) and second order (**d**,**e**,**f**) phase transition (from Ref. [71]).

**Domains and Domain Walls**

Below $T_C$, at least two of the aforementioned six equivalent spontaneous polarizations in the tetragonal symmetry (*e.g.* $BaTiO_3$ single crystal), can develop according to the electric and elastic boundary conditions imposed onto the lattice. The regions in the crystal that are uniformly polarized in each of these directions are referred to as ferroelectric domains. To minimize the electrostatic and elastic energy of the system, the differently orientated domains are separated by the boundaries or regions with a width of about several lattice constants, which are defined as domain walls.[62] There are 180° and non-180° (such as 90° domain wall in the tetragonal crystal) ferroelectric domain walls, along which the orientations of spontaneous polarizations are antiparallel or perpendicular (for 90°), respectively. As shown in Fig. 2.6, below Curie temperatures, domains separated by 180° walls are formed to minimize the depolarizing fields (electrostatic energy) that are associated with surface charges, which are purely ferroelectric domains. However, domains separated by 90° walls are formed to minimize the elastic energy associated with the mechanical constraints of the crystal and reduce the depolarizing field, which contain both the ferroelastic and ferroelectric domains.[70,81,82] The virgin domain pattern depends on many factors including the crystal symmetry, the defect structure, the magnitudes of the spontaneous polarization, the electrical conductivity, and the elastic and dielectric compliances as well as the history of the crystal preparation and sample geometry.[83]

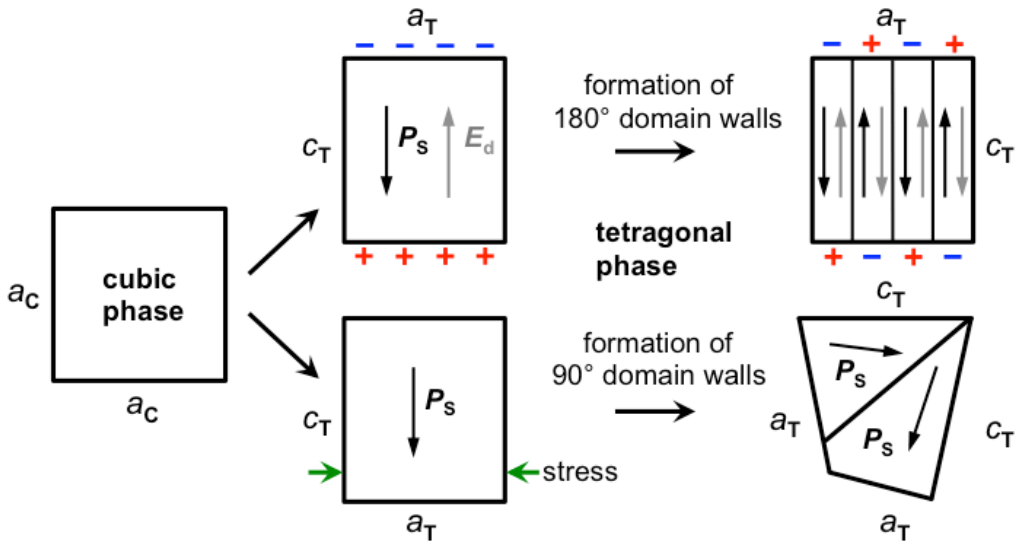


Figure 2.6 Mechanisms of the formation of 180° and 90° ferroelectric domain walls in a tetragonal symmetry (adapted from Ref. [84]).

There is the complex set of elastic and electric boundary conditions in ferroelectric ceramics or polycrystalline films. Consequently, many domains can be formed in an individual grain as shown in Fig. 2.7. Because of the random distribution of the grain orientations, the direction of associated spontaneous polarizations through the whole material is also random, causing zero net macroscopic polarization $P_S = 0$ (Fig. 2.7(a)) in a so-called "virgin" ferroelectric (before poling). Consequently, the macroscopic physical properties, such as pyroelectric and piezoelectric effects cannot be observed. However, by applying a strong external electric field $E$ (typically in the range of 10−100 kV/cm) at an elevated temperature, the ferroelectric material will be in a poled state because of the reoriented domains within individual grains in the direction of the applied field (Fig. 2.7(b)). Thus, macroscopically pyroelectric and piezoelectric properties can be revealed in the poled state of ferroelectric. This is called poling or the switching process of the ferroelectric domains in the external electric field, by which the grains cannot be reoriented.

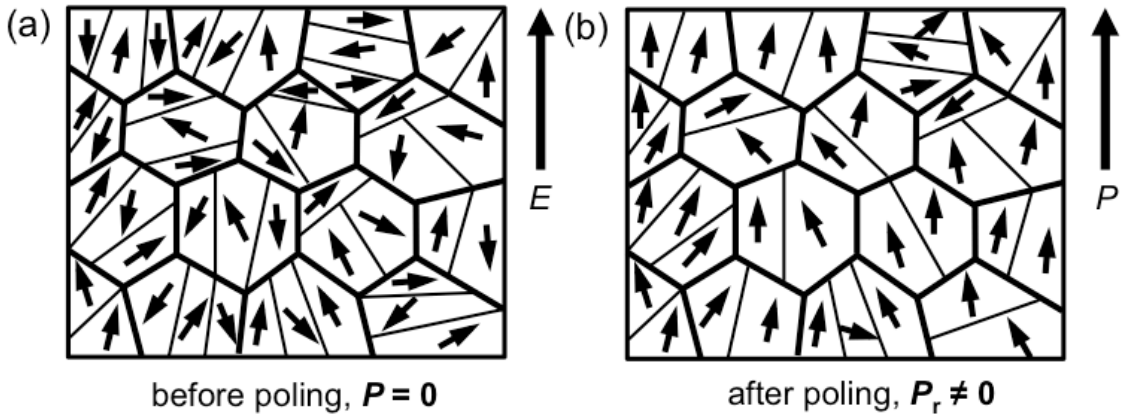


Figure 2.7 Domain orientations before (**a**) and after (**b**) poling a polycrystalline ferroelectric having randomly orientated grains. Many domain walls are still present after the poling process, but the net remanent polarization $P_r$ is nonzero.

**Macroscopic Hysteresis Loops**

The domain reversal or switching from one state to another state using an applied electric field, takes the form of a signature of the bulk ferroelectric called a "hysteresis loop (*P*-*E* loop)",[70,85] as illustrated schematically in Fig. 2.8. Experimentally, these macroscopic hysteresis loops can be measured using the Sawyer-Tower method.[9] In the initial state marked as (*A*) in Fig. 2.8, because the domains are randomly aligned, the net macroscopic polarization ***P*** is zero (*cf.* state 1). By applying external electric fields, domain wall motions occur, which can lead to domain reorientations accompanied by domain nucleation and growth. As shown in Fig. 2.9, there are reversible or irreversible domain-wall motions, depending on the distribution of the local lattice energy potential generated by lattice defects.[70,86] The reversible domain wall motion (*i.e.* the motion in the potential well *a*, Fig. 2.9) is the effect of applying small electric fields, and the polarization linearly increases with the applied electric field (*cf.* segment of *AB* in Fig. 2.8). In this process, the electric field is not strong enough to change the domain orientations but can vibrate the domain walls around an equilibrium position.[87]

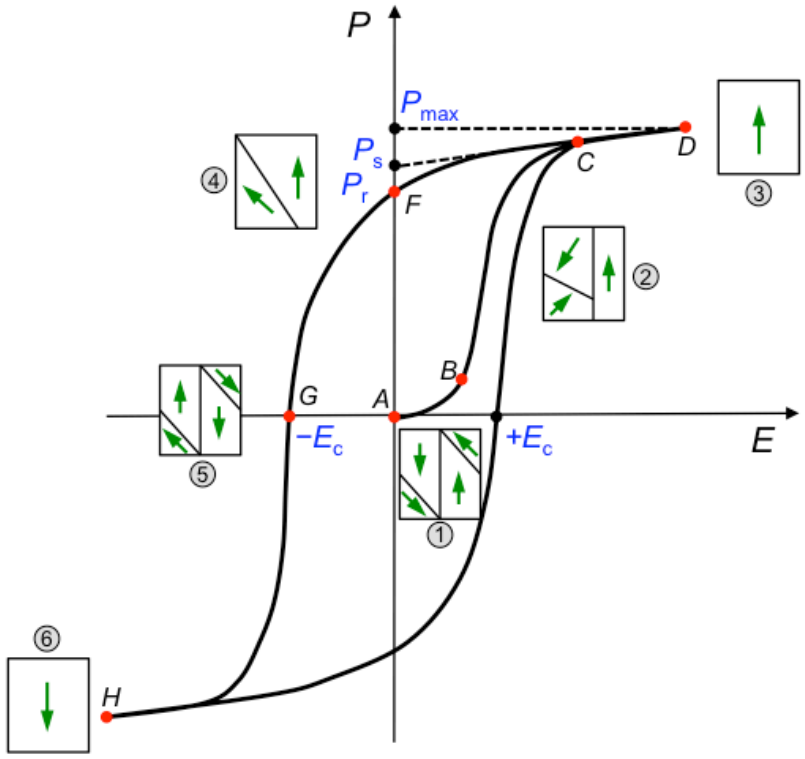


Figure 2.8 Representative macroscopic hysteretic behavior of the ferroelectric polarization versus the applied electric field, (*P*-*E*) hysteresis loop. Circles with arrows represent the domain orientation of the material at the indicated fields.

Switching off the external electric field, the domain wall can move back to its initial location, which can explain why this process is reversible.[68] By further increasing the strength of the applied field that reaches the domain poling process (segment *BC*, Fig. 2.8), the applied electric field is strong enough to move the domain wall into the new equilibrium positions by overcoming the adjacent potential barriers, *cf.* from potential well *a* to *b* in Fig. 2.9. This irreversible motion of the domain walls causes domains to irreversibly switch toward the direction

of the external electric field (*cf.* state 2 in Fig. 2.8). Consequently, the polarization of the system increases non-linearly, when the strength of the applied electric field increases.

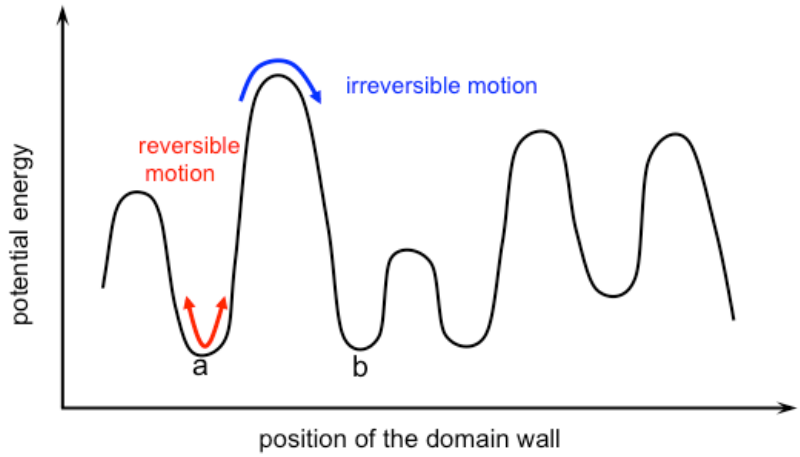


Figure 2.9 Schematic drawing of the single domain wall displacements in a medium containing random defects (adapted from Ref. [86]).

Once the switchable domains are all aligned (*C*), the polarization ($P$)-field ($E$) dependence comes to a linear relationship (segment *CD*) and the polarization reaches a maximum value $P_{\max}$ (*D*), *cf.* state 3 in Fig. 2.8. Thus, ferroelectric domain patterns are decisive in the ferroelectric behavior. Taking into account the random orientations of inherent grains in polycrystalline ceramics, and the stray energy, defects and/or mechanical stresses in ceramics, the saturated domain state is generally not a monodomain. Spontaneous polarization $P_S$ can be acquired by extrapolating the linear portion *CD* to the polarization axis (or zero-field axis). Decreasing the field strength, domains can back-switch to crystallographically allowed directions in response to local electric and mechanical fields. Because of the irreversible domain switching, the net polarization is nonzero at zero electric field, defining a remanent polarization $P_r$ (*cf.* state 4 in Fig. 2.8), following the path *DCF*. As the electric field decreases to a sufficient negative value (coercive field, $-E_c$), the polarization decreases following the path *FG* to a zero value (point *G*). Further decreasing the field leads to the negative polarization with a reversed domain orientation (*H*) compared with *D*, *cf.* state 5 in Fig. 2.8. A subsequent increase of the field induces the negative remanent polarization $-P_r$ and then a positive $+E_c$.

Accompanied by the electric field-induced polarization reversal, the strain-field hysteresis can be generated because of the existence of the converse piezoelectric effect and the electrostriction in ferroelectrics. As shown in Fig. 2.10, a characteristic butterfly-shaped loop, the *S*-*E* hysteresis loop, is the consequence of the domain reversal under the influence of an external electric field. Thus, at any given electric field strength, the piezoelectric coefficient can be calculated using $d_{33} = S_{33}/E_3$, which is the slope of the strain curve. The negative strain $S_{neg}$ occurs because of the compression of the classical ferroelectric or non-ergodic ferroelectric ceramics from the reversed strain state ($S_{33} = 0$) to G where the poled polarization of domains switch back to zero, and is about to begin the domain switching in the opposite direction under the negative electric field.

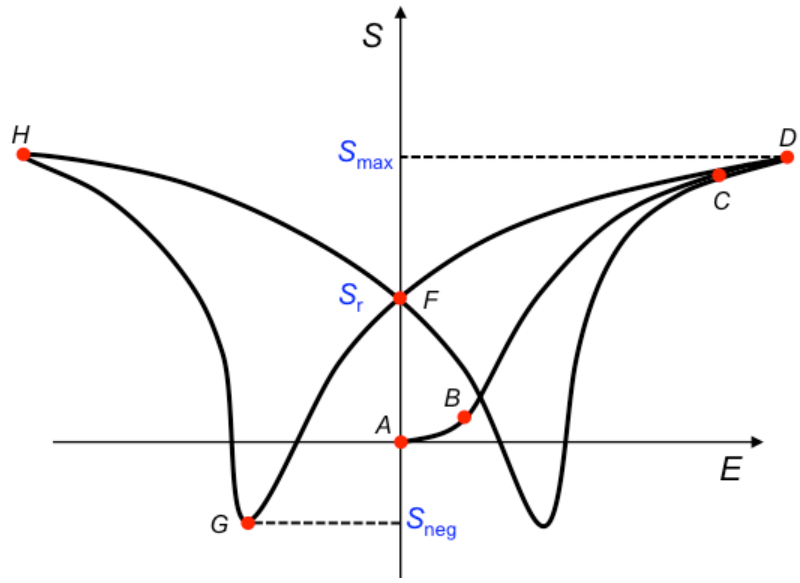


Figure 2.10 Schematic description of the electric field-induced strain loop originating from the converse piezoelectric effect in ferroelectrics.

**Local Hysteresis Loops**

The macroscopic hysteresis loops are the average response of the overall dipole moments of the individual domains in the bulk that is subjected to an external electric field. An ideal ferroelectric hysteresis loop should be symmetrical. However, in reality, the shape of the loops can be strongly affected by many factors, such as the charged defects, mechanical stresses, measurement conditions, thickness of the samples, material composition, and thermal treatment. Therefore, local hysteresis loops in the different locations in the ferroelectric bulk should differ from each other and from the macroscopic *P*-*E* loops. The local hysteresis loops can be measured by switching spectroscopy PFM (SS-PFM) that will be introduced in Chapter 2.3.3.

## 2.2 Relaxor Ferroelectrics

### 2.2.1 Characteristics of Relaxor Ferroelelctrics

Ferroelectrics with relaxor properties in the $ABO_3$ perovskite structures were first discovered by Smolensky *et al.* in the mid 1950s.[18,88] As the name suggests, a relaxor ferroelectric (abbreviated as "relaxor") is closely related to a conventional ferroelectric but shows peculiar behaviors that have attracted considerable attention.[8,89] The significant macroscopic characteristics of relaxors that are different from conventional ferroelectrics are shown in Fig. 2.11 and summarized as follows:[89]

- A relaxor is characterized by an absence of both spontaneous macroscopic polarization and macroscopic structural symmetry breaking, which is often described as a pseudocubic crystal structure.
- An electric field (***E***)-induced polarization (***P***), that features a smooth decrease of remanent polarization in a pinched *P*-*E* loop over a large temperature regime that results from the emergence and growth of local polar

nanoregions (PNRs) below Burns temperature $T_B$ is typical for a relaxor. However, a conventional ferroelectric is characterized by a square hysteresis *P*-*E* loop with a large remanent polarization up to Curie temperature $T_C$ (*cf*. Fig. 2.11(a) and (b)).

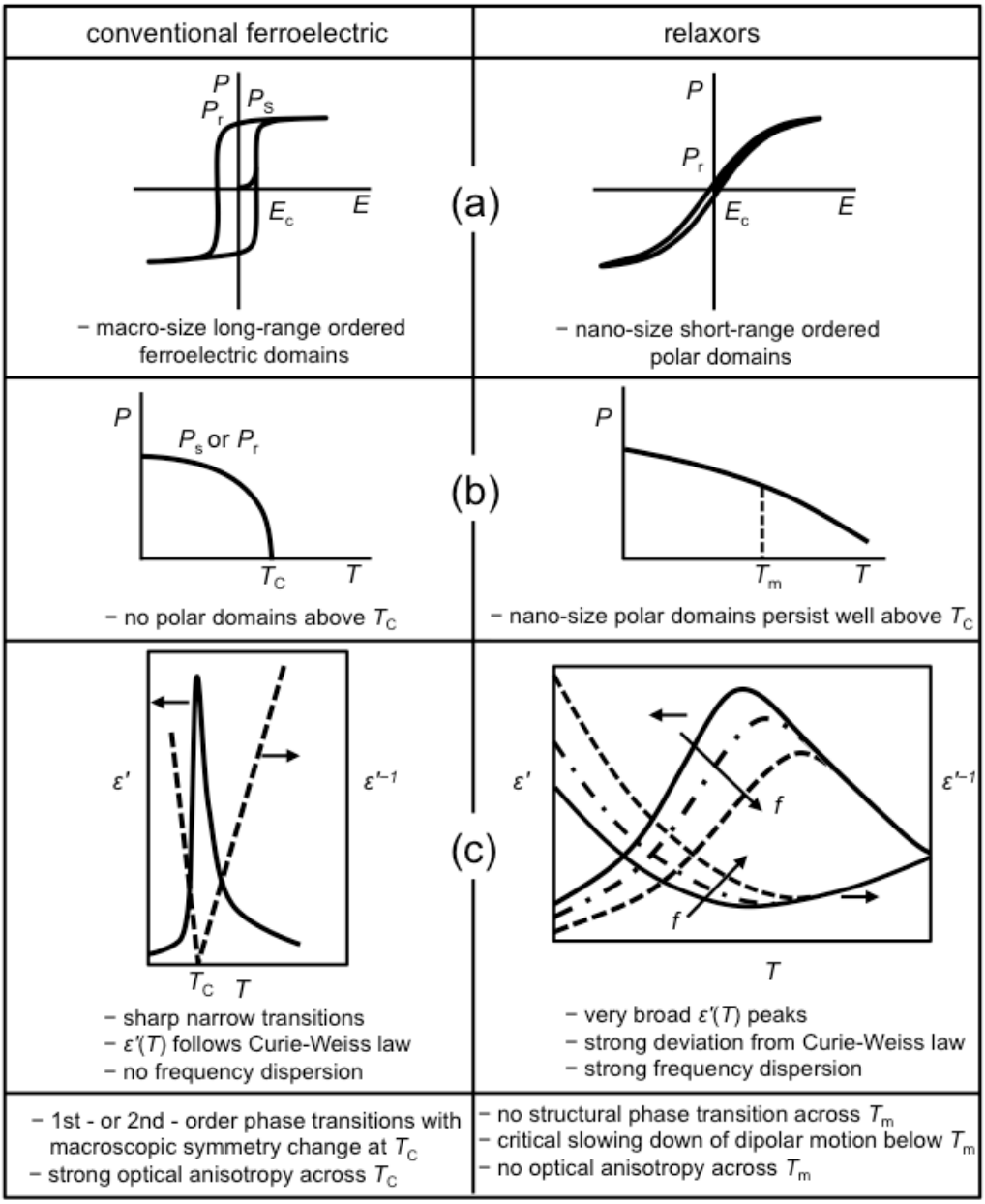


Figure 2.11 Comparison of the main characteristics that are representative of relaxor ferroelectrics and conventional ferroelectrics (**a**) polarization (*P*) hysteresis, *P*-*E* loop, (**b**) temperature dependent polarization, (**c**) dielectric permittivity $\varepsilon(T)$ versus temperature *T* for different frequencies. $T_C$ is the Curie temperature of a ferroelectric, corresponding to the phase transition from the paraelectric to the ferroelectric state. In a relaxor, $T_m$ is the characteristic temperature where the maximum dielectric constant occurs, and $T_m$ varies as the change of frequency (adapted from Ref. [82]).

- A strong frequency dispersion of the maximum dielectric permittivity $\varepsilon(T_m)$ over a broad temperature range (Fig. 2.11(c)) characterizes a relaxor. The peak value of the dielectric constant shifts to higher temperatures and decreases in magnitude with increasing frequency and is thus characterized by a strong deviation from

the Curie-Weiss law, which is obeyed at $T \geq T_C$ (Fig. 2.11(b)).[89,90] Conversely, a dielectric permittivity that is frequency-independent and that shows a sharp and narrow peak at $T_C$ can be found for conventional ferroelectrics.

- Cooling to $T_B$, the relaxor system in the paraelectric state transforms to an ergodic relaxor state with the presence of randomly oriented nanometer-scaled PNRs. These short-range ordered PNRs in relaxors are thought to be embedded into the long-range disordered cubic structure, which is in contrast to the long-range order in ferroelectrics.
- The relaxor system can be transformed into the ferroelectric state by applying a sufficiently high electric field or zero-field cooling.

Relaxors have great potential for many applications for numerous reasons: the high electrostrictive coefficient can be used for actuators, the large dielectric permittivity is favorable in capacitors, the novel electro-optical characteristics can be exploited as shutters or optical modulators, and the large electric field-induced strain response is comparable to the most used commercial lead-containing ferroelectric, such as PZT piezoceramic. Thus, relaxors are potential candidates for components such as actuators, sensors, generators, and transducers.[5]

**Relaxor Perovskite Materials**

The relaxor behavior can mainly be observed in mixed perovskite compounds, as shown in Table 2.1, which lists a few typical relaxors with lead-containing perovskite compounds. In these relaxor systems, the B site is occupied by one, two, or more heterovalent cations, such as $Mg^{2+}$ and $Nb^{5+}$, $Sc^{3+}$ and $Ta^{5+}$, and $Zn^{3+}$ and $Nb^{5+}$ in $Pb(Mg_{1/3}Nb_{2/3})O_3$ (PMN), $Pb(Sc_{1/2}Ta_{1/2})O_3$ (PST) and $Pb(Zn_{1/3}Nb_{2/3})O_3$ (PZN), respectively.[18,91-93] All of these compounds share the standard $ABO_3$ perovskite structure. Another example is the non-stoichiometric complex perovskite solid solution, *e.g.*, $(Pb_{1-3/2x}La_x)(Zr_{1-y}Ti_y)O_3$ (PLZT), in which the substitution of $La^{3+}$ for $Pb^{2+}$ ions necessarily leads to vacancies on the A sites. These A-site vacancies locally inhibit the displacement of the Zr/Ti atoms from the central positions and disrupt the ferroelectric order.[39] Most recently, relaxor characteristics were also observed in the lead-free perovskite solid solutions based on $Bi_{1/2}Na_{1/2}TiO_3$ (BNT), $Bi_{1/2}K_{1/2}TiO_3$ (BKT) and $(K_{1/2}Na_{1/2})NbO_3$ (KNN).[94] The essential condition for the occurrence of relaxor-like behavior is the existence of a compositional disorder (micro-heterogeneous regions), which is usually a disorder in the arrangement of different ions with different valences or sizes on the crystallographically equivalent sites of the perovskite $ABO_3$ structure.[18,95]

Several models describing the physical mechanisms behind the macroscopically observable relaxor behavior have been proposed, including the diffuse phase transition model,[88,96] the superparaelectric model,[89] the dipolar glass model,[30] the random-field model,[97] the random-site model,[98] the spherical-random-bond–random-field model,[99] and the bi-relaxation model.[100] However, none of these models provides a complete understanding of the mechanisms behind and the origin of relaxor behavior. The commonality in all these models is the focus on studying the compositional fluctuation-induced local chemical order−disorder distribution and the short-range polar clusters or nanoregions.[36,90,92,95,101,102]

Table 2.1 Examples of complex perovskites characterized as typical relaxors (adapted from Ref. [36]).

| | | |
|---|---|---|
| B-site complex | $Pb(Mg_{1/3}Nb_{2/3})O_3$ | PMN |
| | $Pb(Zn_{1/3}Nb_{2/3})O_3$ | PZN |
| | $Pb(Fe_{2/3}W_{1/3})O_3$ | PFW |
| | $Pb(Sc_{1/2}Nb_{1/2})O_3$ | PSN |
| | $Pb(Sc_{1/2}Ta_{1/2})O_3$ | PST |
| | $Pb(In_{1/2}Nb_{1/2})O_3$ | PIN |
| A-site complex | $(Pb_{1-3x/2}La_x)(Zr_yTi_{1-y})O_3$ | PLZT |
| | $(Pb_{1-3x/2}La_x)TiO_3$ | PLT |
| | $(Pb_{1-x}Ba_x)(Zr_yTi_{1-y})O_3$ | PBZT |

**Compositional Order and Disorder in Complex Perovskites**

The chemical/compositional disorder in the complex perovskite relaxors has been believed to be responsible for the diffuse phase transition. It has been observed in complex perovskite ferroelectric solid solutions that as the composition becomes close to a favorable homogeneous distribution representing the structural ordering, the phase transition sharpens and the dielectric dispersion weakens[103,104] (*e.g.* $\varepsilon$ *vs.* $T$ curve for a ferroelectric material in Fig. 2.11(c)). Using lead-scanium-tantalate $Pb(Sc_{1/2}Ta_{1/2})O_3$ (PST) as a suitable example,[105,106] Setter and Cross[91] showed that the degree of order in B-site cations ($Sc^{3+}$ and $Ta^{5+}$) can be controlled through the suitable annealing treatment. They determined an order parameter $S_O$ that was experimentally defined by the square root of the intensity of the (111) superlattice reflection that was normalized by the intensity of the adjacent (200) normal lattice reflection. As shown in Fig. 2.12, a sharp phase transition in the PST single crystal with a $S_O$ of 0.8 was observed, while a highly dispersive phase transition was shown in the PST crystal with a lower $S_O$ of 0.35.[91] If the B-site cations were completely ordered, *i.e.* $S_O = 1.0$, the PST single crystal would behave like a normal ferroelectric, exhibiting a sharp ferroelectric to paraelectric transition at approximately 25 ºC, which was estimated using the Curie-Weiss law.

The physical mechanism of the formation of the order-disorder can be explained in the example of the disordered $ABO_3$ perovskite system with trivalent and pentavalent ions sharing the B site, *e.g.* $A(B^{+3}_{1/2}B^{+5}_{1/2})O_3$. The ground state should be compositionally ordered, meaning $B^{+3}$ and $B^{+5}$ occupy their own respective crystallographically equivalent B-site sublattices to minimize the electrostatic and elastic energies in the system induced by the different valence-induced charges or different ionic radii between $B^{+3}$ and $B^{+5}$ ions. This ordering process is a relaxation process of site exchange between $B^{+3}$ and $B^{+5}$ cations via thermal diffusion, which can be determined by the size and charge difference between the B cations.[107] For some complex perovskites, such as the disordered as-sintered PST and PSN ceramics, which have a finite relaxation time (thermal diffusion process) of the ordering at an appropriate heat treatment, an order-disorder phase transition can take place, *e.g.* long-range ordering with $S_O$ of 0.86 in PST ceramics using long-term annealing ($\geq$ 24 h) at 1000 °C.[105,107,108] The

ordered arrangement of ions in the PST unit cell is illustrated in Fig. 2.13, where $Sc^{3+}$ and $Ta^{5+}$ ions are alternatively located on adjacent B sites, creating a superstructure with a complete translational symmetry.[106]

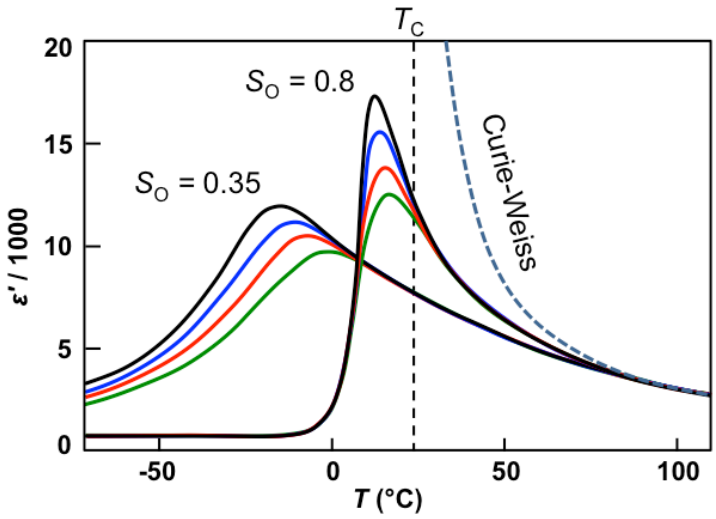


Figure 2.12 Temperature-dependent dielectric permittivity of a $Pb(Sc_{1/2}Ta_{1/2})O_3$ single crystal for two different degrees of compositional ordering $S_O$. The Curie-Weiss law was applied to estimate the Curie point (from Ref. [109]).

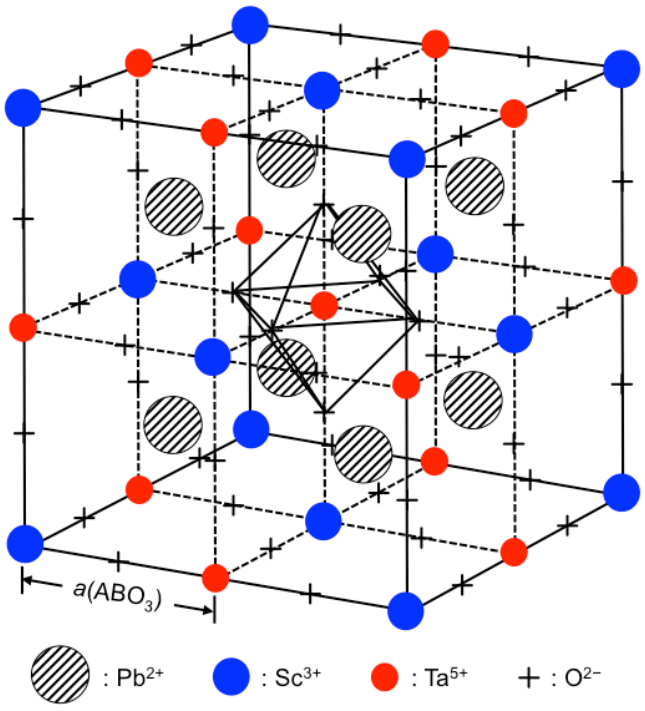


Figure 2.13 Structure of ordered perovskite $Pb(Sc_{1/2}Ta_{1/2})O_3$ (adapted from Ref. [91]).

Conversely, such a sudden order-disorder phase transition cannot occur in most of relaxor perovskites, such as the prototypical relaxor PMN, because the relaxation time (thermal diffusion) for the ordering is so long that the disorder cannot be changed by any heat treatments. Thus, the resulting quenched material at low temperatures exhibits a local inhomogeneous compositional disorder in the relaxor system as a consequence of an incomplete ordering process, resulting in the short-range ordered regions embedded into a disordered matrix. Using the

charge balanced "random-site" model, a schematic diagram of the arrangement of B ion arrangements in a PMN relaxor was suggested, as shown in Fig. 2.14.[36,110] In the locally ordered B-site distribution region (inside the solid line) where the stoichiometry $Pb(Mg^{2+}_{1/3}Nb^{5+}_{2/3})O_3$ is preserved, one of the B-sublattices (drawn with a dashed line) is occupied exclusively by $Nb^{5+}$ (red circle), whereas the $Mg^{2+}$ and the rest of $Nb^{5+}$ randomly occupy the remaining B sites in a ratio of 2:1.[110]

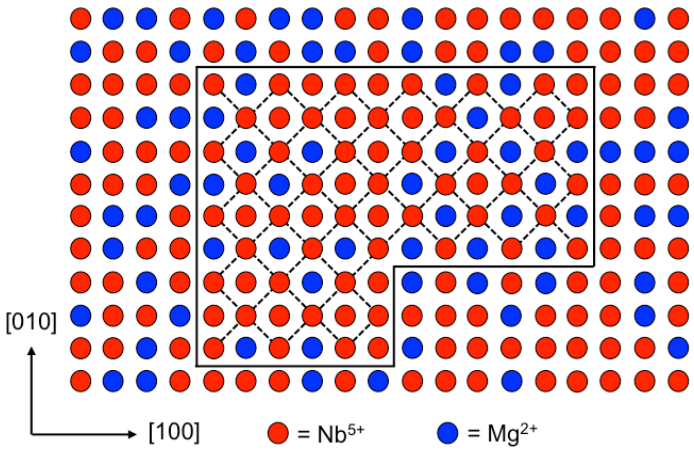


Figure 2.14 Schematic diagram of ordered chemical nanoregions (the area in the solid line) embedded in the disordered matrix of the $Pb(Mg^{2+}_{1/3}Nb^{5+}_{2/3})O_3$ perovskite. One of the two sublattices inside the ordered nanoregion (dashed line) is formed by $Nb^{5+}$ ions only, the other sublattice inside the ordered nanoregion exhibits a random distribution of $Nb^{5+}$ and $Mg^{2+}$ based on the "random site" model (adapted from Ref. [36]).

A relaxor state results from an incomplete phase transition towards a complete thermal equilibrium, leading to a metastable state during observation time. The principle behind this incomplete phase transition is the chemical disorder and the crystal imperfection that lower the local symmetry around the ordered region. In the end, a diffuse phase transition occurs, where the dielectric permittivity at $T_m$ exhibits a broad peak and is characterized by strong frequency dispersion. Thus, the chemical disorder in relaxor systems plays a crucial role in contrast to the conventional ferroelectrics. In conventional ferroelectrics with a negligible chemical disorder, the ferroelectricity is a total average over the local chemical disorder/order as revealed by conventional crystallographic studies, which cannot reflect the variations of the local crystal chemistry. When the degree of the chemical disorder is high enough to disturb the entire long-range ordering in a conventional ferroelectric, the random inhomogeneity occurs and leads to relaxor properties. Thus, in a disordered relaxor system, ferroelectric properties (*i.e.*, $P_S$ and $T_C$) vary from one nano-/microscopic region to another.[103] This symmetry-breaking on the local scale causes the formation of a short-range ordered and polarized structure, *i.e.* PNRs, below $T_B$. These PNRs are thermally fluctuated between the equivalent polarization directions and embedded into a paraelectric matrix as shown in Fig. 2.15. It has been confirmed by diffuse neutron scattering and X-ray scattering experiments,[111-114] when cooling down the relaxor system to the temperature $T_B$, highly fluctuated PNRs with the size of 1−5 nm emerge. As decreasing the temperature decreases, these PNRs further grow in size and dynamically slow down.[92] Below the freezing temperature $T_f$, PNRs freeze and the relaxor behaves similarly to a dipolar glass.[115,116]

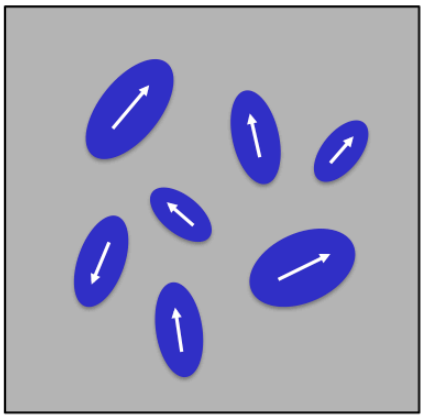

Figure 2.15 Schematic of polar nanoregions embedded into a cubic matrix.

**Random Field**

In conventional ferroelectrics, because of the continuous symmetry of the order parameter, many properties can be explained by the mean-field approximation whose basic physical idea is that each ion on the lattice site could 'feel' the same average field produced by the other lattice ions.[117] As a result, below $T_C$, the ions in the lattices consequently shift in a cooperative manner forming macroscopically long-range order domains.[117] It is expected that each domain can be characterized by a Debye-like relaxation time $\tau$.[90,117] The size and state of the ferroelectric domains are determined by the electrostatic and elastic energy.

Conversely, for the $ABO_3$ perovskite relaxor systems, the random lattice disorder can be generated by the substitutional disorder, vacancies, and other lattice imperfections, leading to the random-site dipolar entities in the host lattice.[90] Thus, the distribution of the strong local random field (electric and/or strain field) has to be considered in the relaxors, *i.e.*, different ions in a given lattice 'feel' different fields induced by other lattice ions, defects and impurities.[117] The random fields in relaxors are largely uncorrelated and quenched, which plays a crucial role in the thermal evolution and stabilization of PNRs during cooling.[118] As shown in Fig. 2.16, in a relaxor system of *c*-cut $Sr_xBa_{1-x}Nb_2O_6$ (SBN) single crystal, the PNR size decreased with an increase in the $Sr^{2+}$: $Ba^{2+}$ ratios.[119] Indirectly, this indicated an enhancement of the random filed with the increase of the chemical disorder in the relaxor system.[118] Recently, using rigorous modeling and phase field simulations, Wang *et al.* reported that the random field effect is stronger when the defect concentration is higher in the disordered ferroelectric system (*i.e.* relaxors with higher chemical disorder).[120] Under the influence of the random field, the long-range dipolar interactions of PNRs fluctuate to different degrees through the host lattice, which destroys the conventional ferroelectric phase transition in relaxor systems.[90,118,121,122] Thus, a more complex relaxational behavior with a distribution of different relaxation times that are relatively long, or up to infinity can be observed in relaxors compared with the conventional ferroelectrics.[90] Therefore, the mean-field approximation is not applicable to the relaxor system because there are no possible long-range interactions tending to suppress the inherent strong fluctuations of the small PNRs within the paraelectric matrix.[90] The random-field model was first proposed by Westphal, Kleemann and Glinchuk (WKG model) in a PMN relaxor, based on the random

distribution of $Mg^{2+}$ and $Nb^{5+}$ at B sites resulting in the charges in the local chemically ordered regions.[97,102]

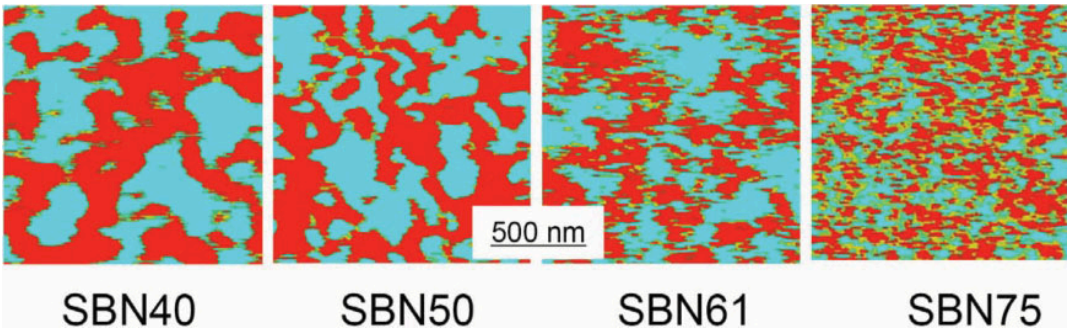


Figure 2.16 Surface polarization distributions in the relaxor material of $Sr_xBa_{1-x}Nb_2O_6$ single crystals characterized by vertical piezoresponse force microscopy, corresponding to compositions (**a**) SBN 40, (**b**) SBN 50, (**c**) SBN61 and (**d**) SBN75, respectively (from Ref. [118]).

### 2.2.2 Temperature-dependent Phase States in Relaxors

**Paraelectric State**

At high temperatures well above the Burns temperature $T_B$, the dipole moments associated with the dipolar entities already locally exist because of the charge imbalance introduced by the chemical disorder. However, the thermal fluctuations are so high that these dipole moments cannot manifest themselves, leading to a zero value of the net polarization. This state of the system is called the paraelectric (PE) state, as shown in Fig. 2.17.[82] The permittivity $\varepsilon(T)$ follows the Curie-Weiss law at high temperatures.

**Ergodic Relaxor State**

Upon cooling, the random-site dipoles can polarize the adjacent unit cells within the range of the correlation length $\xi$ of the host, shown in Fig. 2.18.[82] This correlation length $\xi$ increases with decreasing temperature. Cooling down to $T_B$, where the deviation from the Curie-Weiss law occurs, some dipole moments of the polarized nanoregions become well defined. These nanoregions are called PNRs, which are highly dynamic, lead to the transformation of the system from a paraelectric state into an ergodic relaxor state.[93] Below $T_B$, PNRs grow in both size and number according to the random-field potential.[71,90] In the ergodic relaxor state, the dipole moments of PNRs are weakly correlated and capable of thermally fluctuating as proposed by Cross *et al.*[89] As the temperature decreases, the dielectric permittivity increases, which is attributed to the dynamic slowing down of PNRs. Because a broad distribution of PNR sizes and random PNR-PNR interactions yield a broad distribution of relaxation times, a very broad frequency dependence of the dielectric permittivity at the maximum temperature $T_m$ occurs. The term "ergodic" was introduced by Boltzmann from the Greek words for path (*odos*) and work (*ergon*) to describe the energy surfaces in statistical mechanics.[123] An ergodic process (ergodicity) is used to describe a certain dynamic system in which the time average of a certain property of one sequence of events is equal to the ensemble average over the entire space, under appropriate conditions.[23] In solid state physics, the terminology, ergodicity, was used to describe magnetic spin glasses that are disordered

systems exhibiting a freezing transition.[124] Similarly, Viehland *et al*. used the terminology in the disordered relaxor systems.[30,125]

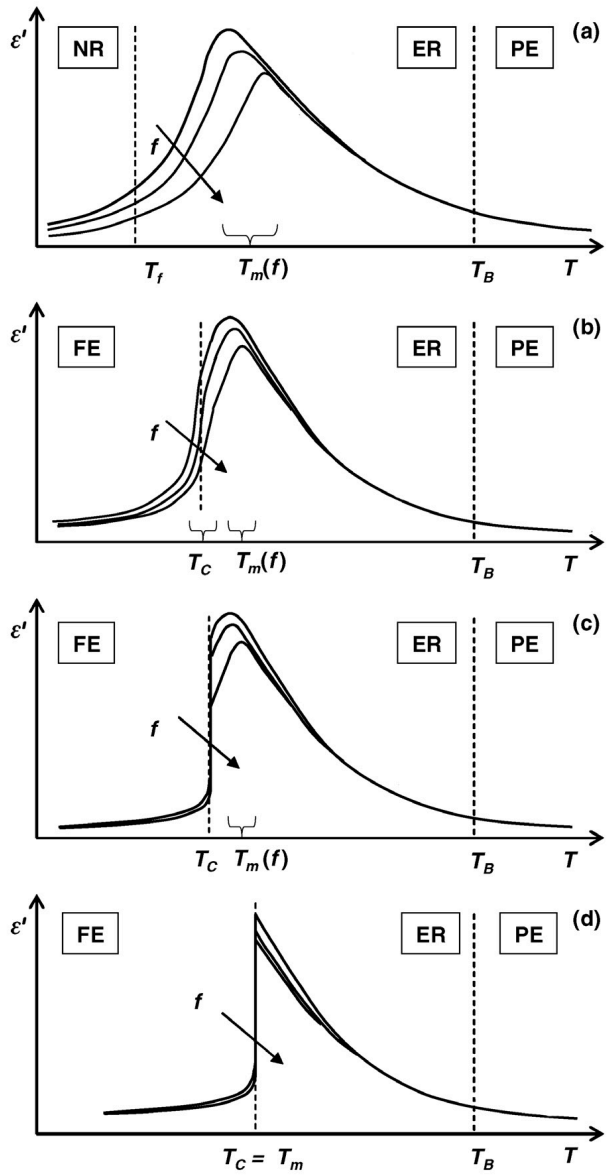


Figure 2.17 Temperature dependence of the dielectric permittivity and corresponding relaxor states. (**a**) Canonical relaxor freezing from an ergodic relaxor (ER) to a non-ergodic relaxor state (NR), (**b**) crystal with a diffuse phase transition from an ergodic relaxor state to a ferroelectric state (FE) at $T_{\mathrm{C}} < T_{\mathrm{m}}$, (**c**) crystal with a sharp phase transition from an ergodic relaxor state to a ferroelectric state at $T_{\mathrm{C}} < T_{\mathrm{m}}$, and (**d**) crystal with a sharp phase transition from an ergodic relaxor state to a ferroelectric state at $T_{\mathrm{C}} = T_{\mathrm{m}}$. A paraelectric state (PE) exists above Burns temperature, $T_{\mathrm{B}}$. The arrow indicates the increase of the frequency, $f$ (from Ref. [36]).

The term "ergodic" in relaxors is not strict as it is in statistics. It is more correct to use the varying degrees of ergodicity. In the ergodic relaxor state, the degree of the ergodicity of the system decreases with the decrease in temperature. In the state with a higher degree of ergodicity, *i.e.* at the temperature well below the $T_{\mathrm{B}}$, PNRs thermally fluctuate and rotate freely in the direction of the random fields. Thus, after removal of an external

stimulus, the high motion of PNRs leads to that the system subsequently returns to the initial state, *i.e.* lowest free energy state. Macroscopically, there is no measurable remanent polarization in the ergodic relaxor state, *i.e.* the net polarization $\sum \boldsymbol{P}_i = 0$. However, the net square polarization is not zero, $\sum \boldsymbol{P}_i^2 \neq 0$, because of the emergence of PNRs.[95] Thus, physical properties depending on $\boldsymbol{P}^2$ can be affected by the existence of PNRs, such as electrostriction[89] and quadratic electro-optic effects as manifested in birefringence or second-harmonic generation.[126]

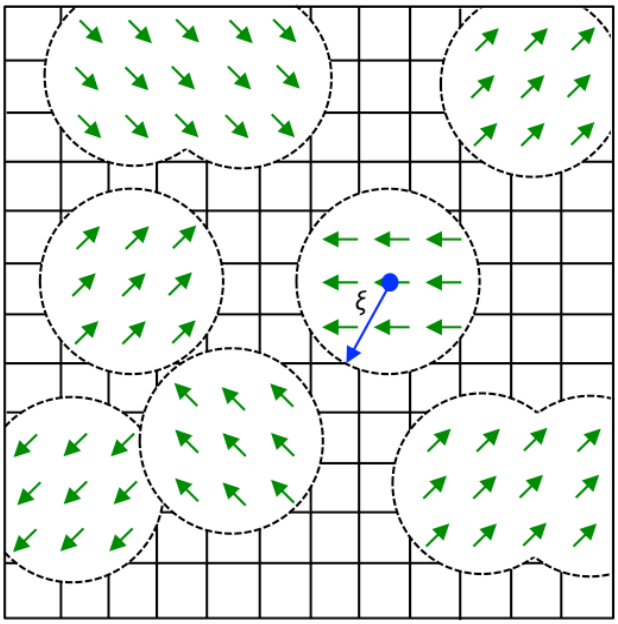


Figure 2.18 Emergence of a random-site dipole-induced polarization in several unit cells determined by the correlation length $\xi$ of the host forming polar nanoregions. The green arrows indicate the individual dipole (adapted from Ref. [90]).

**Low Temperature Non-ergodic and Ferroelectric State**

Upon further cooling, principally, two transitions are possible: a transition from an ergodic relaxor state to a non-ergodic relaxor state, or to a long-range ordered ferroelectric state.[23,36,57] In the first case, the sizes of PNRs grow with the increasing correlation length $\xi$ of the host lattices, and the slowing-down of the dynamics of PNRs proceeds.[90] Eventually at $T_f$, the system has a glassy-like transition, which transforms to a non-ergodic relaxor state. The ergodicity is broken because of the longest relaxation time divergence at $T_f$. Consequently, the stable ground state cannot be achieved at the laboratory time scales. This $T_f$ is called the freezing temperature, and it can be estimated by fitting the frequency dependence of the temperature of the dielectric permittivity maximum $T_m$ to the Vogel-Fulcher law[30,127,128]

$$f = f_D \exp\left(-\frac{E_a}{k_B(T_m - T_f)}\right), \tag{2.17}$$

where $E_a$ is the activation energy, $f_D$ is the Debye frequency, and $k_B$ is the Boltzmann constant. This law was first demonstrated by Viehland *et al.* on relaxors in their dipolar glassy state.[30] With decreasing temperature, the size of PNRs gradually increases and saturates in the non-ergodic relaxor state, which can be experimentally

defined as the correlation length $\xi$ of the atomic displacements contributing to the diffuse scattering. As observed by neutron elastic diffuse scattering,[35] the size of emerging PNRs in the PMN relaxor was around 1.5 nm at $T_B$, and it increased to 7 nm at 10 K, as shown in Fig. 2.19.

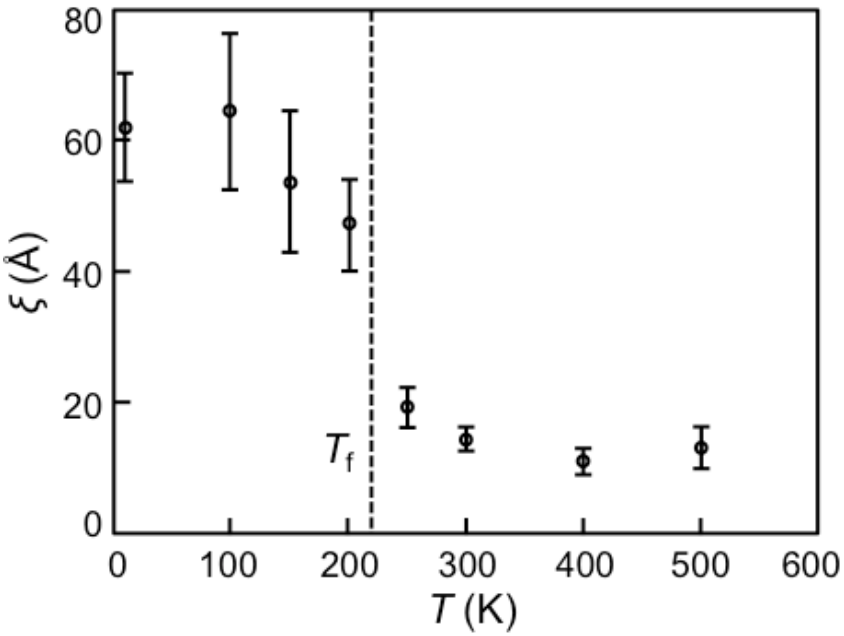


Figure 2.19 Correlation length $\xi$ of PNRs in a PMN relaxor crystal as a function of temperature. The vertical dashed line indicates the freezing temperature $T_f$ (from Ref. [35]).

In contrast to the evolution of PNR size, the number of PNR significantly decreases because smaller PNRs aggregate to larger ones from the ergodic to non-ergodic relaxor state, showing local collective or cooperative effects similar to the classical ferroelectric. This is derived from the transformation of magnetic spins in the glasses from a magnetically disordered ergodic relaxor to a frozen non-ergodic relaxor state.[30,124] The terminology "non-ergodicity" in contrast to the definition of "ergodicity" corresponds to the different phenomena between the time average and the thermodynamic ensemble average of the properties. The transition from the ergodic to non-ergodic relaxor state defines the class of canonical relaxors exemplified by PMN, PSN, PST, and PZT doped with large amounts of La.

In the second case, PNRs are large enough to permeate the whole sample. Thus, the system will undergo a static, cooperative ferroelectric phase transition at $T_C$ and establish a low-temperature long-range ordered ferroelectric ground state with the appearance of a macrodomain state, as shown in Fig. 2.17(b–d). The Curie temperature $T_C$ is at or below $T_m$. Macroscopically, there is a clear change of the crystal structure, *e.g.* from cubic to tetragonal. The different sharpness or diffuseness of the transition from an ergodic relaxor state to a ferroelectric state is a result of different degrees of compositional disorder or random fields characterizing the relaxor properties. The relaxors that undergo transition from the ergodic relaxor state to a long-range ordered ferroelectric state are called non-canonical relaxors.

**Static and Dynamic PNRs in Relaxors**

In the non-ergodic relaxor state (below freezing temperature) where the system loses the ergodicity completely, the PNRs freeze entirely and are truly static.[115,120,129,130] Thus, the spatial and temporal averages are no longer the same, which suggests that the macroscopic polar order, *i.e.* ferroelectric state, can be induced and remain stable after removing the external stimulus.[131] In the ergodic relaxor state, PNRs are highly dynamic and are weakly correlated, *i.e.* reorientation of the PNRs dipole moments because of the thermal motion, which leads to that spatially and temporally averaged behavior is macroscopically same. Interestingly, several work reported that coexistence of the dynamic and static behavior of PNRs is the crucial effect on the macroscopic behavior of the ergodic relaxor.[132,133] Kalinin *et al*.[133] reported that in a macroscopically ergodic relaxor material of PMN-10PT, both static and dynamic PNRs coexist locally. The static PNRs is responsible for the formation of the labyrinthine domain structure, while the dynamic PNRs contribute to the observed relaxation behavior. Using phase field simulations, a precursory polar state, *i.e.* the static PNRs, as shown in Fig. 2.20, was found at temperatures higher than $T_f$. These static PNRs coexist with the dynamic PNRs in the ergodic relaxor state, which slow down the overall dynamics of PNRs upon cooling.[120,134] Thus, the exceptional performances of relaxors are the overall effect of the interplay between the dynamic and static PNRs under the external stimulus.[134] Reflecting the microscale or nanoscale, the inhomogeneous distribution of the dynamic PNRs and static PNRs in the macroscopically ergodic relaxor state leads to diffusion of the degree of ergodicity associated with the relaxation times.[135] Kalinin *et al*.[136] observed that both fast and slow relaxing regions in the ergodic relaxor phase of a PMN-10PT crystal using the spectroscopic PFM method, confirmed the presence of mesoscopic dynamic heterogeneities. They speculated that these heterogeneities could be related to the spatial variation of the freezing temperature on the nanoscale, which is virtually attributed to the varying distribution of the lattice defects. It was suggested that in lead-based relaxors, dynamic PNRs exist both in compositionally ordered and disordered regions, whereas static PNRs occur in the compositionally ordered regions.[115,137] However, in the lead-free relaxor piezoelectric ceramics, the relationship between the chemical order-disorder and the dynamics of PNRs is not clear. It is noteworthy that the term of "quasi-static" is used to describe the static PNRs in the ergodic relaxor state, to distinguish them from the truly static PNRs in the non-ergodic relaxor state.

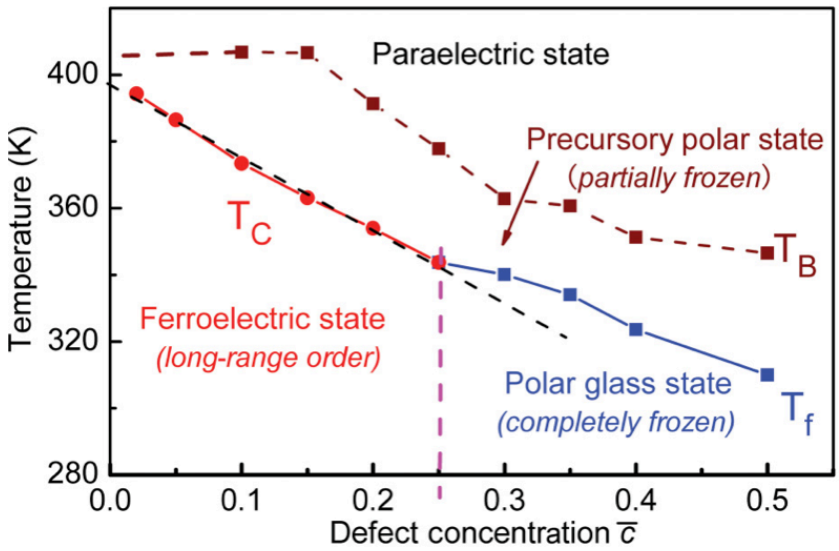


Figure. 2.20 Temperature-dependent polar state in the A-site substituted ferroelectric system with different defect concentration $\bar{c}$ obtained by the phase field simulation. The canonical relaxor ferroelectrics have a low-temperature glass state (non-ergodic relaxor state), when the defect concentration is higher than 0.25. Conversely, the low-temperature ferroelectric state occurs in the doped-ferroelectrics with defect concentration lower than 0.25. Upon cooling, the precursory polar state (static PNRs) occurs at Burns temperature $T_B$ (from Ref. [120]).

### 2.2.3 Field-induced Transitions in Canonical Relaxors

Macroscopically, a canonical relaxor remains in a non-polar crystal structure and the ferroelectric phase remains unattainable without applying sufficiently high external electric fields. The long-range ordered ferroelectric state can be induced in two possible ways: either by applying sufficiently high *dc* bias fields during cooling (field cooling, FC), or by applying sufficiently high *dc* fields after the zero field cooling (ZFC) down the system to the non-ergodic state.[28] The field-induced long-range ordered ferroelectric state is characterized by additional peaks that occur in the dielectric responses.[138-140] For example, in the canonical relaxor PMN, the long-range ordered ferroelectric state could be induced by cooling down a PMN monocrystal or a PMN ceramic while applying a *dc* bias field higher than the critical field $E_{\mathrm{th}} \approx 1.7\ \mathrm{kV/cm}$ or higher than $E_{\mathrm{th}} \approx 4\ \mathrm{kV/cm}$, respectively.[138,141] Based on two different approaches to obtain the ferroelectric state, a schematic phase diagram exhibiting the different phases as a function of the temperature and the applied external electric field is shown in Fig. 2.21. The phase diagram can be experimentally obtained by measuring the temperature- and field-dependent dielectric permittivity. As shown in Fig. 2.21(a), with the FC approach below the critical electric field $E_{\mathrm{th}}$, the relaxor system undergoes a transition from the ergodic to the non-ergodic state (line *D* in Fig. 2.21(a)) at the freezing temperature $T_{\mathrm{f}}$. The transition lines from the ergodic relaxor state to the ferroelectric state obtained from both approaches coincide, *c.f.* lines *A* and *E* in Fig. 2.21. However, the transition lines from the non-ergodic relaxor state to the ferroelectric state from both approaches are different. The critical fields to induce the long-range ordered ferroelectric state from the non-ergodic relaxor state are higher on the sample that has reached its non-ergodic relaxor state by the ZFC (line *F* in Fig. 2.21(b)) than the ones obtained by the FC treatment (line *C* in

Fig. 2.21(a)). With FC-zero field heating (ZFH) approach, the depolarization temperature $T_d$ can be defined (line *B* in Fig. 2.21(a)), where the macroscopic polarization is destroyed. The field-induced transition in a relaxor is a process to surpass the local random field by correspondingly applying a sufficient *dc* bias at different temperatures. The applied field directly acts on the PNRs to generate micro-sized or long-range ordered domains. However, because of the different nature of PNRs, which can exist in two states as previously mentioned, and the existence of the random fields, the stabilities of the field-induced ferroelectric states differ. The field-induced ferroelectric order in the non-ergodic state is stable below $T_d$ even after removing the field, because the PNRs are static and highly correlated with each other. By heating the system to $T_d$, this ordered ferroelectric state can be broken and transforms into the ergodic relaxor state. An induced ferroelectric order from the ergodic relaxor state can only be stable under a sufficiently high external electric field, where highly dynamic PNRs can be aligned to generate a large saturated polarization. Once the field is removed, the remanent polarization strongly decays and the system relaxes to the ergodic relaxor state.

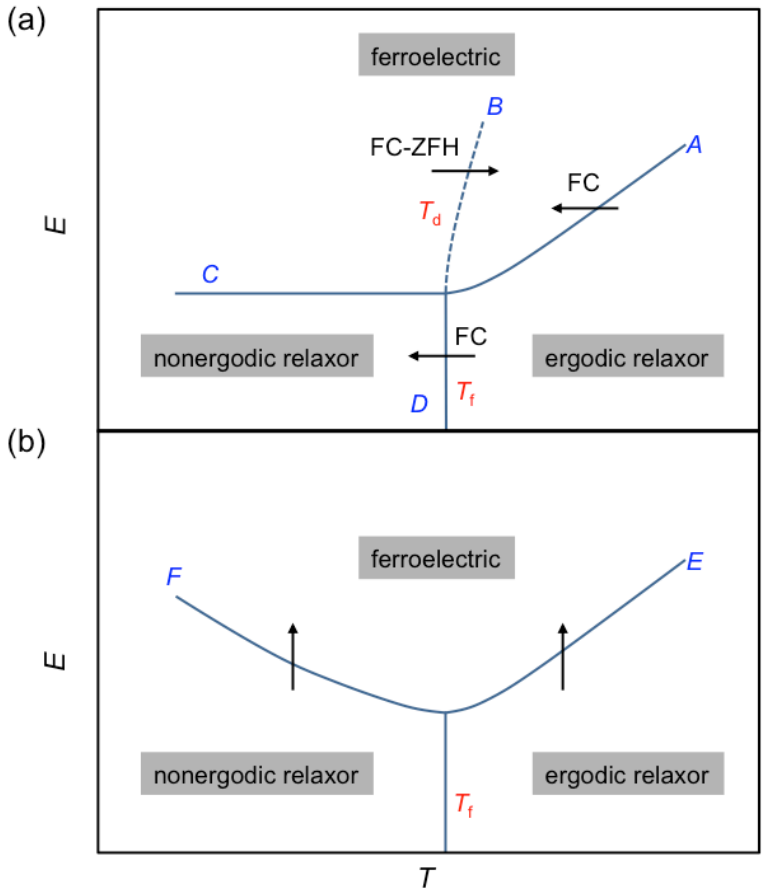


Figure 2.21 Schematic electric field–temperature phase diagram in a 9/65/35 PLZT canonical relaxor ceramic when (**a**) a long-range ordered ferroelectric state is induced by applying sufficient *dc* fields during cooling or (**b**) by applying sufficient *dc* fields after the non-ergodic relaxor state has been reached. Arrows indicate the direction of the crossover of transition lines (adapted from Ref. [28]).

### 2.2.4 Bismuth Sodium Titanate $Bi_{1/2}Na_{1/2}TiO_3$-based Lead-free Relaxor Ferroelectric Ceramics

Perovskite-structured compounds based on barium titanate $BaTiO_3$ (BT), potassium sodium niobate $(K_{1/2}Na_{1/2})NbO_3$ (KNN), bismuth sodium titanate $Bi_{1/2}Na_{1/2}TiO_3$ (BNT) and bismuth potassium titanate $Bi_{1/2}K_{1/2}TiO_3$ (BKT), which are characterized by promising piezoelectric properties, have been identified as competitive lead-free solid solutions to replace the lead-containing materials in response to the environmental regulations.[7,10,11,15,142,143] To date, a reduced remanent polarization, a reduced remanent strain, and an irreversible strain have become common features observed in lead-free relaxor materials with increased ergodicity suitable for actuator applications.[5] Among them, the A-site active BNT is considered to be a promising lead-free piezoelectric material discovered by Smolenskii *et al.* in 1960.[144,145] In addition, BNT exhibits a PLZT- and PMN-like relaxor behavior induced by the *A*-site disorder,[146-148] *i.e.* the strong frequency dispersion of the dielectric permittivity at $T_m$ (approximately at 340 °C), the depolarization temperature is about 185 °C, and the characteristic phase transition from the cubic ($Pm\bar{3}m$) to the tetragonal ($P4bm$), and tetragonal to rhombohedral symmetry ($R3C$) occurs at approximately 540 °C and 300 °C, respectively.[149,150] The existence of PNRs embedded into the cubic phase and their growth upon cooling[151-153] was suggested based on X-ray diffraction (XRD), neutron diffraction, transmission electron microscopy (TEM), and Raman spectroscopy measurements. However, the high coercive field $E_c = 7.3\ \mathrm{kV/mm}$ and high conductivity in pure BNT systems restrict the poling procedure and therefore hinders the practical application.[6,154] Thus, the modified BNT using other perovskite materials became increasingly important, where especially the morphotropic phase boundary (MPB)-based composition that has been intensively studied because of its excellent electromechanical properties, *e.g.* the large normalized strain ($S_{max}/E_{max}$) of $> 500\ \mathrm{pm/V}$.[5,14,22,154,155] The electric field-induced output strength is even surpassing the one of PZT-based counterparts.[6,7]

The compounds for BNT modification include materials such as BT, ST, BKT, $NaNbO_3$, and $KNbO_3$. BNT-based systems have been identified to macroscopically exhibit a pseudo-cubic symmetry and feature the relaxor behavior. The PNRs in BNT-based relaxors are suggested to be embedded into the cubic matrix, which plays a crucial role in the field- and temperature-dependent evolution of electrical properties.[5,22,36,156-158] It was suggested that the origin of the large electromechanical response in BNT-based piezoceramics is attributed to the reversible transition from an ergodic relaxor state to a ferroelectric state and irreversible transition from a non-ergodic relaxor state to a ferroelectric state upon the application of a sufficiently large external electric field.[5,57,159-161]

#### Modified Morphotropic Phase Boundary Composition of BNT-BKT

Morphotropic phase boundary (MPB) is the phase boundary between two ferroelectric states, generally between the tetragonal and rhombohedral phases. Relaxors with MPB compositions have many advantages for practical applications.[70] Among the modified BNT systems, the binary BNT-BKT compounds with 18−22 mol% BKT, which provides a MPB region, are most appealing because of the high performance piezoelectric properties.[162,163] Here, BKT has a tetragonal symmetry at room temperature.[164,165] It has been reported that by

compositionally modifying the BNT-BKT system, superior piezoelectric ceramics can be realized.[7,166-172] For example, the incorporation of $BiZn_{1/2}Ti_{1/2}O_3$ (BZT) or $BiMg_{1/2}Ti_{1/2}O_3$ (BMT) into the MPB composition of BNT-BKT resulted in a high normalized strain, attributed to the introduction of the mixed B sites.[15,171,172] In addition, these ergodic compositions feature negligible fatigue behavior.[173,174] Other studies focused on engineering a composition in the proximity of the MPB with iso- and aliovalent dopants on the A and/or B sites to improve the electromechanical properties, because small doping amounts can modify the electrical properties considerably because of the formation of the cation vacancy, oxygen vacancy/holes, and chemical pressure.[13,175-178] The element La has been widely used in several perovskite materials such as $Pb(Zr,Ti)O_3$, and $Ba_{1/2}Na_{1/2}TiO_3$.[178-180] Isovalent La-doping was shown to be a viable approach to tailor the dielectric and electromechanical properties of the BNT-BKT system.[175,178]

**Core-shell Relaxor Piezoelectric Ceramics**

In addition to the compositional modifications of the lead-free piezoceramics, structure tailoring is another effective approach to enhance the field-induced strain and decrease the coercive field through a modified processing procedure. The synthesis of a bulk ceramic with the heterogeneous core-shell microstructures has been a recent approach for improving the electromechanical response in large strain actuation applications while reducing the hysteresis.[159,181-184] The notable core-shell microstructure can be schematically shown in Fig. 2.22.[181,185] Within each individual grain, the core features a ferroelectric or non-ergodic state, whereas the surrounding shell exhibits an average paraelectric or ergodic state. Recently, it was reported that the addition of the composition $SrTiO_3$ (ST) ranging between 22–28 mol% to BNT effectively decreased the electric field required to achieve the large strain output.[155,181,182] In BNT-25ST ceramic, a strain output of more than 0.25% at 4 kV/mm and a piezoelectric coefficient $d_{33}^{*} \approx 600\ \mathrm{pm/V}$ at 4 kV/mm were reported.[186,187] The enhanced piezoelectric responses are attributed to core-shell microstructures detected in BNT-ST ceramics.

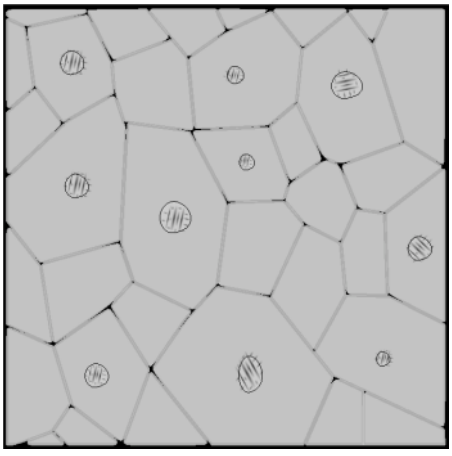

Figure 2.22 Schematic representation of the core-shell microstructure. Within individual grains, the cores feature the non-ergodic or ferroelectric state reflected with clear domain contrast (circular regions), which are surrounded by the non-polar shell exhibiting the ergodic relaxor state or paraelectric state (from Ref. [185]).

The formation of a core-shell microstructure is driven by the low diffusion rate of Sr during the sintering process, which leads to nanometer-sized, Sr-depleted regions that eventually turn into rhombohedral core regions. The core-shell structure is a non-equilibrium metastable state that can be removed gradually by extending the sintering time. Thus, the core density and average grain size can be further engineered. Both parameters are crucial factors for the macroscopic electromechanical performance of the core-shell ceramics.[182] The core-shell interface between the coherent heterophases also has a considerable effect on the macroscopic properties under an electrical stimulus.[188-191] However, the physical mechanism of the domain evolution at the core-shell interface and the respective structure-property relationship remain unexplored for both dielectric and piezoelectric materials.

The relaxor properties can be enhanced through the composition or structural modification for the field-induced high strain applications.[23,25,29] Generally, large strain response in the lead-free relaxors is associated with a reversible field-induced transition from a macroscopic ergodic relaxor state to a ferroelectric state with a long-range order.[5,189,192] The decisive factors for this transition and the distinctive macroscopic characteristics in relaxors are the existence, dynamic properties, and distribution of PNRs. Since the discovery of PNRs in relaxors, many studies have focused on how local dynamic or static PNRs determine the macroscopic relaxor states by investigating the temperature- or electric field-dependent dynamics of these PNRs. However, little is known about the local electromechanical performances of PNRs in both the ergodic or non-ergodic relaxor states, the PNR-PNR interactions through the host lattices, the dynamics of PNRs, as well as the role PNRs play in the electric field-induced transition from the relaxor to ferroelectric state. These are essential to the peculiarities of relaxors and have to be thoroughly investigated for a complete understanding of the fundamental physical mechanisms, which will lead to competitive lead-free relaxor ferroelectric devices.

## 2.3 Piezoresponse Force Microscopy

In this Chapter, the principle of the atomic force microscope (AFM) will be introduced. A description of the basic operating principle of the piezoresponse force microscope and its advanced modes is presented below.

### 2.3.1 Operating Principle of the Atomic Force Microscope

Scanning probe microscopy (SPM) techniques based on the principle of a near field probe imaging a surface by lateral scanning can be mainly classified as scanning tunneling microscopy, near field scanning optical microscopy and atomic force microscopy. The main advantage of SPM techniques is that it can provide a lateral resolution down to the atomic scale in real space. As the name suggests, scanning tunneling microscopy (STM) is used to measure the tunneling current, which can be used only for conducting samples. In contrast, an AFM measures forces between the tip and sample, which makes it probably the most valuable tool in the field of nanotechnology, because it can characterize all kinds of materials differing by the surface properties, ranging from topography and electrical to magnetic properties.

As shown in Fig. 2.23, the AFM functions with a probe, consisting of a sharp tip attached to the end of a spring-like cantilever. The typical size of the tip apex is approximately 10–20 nm of the radius of curvature. Thus, physical or chemical surface properties with high spatial resolution can be achieved by AFM (typically sub-nanometer in $z$ direction and a few tens of nanometers of lateral resolution). While approaching the tip towards the sample surface under study, a deflection of the cantilever that is proportional to the tip-sample force occurs. The force acting on the spring/cantilever can be quantified by Hook's law, expressed as $F = -kz$, where $F$ is the force, $k$ the spring constant and $z$ is the deflection of the cantilever. The deflection is measured by a 4-segmented photodiode by observing the motion of the detected laser beam reflected off the back of the cantilever. The vertical deflection and the torsional motion of the cantilever can be determined through the different light intensities on the photodiode segments by ((A+B)-(C+D))/(A+B+C+D) and ((A+C)-(B+D))/(A+B+C+D), respectively (Fig. 2.23). For any operation mode, one of the observables (control variable) detectable by the photodiode, *e.g.* vertical deflection (contact mode) or vertical vibration amplitude/frequency (amplitude/frequency modulation) is compared to a set-point value and processed in a feedback loop where the tip-sample distance is varied to maintain the control variable at a constant value. The variation of the tip-sample distance during scanning allows mapping of the surface topography in all AFM modes. A scanner made of a piezoelectric-ceramic is used to precisely position the sample (or tip/cantilever) in the lateral ($x$, $y$) and vertical ($z$) directions. An image is achieved by scanning the tip across the surface line by line where each line of the recorded area is scanned twice (trace and retrace lines).

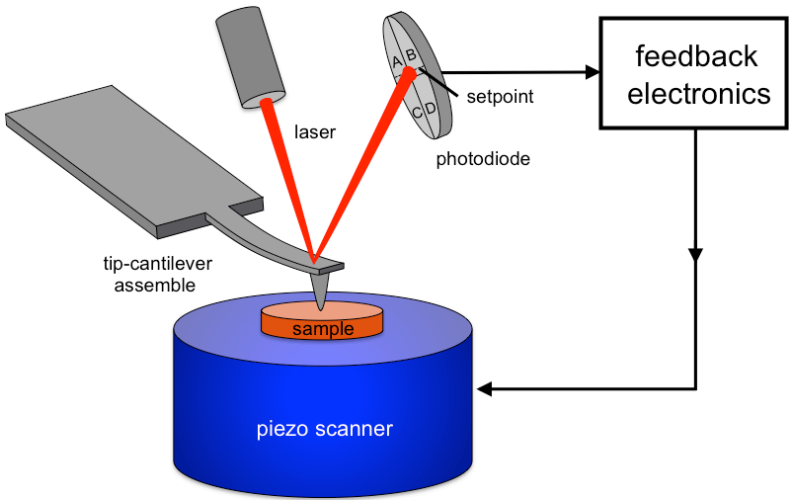


Figure 2.23 Schematic illustrating the operating principle of a conventional AFM in contact mode.

### 2.3.2 Principle of Piezoresponse Force Microscopy

The basic idea of PFM was to use a conductive tip/cantilever as a movable top electrode to detect the local polarization of ferroelectric samples.[193-196] This method was first introduced by Güthner and Dransfeld *et al.* in 1992.[43] They employed an AFM for both domain manipulation (applying $dc$ voltage) and detection (applying $ac$ voltage) of the micron-sized domains in a ferroelectric copolymer sample, vinylidene fluoridetrifluoroethilene.[43] Soon after that, the technique was further developed and applied to characterize the

domain structure and polarization reversal in ferroelectrics, because of the increasing need of ferroelectrics in nonvolatile random access memory devices with high-speed access and for high-density data storage. Thus, there is a need for microscopic insights into the physical mechanisms behind the working principle of these materials.[44-46,197]

PFM is based on the contact AFM mode to detect the electrical bias-induced surface deformation on the nanoscale, as shown in Fig. 2.24.[196] In the case of stress-free ferroelectric materials characterized by a homogeneous spontaneous polarization in the vertical direction, a driving voltage $V_{\mathrm{tip}} = V_{\mathrm{dc}} + V_{\mathrm{ac}}\cos(\omega t)$ is applied to the tip, leading to a surface vibration $z = A_{\mathrm{dc}} + A_{\mathrm{ac}}\cos(\omega t + \varphi)$ that results from the converse piezoelectric effect. The $dc$ bias $V_{\mathrm{dc}}$ is applied in case domain switching is intended. The probing voltage $V_{\mathrm{ac}}$ should be high enough to obtain a detectable response of the local ferroelectric domains but sufficiently low to avoid tip-induced local switching effects.[52,53] The phase shift $\varphi$ between the driving signal and the piezoresponse signal yields information about the polarization direction of the domains beneath the tip. The piezoresponse amplitude, $A_{\mathrm{ac}} = d_{33}^{\mathrm{eff}} V_{\mathrm{ac}}$, is a measure of the local electromechanical activity, which is the first harmonic component of the biased-induced tip deflection. Caution should be taken because the vertical piezoelectric coefficient $d_{33}^{\mathrm{eff}}$ that is measured by PFM is an effective $d_{33}$ that is different from the macroscopic $d_{33}$. This effective piezoelectric coefficient $d_{33}^{\mathrm{eff}}$ is a local value that is influenced by many factors such as cantilever/tip quality, the tip-sample contact mechanic properties, surface quality, piezoelectric tensor of the sample, and the crystallographic and real space orientation of the sample.

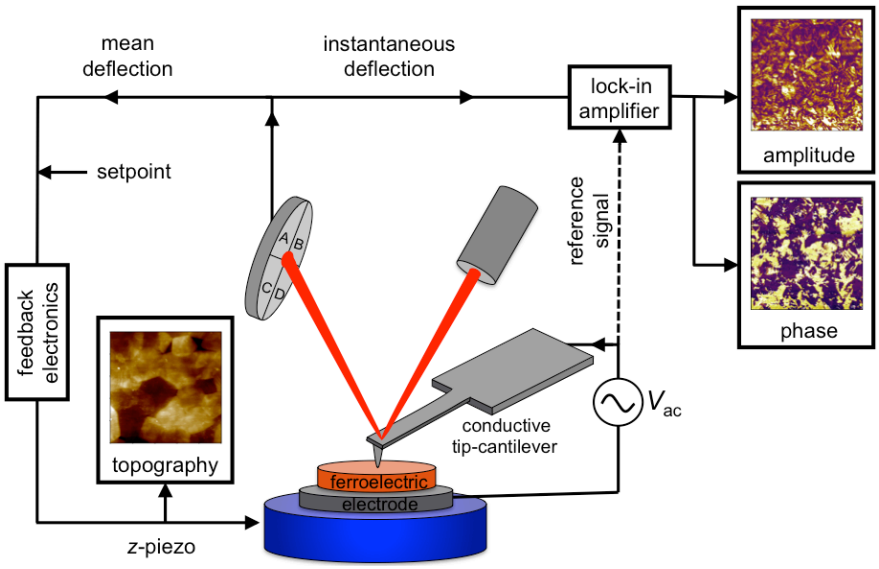


Figure 2.24 Schematic illustrating the operating principle of PFM.

For the surface domains orientated downwards (also called $c^-$ domains), a positive (negative) excitation field $E$ could induce the expansion (contraction) of the sample, as shown in Fig. 2.25(a). The corresponding phase shift is 0°, *i.e.* surface deformation and driving voltage are in-phase (Fig. 2.25(b)). However, for the upward domains (also called $c^+$ domains), a positive (negative) excitation voltage $E$ causes the contraction (expansion) of the

sample surface, as shown in Fig. 2.25(c). A corresponding out-of-phase piezoresponse with a phase shift of 180° is detected (Fig. 2.25(d)).

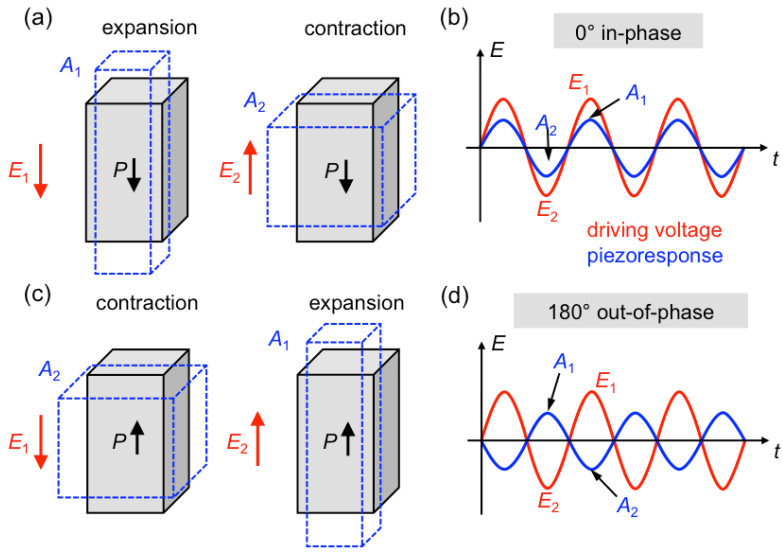


Figure 2.25 Deformation of the sample and phase shift of the piezoresponse with respect to the excitation voltage in the cantilever's vertical bending direction. (**a**) The surface expands and contracts when a downward orientated domain is in parallel and antiparallel with the external electric field $E$, respectively, and (**b**) in-phase $\varphi = 0°$ piezoresponse occurs; (**c**) surface contracts and expands when an upwards-orientated domain is in antiparallel and parallel with the electric field, respectively, and (**d**) an out-of-phase $\varphi = 180°$ piezoresponse occurs.

The principle of the in-plane piezoresponse detection (*i.e.* piezoelectric coefficient $d_{15}^{\text{eff}}$) of the sample surface measured by lateral PFM (LPFM)[48] is shown in Fig. 2.26. Here, the tip-sample contact mechanics induce a torsional motion around the cantilever long axis. To reconstruct all three components of piezoresponse signal by PFM, the sample has to be rotated by 90° for the acquisition of both $x$- and $y$-lateral components. In combination with vertical PFM (VPFM), the 3-dimensional sample surface analysis can be completed using vector PFM.[47] Using multiple lock-in amplifiers, the in-plane and out-of-plane piezoresponse signals can be simultaneously extracted as phase and amplitude piezoresponse signals together with topography.

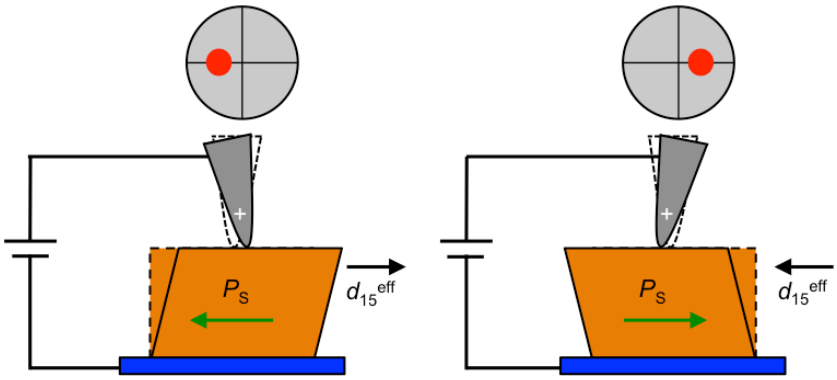


Figure 2.26 In-plane piezoelectric effect investigated by lateral PFM. The driving electric field is oriented perpendicular to the lateral domains resulting in a shear deformation at the sample surface related to the $d_{15}^{\text{eff}}$ piezoelectric coefficient. The cantilever consequently executes a torsional vibration, causing a lateral deflection of the laser-beam.

### 2.3.3 Modes of Piezoresponse Force Microscopy

**Single Frequency Piezoresponse Force Microscopy**

In PFM, besides the driving amplitude, the choice of the driving frequency strongly influences the amplitude of the piezoresponse signal, which is given by $A_{\mathrm{ac}} = d_{33}^{\mathrm{eff}} V_{\mathrm{ac}} Q$. Here, $Q$ represents the quality factor describing the energy losses in the system, which is equal to 1 when choosing a driving frequency far below the first tip/cantilever–sample contact resonance frequency (low-frequency PFM). The ultimate detection limit of $A_{\mathrm{ac}}$ is restricted to the thermal noise (approximately 30 pm), which determines the minimum driving amplitude. The maximum driving voltage $V_{\mathrm{ac}}$ should be one or two orders of magnitude smaller than the coercive bias for achieving quantitative measurements. In addition, a high driving voltage can induce tip and sample degradation. Thus, for ferroelectric materials characterized by a weak piezoelectric response and/or a small size of the domains (*e.g.* PNRs), contact resonance PFM was developed to effectively enhance the signal-to-noise ratio (SNR) and to allow for significantly lower driving voltages.[198] In this technique, the driving frequency is chosen in the vicinity of the contact resonance frequency that exploits the high $Q$-factor that is typically 10–100 in air for PFM cantilever/sample systems. Consequently, the piezoresponse amplitude $A_{\mathrm{ac}}$ can be effectively amplified by a factor of ~ $Q$ depending how close the driving frequency is chosen to the contact resonance frequency. However, a large variation of the contact resonant frequency of the system can be induced by topographic cross-coupling that is caused by the change of the tip-surface contact mechanics, which in turn has its origin in the roughness of the samples, the inhomogeneity of the mechanical properties of the sample surface and a possible cantilever/tip degradation.[53,198-200] The excitation frequency can thus change to far off the resonant range during scanning and a piezoresponse amplification that is always at the same level, is not guaranteed. This leads to a difficult interpretation of the measured domain orientation (phase signal) and the magnitude of the piezoresponse (amplitude signal). To minimize these effects, a technique allowing for permanently tracking the instantaneous contact resonance between the tip and the sample surface is needed.

**Dual AC Resonance Tracking Piezoresponse Force Microscopy**

Based on a multifrequency approach, the dual *ac* resonance tracking (DART) methodology has been developed to minimize the topographical crosstalk and the influence of tip-sample contact mechanics on the detected electromechanical signals.[201,202] DART can improve the sensitivity of the measured piezoresponse signal and extract the local electromechanical properties more accurately with respect to the vertical vibration of the cantilever compared to the abovementioned single frequency contact resonance mode in PFM.[203] Thus far, the DART-PFM mode has been reported in the literature for flexural vibrations of the cantilever.[202,203] The concept can be transformed to the torsional motion/vibration of the cantilever as well. The torsional DART-PFM (TDART-PFM) can be used to characterize domains with an in-plane polarization that is complementary to conventional DART-PFM.[204] By combining the DART mode applied to the vertical cantilever vibration with the torsional oscillation in two orthogonal in-plane directions ($x$ and $y$), the complete 3-dimensional ($x$, $y$ and $z$) information of the orientation polarization vector on a ferroelectric surface can be visualized using very high

resolution and minimum topographical and mechanical crosstalk between the tip and the sample surface. The details about TDART will be introduced in Chapter 3.1.

**Switching Spectroscopy Piezoresponse Force Microscopy**

Switching spectroscopy PFM (SS-PFM) can generate local hysteresis loops on ferroelectric materials, which can provide local information about an imprint, the local work of switching, coercive biases, nucleation biases, saturation and remanent responses.[205,206] The obtained SS-PFM maps can be readily correlated with the surface topography or other AFM achievable quantities to establish a relationship between the local switching properties and nanostructures on the surface of ferroelectrics. As shown in Fig. 2.27(a), the implementation of SS-PFM is similar to the acquisition of force-distance curves but additionally an electric waveform $V_{\mathrm{tip}} = V_{\mathrm{dc}} + V_{\mathrm{ac}}\cos(\omega t)$ is applied to the conductive cantilever/tip. A SS-PFM map on a $N \times M$ mesh is obtained by moving the tip point by point after each hysteresis loop. For the acquisition of a single hysteresis loop, the tip is fixed at a chosen location on the surface. The applied waveform is a square wave $V_{\mathrm{dc}}$ that steps in magnitude with time superimposed by a $ac$ signal (blue waves) (Fig. 2.27(b)). The poling field $V_{\mathrm{dc}}$ is comprised of a sequence of pulses with increasing/decreasing amplitudes over a time length $t_1$ (on-state) and intervals of zero bias lasting for $t_2$ (off-state). The envelope of this poling waveform is specified by a triangular waveform with a specified amplitude and period (red dashed wave form in Fig. 2.27(b)). The superimposed *ac* signal is the driving signal with an amplitude $V_{\mathrm{ac}}$ and frequency $\omega$ (normally corresponding to the contact resonance frequencies) used to read out the on-state and off-state oscillation amplitude/phase signals. The corresponding loops (one cycle = one hysteresis loop) are typically called bias-on and bias-off hysteresis loops, respectively. The bias-off hysteresis loops are related to the remanent piezoresponse signal measured between consecutive *dc* bias steps with the $dc$ bias switched off. The bias-on hysteresis loops, however, are influenced by the electrostatic interactions generated by the electrical field beneath the tip.[39] This leads to a substantially lower detected coercive field, and a higher slope and response of the hysteresis loop compared to the hysteresis loop measured in the off-state including an inversion of the loops.[40] A single hysteresis loop as the effective piezoelectric response *PR* versus the applied electric field can be calculated from the amplitude and phase response, as given in the following equation:

$$PR = A_{\mathrm{h}}\cos(\phi_{\mathrm{h}})/V_{\mathrm{ac}}, \tag{2.18}$$

where $A_{\mathrm{h}}$ is the amplitude hysteresis loop and $\phi_{\mathrm{h}}$ is the respective phase hysteresis loop.

An ideal hysteresis loop that originates from a purely electromechanical response, and obtained using SS-PFM is shown in Fig. 2.27(c). It contains the forward response $R^+(V)$ and reverse $R^-(V)$ response branches. $R_{\mathrm{init}}$ is the initial response. The imprint is defined as $(V^+ + V^-)/2$ whose $V^+$ and $V^-$ are the positive and negative coercive biases, respectively. The remanent switchable response is $R_0 = R_0^+ - R_0^-$, where $R_0^+$ and $R_0^-$ are defined as positive and negative remanent responses, respectively. $R_{\mathrm{s}} = R_{\mathrm{s}}^+ - R_{\mathrm{s}}^-$ is the maximum switchable response obtained by calculating the difference between the positive $R_{\mathrm{s}}^+$ and the negative $R_{\mathrm{s}}^-$ saturation

responses. The voltages $V_c^+$ and $V_c^-$ at the crossover between the constant and rapidly changing regions of the loops are defined as the forward and reverse domain nucleation voltages, respectively.

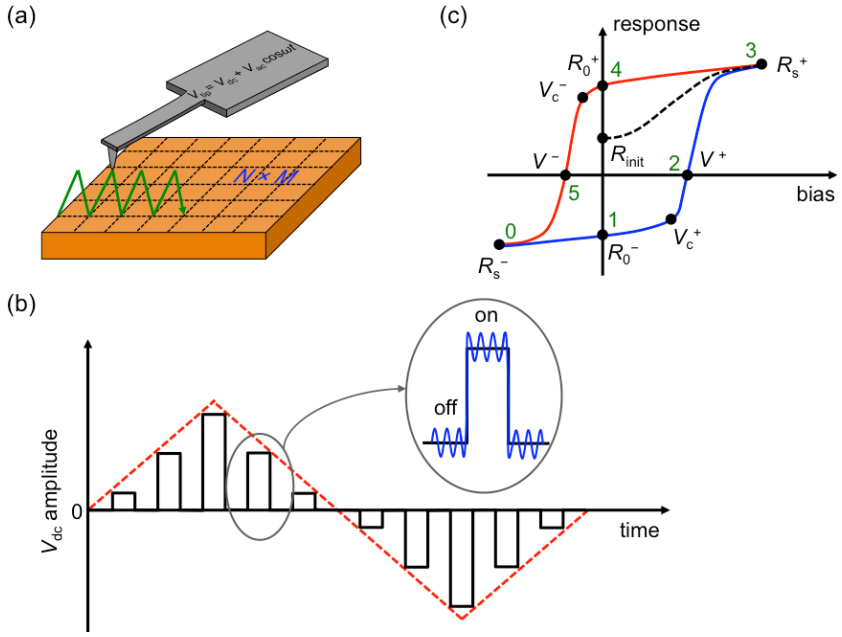


Figure 2.27 Working principle of SS-PFM. (**a**) Maps containing local hysteresis loops at each point on a $N \times M$ mesh. (**b**) Applied electric waveform and data acquisition sequence for each hysteresis loop, and (**c**) representative PFM hysteresis loop (adapted from Ref. [206]).

In reality, the hysteresis loops obtained by SS-PFM can be extremely sensitive to the experimental conditions, such as the tip-surface contact quality, environmental effects, instrumental artifacts, the finite driving amplitude and the influence of the electrostatic forces. To minimize electrostatic contributions, stiff cantilevers are recommended to be used. Hysteresis loops in PFM describing the nucleation of a single domain at a single location under the tip and the development of domains, can be fundamentally different from the macroscopic hysteresis loops that characterize the nucleation, growth and interaction of multiple separated domains. In the strong indentation regime, the shape of the PFM hysteresis loop has been deeply analyzed by Kalinin *et al.*[207] and Jesse *et al.*,[206] and can be described as follows:

$$PR = d^{\mathrm{eff}}\{1 - 5\beta\sigma_{\mathrm{wall}}\pi^2/(8P_{\mathrm{S}}V_{\mathrm{dc}})\}, \tag{2.19}$$

where $d^{\mathrm{eff}}$ is the effective electromechanical response of the material, $\beta$ is a proportionality coefficient between the surface potential and the potential at the domain boundary, $\sigma_{\mathrm{wall}}$ is the direction-independent domain wall energy, $P_{\mathrm{S}}$ is the polarization. This model is based on the point charge approximation that is valid when the vertical distance from the center of the contact area is larger than the tip-surface contact radius.[208] When the domain wall energy and the magnitude of spontaneous polarization are known, the local coercive voltages can be estimated from Equation (2.19). From the thermodynamic point of view, as shown in Fig. 2.27, if there is no pinning effect while switching, the domains grow and shrink instantaneously in response to the tip bias inducing

a reversible hysteresis proceeding along 1-2-3-2-1-0 in blue branch of Fig. 2.27. Whereas considering a weak pinning effect in the model, the nucleation and growth of the new domain will dominate and the whole hysteresis loop will proceed along 1-2-3-4-5-0 in the red branch of Fig. 2.27.[206]

**High-speed Piezoresponse Force Microscopy**

Several work were reported on increasing the PFM scanning velocity to improve the temporal resolution for studying the dynamic effects of ferroelectric domains. To improve the signal-to-noise ratio, the higher frequency contact resonances in lower MHz can be considered in high-speed PFM imaging, because the higher frequency providing more *ac* periods of piezoresponse at each pixel increases the residing time of tip on the sample surface. The precondition is that the sample surface must be flat enough to minimize the influence of the mechanical properties. The chosen samples were ferroelectric thin films, that are topographical optical-flat and are characterized with the opposite 180° domain. The scan rate can be increased to 128 lines/s to study the domain wall motion and the domain nucleation and growth by imposing the *dc* voltage (poling) to *ac* voltage (scanning). Few works related to high-speed PFM were reported to study the relaxation properties of PNRs on the relaxor piezoceramics on which surface roughness is comparably high. It becomes essential to improve the velocity of PFM scanning to resolve the dynamics of PNRs associated with the local relaxation mechanism of the lead-free relaxor piezoceramics.

# 3 Cumulative Part of the Present Thesis

The cumulative part of the present thesis is divided into three parts. The first part Chapter 3.1, which is reported in the publication of [1], is related to the development of a dual *ac* resonance tracking PFM mode in the torsional vibration (TDART) of the cantilever/sample surface based on the DART-PFM in the vertical vibration of the cantilever. Compared to the single frequency PFM mode, the application of TDART in lead-free relaxor piezoceramics $(1-x)(Bi_{1/2}Na_{1/2}TiO_3\text{-}Bi_{1/2}K_{1/2}TiO_3)\text{-}x(BiMg_{1/2}Ti_{1/2}O_3)$ allows for the visualization of fine substructures within the monodomains, suggesting the existence of PNRs. The domain structures of the PNRs are visualized with high precision, and the local electromechanical characteristics of the sample are quantitatively mapped using DART-PFM with vertically and torsionally vibrating cantilevers. The following Chapter 3.2 focuses on studying the local relaxation behavior and PNRs dynamics in two kinds of relaxor ceramics: Na or K replaced by 1 at. % La in the initial material $0.8Bi_{1/2}Na_{1/2}TiO_3\text{-}0.2Bi_{1/2}K_{1/2}TiO_3$, of which both are macroscopically characterized at room temperature by the ergodic relaxor state but with different degrees of ergodicity. The single frequency PFM with a scanning velocity of about 5 μm/s (conventional PFM) is applied to observe the relaxation behavior of the tip-induced ferroelectric domains on both samples, and the local hysteresis loops on the selective locations of both samples are measured by SS-PFM, which correlates to the publication of [2]. Owning to the fact that PNRs are highly dynamic in both ergodic relaxor systems, the PFM with a scanning speed of approximately 117 μm/s (high-speed PFM) is developed. An in-depth study of the relaxation mechanisms and the quantification of the nanoscale relaxation times of both relaxor ferroelectrics are introduced through analyzing the high-temporal image series. In the end, the different types of PNRs are discovered based on the local distribution of ergodicity. The third part that is reported in the publication [3] is related to unraveling the interfacial core-shell interaction by studying the relaxation behavior of the tip-induced ferroelectric domains in a lead-free relaxor ferroelectric ceramic $0.75Bi_{1/2}Na_{1/2}TiO_3\text{-}0.25SrTiO_3$, which features a core-shell microstructure with different polarization states and local structures, and is characterized by a large strain output, using PFM. In combination with the phase field simulation, the PFM-observed phenomenon of tip-induced ferroelectric domain evolution at the core-shell interface is well explained. Additionally, the core-shell interplay under the external electric field and the respective microstructure-property relationship are concretized.

## 3.1 Visualization of Polar Nanoregions in $(1-x)(Bi_{1/2}Na_{1/2}TiO_3\text{-}Bi_{1/2}K_{1/2}TiO_3)\text{-}x(BiMg_{1/2}Ti_{1/2}O_3)$ Relaxor Ferroelectrics via Piezoresponse Force Microscopy in Torsional Dual *AC* Resonance Tracking Mode

The content of this Chapter is published in:

[1] Na Liu, Robert Dittmer, Robert W. Stark and Christian Dietz, "Visualization of polar nanoregions in lead-free relaxors via piezoresponse force microscopy in torsional dual *ac* resonance tracking mode", *Nanoscale*, ***7***, 11787 (2015).

In the present Chapter, a torsional dual *ac* resonance tracking (TDART) - piezoresponse force microscopy (PFM) mode for detecting the in-plane components of the polarization in the lead-free piezoceramics $(1-x)(Bi_{1/2}Na_{1/2}TiO_3\text{-}Bi_{1/2}K_{1/2}TiO_3)\text{-}x(BiMg_{1/2}Ti_{1/2}O_3)$ that feature relaxor properties is presented, and the respective piezoresponse signals (amplitude and phase) with those obtained in the single frequency (SF) excitation mode are compared. A higher signal-to-noise ratio (SNR) and reliability of the image of TDART technique for visualizing the domain structures of the polar nanoregions (PNRs) of relaxor ferroelectrics is demonstrated. The damped simple harmonic oscillator model (DSHO) is applied to facilitate the quantitative mapping of the local electromechanical properties of the relaxor ferroelectrics in three dimensions.

### 3.1.1 Experimental and Method

#### Sample Preparation

To demonstrate the imaging capability of the TDART-PFM mode and quantitatively map the local three-dimensional piezoelectric properties, two compositions of lead-free piezoceramic samples, $0.81Bi_{1/2}Na_{1/2}TiO_3\text{-}0.19Bi_{1/2}K_{1/2}TiO_3$ and $0.97(0.81Bi_{1/2}Na_{1/2}TiO_3\text{-}0.19Bi_{1/2}K_{1/2}TiO_3)\text{-}0.03(BiMg_{1/2}Ti_{1/2}O_3)$, which are hereafter referred to as 0BMT and 3BMT, respectively, were used. To produce these two samples following the mixed oxide route, oxides and carbonates of the respective elements (all from Alfa Aesar GmbH & Co. KG, Karlsruhe, Germany) were used to synthesize the abovementioned compositions. The reagent grade raw materials MgO (99.0%), $Bi_2O_3$ (99.975%), $Na_2CO_3$ (99.5%), $TiO_2$ (99.9%) and $K_2CO_3$ (99.0%) were mixed according to the stoichiometric formula and milled with zirconia balls in ethanol for 24 h at 250 rpm using a planetary mill (Fritsch Pulverisette 5, Idar-Oberstein, Germany). Subsequently, the slurry was dried at 100 °C and the resulting powder was calcined for 3 h at 900 °C in covered alumina crucibles. After another milling step of 24 h, the pestled and sieved powders were shaped by manual uniaxial pressing into pellets of 10 mm in diameter. Then, the green bodies were further compacted by hydrostatic pressure of 300 MPa. Sintering was performed with a ramp rate of 10 K/min at 1100 °C for 3 h in covered alumina crucibles. To minimize the loss of volatile

elements, samples were covered with an atmospheric powder of the same composition. For the PFM observations, the sintered samples were ground down to approximately 250 µm and subsequently polished using polycrystalline diamond paste with abrasive particles of 15 µm, 6 µm, 3 µm, 1 µm and 0.25 µm (DP-Paste P by Struers A/S, Ballerup, Denmark) for 1 h each. The finishing was performed in a final polishing step of 15 min with a colloidal silica polishing suspension (Buehler Mastermet by Buehler GmbH, Düsseldorf, Germany). The samples were then annealed at 400 °C at a heating rate of 2 K/min for 2 h and cooled down to the room temperature naturally. The samples were pasted on a metal plate with the silver for PFM measurements. The ferroelectric standard PIC 151 that is a modified lead zirconate tiatnate (PZT) material was purchased from PI ceramic GmbH (Lederhose, Germany) and was measured by PFM as is, *i.e.* in the initial state of the ferroelectric domain structure.

**Macroscopic Measurements and Sample Characterization**

For the macroscopic electrical measurements of samples 0BMT and 3BMT, the sintered pellets were ground, polished and painted with silver paste, which was burned in at 400 °C. The temperature-dependent relative permittivity, $\varepsilon_r$, and loss factor, $\tan\delta$, were determined with an LCR-meter HP 4284A (Hewlett-Packard Co., Palo Alto, CA, USA) at a heating rate of 2 K/min at 0.1 kHz, 1 kHz, 10 kHz, 100 kHz and 1000 kHz using a Nabertherm LE4/11/R6 box furnace (Nabertherm GmbH, Lilienthal, Germany) with a custom-made sample holder. The permittivity was obtained for samples that were previously poled for 1 min under an electric field of 6 kV/mm at room temperature. Samples for the X-ray diffraction (XRD) studies were poled at room temperature under an electric field of 6 kV/mm. The XRD measurements were performed in theta-2-theta geometry using a Bruker D8 (Bruker Corp., Billerica, MA, USA). Data on field-dependent strain $S(E)$ and polarization $P(E)$ were acquired by means of a Sawyer-Tower setup at 1 Hz employing an optical sensor (Philtec, Inc., Annapolis, MD, USA) and a 15 µF measurement capacitor.

The XRD patterns confirmed a perovskite structure for both materials as shown in Fig. 3.1. There are no indications of an undesirable non-perovskite phase. It is apparent from the asymmetry of the $\{111\}_c$ and the $\{200\}_c$ reflections that both compositions possess a significant non-cubic distortion in their poled states. The strength of the asymmetry of 0BMT is larger than the one of 3BMT, which is attributed to a higher degree of ergodicity in 3BMT than the one in 0BMT. In this respect, the materials share similarities with $(1-x)(0.8Bi_{1/2}Na_{1/2}TiO_3\text{-}0.2Bi_{1/2}K_{1/2}TiO_3)\text{-}x(BiZn_{1/2}Ti_{1/2}O_3)$, which is pseudocubic in the virgin state but develops a tetragonal and rhombohedral phase mixture upon application of a sufficiently large electric field.[15] The dielectric properties were measured as a function of temperature at frequencies of 0.1 kHz, 1 kHz, 10 kHz, 100 kHz and 1000 kHz for both materials in their poled states as shown in Fig. 3.2. Both compositions exhibit remarkable frequency dispersion characteristics of the permittivity and loss tangent factor, tan $\delta$, with temperature. This result indicates that both compositions have a strong relaxor character. It is apparent from the peak in the temperature dependency of the loss tangent factor that 0BMT has a comparably high depolarization temperature, $T_d$, of approximately 100 °C. By contrast, 3BMT does not provide any indication of a peak, *i.e.*, no

depolarization in the examined temperature range from room temperature to 400 °C. It was demonstrated that the introduction of aliovalent B-site ions significantly lowered the $T_d$ of the various BNT-based solid solutions.[209] This evolution is often rationalized by the enhancement of the quenched random fields that impede the formation of a stable long-range order upon poling.

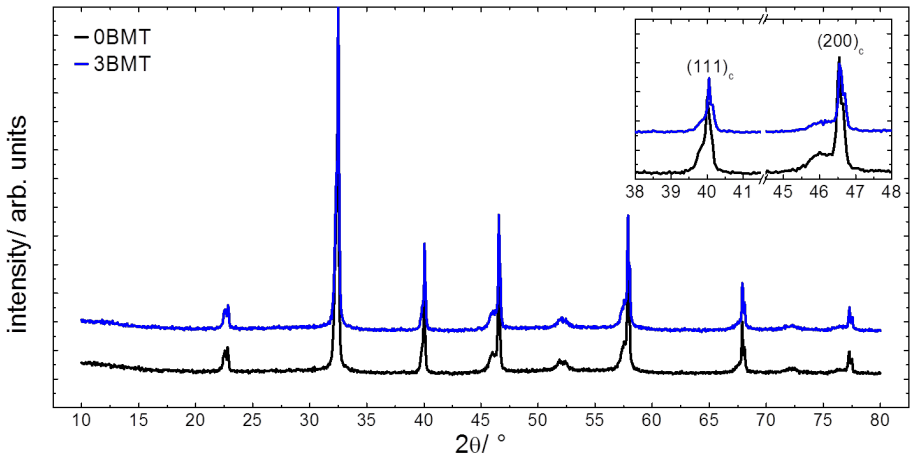


Figure 3.1 X-ray diffraction pattern for 0BMT and 3BMT poled at 6 kV/mm. The inset shows the $\{111\}_c$ and the $\{200\}_c$ reflections of both materials.

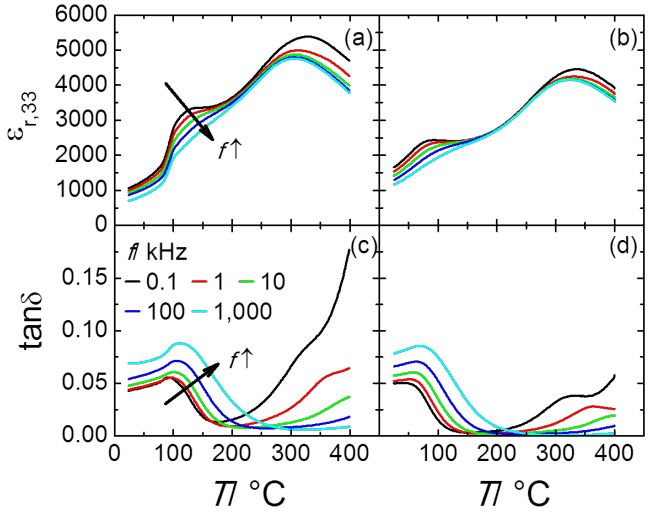


Figure 3.2 Relative dielectric permittivity (top row) and loss tangent $\tan\delta$ (bottom row) at various frequencies for 0BMT (**a** and **c**) and 3BMT (**b** and **d**) in the poled state from room temperature to 400 °C.

Figure 3.3 exhibits the macroscopic bipolar strain $S(E)$ and polarization $P(E)$ loops obtained on the virgin specimens. It can be seen that in the strain curves the field-induced remanent strain $S_{\mathrm{rem}}$ / maximum strain $S_{\mathrm{max}}$ in 3BMT is lower/larger than the one in 0BMT (Fig. 3.3(a)). In addition, a lower remanent polarization $P_{\mathrm{rem}}$ in 3BMT and a more pronounced pinching $P(E)$ loop is observed in 3BMT compared with 0BMT (Fig. 3.3(b)).The reduced $P_{\mathrm{rem}}$ and $S_{\mathrm{rem}}$ proved that the highly-doped lead-free relaxor 3BMT features a higher degree of ergodicity than 0BMT.[5]

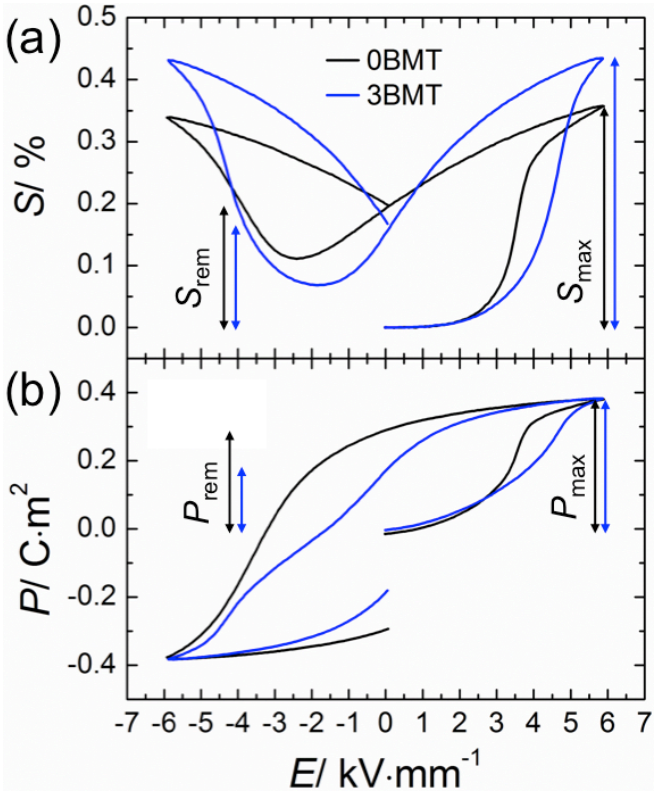


Figure 3.3 Macroscopic bipolar strain $S(E)$ (**a**) and polarization $P(E)$ loops (**b**) on a virgin state for 0BMT (black loop) and 3BMT (blue loop).

**Piezoresponse Force Microscopy Imaging**

PFM measurements were performed in the SF- and DART-PFM modes with a Cypher AFM (Asylum Research, Santa Barbara, USA). Conductive cantilevers, ASYELEC-02 and AC240TM (Asylum Research), with tip-coatings of Ti/Ir (5/20) and Ti/Pt (5/20) were used. The nominal spring constants for both types of cantilevers were 42 N/m and 2 N/m with a fundamental resonance frequency of the free tip-vibration (non-contact resonance) of approximately 300 kHz and 70 kHz, respectively. The first contact resonance frequencies for the torsional motion of the tip were in the range of 1.8–2.0 MHz for the stiff and 630–650 kHz for the soft cantilever. The exact values depended on the local tip-sample contact stiffness and the cantilever/tip properties. For the SF-PFM measurements, a driving frequency approximately 4 kHz below the contact resonance frequency was chosen. To collect the data for the quantitative piezoresponse properties of the sample by DART-PFM in three dimensions, the vertical and torsional components were measured. After acquiring the image for the flexural vibration of the cantilever and the torsional vibration in one direction ($x$-direction), a subsequent physical 90° rotation around the $z$-axis of the sample was performed and the orthogonal component ($y$-direction) was recorded by rescanning the same area of interest. All of the PFM images were taken with a lateral resolution of 256 × 256 pixel. AC driving voltages of 2 V for the comparison experiments between SF- and TDART-PFM modes and 2.5 V for the quantitative mapping experiments were applied to the tip while scanning perpendicular to the length of the cantilever with a tip velocity of 2.5 µm/s. All piezoresponse amplitude values are given in arbitrary units and normalized by the maximum amplitude range found within the cross-sectional

profiles. For the DART-PFM measurements, the contact resonance $f_0^t$ in the torsional vibration of the cantilever was determined and the difference between the two excitation frequencies $f_{1,2}$ was set to $\Delta f = 8$ kHz ($f_{1,2} = f_0^t \pm 4$ kHz). The frequency feedback loop thus tracked a constant amplitude difference. The frequency difference of 8 kHz was in the range of the imaging bandwidth, which is typically in the order of several kilohertz.[203] The *P* (proportional) and *I* (integral) gains for the topography feedback loop and the scanning speed were optimized for a maximum overlap of the trace and retrace curves and to avoid ringing. To keep the measurements obtained in TDART method comparable to those in SF-PFM mode, the same parameters for the topography feedback were chosen. The filter bandwidth of each lock-in amplifier was set to 5 kHz. The minimum detectable amplitude change of the lock-in amplifier can be roughly estimated to 60 $\mu$V for a 5 kHz bandwidth, as shown in Fig. 3.4. From the inverse slope ($S_1^{-1} = \frac{df_1}{dA_1} \approx 2890$ Hz/mV) of the resonance peak of an ASYELEC-02 cantilever on the 3BMT sample surface at the detection point (point 1, in Fig. 3.5), a minimum detectable frequency shift of $df_1 \approx 170$ Hz was estimated. The same limit applies for the SF technique because the drive frequency was set to the same point of the resonance. The frequency sensitivity could be optimized further ($df_2 \approx 30$ Hz) by choosing the point with the largest slope (smallest inverse sensitivity, point 2, Fig. 3.5) at the expense of a less robust frequency feedback. The imaging resolution of PFM can be estimated from the width of the domain wall.[210] The domain wall width $W$ was estimated using the fitting formula[211]

$$X(x) = A \ \tanh\left(\frac{x}{W}\right) + B \ \arctan\left(\frac{x}{W}\right) \tag{3.1}$$

to the phase shift data obtained at the domain boundary in the analysis software Igor Pro v6.36 (WaveMetrics Inc., Lake Oswego, USA). Here, *A* and *B* are fitting parameters setting the height of the phase range. The topography images were first-order flattened to remove the tilt of the sample surface.

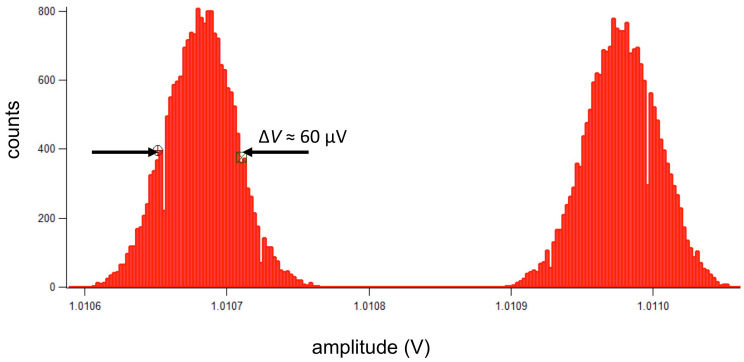


Figure 3.4 Estimation of the amplitude resolution. To estimate the amplitude resolution, the drive amplitude was stepped between two values. The output of the lock-in amplifier (measured amplitude) is shown as a histogram. The histogram shows a bimodal distribution around both driving amplitude values. The full width at half maximum of the peaks (≈ 60 $\mu$V) is mainly determined by noise, digitalization and the transient response of the circuitry. It thus provides a rough estimate for the minimum detectable amplitude difference (the bandwidth filter was set to 5 kHz).

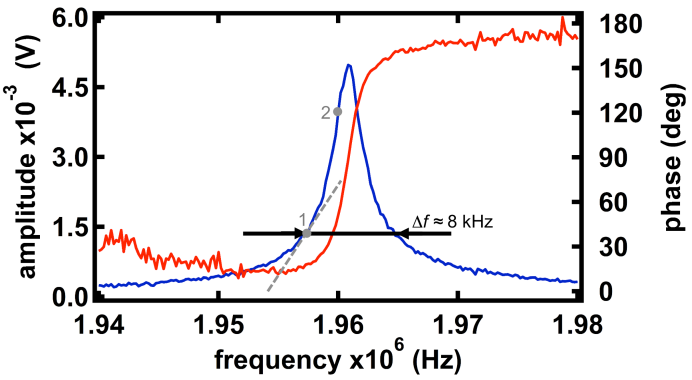


Figure 3.5 Amplitude (blue, left axis) and phase (red, right axis) versus excitation frequency of the torsional vibration of an ASYELEC-02 cantilever on a 3BMT sample surface applying an *ac* voltage 3 V to the tip. The frequency range for the frequency feedback loop is indicated by the arrows. Point 1 marks the detection point for the amplitude at $f_1$. The inverse slope ($S_1^{-1} = \frac{df_1}{dA_1} \approx 2890$ Hz/mV) is marked by the gray dashed line determining the minimum detectable frequency shift. The maximum slope (minimum inverse slope) of the resonance curve can be found at point 2 ($S_2^{-1} = \frac{df_2}{dA_2} \approx 465$ Hz/mV).

## Methodology

### *Dual AC Resonance Tracking in the Torsional Vibration PFM Mode*

The basic principle of DART-PFM is illustrated in Fig. 3.6(a).[203,204] A dual frequency electrical signal with two sinusoidal waves of frequencies $f_1$ and $f_2$ closed to each other is applied to a conductive cantilever that is brought into contact with the ferroelectric sample surface. The resulting cantilever deflection caused by the electromechanical coupling between the tip and the piezoelectric sample surface is recorded by a photodiode through a laser reflected on the backside of the cantilever. The generated signal is analyzed by two lock-in amplifiers, providing the amplitudes $A_1$ and $A_2$ and the phase shifts $\varphi_1$ and $\varphi_2$ at the two excitation frequencies, respectively. To track the instantaneous contact resonance frequency during scanning, the difference between the two amplitude response $\Delta A = A_1 - A_2$, is taken as an error signal for the feedback loop. The principle of the contact resonance tracking is illustrated in in Fig. 3.6(b). The two excitation frequencies, $f_1$ and $f_2$, are chosen on either side of the tip-sample contact resonance frequency, $f_0$, with the corresponding difference of $\Delta A = A_1(f_1) - A_2(f_2)$. When the contact resonance shifts during imaging from $f_0$ (solid line) to a smaller value $f_0'$ (dashed line) because of a change in the mechanical coupling between the tip and sample surface, the amplitude $A_1$ increases to $A_1'$, whereas the amplitude $A_2$ decreases to $A_2'$. In the case of a positive shift of the contact resonance frequency, the change of the amplitudes is reversed. Tracking of the contact resonance by a feedback loop is realized by maintaining the amplitude difference $\Delta A$ at a constant value, through variation of the driving frequencies, $f_1$ and $f_2$. Thus far, the DART-PFM mode has been reported in the literature for flexural vibrations of the cantilever.[202,203] Herein, we suggest applying this method to torsional vibrations of the cantilever as well. This torsional DART-PFM mode can be used to characterize domains with an in-plane polarization complementary to conventional DART.

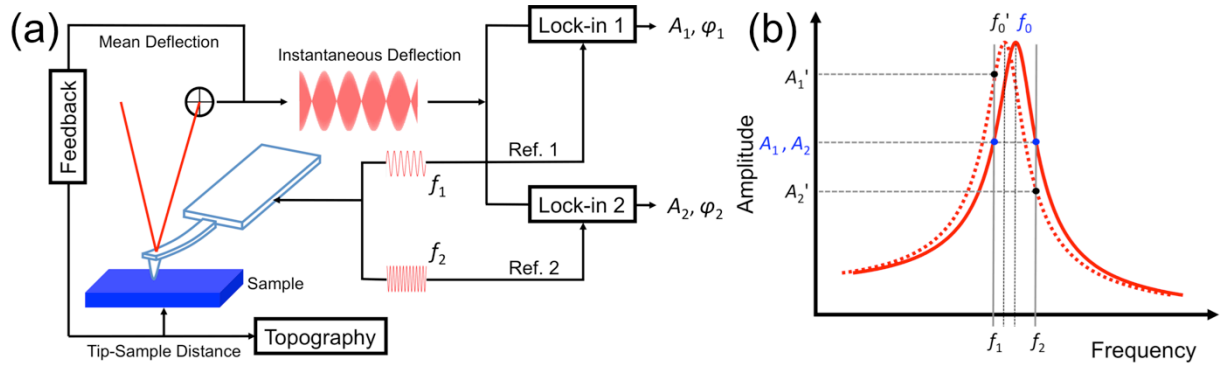


Figure 3.6 Principle of dual *ac* resonance tracking piezoresponse force microscopy mode. (**a**) Scheme and (**b**) principle of contact resonance frequency tracking.

***Damped Simple Harmonic Oscillator (DSHO) Model***

The tip-sample contact mechanics can be modeled as decoupled damped simple harmonic oscillators as shown in Fig. 3.7, where a Newtonian damper and a Hookean elastic spring are connected in parallel. The sample surface motion, induced by the dual *ac* excitation, is characterized by the drive amplitude ($A_{\mathrm{dr},i}$) and drive phase ($\varphi_{\mathrm{dr},i}$) in each direction $i \in \{x, y, z\}$. Each direction features a contact resonance frequency, $f_{0,i}$, as a result of the elastic energy and a quality factor, $Q_i$, representing the energy loss of the respective system. This sample motion in turn drives the tip-cantilever system and results in the measured amplitudes $A_{1,i}$ and $A_{2,i}$ and the phase shifts $\varphi_{1,i}$ and $\varphi_{2,i}$ at the excitation frequencies $f_{1,i}$ and $f_{2,i}$, respectively. The four unknown parameters, $A_{\mathrm{dr},i}$, $\varphi_{\mathrm{dr},i}$, $f_{0,i}$ and $Q_i$, described by the DSHO model contain complete information regarding the local piezoelectric coefficient of the ferroelectric sample, the local polarization orientation, and the conservative and dissipative nature of the tip-sample contact. Calculating these parameters in the *x*-, *y*- and *z*-directions from the corresponding amplitudes $A_{1,i}$, $A_{2,i}$ and phase $\varphi_{1,i}$, $\varphi_{2,i}$ allows for the quantitative mapping of the local electromechanical properties of the ferroelectric material.[203,212,213]

***Calculation of DSHO Model Parameters: $A_{dr,i}$, $\varphi_{dr,i}$, $f_{0,i}$ and $Q_i$***

The four parameters, $A_{\mathrm{dr},i}$, $\varphi_{\mathrm{dr},i}$, $f_{0,i}$ and $Q_i$, in the *x*-, *y*- and *z*-directions need to be calculated to fully describe the DSHO model. These parameters can be expressed by:[203,214]

$$f_{0,i} = \sqrt{f_{1,i} f_{2,i} \frac{f_{2,i}X_{1,i} - f_{1,i}X_{2,i}}{f_{1,i}X_{1,i} - f_{2,i}X_{2,i}}}, \tag{3.2}$$

$$Q_i = \frac{\sqrt{f_{1,i} f_{2,i} (f_{2,i}X_{1,i} - f_{1,i}X_{2,i})(f_{1,i}X_{1,i} - f_{2,i}X_{2,i})}}{f_{2,i}^2 - f_{1,i}^2}, \tag{3.3}$$

$$A_{\mathrm{dr},i} = A_{1,i} \frac{\sqrt{(f_{0,i}^2 - f_{1,i}^2)^2 + (f_{0,i} f_{1,i}/Q_i)^2}}{f_{0,i}^2}, \tag{3.4}$$

$$\varphi_{\mathrm{dr},i} = \varphi_{1,i} - \tan^{-1}\left(\frac{f_{0,i} f_{1,i}}{Q_i(f_{0,i}^2 - f_{1,i}^2)}\right), \tag{3.5}$$

with $X_{j,i} \equiv Q_i\left(f_{0,i}^2 - f_{j,i}^2\right)/f_{0,i}\, f_{j,i}$. The amplitudes ($A_{1,i}$, $A_{2,i}$) and phase ($\varphi_{1,i}$, $\varphi_{2,i}$) at the corresponding driving frequencies $f_{1,i}$ and $f_{2,i}$ can be obtained by DART-PFM in the vertical ($z$-direction) and torsional vibration ($x$- and $y$-directions) of the cantilever to calculate the parameters of the DSHO model. Because the difference between the two excited frequencies, $\Delta f_i = f_{2,i} - f_{1,i}$, is always constant, only one frequency (typically $f_{1,i}$) is needed. To obtain the precise results, a restricted condition of $\varphi_{2,i} > \varphi_{1,i}$ is required for $f_{2,i} > f_{1,i}$.[212]

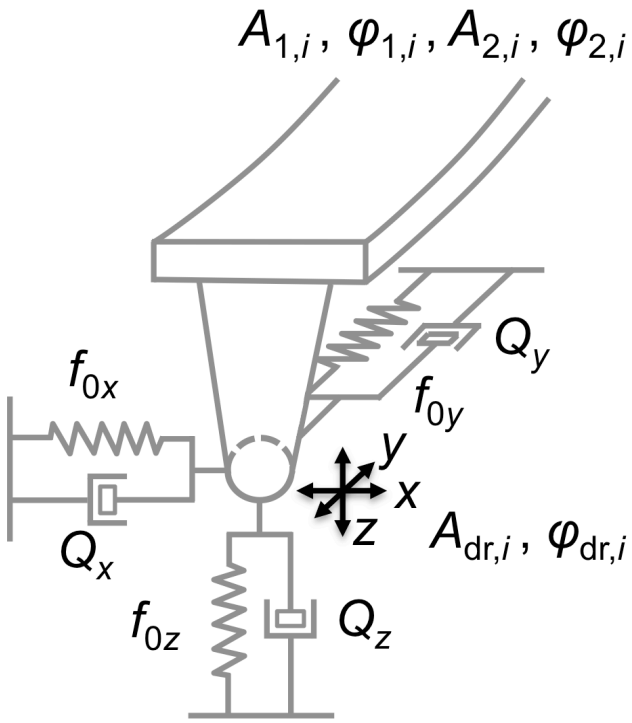


Figure 3.7 Simplified model of the cantilever tip-sample contact mechanics as independent damped simple harmonic oscillators in three dimensions. In the scheme, "$i$" represents the space direction in either $x$, $y$ or $z$.

### 3.1.2 Results and Discussion

**Increased Reliability of Image and Reduced Topographical Crosstalk by TDART-PFM**

The SF-PFM mode in the lateral vibration of the cantilever was compared with the TDART-PFM mode on the relaxor ferroelectric sample, 0BMT, with respect to the amplitude (Fig. 3.8) and phase (Fig. 3.9) piezoresponse. The amplitude image is a measure of the magnitude of the local electromechanical response, whereas the phase image provides a map of the domain orientation below the tip in the corresponding sample direction. A clear lateral domain contrast is visible by the two PFM modes in these figures. Fig. 3.8 shows the piezoresponse amplitude signals measured by SF- (a) and TDART- (b) PFM, both depicting a triangle-shaped domain in the

center of the images. By drawing the cross-sectional profiles (Fig. 3.8(c)) at the position as indicated by the blue line in Fig. 3.8(a), the different domains, including the domain walls, become visible and a comparison between the two modes can be made. Remarkably, the cross-sectional profile of the amplitude response within the triangle-shaped domain region, highlighted in gray, shows an amplitude value for the TDART mode (red line) approximately 24 %, on average, higher than that of the SF technique (black line), though both profiles coincide in the outer regions. Additionally, at the domain walls, the slope of the red curve obtained by TDART-PFM is greater than that of the black line (SF-PFM). The higher amplitude value determined in the central domain is a consequence of the increase of the contact resonance frequency (change from 638 kHz to 641 kHz, see inset Fig. 3.8(c)), which leads to a smaller amplitude at the corresponding excitation frequency in the SF-PFM mode. The TDART technique, however, tracks the instantaneous contact resonance, hence, always amplifies the piezoresponse signal by the same amount giving a better reliability of the image. The reduced width of the domain wall itself implies a greater lateral resolution obtained by TDART-PFM compared to the SF-PFM technique.

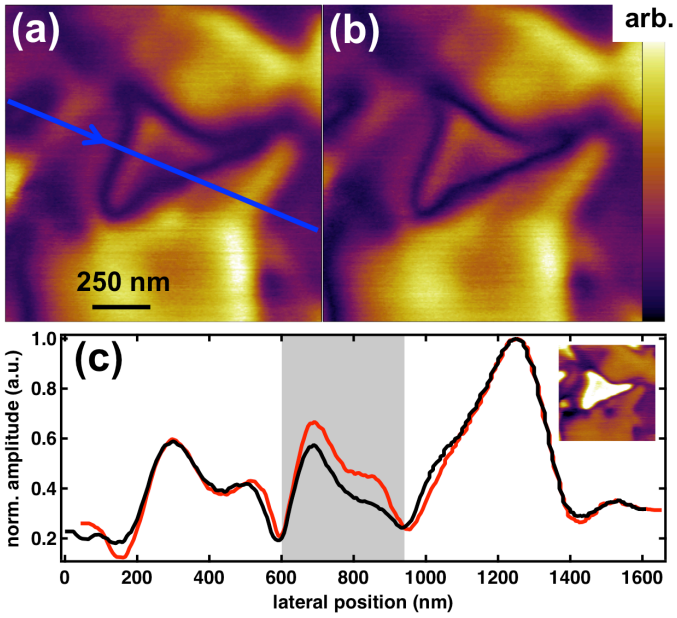


Figure 3.8 Comparison of the piezoresponse amplitude images of the relaxor, 0BMT, measured by (**a**) SF-PFM and (**b**) TDART-PFM. (**c**) Cross-sectional profiles drawn along the blue line in (**a**). The black and red lines correspond to the normalized amplitude response measured by SF- and TDART-PFM, respectively. The region highlighted in gray indicates the extension of the center domain in this particular direction. The inset shows the corresponding contact resonance frequency image (color bar: 637–640 kHz).

Figure 3.9 shows the phase response of the same area measured by SF- (a) and TDART- (b) PFM, as well as the respective cross-sectional profiles (c). Both phase images feature two dominant phase values that can be attributed to the two possible domain orientations in the particular direction of the observation. A bright dot (encircled by the blue circle) directly below the central domain is visible in the SF-PFM image. Highlighted by the blue ellipse and the arrows in the cross section, the phase profile measured by SF-PFM clearly deviates from

the profile obtained by TDART with a bump/hollow combination rather than a flat area at the same position. The associated topography image (see inset of Fig. 3.9(c)) exhibits a hole approximately 500 pm in depth at this exact position. For clarity, the topographical profile was added into the cross section, which indicates the correlation between the height and phase. In the case of the SF-PFM technique, this artifact was caused by topographical crosstalk induced by the feedback loop keeping the mean deflection signal constant during scanning. At the falling edge, the deflection of the cantilever changes to lower values, forcing the *z*-piezo to move the tip towards the sample surface to trace the topography. A sloped topography, however, can only be tracked with residual error. As a consequence, the contact resonance shifts to lower frequencies and hence the phase shifts to larger values compared to the contact resonance corresponding to the given deflection set-point (note that the phase data shown in Fig. 3.9 corresponds to the retrace curve, *i.e.*, the scan direction was from right to left). At the rising edge, the topography error has the opposite sign; thus, the contact resonance frequency shifts to higher values and smaller phase shifts. These variations lead to a wave-like shape of the phase shift profile in SF-PFM as shown in Fig. 3.9(a). In TDART-PFM mode, however, this artifact is corrected by the additional feedback loop tracking the instantaneous contact resonance. In addition, the slope derived from the phase profile obtained by TDART-PFM (red) is higher than that measured by the SF technique at the right domain wall between the central and outer domains, corroborating the higher lateral resolution for the TDART-PFM mode previously confirmed by the amplitude signal.

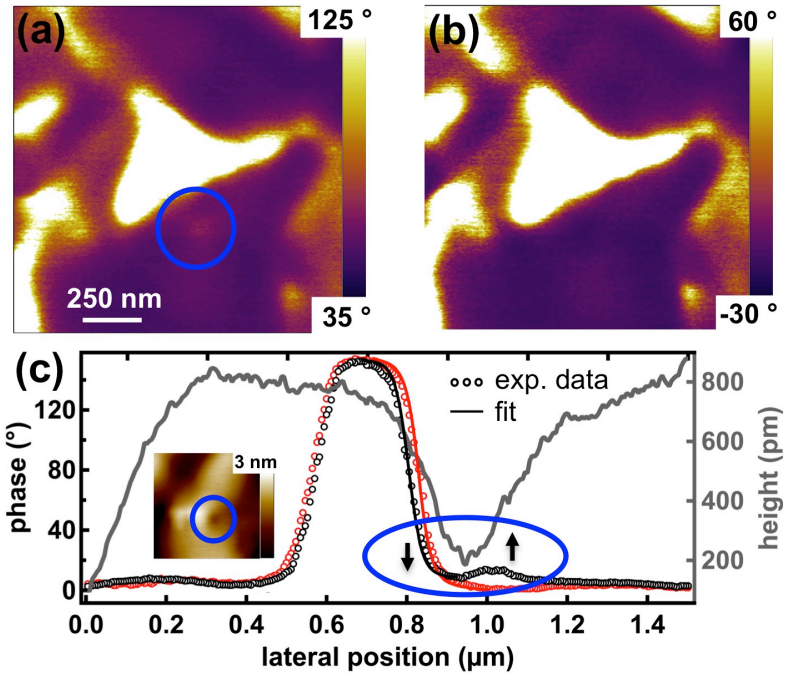


Figure 3.9 Comparison between the phase signals of the 0BMT sample surface measured by (**a**) SF- and (**b**) TDART-PFM modes. (**c**) Cross-sectional profiles of the SF-PFM (black dots) and TDART-PFM (red dots) phase signals. The gray line corresponds to the respective topographical profile. The inset in (**c**) shows the topographical image, in which the encircled area is the position of the hollow in the profile. Upward and downward arrows show the falling and rising edges of the hole, which had to be compensated by the feedback loop, leading to imaging artifacts. The black and red solid lines correspond to the fit data for the phase values at the right domain wall (phase data was shifted for the fit).

To quantify the lateral resolution for both modes, an approach suggested by Jungk *et al.* was used.[211] Equation (3.1) was fitted to the cross-sectional phase profiles in order to extract the full width at half maximum $W$ as a measure for the domain wall width (right side of the peaks, Fig. 3.9). A domain wall width of $(38 \pm 3)$ nm for the TDART-PFM and $(42 \pm 2)$ nm for the SF-PFM technique were obtained, corroborating the above-mentioned assumption. Additionally, TDART-PFM clearly reduces crosstalk originated by topographical features when a bump or hollow causes a major shift in the contact resonance frequency (blue highlighted regions, Fig. 3.9).

The comparison between SF- and TDART-PFM was also performed on a ferroelectric standard PIC 151 (lead-zirconate-titanate, PZT) sample. As shown in Fig. 3.10, small features were revealed in the amplitude image that could not be resolved by the SF-PFM (see arrows in amplitude images in Fig. 3.10), whereas the corresponding phase images exhibited the same lateral distribution of ferroelectric in-plane domains.

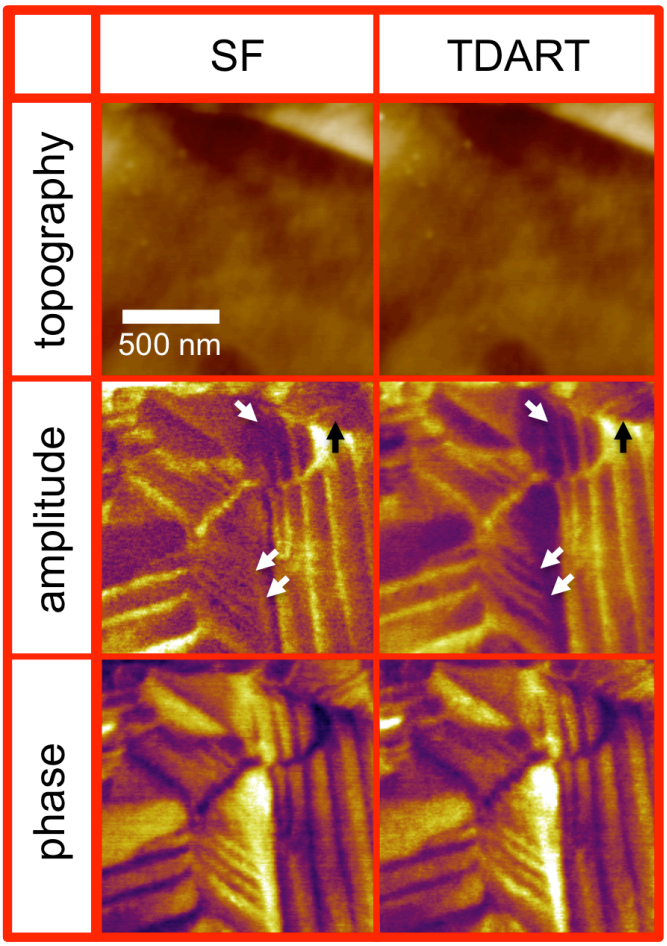


Figure 3.10 Comparison between the SF-PFM (left column) and the TDART-PFM techniques (right column). The topography (top row), amplitude (middle row) and phase (bottom row) images obtained on piezoelectric standard material PIC 151 are shown. The TDART-PFM amplitude image clearly reveals a riffled structure that could not be resolved by SF-PFM (see locations indicated by the arrows). The corresponding phase images exhibit the same lateral distribution of ferroelectric in-plane domains.

**Quantitative Mechanical Surface Properties and Three-dimensional Visualization**

The combination of TDART and vertical DART (VDART)-PFM enables three-dimensional visualization of the local piezoresponse of the 3BMT sample. Gannepalli *et al.* developed a routine to transfer the observables provided by DART-PFM into quantitative information of the local mechanical sample properties.[203,214] Equations (3.2)–(3.5) were applied to calculate the DSHO model parameters for the tip-sample contact based on the experimental results of the VDART- and TDART-PFM for the 3BMT sample, leading to the local mechanical and piezoresponse properties in all three spatial directions (Fig. 3.11). Figure 3.11(a) shows the topographical image of the sample surface. The sample exhibits holes on the surface that are 150–200 nm in diameter and several nanometers (1–4 nm) in depth. Maps of the calculated DSHO model parameters for the drive amplitude, drive phase, quality factor and contact resonance frequency in the *z*-, *x*- and *y*-directions are given in Fig. 3.11(b–e) for $A_{\mathrm{dr},z}$, $\varphi_{\mathrm{dr},z}$, $Q_z$, and $f_{0,z}$; Fig. 3.11(f–i) for $A_{\mathrm{dr},x}$, $\varphi_{\mathrm{dr},x}$, $Q_x$, and $f_{0,x}$; and Fig. 3.11(j–m) for $A_{\mathrm{dr},y}$, $\varphi_{\mathrm{dr},y}$, $Q_y$, and $f_{0,y}$. Dashed lines highlight the potential domain walls at the sample surface where the associated strength of the piezoresponse signal is weak in these areas. In most portions of the imaged area, however, the requirements of the DSHO model are fulfilled. The true drive phases $\varphi_{\mathrm{dr},x}$ and $\varphi_{\mathrm{dr},y}$ of the 3BMT sample reveal a clear phase contrast between the ferroelectric domains in both *x*- and *y*-torsional components, suggesting differently orientated domains (Fig. 3.11(g) and (k)), whereas a weak vertical polarization is apparent in Fig. 3.11(c). This implies that the out-of-plane component of the piezoresponse is less pronounced than the associated in-plane components of the same domains.

The images of the drive amplitudes $A_{\mathrm{dr},x}$ and $A_{\mathrm{dr},y}$ (Fig. 3.11(f) and (j)) represent the local lateral piezoresponse coefficients. In particular, the $A_{\mathrm{dr},x}$ image taken in the *x*-direction reveals extremely fine domain features compared to the vertical amplitude response (Fig. 3.11(b)). This observation can be ascribed to two contributions: (1) the strong and permanent mechanical contact between the tip and sample that is better for lateral rather than vertical vibrations; (2) the large in-plane piezoelectric coefficients of the sample.[215] The true local contact resonance frequencies, $f_{0,i}$, that mainly depend on the tip-surface contact stiffness,[203,214,216] are visualized in the maps of Fig. 3.11(e), (i) and (m) for the *z*-, *x*- and *y*-directions, respectively. The resonance frequencies $f_{0,y}$ and $f_{0,z}$ show the structures that are related to the topography, whereas $f_{0,x}$ exhibits features that are connected to those obtained in the driving amplitude image (Fig. 3.11(f)) in the sample direction. A difference in the contact resonance frequency between the *x*- and *y*-torsional directions of approximately 20 kHz (*cf.* Fig. 3.11(i) and (m)) was also observed. Differences in the tip-sample contact mechanics because of discrepancies in the sample coupling conditions in the three spatial directions cause this deviation. In addition, Fig. 3.11(d), (h) and (l) map the calculated $Q$-factor in the *z*-, *x*- and *y*-directions, respectively, as the damping of the tip-sample system. The damping in the *z*- and *y*-directions is uniform ($Q_z \approx 100$ and $Q_y \approx 150$), whereas in the *x*-direction a clear contrast is observed ($Q_x \approx 170{-}400$). This result is another indication that the mechanical coupling between the tip and the sample and/or the mechanical surface properties itself varies in the distinctive

sample directions; therefore, a three-dimensional characterization technique is necessary to fully describe the local electromechanical properties of the sample surface.

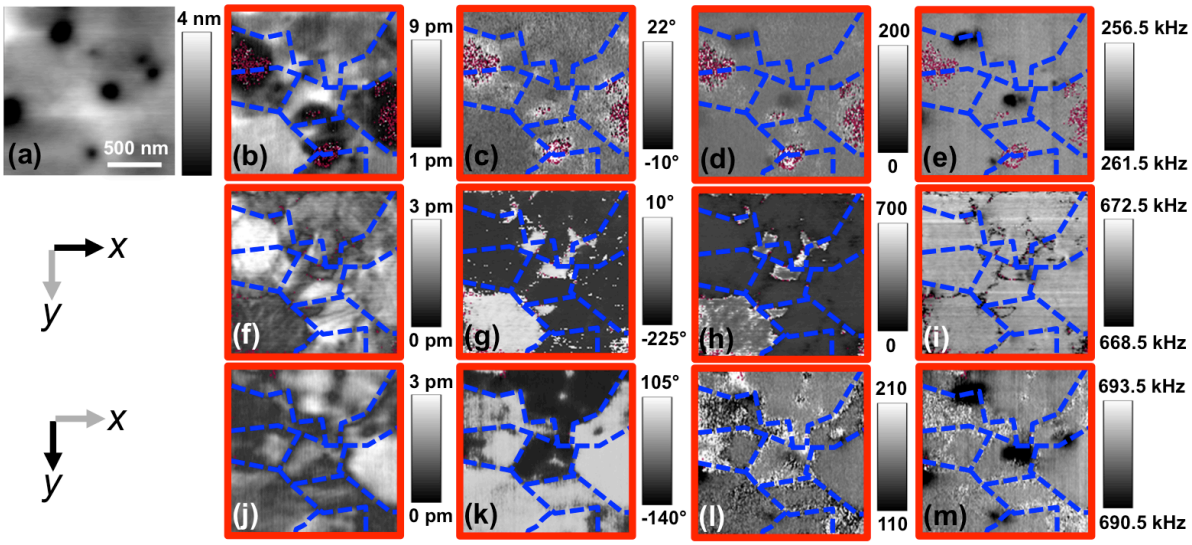


**F**igure 3.11 Mechanical sample properties quantified by the decoupled damped simple harmonic oscillator model in three dimensions. (**a**) Topography and (**b**−**m**) calculated DSHO model parameters in the *x*-, *y*- and *z*-directions calculated by transforming the data obtained by vertical and torsional dual ac resonance tracking. (**b**), (**c**), (**d**), and (**e**) represent the drive amplitude ($A_{\mathrm{dr},z}$), drive phase ($\varphi_{\mathrm{dr},z}$), the quality factor ($Q_z$) and contact resonant frequency ($f_{0,z}$) in the *z*-direction, respectively. Accordingly, (**f**), (**g**), (**h**), (**i**) represent $A_{\mathrm{dr},x}$, $\varphi_{\mathrm{dr},x}$, $Q_x$, $f_{0,x}$, in the *x*-direction and (**j**), (**k**), (**l**), (**m**) correspond to $A_{\mathrm{dr},y}$, $\varphi_{\mathrm{dr},y}$, $Q_y$, $f_{0,y}$ in the *y*-direction. Dashed lines indicate the domain walls for better comparison of the images. The red dots indicate invalid pixels where the model assumption $\varphi_{2,i} > \varphi_{1,i}$ was not fulfilled.[203]

The quantified data obtained in all three dimensions can be represented in single maps as showed in Fig. 3.12 using a similar approach as Kalinin *et al.*[217] Figure 3.12(a) shows the local distribution of the true drive amplitude, $A_{\mathrm{dr},i}$; Fig. 3.12(b) shows the drive phase, $\varphi_{\mathrm{dr},i}$; Fig. 3.12(c) shows the quality factor, $Q_i$; and Fig. 3.12(d) shows the contact resonance frequency, $f_{0,i}$, in the vertical direction. The blue dashed lines in the images highlight differently oriented domains. Arrows pointing to the left and up refer to negative drive phase values in the *x*- and *y*-directions. The strength of the respective signal for the *x*- and *y*-directions is encoded in the gray scale color inside the arrows. The color-coded arrows provide the complimentary information for the three-dimensional visualization of the quantitative sample properties. This data representation allows the observer to conveniently get an overview of the electromechanical properties in three dimensions at a glance, avoiding the necessity of elaborate three-dimensional visualization.

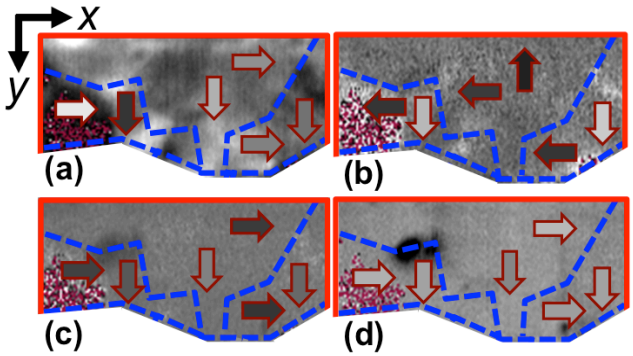


Figure 3.12 Visualization of the calculated DSHO model parameters obtained by DART accomplished in three spatial directions. (**a**) Drive amplitude ($A_{\mathrm{dr},i}$), (**b**) drive phase ($\varphi_{\mathrm{dr},i}$), (**c**) quality factor ($Q_i$), and (**d**) contact resonance frequency ($f_{0,i}$) based on the data of Fig. 3.11 (upper portion). Dashed lines indicate the domain walls of the different ferroelectric domains. The arrows point out the orientation of the respective parameter of each domain and the gray scale value encodes the strength for the *x*- and *y*-directions. The color bar is the same as in Fig. 3.11. The red dots in these images indicate invalid pixels.

**Detection of Polar Nanoregions**

Using TDART-PFM, it was observed that an improved lateral resolution of the in-plane orientation of the ferroelectric domains on different relaxors, *e.g.*, 3BMT that possesses a higher electric field-induced strain compared to 0BMT. Figure 3.13 shows the topographical image (Fig. 3.13(a)) and the local distribution of the in-plane domain orientation at the sample surface measured by SF-PFM (Fig. 3.13(b) and (c)) and TDART-PFM (Fig. 3.13(e) and (f)), as well as a map of the driving frequency $f_1$ (Fig. 3.13(d)). The amplitude (Fig. 3.13(b) and (e)) and phase images (Fig. 3.13(c) and (f)) reveal the absence of a long-range ordered ferroelectric domain structure that would be typical for classical ferroelectric systems. Instead, polar clusters with a minimum size of a few tens of nanometers were detected. Comparing the phase images of both techniques, an enhanced phase contrast in the case of TDART-PFM (Fig. 3.13(f)) compared to the SF-PFM technique was observed (Fig. 3.13(c)). The phase image measured using the TDART technique shows a clear distribution of the ferroelectric domains with a sharp transition at the interphase between different domain orientations. The image contrast reveals that the phase signal appropriately follows the domain distribution with a constant phase value for each state, hence, it can be reliably considered for visualizing solely the domain orientation. In contrast, the phase image obtained by SF-PFM exhibits features within single domains most probably generated by crosstalk between the amplitude and phase channels, caused by noise or topography. This effect becomes particularly apparent as the white dots in Fig. 3.13(c).

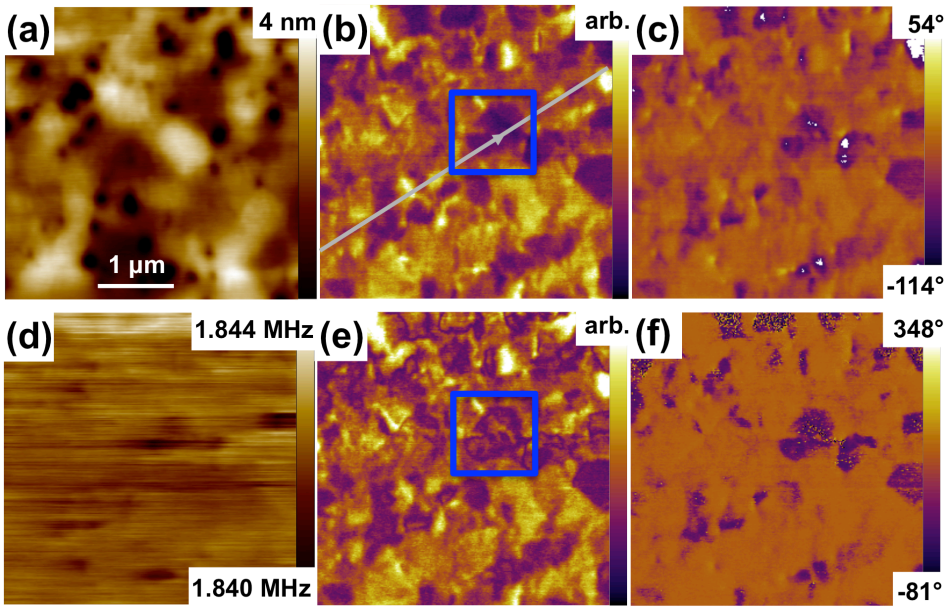


Figure 3.13 Comparison between the piezoresponse amplitude and phase images of a 3BMT ferroelectric sample measured by SF-PFM (upper row) and TDART-PFM (lower row). (**a**) Respective sample topography. (**b**) Amplitude and (**c**) phase response images obtained by SF-PFM. (**e**) Amplitude and (**f**) phase response measured by TDART-PFM. (**d**) Map of the driving frequency $f_1$ (below the contact resonance) in TDART-PFM. (**e**) The area within the blue rectangular frame exhibits a fine domain structure for TDART-PFM with additional features visible compared to the SF-PFM technique (**b**). This fine structure can be explained by PNRs.

Additionally, more distinctive features in the TDART-PFM amplitude signal with sharply defined boundary were found. This observation becomes highly apparent when focusing on the blue-framed area. A magnified area of this region is displayed for both SF-PFM (Fig. 3.14(a)) and TDART-PFM (Fig. 3.14(b)). Only the TDART-PFM technique reveals features that are considerably smaller than hundreds of nanometers. Figure 3.14(c) compares the cross-sectional profiles obtained using both techniques (SF-PFM − black line; TDART-PFM − red line) for the entire distance drawn along the gray line indicated in Fig. 3.13(b). The two profiles depict similar tendencies except in the region of the enlarged area highlighted by the gray box. In this region, the profile measured by TDART-PFM shows peaks invisible in the black line obtained by SF-PFM, which corroborates the visual impression of a higher contrast apparent in Fig. 3.14(b).

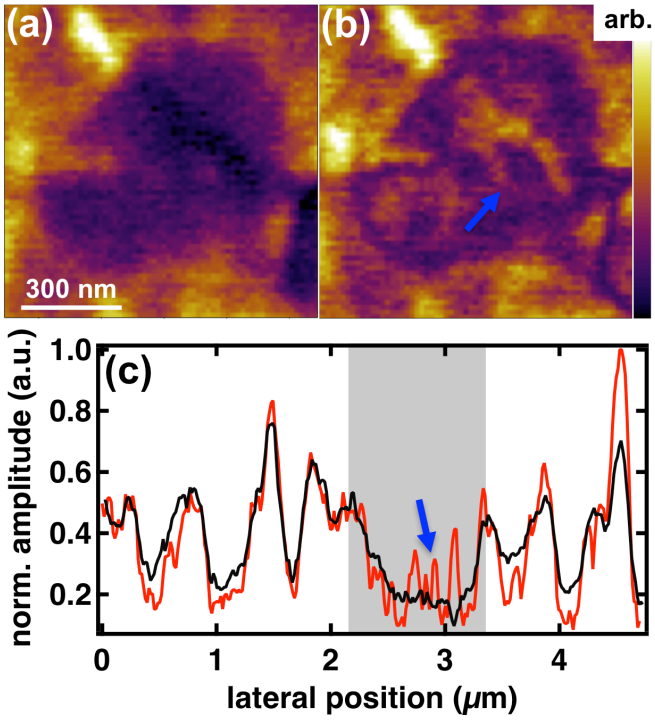


Figure 3.14 Visualization of polar nanoregions. Enlarged areas of the region marked with a blue frame in the amplitude images of Fig. 3.13 for (**a**) SF-PFM and (**b**) TDART-PFM. (**c**) Respective cross-sectional profiles along the gray line are indicated in Fig. 3.13 for SF-PFM (black line) and TDART-PFM (red line). The gray box highlights the nanostructured region (arrow) in (**b**), which can be interpreted as the signature of polar nanoregions. The size of these regions is approximately 50 nm.

In principle, noise and feedback lagging or ringing might cause very tiny features in the amplitude and phase images that can be misinterpreted as PNRs. To corroborate the detectability of PNRs by TDART-PFM, nanoscale features prevailing in the amplitude images were focused on. These features were repeatedly scanned at scan angles parallel and perpendicular to the cantilever axis. Figure 3.15 shows the topography (top row), amplitude (middle row) and phase images (bottom row) of a 3BMT sample measured by SF-PFM (left two columns) and TDART-PFM (right two columns). The left column for each mode was obtained by scanning at an angle of $\alpha_{\mathrm{scan}} = 0°$, *i.e.* with the fast scan axis in the same direction as the long axis of the cantilever, whereas the right column was scanned perpendicular to the cantilever axis. The features indicated by the arrows appear in both images irrespective of the scan direction, and exist after repeated scans. This demonstrates that noise or feedback induced artifacts as origin of such features can be excluded. Furthermore, these nanoscale features are hardly visible in the amplitude image obtained by the SF-PFM mode. Notably, the orientation of some features apparent in the phase images measured by SF-PFM strongly depends on the scan direction as indicated by the encircled area (left two images, bottom row). Furthermore, the similar trends of the cross-sectional profiles in Fig. 3.14(c) outside the region highlighted in gray indicate that the noise level was similar for both imaging techniques. Analyzing the width of the peaks within the gray area in the profile through the full width at half maximum, a domain size of approximately 50 nm (marked by a blue arrow) was measured.

Thus, these tiny structures can be interpreted as the signatures of PNRs, which are difficult to be visualized with other microscopic techniques.

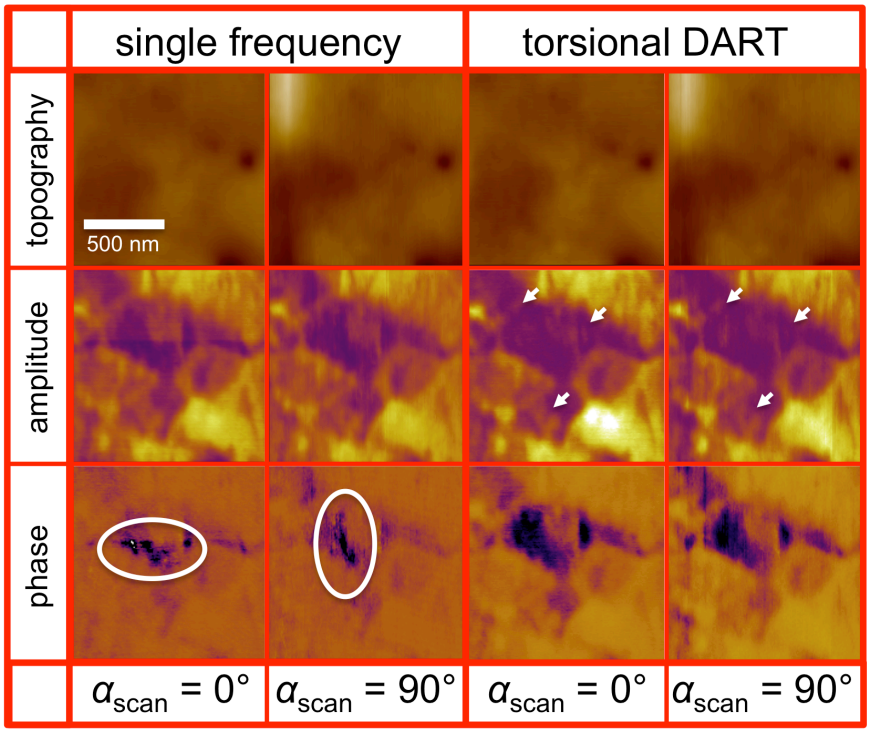


Figure 3.15 Comparison between the SF- (left two columns) and the TDART-PFM technique (right two colums). Topography (top row), amplitude (middle) and phase (bottom) images of a 3BMT sample. The images were measured in different scan directions as noted at the bottom. Arrows indicate similar features that are independent of the scan direction with respect to the sample, whereas the encircled areas highlight a region showing a domain orientation that indeed depends on the scan direction. Color bars: topography 0–8 nm, amplitude arbitrary, phase -19°–58°, -16°–54°, 53°–233°, 48°–228° (from left to right).

### 3.1.3 Statement of Personal Contribution

[1] Na Liu, Robert Dittmer, Robert W. Stark and Christian Dietz, "Visualization of polar nanoregions in lead-free relaxors via piezoresponse force microscopy in torsional dual *ac* resonance tracking mode", *Nanoscale*, *7*, 11787 (2015).

The initial idea to apply DART-PFM in torsional vibration was from myself. As a result of elaborated discussions with Dr. Christian Dietz, technological assists from Dr. Florian Johann (Asylum Research, Oxford Instruments GmbH) and Dr. Christian Dietz, the idea could be realized on the lead-free relaxor ferroelectrics provided and macroscopically characterized by Dr. Robert Dittmer. All experimental work with respect to the PFM characterizations was carried out by myself. The data analysis with respect to PFM results were done by

myself. The manuscript was written by myself and revised and approved by Dr. Christian Dietz and Prof. Dr. Robert Stark.

## 3.2 Nanoinsight into Relaxation Behavior and Ergodicity Distribution in La-doped $Bi_{1/2}Na_{1/2}TiO_3$-$Bi_{1/2}K_{1/2}TiO_3$ Relaxors via Piezoresponse Force Microscopy

The content regarding to the conventional PFM in this Chapter is published in:

[2] Matias Acosta, Na Liu, Marco Deluca, Sabrina Heidt, Ines Ringl, Christian Dietz, Robert W. Stark and Wook Jo, "Tailoring ergodicity through selective A-site doping in the $Bi_{1/2}Na_{1/2}TiO_3$-$Bi_{1/2}K_{1/2}TiO_3$ system", *Journal of Applied Physics*, ***117***, 134106 (2015).

In the present Chapter, two kinds of relaxor piezoelectric ceramics, Na or K replaced by 1 at. % La in the system of $0.8Bi_{1/2}N_{1/2}TiO_3$-$0.2Bi_{1/2}K_{1/2}TiO_3$, were chosen for PFM investigations. Macroscopically, the freezing temperatures $T_f$ of the two variants are different and slightly higher than the room temperature. Consequently, both samples are characterized by an ergodic relaxor state. Because of the different $T_f$, the relaxor states of the two samples have different degrees of ergodicity. The degree of ergodicity is known to play a crucial role for the relaxor properties. To study the local distribution of ergodicity, the relaxation behavior of a tip-induced ferroelectric domain and local hysteresis loops are measured by PFM with a scanning velocity of approximately 5 μm/s which are then compared to the macroscopic dielectric and electromechanical properties. Owing to the high dynamic nature of PNRs in the ergodic relaxor state, the scanning velocity of 5 μm/s typically used in conventional PFM is insufficient to visualize the fast relaxation of the induced domain right after poling. Thus, we optimized the scanning parameters for high-speed PFM for tip velocity up to 117 μm/s. With this technique, image series with high temporal resolution could be obtained on the chosen areas of both samples after tip poling. Thereby the local distribution of the ergodicity, the local dynamics of PNRs, and the relaxation mechanisms of the lead-free relaxor piezoceramics could be unraveled.

### 3.2.1 Experimental and Method

**Sample Preparation, Macroscopic Measurements and Characterization**

The system of $0.8Bi_{1/2}N_{1/2}TiO_3$-$0.2Bi_{1/2}K_{1/2}TiO_3$ with a morphotropic phase boundary composition was chosen as initial material. By replacing Na and K by 1 at. % La, two samples with the stoichiometric formulas $Bi_{0.5}Na_{0.39}K_{0.1}La_{0.01}TiO_3$ (BNTNa) and $Bi_{0.5}Na_{0.4}K_{0.09}La_{0.01}TiO_3$ (BNTK), respectively, were designed. The materials were prepared by a conventional solid state route using $Bi_2O_3$ (99.975%), $Na_2CO_3$ (99.5%), $K_2CO_3$ (99.0%), and $La_2O_3$ (99.9%) as raw materials (Alfa Aesar GmbH & Co., Germany). Calcination was done at 850 °C for 3 h, and sintering at 1150 °C for 2 h. The processing route is the same as that in Chapter 3.1.1. The temperature- and frequency-dependent real relative permittivity of the unpoled samples was measured by using a commercial impedance analyzer (Novocontrol Technologies, Impedance analyzer Alpha-A, Germany)

equipped with a cryostat during cooling. Frequencies ranging from 0.1 Hz to 1 MHz with amplitude of 1 V in the temperature range from −150 °C to 250 °C and a cooling rate of 1 K/min were employed. For the electric field-dependent polarization $P(E)$ and strain $S(E)$ measurements of virgin samples at room temperature were measured with a standard Sawyer-Tower at 1 Hz employing a 10 µF measurement capacitor and an optical sensor (Philtec, Inc., Annapolis, MD, USA).

Both samples behave a canonical relaxor properties indicated by a frequency dispersion of the dielectric permittivity maximum and the decreased magnitude of the peak value of dielectric permittivity when increasing the temperature, as shown in Fig. 3.16.[57] As presented in Fig. 3.17, the freezing temperatures ($T_f$) of the samples of BNTNa and BNTK are (253 ± 12) K (black square) and (283 ± 9) K (red square), respectively, which were fitted with the Vogel-Fulcher relationship (Equation (2.17)).[30,127,128] Because freezing temperatures ($T_f$) for both samples are slightly below the room temperature, both sample are macroscopically categorized as ergodic relaxors at room temperature.[57] Given that the $T_f$ of BNTK is higher than the one of BNTNa (square symbols in Fig. 3.17), the bipolar polarization and strain loops obtained (inset (B) and (C) in Fig. 3.17) on virgin specimens exhibit a lower remanent polarization and strain and more pronounced pinching of the $P(E)$ loop of BNTNa in comparison with BNTK sample, the sample BNTNa thus macroscopically presents a higher degree of ergodicity than the sample of BNTK at room temperature.[5] At the microscale, it has been assumed that in the relaxors, which express a freezing temperature in close to room temperature, the ergodic and non-ergodic states coexist.[57,136] For example, it was reported that in a canonical relaxor single crystal PMN-10PT with a freezing temperature of approximately 270 K, both dynamic and static mesoscopic disorder concurrently act on the relaxation behavior.[133]

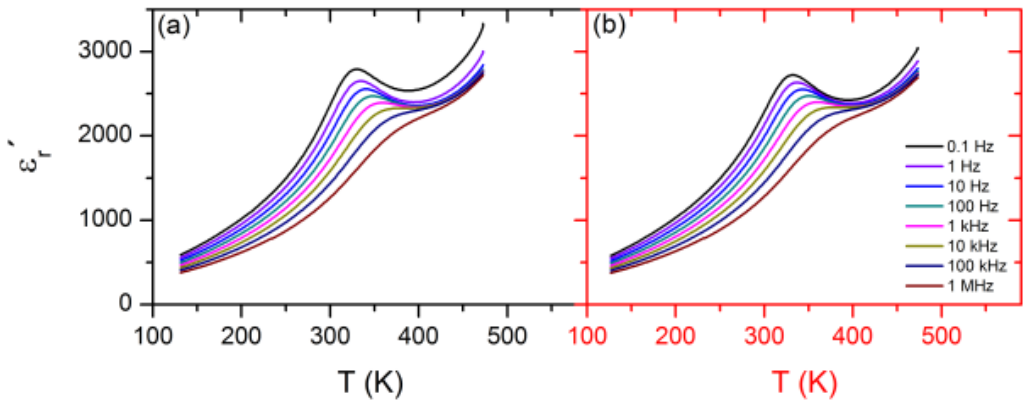


Figure 3.16 Real part of the relative dielectric permittivity of (**a**) BNTNa relaxor and (**b**) BNTK relaxor as the function of frequency and temperature.

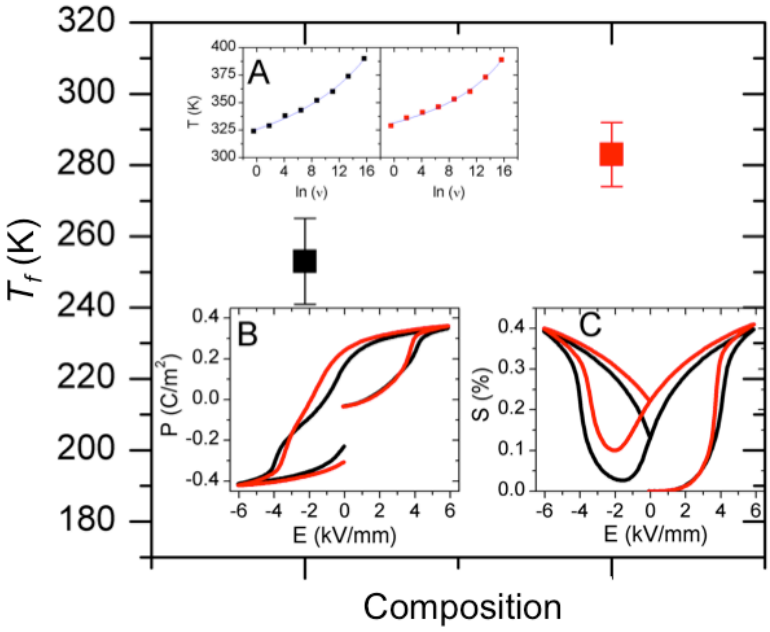


Figure 3.17 Freezing temperature (square symbols), and polarization $P(E)$ and strain $S(E)$ curves obtained for BNTNa sample (black) and BNTK sample (red). Inset (**A**) displays the fitting curves utilized to determine $T_f$, (**B**) and (**C**) exhibit the $P(E)$ and $S(E)$ curves on the virgin state of both samples, respectively.

**Conventional Piezoresponse Force Microscopy**

***Vertical Poling and Imaging***

A Cypher AFM with Ti/Ir (5/20) coated conductive cantilevers ASYELEC-01 (Asylum Research an Oxford Instruments company, Santa Barbara, CA) was used for the PFM study. The nominal spring constant of this type of cantilevers was $k = 2$ N/m with a nominal fundamental resonance frequency $f_0 = 70$ kHz. All PFM images were acquired on mirror-polished and annealed sample surfaces (same procedure as in Chapter 3.1.1). PFM Images with a resolution of 256 × 256 pixels using a constant loading force of approximately $F = 120$ nN were acquired using DART-PFM mode in the vertical vibration of the cantilever.[202] A driving voltage $V_{ac}$ of 3 V was applied to the tip while scanning perpendicular to the length axis of the cantilever with a velocity of 5 µm/s. The chosen areas of 1 × 1 µm$^2$ on both samples were poled by scanning the sample surface line-wise with a tip velocity of 5 µm/s and simultaneously applying a $dc$ electric field of −10 V. The scan direction was from top to bottom, and the acquisition time for one image approximately 8 min. Topography images were first-order flattened, and all other images were leveled by a line-wise offset subtraction.

***Local Hysteresis Loops***

Local bias-on and bias-off hysteresis loops on the sample surface were acquired by the SS-PFM method implemented in DART-PFM mode.[39] An 1 V $ac$ voltage for reading out the signal was superimposed to a poling $dc$ waveform having a stepwise increasing/decreasing rectangular pulse starting initially from 0 V. The maximum poling voltage was 8 V. A pulse time of 25 ms in 100 steps was chosen for each oscillation cycle

with a bias-off time equal to the pulse time. The piezoresponse were calculated by Equation (2.18). A total number of seven cycles per position were averaged to achieve the final hysteresis loops representative for each sample. The on- and off-state loops were obtained at the same sample positions, which could extract the electrostatic influence of the applied electric field on the piezoresponse signal. Because the hysteresis loops obtained on different samples were recorded under same experimental conditions, they are thus relatively comparable to each other.

**High-speed Piezoresponse Force Microscopy**

***Vertical Poling and Imaging***

A Cypher AFM with conductive cantilevers PPP-NCHPt (Nanosensors, Neuchatel, Switzerland) for all high-speed PFM experiments was employed. The cantilevers, coated with Cr/PtIr in thickness of 5 nm / 25 nm to provide conductivity and mechanical resistance, exhibited a norminal radius of 30 nm and nominal spring constants of 42 N/m. To induce a long-range ordered ferroelectric domain, an 1 × 1 $\mu m^2$ large area was poled by applying a +10 V to the tip kept in contact with the sample surface with a constant force of approximately 385 nN. The resulting strength of the electric filed around the tip was sufficient to pole the surface when scanning 256 lines within the squared area using a scan rate of 0.5 Hz (approximately 5 µm/s). Temperature and relative humidity in the laboratory during the measurements were (301 ± 2) K and (36 ± 5) %, respectively. The subsequent relaxation process of the tip-induced ferroelectric domain was visualized by the developed high-speed PFM in the single frequency mode.[36] The cantilever was electrically driven in contact resonance frequencies with $f_y = (1130 \pm 20)$ kHz for the vertical and $f_1 = (1830 \pm 20)$ kHz for the lateral cantilever motion, and the driving $ac$ voltage $V_{ac} = 1$ V at a scan angle of 90°. Special attention was paid to find a spot on the sample surface with a low root-mean-square roughness and without pores that could potentially damage the tip. To adequately follow the relaxation process of the poled domain with a sufficient time resolution, the scanning parameters had to be optimized for fast imaging rates in PFM, and the respective details are given in the following Chapter. A suitable scan size was 3 × 3 $\mu m^2$ with the same center location as the previously poled area. The optimum mean force (approximately 385 nN) and integral gain ($I_G = 70$) applied during scanning were evaluated, based on a minimum deviation of the trace and retrace images of the topographical scan and on a small domain wall width measured at the edge between a poled and unpoled region on the BNTK sample, respectively. The chosen scan rate of 19.5 Hz corresponding to a tip velocity of approximately 117 µm/s results in a reasonable domain wall width, a small amount of artifacts in the topography, amplitude and phase images, and low tip wear with no significant ringing. Compared with reported work in the field of high-speed PFM/AFM on the flat surface, *e.g.* measuring ferroelectric domain nucleation[59] and switching[60,61] or studying biological membranes,[218] the tip velocity and the resulting image acquisition rate accomplished in this study is sufficient to classify the method as high-speed PFM. The detailed process of parameter optimization including the applied force ($F_{ts}$) to the tip-sample ensemble, scan rate, integral gain ($I_G$) for high-speed PFM imaging will be introduced in the following Chapter. Note that the scan direction was from top to bottom.

***Parameter Optimization for high-speed PFM Scanning***

To optimize the essential scanning parameters for high-speed PFM, the sample BNTK was chosen due to the higher stability of the field-induced ferroelectric domain in comparison with that on the BNTNa sample. In order to obtain a suitable mean tip-sample setpoint force $F_{\mathrm{ts}}$, four phase images of a tip-induced ferroelectric domain were captured successively by vertical PFM in the single frequency mode with a scan rate of 19.5 Hz and corresponding mean forces 190 nN, 385 nN, 575 nN, and 770 nN, as shown in Fig. 3.18 as insets (a−d). The domain wall width apparent in the averaged cross-sectional profile (green boxes indicate the location in the inset of Fig. 3.18) was then calculated by Equation (3.1), and the force corresponding to a minimized apparent domain wall width was chosen as an optimized mean force, that was approximately $F_{\mathrm{ts}} = 385$ nN.

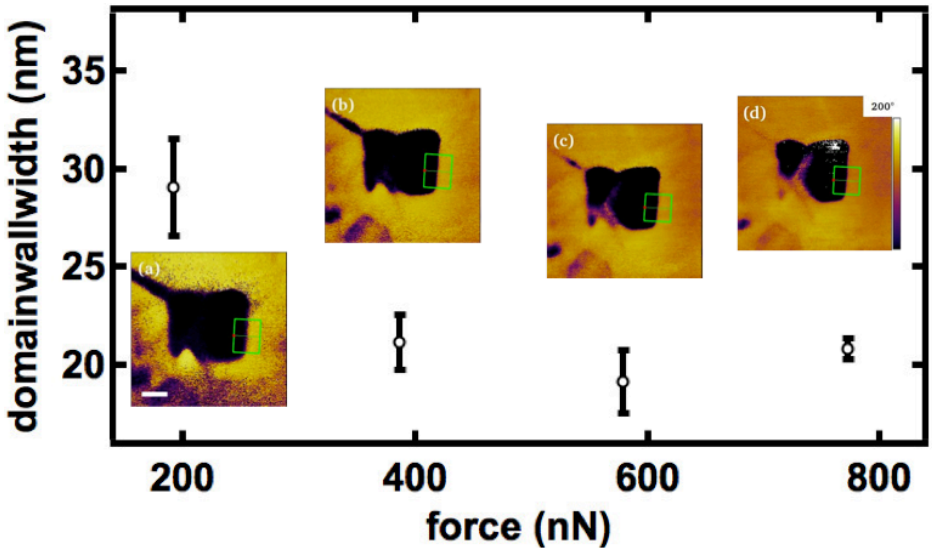


Figure 3.18 Optimization of the mean tip-sample force. Domain wall widths were calculated from the cross-sectional profiles obtained from the marked green boxes in the phase images at different tip-sample forces and at a scan rate of 19.5 Hz. Insets (**a**−**d**) are the vertical phase images having the scale bar of 500 nm and color bar range of 0°−200°.

To find an appropriate scan rate (tip velocity = scan rate × length of each scan line × 2) which is fast enough to observe the relaxation processes and allows for a precise feedback, phase images of a tip-induced domain were captured by a PFM tip where different scanning velocities at a constant force of approximately 385 nN were applied. The corresponding domain wall widths were then calculated from the cross-sectional profiles at the positions indicated in the insets of phase images as shown in Fig. 3.19 (same marking region as in Fig. 3.18). A reasonable scan rate was chosen at approximately 19.5 Hz (tip velocity $\approx$ 117 µm/s, $\approx$ 13 s/frame), because the domain wall width was smallest at the scan rate of 19.5 Hz, and imaging artifacts and tip degradation occurred at higher scan rates. Another crucial parameter for high-speed PFM scanning is the integral gain $I_{\mathrm{G}}$ that determines the response time of the feedback loop. A proper integral gain ($I_{\mathrm{G}}$) was found based on a minimum deviation of the trace and retrace images of the topographical scans obtained at the optimized scan rate and mean force. As shown in Fig. 3.20, the smallest apparent height deviation with a symmetric distribution can be obtained by choosing an integral gain $I_{\mathrm{G}}$ of 70.

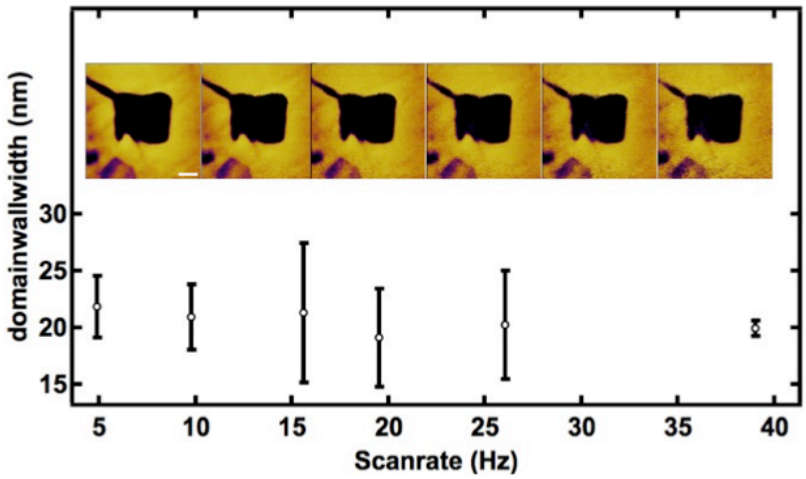


Figure 3.19 Optimization of the scan rate. Domain wall widths were calculated from the vertical phase images. The images were captured by subsequently scanning the same area with a tip loading force of approximately 385 nN applying different scan rates. Phase images with a scale bar of 500 nm and a color bar range of 0°−200° are shown as insets.

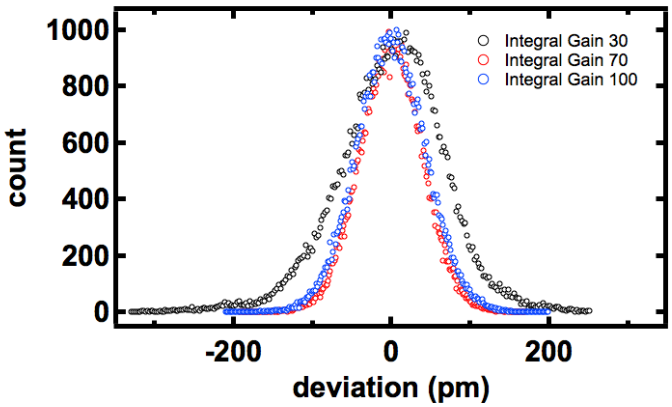


Figure 3.20 Optimization of the integral gain ($I_G$). Histograms of the apparent height deviation obtained by subtracting the trace and retrace topographical images at $I_G$ = 30 (black circle), 70 (red circle) and 100 (blue circle) were compared.

***Relaxation Measurements and Image Processing***

To obtain the data points of the relaxation curves on each specimen, the cumulative histogram of the phase values apparent inside the framed area of the PFM phase images captured at different times after poling were drawn. The first phase image captured right after poling was considered as fully poled and a threshold was defined accordingly: all values below (above) the threshold corresponded to the poled (relaxed) area (a threshold of 0° was appropriate for this work). The values read out at the threshold phase correspond to the probability density of poled area at given times, and the probability density of poled area versus time describe the relaxation curves. In order to obtain the relaxation times of the poled area on each specimen, the relaxation curves were fitted using the well-known empirical relaxation law, Kohlrausch-William-Watts (KWW) expressed by:[25,115,219,220]

$$P_{\text{poled}} = P_{\text{init}} e^{-(\frac{t}{\tau})^{\beta}}, \tag{3.6}$$

where $P_{\text{poled}}$ is the poled area density at a given time $t$, $P_{\text{init}}$ is the initial poled area density ($P_{\text{init}}$ was set to 100% because the first phase image was considered as fully poled), $\tau$ is the characteristic relaxation time and $\beta$ is the stretching factor of the exponential function. Fitting was accomplished with Igor Pro v6.36 (WaveMetrics Inc., Lake Oswego, USA). Topography images were first-order flattened to remove sample tilt and to correct for thermal drift whereas amplitude and phase data was retained original. Successive PFM images including vertical/lateral amplitude and phase images were always captured from the top to bottom direction and stacked together to create movies with 5–10 fps. The real-time as well as the current image index are given in the bottom row of each movie (the movies can be seen in the attached CD).

The relaxation dynamics of each pixel within the framed areas in the PFM phase images were also studied to further analyze the relaxation behavior of a tip-induced domain within the pixel range, because the size of each pixel was proximal to the lateral size of the individual PNRs or PNR clusters. An appropriate threshold of 0° phase value was defined to distinguish between pixels corresponding to the poled (< 0°) and the relaxed (> 0°) pixels. When the phase value of a certain pixel exceeded the chosen threshold value (0°), the time stamp of that particular image was read out and assigned to this pixel. The pixel was then defined as relaxed. Thus, the resulting histograms were interpreted as the distribution of the relaxation times of individual pixels in the recorded PFM phase images. The time interval between the poled pixels and the relaxed state of pixels within the framed areas was evaluated with Matlab R2013a (The MathWorks, Inc., Natick, MA).

### 3.2.2 Results and Discussion

**Relaxation Behavior Observed by Conventional Piezoresponse Force Microscopy**

Figure 3.21 shows piezoresponse images 5 × 5 μm$^2$ of the virgin domain state of BNTNa (a−c) and BNTK (d−f), respectively. The averaged root-mean-squared roughness (calculated from three images of each sample) was approximately (1.5 ± 0.5) nm and (1.6 ± 0.3) nm for the BNTNa and BNTK sample, respectively. The relatively low surface roughness for both samples suggests a minor crosstalk between topography and amplitude/phase piezoresponse channels. Figure 3.21(b) and (e) correspond to the amplitude and Fig. 3.21(c) and (f) to the phase responses of the BNTNa and BNTK sample, respectively. The amplitude images of the initial domain state (Fig. 3.21(b) and (e)) depict regions with distinctive amplitude values on the size of a few micrometers for both samples. The phase response images of the initial state (Fig. 3.21(c) and (f)), however, do not show the clear contrast. The absence of the contrast and the associated phase alignment is typical for relaxors and was previously shown in similar lead-free systems.[25] The typical PNRs of these relaxor materials can hardly be resolved by the conductive PFM tip.[133]

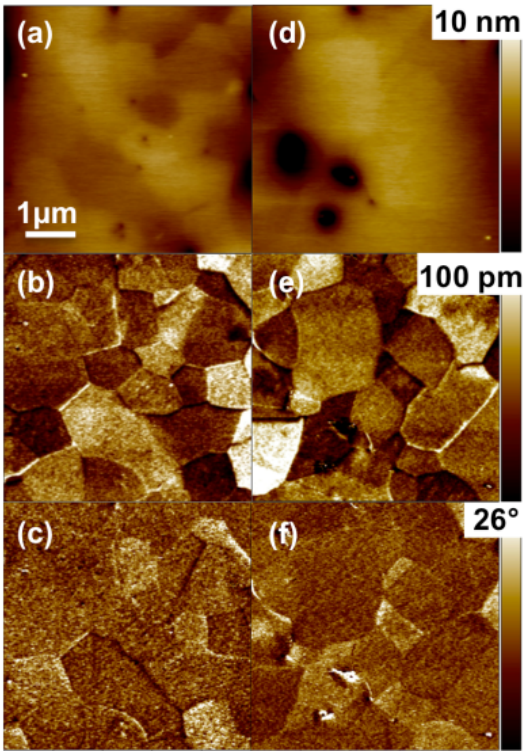


Figure 3.21 Topography ((**a)** and (**d**)), amplitude ((**b**) and (**e**)), and phase images ((**c**) and (**f**)) of the initial domain state of a BNTNa (**a**−**c**) and BNTK sample (**d**−**f**) measured by DART-PFM in vertical vibration of cantilever.

Figure 3.22(a−d) (BNTNa) and Fig. 3.22(e−h) (BNTK) show an image series of the local relaxation process with the amplitude ((a) and (e)) and phase response ((b) and (f)) captured immediately after the poling and the respective amplitude/phase response ("(c) and (g)" and "(d) and (h)") captured 60 min after poling. Immediately after the poling, approximately 80 % of the poled area in the phase response of the BNTNa sample (Fig. 3.22(b)) changed to 180°. In contrast, only 50 % of the framed area (Fig. 3.22(f)) of the BNTK sample could be poled. The majority of the poled areas of both samples relaxed back to the initial domain state as detected 60 min after subsequent PFM imaging (Fig. 3.22(c) and (d), Fig. 3.22(g) and (h)). Compared to the BNTNa sample, a larger region at the upper side of the poling area of the remaining tip-induced domain was observed for the BNTK sample. The results demonstrate that ferroelectric domains could be induced in both samples. However, the tip-induced ferroelectric domains of both samples were unstable with time. A faster relaxation was observed for the BNTNa sample and a larger long-range ordered domain could be initially induced compared to the BNTK sample. These results are attributed to the higher ergodicity of the BNTNa sample. It was already shown that materials with a high degree of ergodicity present incipient features and high-electromechanical response.[5,155,187]

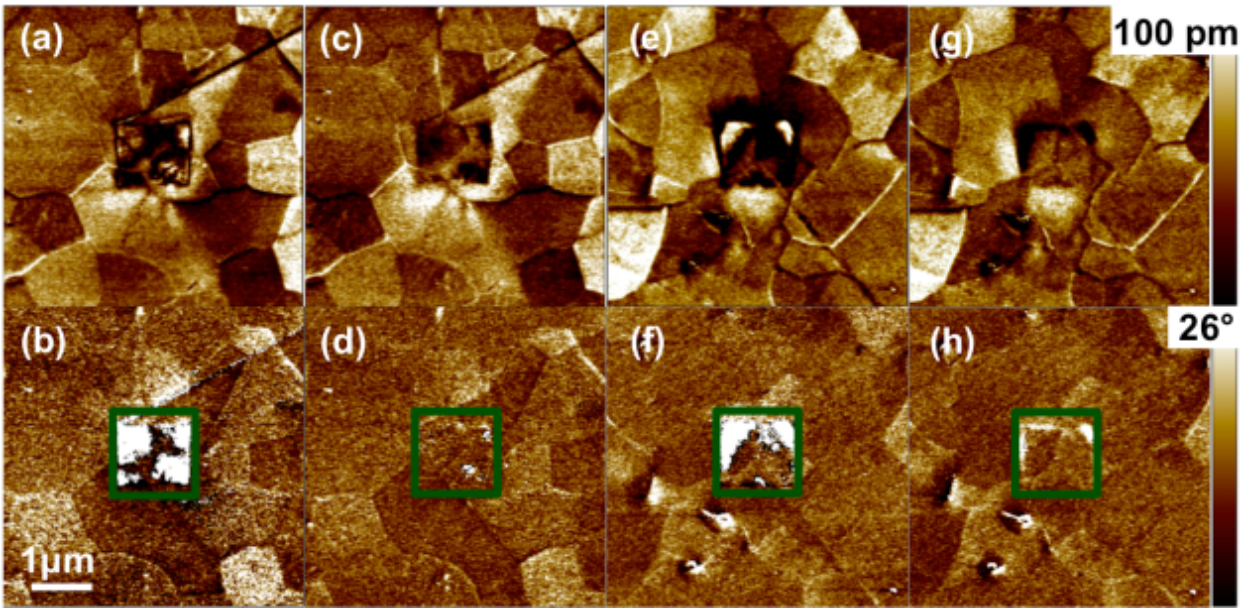


Figure 3.22 Relaxation process of BNTNa sample (**a**–**d**) and BNTK (**e**–**h**) after a local poling experiment. Amplitude (**a** and **e**) and phase (**b** and **f**) response subsequently imaged after poling a 1 × 1 µm$^2$ region in the center (enclosed by the green frame); amplitude (**c** and **g**) and phase (**d** and **h**) response imaged 60 min after poling, respectively. For a better visibility of the piezoresponse, the color bar of the phase images was set to a range smaller than the total recorded phase shift. The values of the white area within the green frames of the phase images (**b**), (**d**), (**f**), and (**h**) correspond to approximately 180°.

Figure 3.23 shows the averaged local hysteresis loops obtained on spots chosen on BNTNa and BNTK samples with bias switched on (a) and off (b). The bias-on hysteresis loops reveal that the maximum local strain value of the BNTNa is higher than that of the BNTK, consistent with macroscopic measurements (Fig. 3.17 insets (B) and (C)). The bias-off results, *i.e.*, the remanent piezoresponse signal, gave the opposite tendency. In both graphs, a larger remanent polarization for the BNTK sample was observed. This phenomenon is also consistent with the macroscopic large signal measurements, indicating that because of the lower ergodicity of BNTK sample, the remanent polarization and strain are macroscopically and microscopically retained in this material. The reason for the discrepancy between bias-off and bias-on hysteresis loops can be explained by the increased tendency to back-switch domains in case of the BNTNa compared with the BNTK, as observed in the poling experiment in Fig. 3.22. This finding, together with the larger remanent polarization, corroborates the higher ergodicity of the BNTNa sample. By analyzing $T_f$ of both materials, it was also revealed a higher ergodicity in BNTNa sample at room temperature as well. These results are in good agreement with the nanoscopic observations. The relaxation behavior of both samples demonstrates that a high electric field can induce macroscopic ferroelectric domains in both relaxor surfaces.

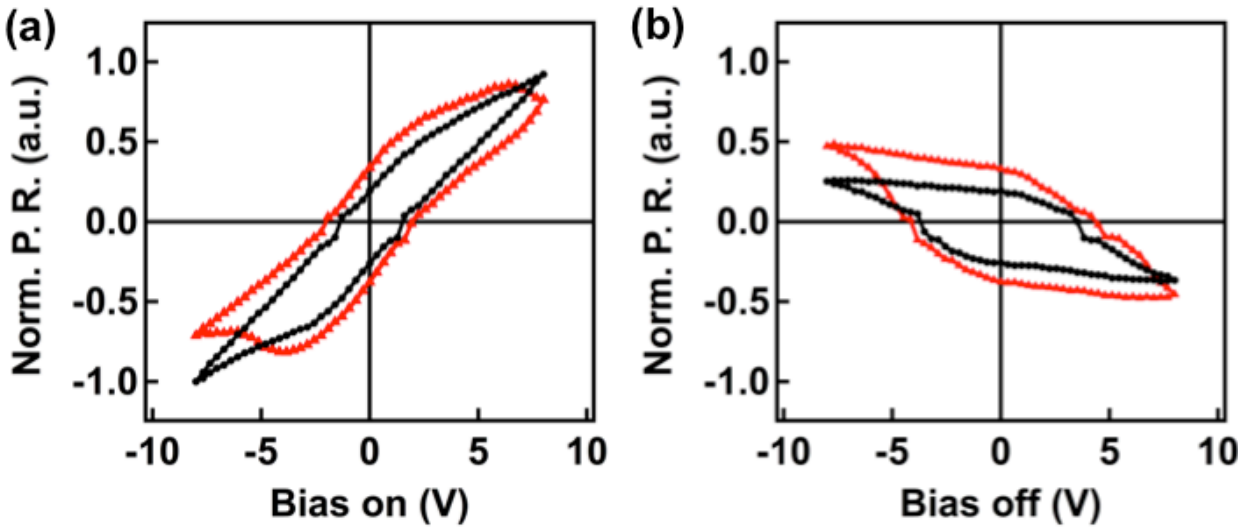


Figure 3.23 Local hysteresis loops acquired on single spots with (**a**) bias-on and (**b**) bias-off for BNTNa (black) and BNTK samples (red). Each loop is an average of 7 single loops taken at the same spot on the sample surface. The normalized piezoresponse (Norm. P.R., proportional was calculated by Equation (2.18) and normalized by the maximum piezoresponse obtained on BNTNa sample (bias-on). Scales in (**a**) and (**b**) are comparable to each other.

The relaxor-to-ferroelectric process is often interpreted by the coalescence of PNRs into the micrometer-size ferroelectric domain through the interactions among PNRs under the sufficiently high external electric field.[23,132] Because both relaxors are macroscopically characterized by the ergodic state, the induced domain is not thermodynamically stable and relaxes back to the ergodic state over time after poling. The decay fashion significantly depends on the local composition distribution, the dynamics of PNRs and their interactions, which cannot be studied by the conventional PFM. The acquisition time of each frame of PFM images was approximately 8 min. Then, considering the additional time consumed on switching the modes, the tip-induced domain can be revealed by PFM only several minutes after poling (so-called dead time). Because PNRs are highly dynamic in the ergodic relaxor state, the poled domain might have partially relaxed to the ergodic state within this dead time, *e.g.* the unpoled area in Fig. 3.22(b) and (f). Therefore, this scanning velocity was insufficient to reveal the nanoscopic relaxation dynamics associated with the local distribution of the ergodicity in both lead-free relaxor piezoceramics. Essentially, the high-speed PFM mode is needed for obtaining high-temporal image series, which allows for an in-depth study of the nanoscopic relaxation dynamics of these relaxors at room temperature.

**Relaxation Behavior Observed by High-speed Piezoresponse Force Microscopy**

***Fast Relaxation Behavior of BNTNa***

The piezoresponse images were repeatedly taken by using high-speed PFM and a movie was created (movie 1 in the attached CD). Figure 3.24 shows the topography (a) and a selection of six representative phase images measured at $t$ = 106 s (b), 130 s (c), 189 s (d), 388 s (f), 685 s (g), and 52 min (h) after the poling, as well as the averaged cross-sectional profiles (500 nm in width) drawn along the domain walls at the indicated positions

(yellow arrows) in Fig. 3.24(b) and (c). Figure 3.25(a–h) and 3.26(a–h) show the magnified phase and amplitude images, in which the detailed nanoscopic relaxation dynamics is presented. A long-range ordered ferroelectric domain is clearly evident immediately after poling (Fig. 3.24(b), enclosed by the white dashed line), which indicates that the applied +10 V to the PFM tip was strong enough to align the PNRs along the external field direction within the poled area. The appearance of domains outside the poled region is attributed to residual charges at the tip after poling, when the tip moved to the bottom side after poling and before capturing the high-speed images for the observation of the relaxation process (poling stripes). The region enclosed by the white dashed line is considered for further analysis of the relaxation process and to calculate the relaxation time. The size of this region (1.23 µm$^2$) is larger than the area that was intended to be poled (1 µm$^2$). This is due to the geometry and dimensions of the cantilever-tip itself, the inhomogeneous distribution of the electric field established during poling, which is not explicitly restricted to the apex. Thus, the electric field at the edge area of the cone can also cause poling. There is a dead time of approximately $t_d$ = 93 s because of switching between the poling and the high-speed PFM observation.

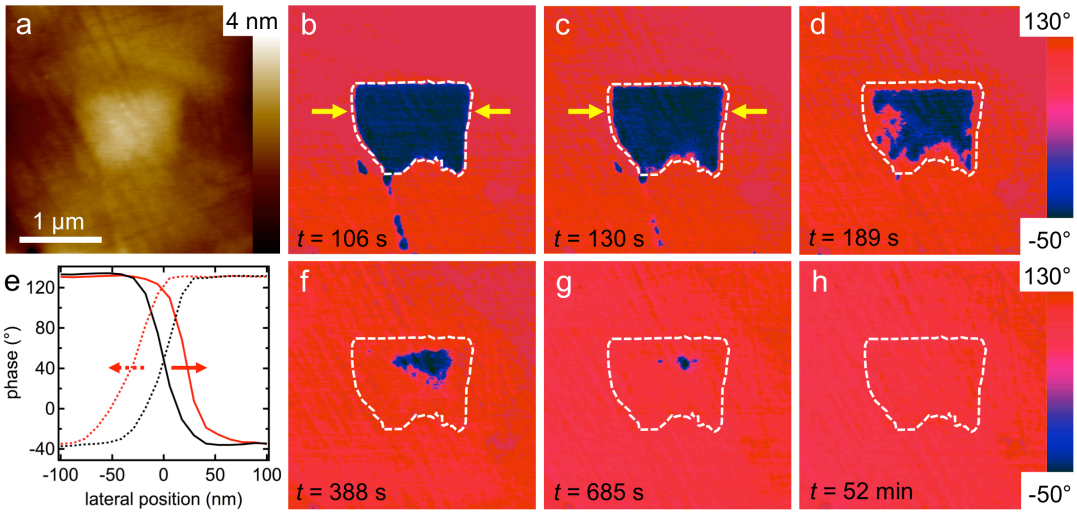


Figure 3.24 Relaxation process of a tip-induced domain on the surface of the BNTNa sample visualized by high-speed PFM. Topographical image of the region of interest (**a**), the vertical piezoresponse phase images taken at $t$ = 106 s (**b**), 130 s (**c**), 189 s (**d**), 388 s (**f**), 685 s (**g**) and 52 min (**h**) after the poling. The region enclosed by the white dashed frame was chosen as initial area for the further analysis of the relaxation. (**e**) Averaged cross-sectional profiles drawn along line between the two yellow arrows at the left (solid lines) and right domain walls (dashed lines) for $t$ = 106 s (black) and $t$ = 130 s (red). Offsets in the lateral position were applied to both transition regions for a better visibility of the domain wall movement.

At beginning of the relaxation process ($t$ = 106 s and $t$ = 130 s), a slowly continuous domain wall motion (boundary between the induced domain and the unpoled area) laterally shrinks the size of the poled area towards the center region. Comparing the lateral position of the domain wall for $t$ = 130 s (Fig. 3.24(e), red lines) with that for $t$ = 106 s (black lines) in the cross-sectional profiles, a migration of the domain walls towards the center of the poled area can be illustrated on both sides (solid lines correspond to the left domain wall, dashed lines to the right). Note that the curves were laterally shifted to compare the domain wall motion during relaxation. At

$t$ = 106 s in Fig. 3.24(b), a curved wall at the bottom of the poled area was observed, where the subsequent relaxation rapidly proceeded towards the center region (see Fig. 3.24(c)). The formation of this curved wall at lower part of the poled area is because the relaxation has already occurred during the dead time. The different wall velocities can be attributed to the different curvature of the phase boundaries, *i.e.*, domain walls. The velocity of the curved domain walls is enhanced over the straight ones because of a higher interfacial energy per unit area of the curved wall. Ganpule *et al.*[221,222] observed a similar phenomenon on PZT thin films. However, from $t$ = 130 s in Fig. 3.24(c) to $t$ = 189 s in Fig. 3.24(d), the poled area at the bottom curved wall did not relax faster than that at the left straight wall. Instead, a rapid relaxation was observed on the left side along with an emergence of a curved and 'rough' wall, whereas the curvatures of the other three walls did not change considerably. We attribute this to different types of dominant PNRs (*i.e.* dynamic or quasi-static PNRs) originated from the chemical inhomogeneity of the specimen. The high chemical disorder within the left area leads to a high amount of dynamic PNRs per unit area (density of dynamic PNRs) comprising a high degree of ergodicity in the virgin state. In contrast, at the bottom region of the poled area the chemical disorder is relatively low, leading to a high amount of quasi-static PNRs and hence a low degree of ergodicity in the virgin state. Consequently, an enhanced dissociation rate of the induced domain to dynamic PNRs is observed on the left side due to the high thermal fluctuation of the dynamic PNRs. It was anticipated that the relaxation process would have started from the top because of the top-to-bottom scanning direction for both, the poling and imaging procedures (scan rates of the poling and imaging were 0.8 Hz and 19.5 Hz, respectively), contrary to our observations. This result implies that the relaxation dynamics strongly depends on the inherent structure of the chosen area. From $t$ = 189 s (Fig. 3.24(d)) to $t$ = 388 s (Fig. 3.24(f)), the induced domain at the curved walls (left, bottom and right walls) relaxed fast. At $t$ = 388 s (Fig. 3.24(f)), a remaining poled area on the top right part of the initially poled area was observed, whose stability can be attributed to the existence of a high density of the quasi-static PNRs. The field-induced domain at the area characterized by a high density of quasi-static PNRs can be more stable. From $t$ = 52 min (Fig. 3.24(h)) on, no phase contrast was observed anymore, indicating that the induced ferroelectric domain has dissociated into dynamic and quasi-static PNRs with small size. These PNRs are unresolvable by PFM because of its limited resolution (approximately 10−30 nm). The reversible transformation from the relaxor to the ferroelectric state confirms an average ergodic behavior of the selected area. The different relaxation times within the poled area verify an existence of regions with different degree of ergodicity originated by the density distribution of dynamic and quasi-static PNRs. The coexistence of the quasi-static and dynamic mesoscopic disorder in the lead-containing ergodic relaxor has been previously reported.[133,134]

Figure 3.25 shows the phase image sequence that further illustrates the nanoscopic relaxation dynamics. Because the bottom curved wall D formed during the dead time, we focus here on the straight walls designated by A, B and C as regions of interest. At the beginning of relaxation process as indicated, no reversed PNRs inside the poled area was observed as apparent in Fig. 3.25(a) and (b), but a wall curving/roughening (see A, B, and C walls in Fig. 3.25(a) and (b)). As an example, regions with different curvatures at the interface between

the remaining poled and relaxed regions can be observed, as indicated by the yellow arrows at wall B in regions 1, 2 and 3 in Fig. 3.25(b). Note that each region corresponds to the poled and unpoled areas as well as the corresponding boundary. In the further relaxation process, the curved wall in region 1 moved towards the center region of the poled area, as can be seen in Fig. 3.25(b−h). In regions 2 and 3, the wall motion proceeded until $t$ = 168 s (Fig. 3.25(d)), and in contrast to region 1 small clusters of relaxed PNRs as indicated by white arrows are observed inside the poled area. Subsequently, a fast spreading process, i.e. a rapid expansion of relaxed PNRs at these nucleation centers eventually merging with the adjacent domain wall motion was revealed as indicated by yellow arrows in regions 2 and 3 of Fig. 3.25(e).

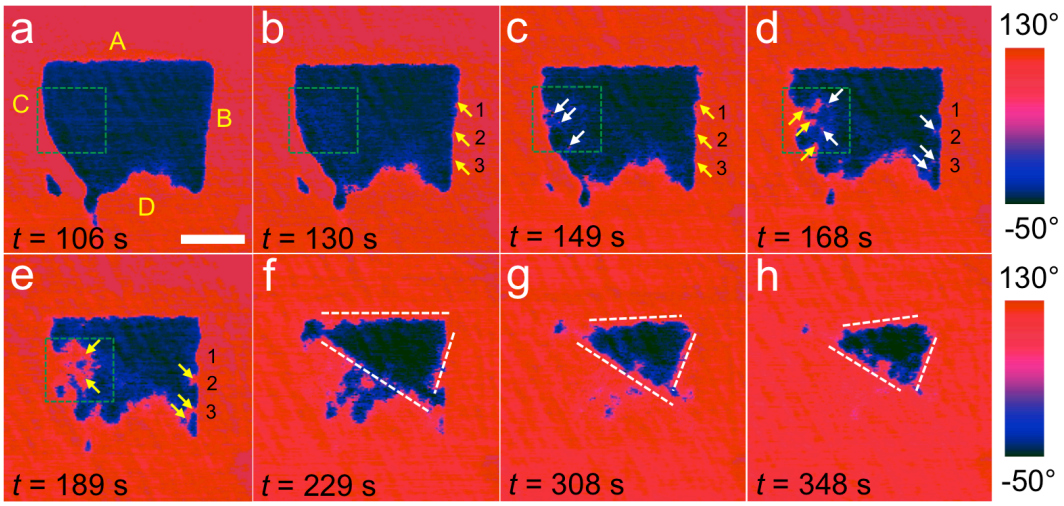


Figure 3.25 Sequence of phase images at different times after poling representing the nanoscopic relaxation process on the surface of the BNTNa sample by high-speed PFM. A, B, C, and D represent the top, right, left, and bottom domain wall in (**a**), respectively. Scale bar 500 nm.

The different relaxation processes observed between region 1 and regions 2/3 can be attributed to the different distribution of dynamic and quasi-static PNRs in the virgin state of the poled area and the unpoled/relaxed area. The wall curving/roughening is triggered by the strong interaction between the domain walls and thermally fluctuating dynamic PNRs from the adjacent unpoled areas. An increased domain wall curvature is caused by a high density of dynamic PNRs proximate to it. This explains the relatively fast motion of the wall in region 1 in the initial relaxation stage compared to regions 2/3 (Fig. 3.25(a−c)). In the next stage, the different types of dominant PNRs (dynamic and quasi-static PNRs) in the virgin states of the poled areas that are close to the curved walls can determine in which way the further relaxation proceeds. A high density of quasi-static PNRs in the vicinity of the proceeding domain wall could slow down the domain wall motion, *e.g.* region 1 in Fig. 3.25(c−f). Contrary, when the curved wall approaches to the area, whose virgin state has a high density of dynamic PNRs, the nucleation sites of the dynamic PNRs occur (indicated by white arrows in regions 2 and 3 of Fig. 3.25(d)). The high curvature of the newly formed wall between the nucleation centers and the surrounding poled areas causes a rapid relaxation around these nucleation sites. Eventually, inner and outer relaxation sites merged and formed a single domain wall. This rapid spreading process after the nucleation of dynamic PNRs

inside the poled area is akin to the reversed-domain growth for back switching observed in conventional ferroelectrics.[222] At the wall C, a similar relaxation process as in region 1 was observed at the upper part in Fig. 3.25(a−h), and a similar one to those observed in regions 2 and 3 was observed in the poled area marked by the green boxes in Fig. 3.25(a−e). As discussed above in Fig. 3.24, a high density of quasi-static PNRs led to a comparably stable triangular-shaped domain (see areas enclosed by triangular lines in Fig. 3.25 (f−h)). In this area, similar relaxation phenomena as described before (*cf.* region 1) were observed in a slower manner owing to the high density of quasi-static PNRs. Gobeljic *et al.*[132] conjectured that in lead-free ergodic relaxor systems, a two-step relaxation process of the tip-induced ferroelectric domain, *i.e.* the collapse of the induced domain to smaller domains, and the subsequent fast decay of these smaller domains into dynamic PNRs. Our observations could enrich this relaxation mechanism.

The amplitude response measured by PFM provides information of the magnitude of strain response to the electrical tip-stimulus. Generally for ferroelectrics, the domain walls do not exhibit a piezoresponse due to the absence of ferroelectric domains within the domain wall. Hence, the black lines observed in the PFM amplitude images can be interpreted as domain walls, where the amplitude response is reduced.[204] In our case, the black lines in the amplitude images correspond to the walls separating the remaining poled from the unpoled/relaxed area, while the dark spots correspond to the unresolvable remaining small polar domains. Figure 3.26(a−h) shows the sequence of amplitude images taken by high-speed PFM at different times.

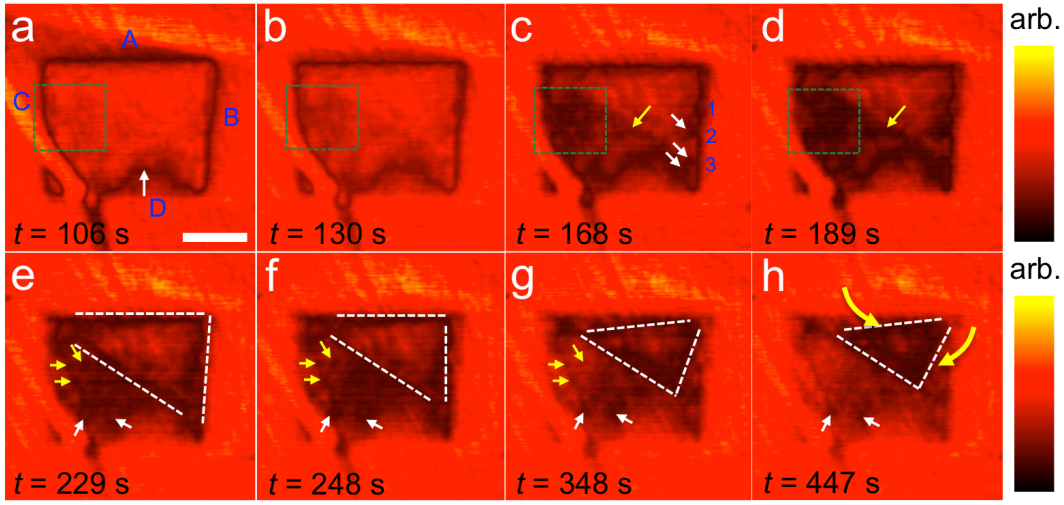


Figure 3.26 Representative amplitude images at different times after poling on the surface of the BNTNa sample captured by high-speed PFM. Scale bar 500 nm.

At $t$ = 106 s (Fig. 3.26(a)), the same amplitude response as in the unpoled area is observed in the poled area, although the corresponding phase exhibits a tip-induced long-range ordered domain (see Fig. 3.25(a)). This can be attributed to the poled volume beneath the surface that has partially relaxed during the dead time leading to a reduced amplitude response of the poled domain, caused by the higher density per unit volume of dynamic PNRs in the volume than at the surface-near region. Below wall D, a dark area can be observed in the amplitude image of Fig. 3.26(a). This indicates that the relaxation has already started during the dead time, whose direction

is indicated by the white arrow in Fig. 3.26(a). We observed that this dark area were only visible in the amplitude images but indiscernible in the phase images (Fig. 3.25(a)), owning to the small size of the remaining poled area and the limited lateral resolution of phase detection by PFM. However, the remaining small domains exhibit an increased density of domain walls per unit area, which can be resolved as reduced amplitude response.

In regions 2 and 3, at the locations of the nucleation of the dynamic PNRs (*cf.* Fig. 3.25), the small curved domain walls are apparent as dark areas highlighted by white arrows in regions 2 and 3 of Fig. 3.26(c). Contrary, no such dark area can be found in region 1, indicating an absence of a nucleation and a subsequent spreading relaxation of dynamic PNRs. At the wall C, within the areas marked by green boxes in Fig. 3.26(a−d), the amplitude response decreases due to an increasing number of the domain walls during relaxation. Starting at $t$ = 229 s, incompletely dissolved domains remain visible as dark spots in the amplitude images as indicated by yellow arrows in Fig. 3.26(e) but indistinguishable in the corresponding phase image. These dark regions gradually vanish (see the yellow arrows in Fig. 3.26(f) and (g)), revealing the completion of the relaxation. The same phenomenon was observed at other areas (white arrows in Fig. 3.26(e−h). For the triangular-shaped area, the hypotenuse appeared at $t$ = 168 s and becomes distinguishable at $t$ = 189 s in the amplitude images, but not identified in the corresponding phase images. In the subsequent relaxation, the hypotenuse keeps comparably straight and moving towards the upper right corner of the poled area. A motion of the upper and right domain wall along the curved yellow arrows (Fig. 3.26(h)) can be identified. We hypothesize that the direction of relaxation of the triangular shaped domain points towards the decrease in the density of the dynamic PNRs. Note that for $t$ > 20 min, no contrast was apparent in the phase images, but the amplitude images still exhibited dark regions revealing the remaining domains at the surface (see movie 2 in the attached CD). Eventually, these dark spots disappeared illustrating the completion of the relaxation. This slowly relaxing residual domains resolved from the amplitude images at the end of the relaxation process might be caused by the local pinning effects originating from the mesoscopic heterogeneities in relaxors.

***Slow Relaxation Behavior of BNTK***

In a further experiment, the relaxation behavior of the BNTK sample, which macroscopically exhibits a lower degree of ergodicity than the BNTNa sample, was studied. Figure 3.27 shows a selection of PFM phase images measured at $t$ = 109 s (a), 150 s (b), 281 s (c), 18 min (d), 31 min (e), 51 min (f), and 19.8 h (g) after poling as well as the PFM amplitude image (h) taken at $t$ = 109 s. The whole relaxation experiment can be seen in movie 2 in the attached CD. The dashed line encloses the area for the analysis of the relaxation time deduced from the bright area in first amplitude image available. It measures 1.59 μm$^2$ and corresponds to 17.7 % of the total observed region of Fig. 3.27. This enclosed area is considered as being poled by the biased tip. The dead time was approximately $t_d$ = 96 s in this experiment. The vertical phase image in Fig. 3.27(a) at $t$ = 109 s reveals a long-range ordered domain indicating that the applied field was high enough to induce the interaction between the isolated PNRs and form a micro domain on the sample of BNTK. At $t$ = 19.8 h in Fig. 3.27(e), the vertical

phase contrast is still present. Compare with the previously discussed fast relaxation on BNTNa, the total relaxation time in BNTK, retained considerably longer (approximately two days). This illustrates that the chosen area in BNTNa is characterized by a higher degree of ergodicity than that in BNTK, which indirectly demonstrates the type of dominant PNRs in BNTNa is the dynamic one and in BNTK the quasi-static one. An interesting phenomenon was observed in BNTK immediately after poling (see Fig. 3.27(a)). The initially poled area is considerably beyond the area enclosed by the dashed line, to which it shrank back within the first 2 min (see Fig. 3.27(b)). We explain this "poling fringe" as follows. The polarization of the tip-induced domain induces a lattice distortion in the neighbor region, which in turn lowers the lattice symmetry and hence switches the neighboring domains. However, the inherent restoring force of the affected lattices is strong enough to provoke a change back to initial state with the lowest energy. We observed this poling fringe outside the projected poled area several times on the BNTK sample and once on the BNTNa sample. This poling circumference was unresolvable in the previously discussed fast relaxation in BNTNa originated from its high density of dynamic PNRs leading to the fast relaxation within the dead time. In contrast to already relaxed amplitude response after poling observed on the BNTNa sample (Fig. 3.26(a)), the corresponding amplitude image in Fig. 3.27(h) exhibits an increased piezoresponse inside the tip-directly poled area. This is due to the high stability of the poled domain aligned from the quasi-static PNRs in the poled volume beneath the surface of BNTK.

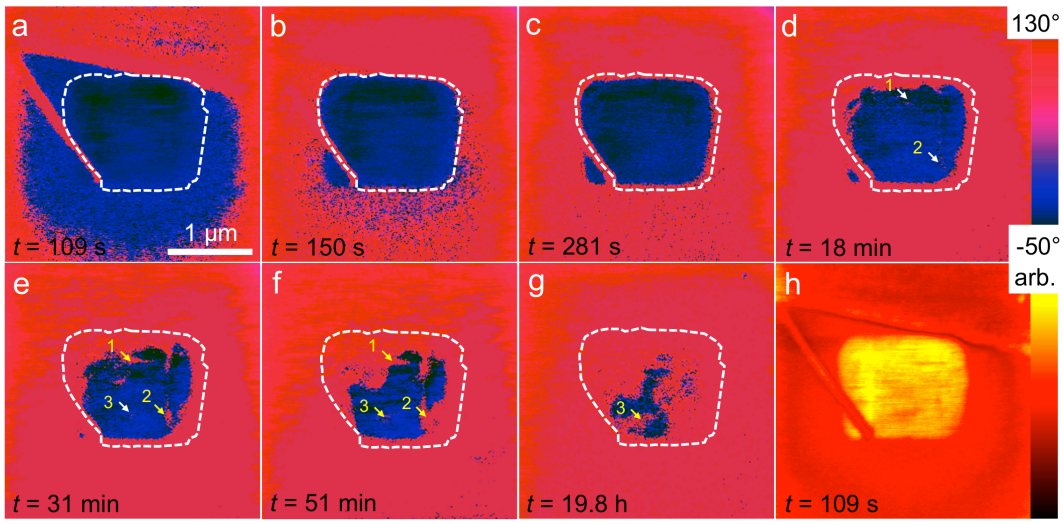


Figure 3.27 Relaxation of a tip-induced domain on the surface of the BNTK sample, which shows macroscopically a lower degree of ergodicity than the BNTNa sample. The image sequence shows selected PFM phase images taken at different times after the poling at $t$ = 109 s (**a**), 150 s (**b**), 281 s (**c**), 18 min (**d**), 31 min (**e**), 51 min (**f**), and 19.8 h (**g**) as well as the amplitude response image (**h**) corresponding to the phase image (**a**).

Although the type of dominant PNRs in the chosen area of the BNTK sample is different from that of the BNTNa sample, similar relaxation mechanisms can be observed. Immediately after poling, the domain wall becomes locally curved at the interface between the poled and unpoled regions (see the walls evolving from Fig. 3.27(b) to (c)). The subsequent relaxation is directed towards the center region of poled domain attributable to

the high density of quasi-static PNRs in that region. Nonetheless, a nucleation (white arrows, Fig. 3.27(b−g)) and a subsequent spreading relaxation (yellow arrows) of dynamic PNRs could be detected. The difference is each step is significantly slower in this area on the BNTK than that on the BNTNa. Overall, a relatively fast collapse of the poled area preferentially starts at the top left region of the tip-poled area can be observed in this chosen area on BNTK. The similar relaxation mechanisms were observed on both samples (BNTK and BNTNa). However, due to the enrichment of quasi-static PNRs in the measured area of BNTK, on average, a considerably slower relaxation in this area was observed compared to the previous experiment.

***Fast Relaxation Behavior of BNTK* and *Slow Relaxation Behavior of BNTNa***

The high (low) degree of ergodicity determined on the macroscale does not necessarily imply a fast (slow) relaxation behavior on the nanoscale. This hypothesis was proven in the next experiment. We repeated the measurements of the previous section at a different location on the BNTK sample. Figure 3.28 shows a selection of vertical phase and amplitude images captured by high-speed PFM after poling at $t$ = 120 s (a) and (d), 141 s (b), 161 s (c) and (e), and 218 s (f). The whole relaxation process can be followed in the movie 3 in the attached CD. The dashed frames indicate the region taken into account for the analysis of the relaxation of the residual poled area after the dead time $t_d$ = 107 s measuring only 5.6 % of the total observed area. The relaxation of the poled area in this particular region of the BNTK sample proceeded even faster than the collapse of the induced domain on the BNTNa sample: $t$ = 218 s after poling, the initially poled region completely relaxed, as observed in the PFM phase images. It indicates that this area on BNTK exhibits a higher degree of ergodicity than the fast relaxing area on BNTNa, implying the presence of an even higher density of dynamic PNRs presented in the local region of BNTK. However, it is expected that the total amount of dynamic PNRs in the whole BNTK sample is low compared to the concentration of quasi-static PNRs and thus the sample macroscopically has a lower degree of ergodicity than that of the BNTNa sample. The amplitude response on the poled area persisted longer and similar relaxation mechanisms could be identified as in previously discussed sessions with respect to nucleation and spreading of dynamic PNRs as indicated by arrows in Fig. 3.28(a) and (b), respectively. We attribute this effect to the local distribution of the chemical disorder caused by the La doping. It is reasonable to assume that regions with a high (low) chemical disorder lead to a high (low) concentration of dynamic PNRs.

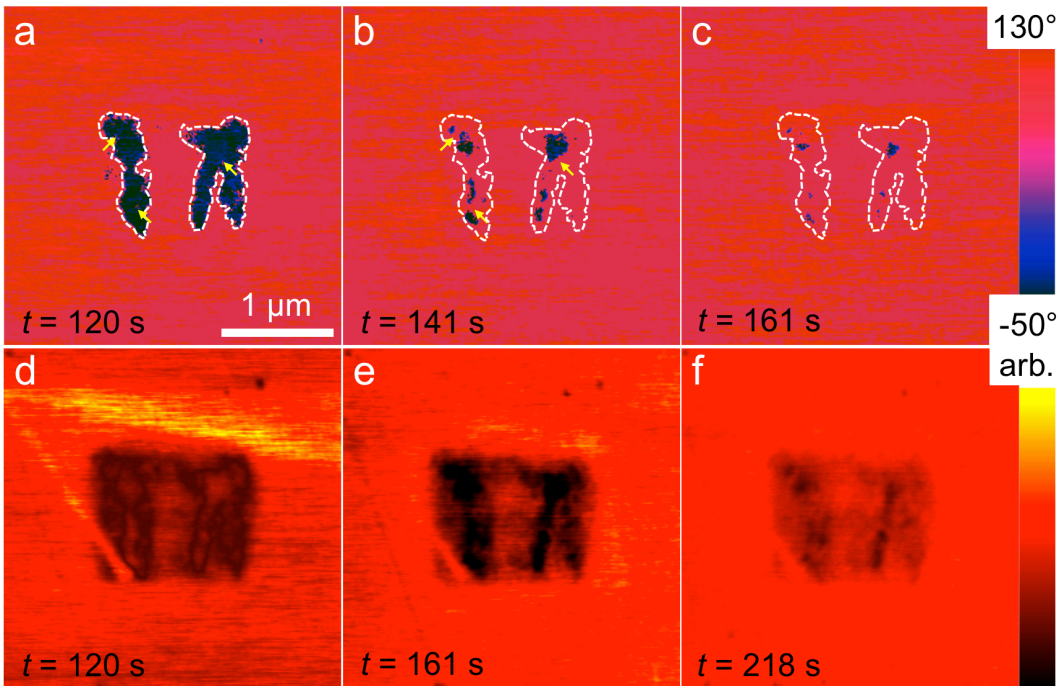


Figure 3.28 Selection of PFM vertical phase (**a**–**c**) and amplitude (**d**–**f**) images captured at $t$ = 120 s (**a**) and (**d**), 141 s (**b**), and 161 s (**c**) and (**e**), and 218 s (**f**) after poling a region of 1 × 1 µm$^2$ in size on BNTK.

Coherently, we observed a slow relaxation behavior on the BNTNa sample, which is characterized by a high degree of ergodicity on the macroscale at room temperature (see Fig. 3.29 and movie 4 in the attached CD). The dead time was approximately $t_d$ = 92 s. Probably due to the increased concentration of quasi-static PNRs in that area, we also observed a poling fringe outside the projected poling area (Fig. 3.29(a)). Correspondingly, the increased amplitude response inside the tip-poled area was also visible after poling (see the vertical amplitude channel in movie 4 in the attached CD). It can be summarized from all four relaxation behaviors that this increased amplitude response inside the poled area could be only observed on the slow relaxing areas due to their high density of quasi-static PNRs. Kan *et al.*[210] reported a two-step relaxation mechanism of the tip-induced domain in a thinned lithium niobate (LNO) crystal involving a slowly lateral shrinkage of domain wall followed by a fast decay after the induced domain beneath the surface has been pinched off. In our case, the fast "pinching-off" of poled domains beneath the surface was observed in fast relaxing areas, which was followed by the lateral shrinkage. The opposite order might be related to a strong screening effect on the relaxor surface and high density of dynamic PNRs beneath the surface. This pinching-off effect proceeded slowly in slow relaxing areas resulting from their high density of quasi-static PNRs.

In this experiment, a small residual portion of the poled area was observable even 22.5 h after performing the poling procedure (Fig. 3.29(c)) corroborating that the ergodicity evaluated on the nanoscale has to be considered as a local phenomenon.

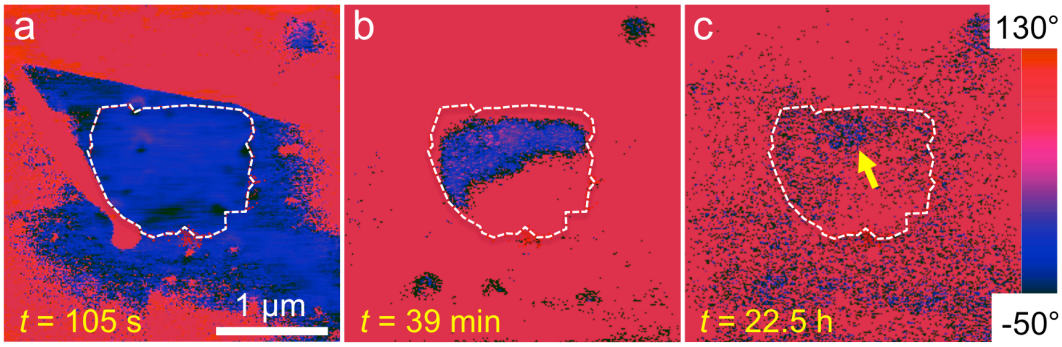


Figure 3.29 Piezoresponse phase images during the slow relaxation of a poled area on a BNTNa sample at $t$ = 105 s (**a**), 39 min (**b**), and 22.5 h (**c**). The arrow in (**c**) indicates the residual polarized area.

***Distribution of Relaxation Times on the Nanoscale***

Within each area, the times needed for the completion of the reversible transition from the relaxor state to the ferroelectric state were different. In order to reveal the distribution of relaxation times, the areas enclosed with the white dashed frames in Fig. 3.24, 3.27, 3.28 and 3.39 were analyzed. The images represent the fast relaxation (fr) and slow relaxation (sr) processes measured on BNTNa, as well as the slow and the fast relaxation processes measured on BNTK, respectively. For the choice of the area, artifacts of aligned and depolarized poling stripes were ignored. To assess the residual poled area, cumulative histograms were created. An example for the BNTNa sample is given in Fig. 3.30(a), where the probability density is plotted for each measured phase value apparent in the PFM phase images at different time steps after poling. In theory, only the phase shift values between the electrical stimulus and the sample response $\varphi$ = 0° (out-of-plane direction with polarization vector pointing downward) or $\varphi$ = 180° (out-of-plane direction with polarization vector pointing upward) can occur for vertical PFM using excitation frequencies substantially below the contact resonance. To enhance the response signal, however, contact resonance PFM was applied. Consequently, the closer the excitation frequency to the contact resonance frequency, the smaller is the difference between the phase shift values of opposed domains. A threshold phase value had to be defined in order to classify whether the phase value of a certain position/area counts as poled or unpoled. Because of the change of tip-sample contact mechanics leading to a change of the contact resonance frequency during scanning, a certain range of phase values corresponds to the poled or unpoled state. The first phase image captured after poling was considered as fully poled and a reasonable threshold phase value of 0° (red vertical line, Fig. 3.32(a)) was defined accordingly: all values below (above) 0° corresponded to the poled (relaxed) area. The probability density of the poled area at 0° as a function of time in a logarithmic plot describes the time-dependent relaxation behavior of the poled area, and is hereafter referred to as a "relaxation curve". Figure 3.30(b) shows a fast (red open circles) and a slow relaxation curve (green closed circles) measured on the BNTNa sample, as well as a fast (black open diamonds) and a slow relaxation curve (blue closed diamonds) measured on the BNTK sample.

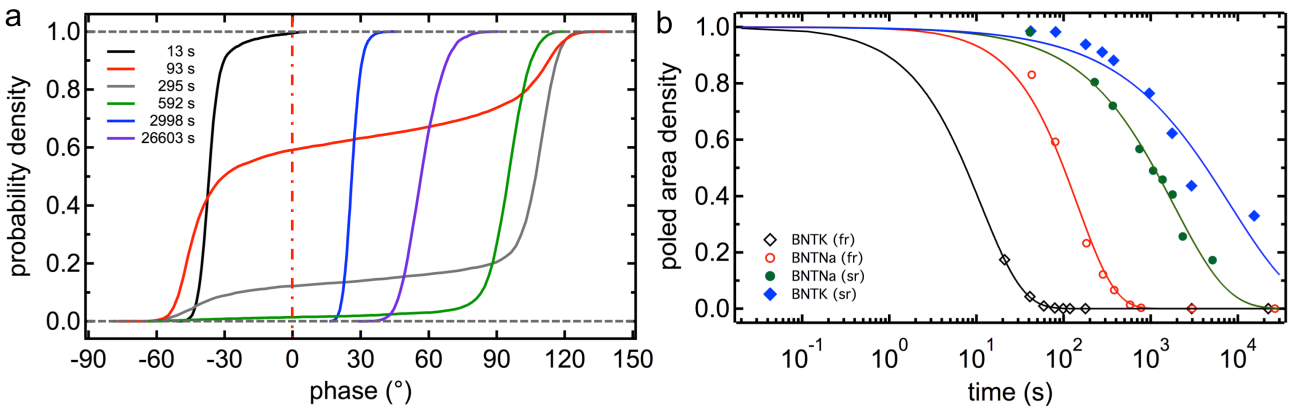


Figure 3.30 Distribution of the relaxation times for the BNTNa and BNTK samples. (**a**) Cumulative distribution of the probability density of each phase value apparent inside the framed area of the PFM phase images captured at different times (*cf.* inserted legends) on the fast relaxation area of BNTNa sample after poling. The 0°-threshold chosen to distinguish between the poled phase values (< 0°) and the relaxed phase values (> 0°) is drawn with a red chain line. The values read out at the phase value of 0° correspond to the probability density of poled domains at given times. (**b**) Relaxation curves of the vertically poled area for the BNTNa and BNTK samples. The experimental data at given times were the values of portability density at the phase values of 0° exampled as in (**a**). Circles and diamonds are the experimental data of BNTNa and BNTK, respectively; solid lines are the fitted curves using the KWW law. Note that the open symbols represent the data of the observed fast relaxation processes whereas the data for the slow relaxation processes is shown by closed symbols.

For each fitting of the relaxation curve, 10 data points were calculated. Note that the first data point is not visible because of its (0,1)-coordinate in combination with the logarithmic plot. The solid lines are the fitted curves applying Equation (3.6), with the fit parameters given in Table 3.1. The excellent agreement of the fit with the data points obvious in Fig. 3.30(b) and underpinned by the low standard deviation gives rise to the conclusion that each relaxation process follows the three proposed mechanisms. Nevertheless, for the slowly relaxing measurements (green and blue data points) the end of the relaxation process was not observed. However, a almost complete depolarization of the induced long-rang ordered domain was expected because of the ergodic behavior of the samples.

Table 3.1 Fitting parameters for the curves (solid lines) plotted in Fig. 3.32(**b**).

| | $\tau$ [s] | $\langle\tau\rangle$ [s] | $\beta$ | $\langle\beta\rangle$ |
|---|---|---|---|---|
| BNTK (fr) | 11.3 | 0.1 | 0.90 | 0.01 |
| BNTNa (fr) | 144.5 | 8.5 | 1.00 | 0.08 |
| BNTNa (sr) | 1840.8 | 108.0 | 0.70 | 0.05 |
| BNTK (sr) | 8183.3 | 2000.0 | 0.58 | 0.08 |

It is worth mentioning that the distribution of relaxation times was analyzed by means of the phase images. The residual smaller domains, uncovered by the amplitude response, were not considered for the calculation. Because of their small number and extension, they can be neglected. The values of the relaxation times given in Table 3.1 represent the time corresponding to approximately 80 % of the full relaxation. The relaxation curves were in good agreement with a stretched exponential function confirming the broad distribution of the relaxation times. The width of this distribution correlates with the exponent value $\beta$. When $\beta$ is close to 1, a single or narrow relaxation time can be reflected. However, when $\beta$ is proximate to 0, an extremely broad distribution of relaxation times is expected. In case of the fast relaxation in BNTNa and BNTK, the high value of $\beta$ indicates that the high density of dynamic PNRs narrows the distribution of the relaxation time. The small value of $\beta$ in case of the slow relaxation in both samples manifests that the presence of quasi-static PNRs in that area, considerably broadens the distribution of relaxation times. The variety of distribution of the relaxation times can be attributed to a difference of the degree of random fields derived from the local chemical inhomogeneity.[223]

Another approach to study the relaxation behavior of a tip-induced domain is to analyze the dynamics of each pixel in the PFM phase images. Each pixel occupies an area in the lateral size of approximately 12 × 12 $nm^2$ which corresponds approximately to the size of individual PNRs or PNRs clusters. To this end, we calculated the time interval between the poled and the relaxed state of each pixel within the framed areas (see Fig. 3.24, 3.27, 3.28, and 3.29) by defining a threshold phase value (0° in this study) above that a pixel counts as relaxed. As shown in Fig. 3.31, the corresponding histograms then present the number of relaxed pixels per time interval. The histograms in Fig. 3.31(a) and (c) exhibit a fast decrease for the fast relaxing areas, whereas in Fig. 3.31(b) and (d), a nearly constant number of pixels relaxes during the complete relaxation process of the slow relaxing areas. Regardless of the sample under observation, the distribution of the amount of individual pixels (PNRs) for the fast relaxing areas exhibits an exponential decay with time (insets of Fig. 3.31(a) and (c)), whereas the histograms for the slow relaxing areas show a nearly constant distribution (insets of Fig. 3.33(b) and (d)). In the virgin state of an area predominantly consisting of dynamic PNRs, weak interactions among the individual PNRs result in an unstable poled domain state. Thus, during relaxation, many nucleation centers of dynamic PNRs with different dimensions arise within the poled area and concurrently stimulate the fast spreading relaxation, which leads to an exponential decay of the relaxing pixels over time. Contrary, in an area dominated by quasi-static PNRs, the poled domain state is relatively stable resulting from the strong interactions among these PNRs. The dynamic PNRs can be taken as being pinned inside the poled area and will be activated when the domain wall approaches their vicinity during relaxation. Hence, cooperative effects as observed in conventional ferroelectrics (sideway motion of the wall) are dominant here leading to a constant distribution of the number of relaxing pixels per time interval. The existence of dynamic PNRs contributes to the disturbance of this constant distribution. Both cases corroborate the assumption of the coexistence of quasi-static and dynamic PNRs in BNTK and BNTNa on the nanoscale, which unravels the mechanism as regards to the coexistence of non-ergodic and ergodic relaxor states on the nanoscale.[57] In this study, we found no indication of a non-ergodic behavior on the nanoscale including purely static PNRs whose poled state does not relax with time. However, we observed the regions in which quasi-static and dynamic PNRs coexist and where the local

concentration and distribution of these PNR types within a given area determine its overall relaxation characteristics.

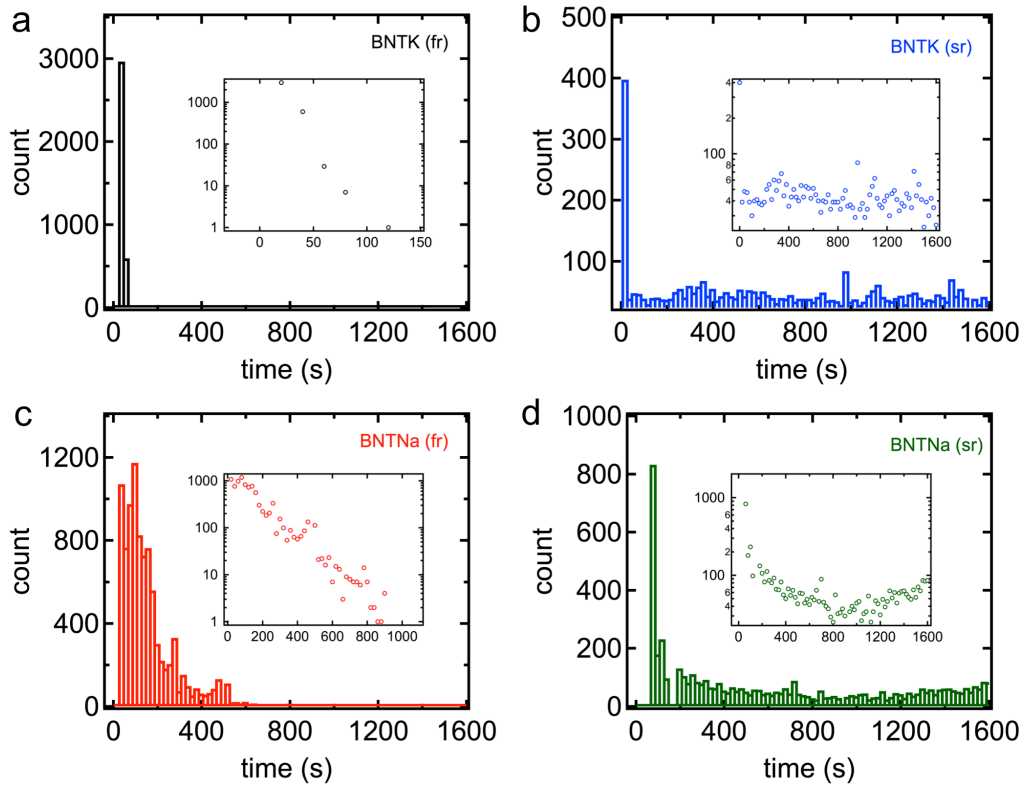


Figure 3.31 Histograms of the distribution of relaxation times of individual pixels. (**a**) Fast and (**b**) slow relaxation measured on the BNTK sample and (**c**) fast and (**d**) slow relaxation detected on the BNTNa sample. Insets show the respective logarithmic plots of the histograms. Note: to minimize false data in the histograms, images with a substantial number of artifacts observable as "jumping" phase values were discarded, causing time gaps for instance in (**d**).

### 3.2.3 Statement of Personal Contribution

[2] Matias Acosta, Na Liu, Marco Deluca, Sabrina Heidt, Ines Ringl, Christian Dietz, Robert W. Stark and Wook Jo, "Tailoring ergodicity through selective A-site doping in the $Bi_{1/2}Na_{1/2}TiO_3$-$Bi_{1/2}K_{1/2}TiO_3$ system", *Journal of Applied Physics*, **117**, 134106 (2015).

All experimental work with respect to the PFM characterizations was carried out by myself. The data processing regarding to PFM results was done by myself with the supervision of Dr. Christian Dietz. The manuscript related to PFM part was written by myself and revised by Dr. Christian Dietz and approved by Prof. Dr. Robert W. Stark.

## 3.3 Revealing the Core-shell Interactions in a Relaxor Piezoceramic $0.75Bi_{1/2}Na_{1/2}TiO_3$-$0.25SrTiO_3$ via Piezoresponse Force Microscopy

The content of this Chapter is published in:

[3] Na Liu, Matias Acosta, Shuai Wang, Bai-Xiang Xu, Robert W. Stark and Christian Dietz, "Revealing the core-shell interactions of a giant strain relaxor ferroelectric $0.75Bi_{1/2}Na_{1/2}TiO_3$-$0.25SrTiO_3$", *Scientific Reports*, **6**, 36910 (2016).

In this Chapter, the virgin domain structure, as well as the switching and subsequent evolution of field-induced ferroelectric domains in a typical core-shell piezoelectric ceramic $0.75Bi_{1/2}Na_{1/2}TiO_3$-$0.25SrTiO_3$ (BNT-25ST), is investigated by means of PFM. The different relaxor states between core and shell are confirmed, and a distinct in-plane domain evolution at the core-shell interface is observed. A responsive phase-electric field relaxor model is established to reflect the experimental observation of the formation of lateral domains and their evolution at the core-shell interface. In combination with phase field simulations, the observed relaxation phenomenon can be well explained. In the end, the effect of the core-shell microstructure on the high strain mechanism in BNT-25ST is envisaged.

### 3.3.1 Experimental and Method

**Sample Preparation**

BNT-25ST was synthesized via a mixed oxide route employing $Bi_2O_3$ (99.975 %), $Na_2CO_3$ (99.5 %), $TiO_2$ (99.9 %), and $SrCO_3$ (99 %) (Alfa Aesar GmbH, Karlsruhe, Germany) as reagent-grade oxides and carbonates. The powders were mixed according to the $0.75Bi_{1/2}Na_{1/2}TiO_3$-$0.25SrTiO_3$ stoichiometric formula. The freezing temperature of BNT-25ST piezoelectric ceramic is approximately 20 °C and the $d_{33}^*$ value is 650 pm/V obtained from the unipolar strain curve at 4 kV/mm with frequency of 1 Hz.[185] Complete processing details of this material can be found elsewhere.[155] The sample preparation processing for PFM measurements is the same as in Chapter 3.1.1.

**Vertical Poling and Imaging**

The PFM measurements were performed using a Cypher atomic force microscope (AFM) (Asylum Research, Santa Barbara, CA). Ti/Ir- (5/20) and Ti/Pt- (5/20) coated conductive cantilevers ASYELEC-02 and AC240TM (both from Asylum Research, Santa Barbara, CA) were used. The nominal spring constants and fundamental resonance frequencies were $k = 40$ N/m and $f = 300$ kHz for the ASYELEC-02 cantilevers and $k = 2$ N/m and $f = 70$ kHz for AC240TM. For PFM imaging, the driving frequencies were set slightly below the respective contact resonance frequencies. Images were taken with a lateral resolution of 256 × 256 pixels; the

tip was scanned perpendicular to the cantilever's length axis. To perform the vertical domain poling, a +10 V *dc* voltage was applied to the tip while it scanned line-wise an area of 1.5 × 1.5 μm$^2$ with a velocity of 1.1 μm/s. The tip-induced domain patterns were successively characterized, with a scan area of 3.0 × 3.0 μm$^2$, after 15 min, 45 min and 90 min. The detailed vector PFM imaging parameters are listed in Table 3.2. Note that the actual contact resonance frequencies can shift due to changes of the tip-surface contact mechanics; hence, the measuring parameters (amplitude, frequency of the driving signal) needed to be frequently adjusted to keep the driving signals in the vicinity of the contact resonance frequency. Topographic images were processed using first-order line flattening to remove the effect of the surface tilt and thermal drift within the fast and slow scan directions. Cross-sectional profiles were averaged over 5 scan lines.

Table 3.2 Piezoresponse force microscopy imaging experimental parameters.

| Cantilever | ASYELEC-02 | | AC240TM | |
|---|---|---|---|---|
| Direction | Vertical | Lateral | Vertical | Lateral |
| Driving amplitude (V) | 3.0 | 2.5 | 3.5 | 3.5 |
| Driving frequency (kHz) | 926 | 1886 | 268 | 736 |
| Scanning speed (μm/s) | 3.1 | | 2.3 | |

**Phase Field Simulation**

Phase field simulations have emerged as attractive computational tools for predicting the evolution mechanisms of field-induced domains in bulk ferroelectrics.[224-226] Based on the random field theory, a generic phase field model,[227] implemented by a finite element calculation, was recently developed for the simulation of the temporal and spatial evolution of the polarization in relaxors. The finite element phase field simulations for the domain evolution in the non-ergodic core (taken as a classical ferroelectric for simulation) and ergodic shell relaxor state were based on the models presented by Wang *et al.*[227] In the simulations, the spontaneous polarization and the electric potential were treated as degrees of freedom. In an ergodic relaxor, the phase field potential $H$ included three terms: the electrostatic energy $H^{\mathrm{ele}}$, the Landau energy $H^{\mathrm{lan}}$ and the gradient energy $H^{\mathrm{grad}}$. The phase field potential $H$ for the simulation was

$$H = H^{\mathrm{ele}} + H^{\mathrm{lan}} + H^{\mathrm{grad}}. \tag{3.7}$$

In the 2-dimensional case,

$$H^{\mathrm{ele}} = -\frac{1}{2}k_{ij}\left(E_i + E_i^{\mathrm{random}}\right)\left(E_j + E_j^{\mathrm{random}}\right) - P_iE_i - P_iE_i^{\mathrm{random}}, \tag{3.8}$$

$$H^{\mathrm{lan}} = \beta_1(a_1 + a_2(P_1^2 + P_2^2) + a_3(P_1^4 + P_2^4) + a_4P_1^2P_2^2 + a_5(P_1^6 + P_2^6)), \tag{3.9}$$

$$H^{\text{grad}} = \beta_2 P_{i,j} P_{i,j}, \tag{3.10}$$

where $k_{ij}$ is the dielectric tensor and $\beta_1$ and $\beta_2$ are the calibration coefficients, which depend on the domain wall energy and the domain wall width, respectively. In this expression, the Einstein notation was implied, in which the indices $i$ and $j$ ranged between 1 and 2. The Landau term $H^{\text{lan}}$ contains an incomplete Taylor expansion up to the sixth order, and the parameters $a_1$ to $a_5$ are based on those used by Cross *et al.*[89] The random field $E_i^{\text{random}}$ was assumed as Gaussian distribution miming the chemical disorder;[97] its strength was controlled by the variance of this distribution. Here, a moderate value of 8 kV/mm was adopted to insure that the random field was neither too strong to allow local domain switching nor too weak to show relaxor properties:

$$\frac{\delta P_i}{\delta t} = -M\left[\frac{\partial H}{\partial P_i} - \left(\frac{\partial H}{\partial P_{i,j}}\right)_j\right], \tag{3.11}$$

where $M$ is a mobility parameter. For the simulation of the non-ergodic core, a model analogous to that used for the ergodic shell relaxors was used, but the random electric field was excluded. Thus, the potential could be written as follows:

$$H_{\text{non-ergodic}} = -k_{ij}E_iE_j - P_iE_i + H^{\text{lan}} + H^{\text{grad}}. \tag{3.12}$$

These models were implemented in the software FEAP[228] using the finite element method. Based on the measured geometric dimensions of the core-shell microstructure and assuming that the region deeper than 500 nm from the surface was not affected by the biased-tip, a non-ergodic spherical core of radius 250 nm surrounded by an ergodic matrix of size 500 × 1000 nm (depth × width) was simulated. A coherent interface was assumed between the core and the shell. Due to the rotational symmetry, the system could be reduced to a 2-dimensional configuration on the *x*-*z* plane for the simulation. The size of the finite elements should be fine enough to resolve the domain structure and to guarantee the precision of the results. Moreover, symmetric boundary conditions were set on the left and right edges of the box to ensure that the simulation represents a periodic case without the boundary effect. The reference potential at the bottom boundary was set to zero, and the electric field was assumed to undergo a linear potential decrease with distance between the top and bottom boundaries. The simulations revealed not only the polarization state of the sample surface but also the domain configuration beneath the surface. For vertical poling, a +10 V $dc$ voltage difference was applied, similar to the PFM experiment. A triangular potential *vs*. time distribution was employed for simulating the increase and the subsequent decrease of the electric field. The quasi-static simulation was performed with a potential increment of 0.1 V. Before poling, the equilibrium polarization distribution in the non-ergodic core and the ergodic shell was awaited.

### 3.3.2 Results and Discussion

Transmission electron microscopy (TEM), scanning electron microscopy (SEM) and energy dispersive X-ray spectroscopy (EDX) showed that BNT-25ST has a core-shell structure with $Sr^{2+}$-depleted cores.[181,182] To identify surface regions with a distinct piezoresponse in the virgin state, we first investigated an untreated sample of BNT-25ST with vector PFM. Figure 3.32 shows different grains and their respective vector orientations of the polarization in the virgin state of the material. Three different regions of interest (roi) were investigated: roi 1: upper row Fig. 3.32(a−f), roi 2: middle row Fig. 3.32(g−l), and roi 3: bottom row Fig. 3.32(m−r). In PFM, the amplitude and phase signals locally represent the magnitude of the electromechanical response and the domain orientation beneath the tip, respectively. It can be clearly seen from the lateral and vertical amplitude and phase signals (Fig. 3.32(a−d), Fig. 3.32(g−j) and Fig. 3.32(m−p)) that these individual grains exhibit distinctive domain contrasts (blue arrows), whereas there is only a weak contrast in the surrounding areas. The presence of central and outer regions indicates the coexistence of two types of domain states. These states can be ascribed to the core-shell microstructure,[155,182] which is related to the non-ergodic and ergodic relaxor states.[181]

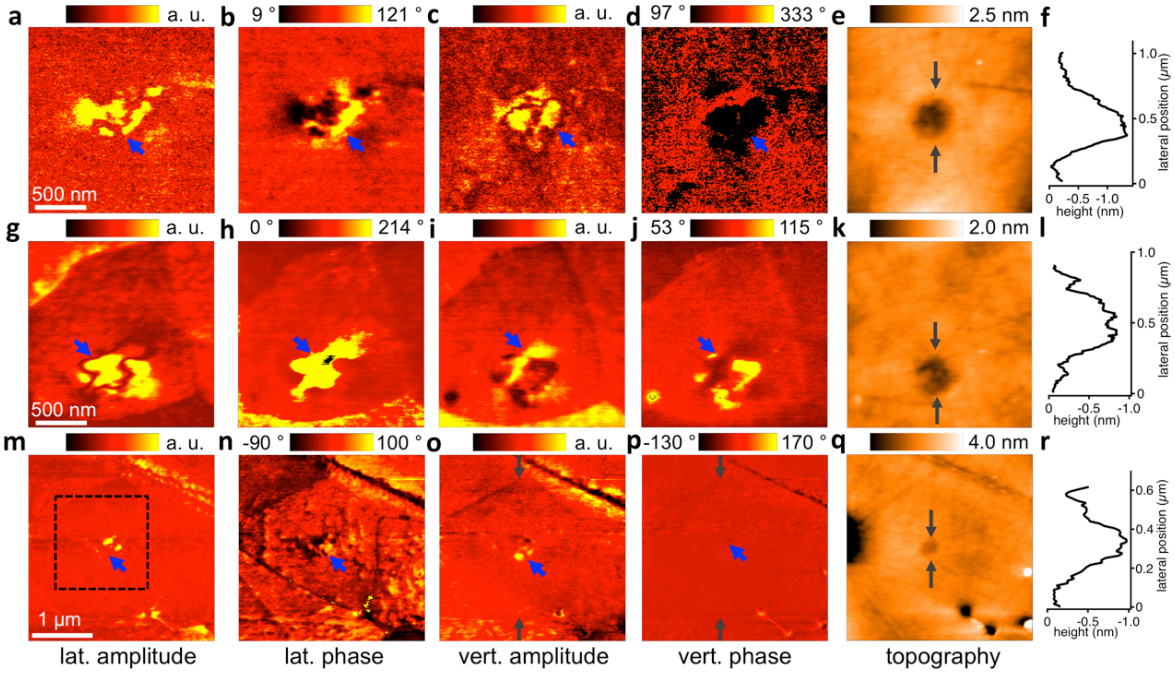


Figure 3.32 Visualization of virgin domain states of core-shell microstructures at three different regions of interest. (**a**–**f**) Region of interest 1. (**g**–**l**) Region of interest 2, and (**m**–**r**) Region of interest 3. Each column shows the same PFM channel for the three regions of interest: (**a**,**g**,**m**) lateral amplitude and (**b**,**h**,**n**) phase, (**c**,**i**,**o**) vertical amplitude and (**d**,**j**,**p**) phase. The respective topography is shown in (**e**,**k**,**q**). The distinct domain structures in the core are revealed (blue arrows). At all three locations, the core is correlated with a depression in the topography, as illustrated in the cross-sectional profiles (**f**,**l**,**r**) drawn along the dark gray arrows. The dashed black frame in (**m**) marks the 1.5 × 1.5 μm$^2$ that was poled (see Fig. 3.34).

The observation of two distinct relaxor states within individual grains is in good agreement with TEM study carried out on the same material.[181] A representative core-shell structure of an individual grain captured by the

vertical PFM phase channel (Fig. 3.32(j)) is magnified in Fig. 3.33, where a typical TEM image of the microstructure of BNT-25ST exhibiting the non-ergodic core (C) and the ergodic shell (S) within an individual grain in the virgin state at room temperature is shown as inset. (Note that TEM and PFM images do not show the same grain). The piezoresponse signal showed a stronger contrast in the lateral channels than in the vertical ones (*cf.* top and bottom row, Fig. 3.32). The domain configurations in the three regions of interest substantially differ. These differences can be attributed to individual grain orientations relative to the global coordinate system in the polycrystalline ceramic.[229] Hence, the ferroelectric domain orientation depends on the grain orientation and on the crystallographically allowed directions, in which the crystal structure of the BNT-25ST is spontaneously polarized. The corresponding topography images of the three different regions of interest are shown in Fig. 3.32(e), (k) and (q). Interestingly, tiny hollows are detected in the core of all three locations. The hollows at roi 1, 2 and 3 are characterized by depths of approximately 1.2 nm, 0.8 nm and 0.9 nm, respectively (see cross-sectional profiles drawn along the direction indicated by the gray arrows). The lateral dimensions of these hollows are 400−700 nm. The occurrence of the tiny hollows in the core is most likely caused by the macroscopic surface polishing or grinding. We speculated that the different chemical compositions of core and shell cause a distinct critical shear strength in both constituents, leading to selectively polishing-induced topographical hollows in the softer material.[181] Thus, the picture of the core embedded in the ergodic shell describes the situation well (Fig. 3.33).

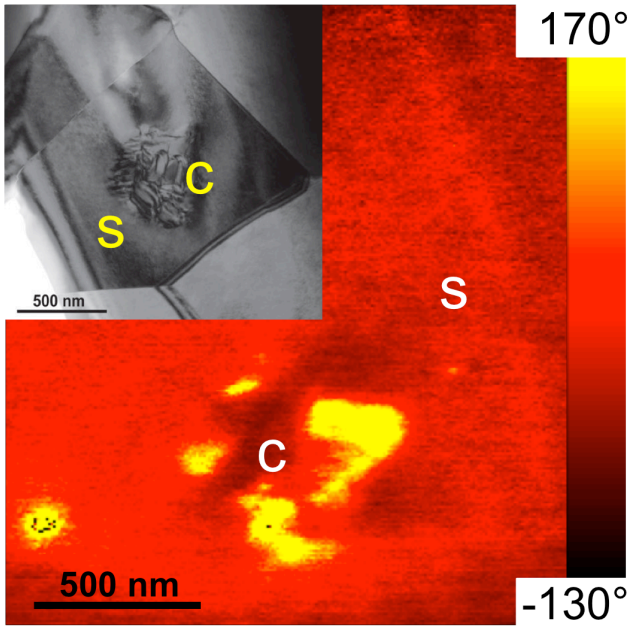


Figure 3.33 Core-shell structure of individual grains. PFM vertical phase image exhibiting distinct contrast in the core region. Inset: Typical TEM micrograph showing the core-shell microstructure (different location). The cores and the shells are marked with the letters C and S, respectively. Note that the contour of the grain is noticeable. TEM image reproduced with permission from Ref. [181], © 2015 Wiley.

In the next step, the response of the material to an external electric field (local poling) and the subsequent relaxation of the tip-induced polarization were investigated. A surface area of 1.5 × 1.5 µm$^2$ was poled within

the region of interest marked by the dashed black frame in Fig. 3.32(m). Then, the same region was analyzed 15 min, 45 min and 90 min later. Figure 3.34 shows the corresponding time series of PFM images. In each row, the PFM data of one time step is summarized. The vertical phase and amplitude signals (Fig. 3.34(a) and (b)) indicate that a long-range ordered and downward-oriented ferroelectric domain (dark area, Fig. 3.34(a)) was successfully induced by the +10 V biased-tip 15 min after poling. However, this domain was slightly larger (approximately 2.0 × 2.0 µm$^2$) than the area that was scanned during the poling procedure (1.5 × 1.5 µm$^2$). This is because the sidewall of the tip cone around the tip apex can additionally contribute to the effective area of the electric field.[195] The tail-shaped trace at the left edge of the poled area was caused by residual charges on the tip as the tip moved away after poling.

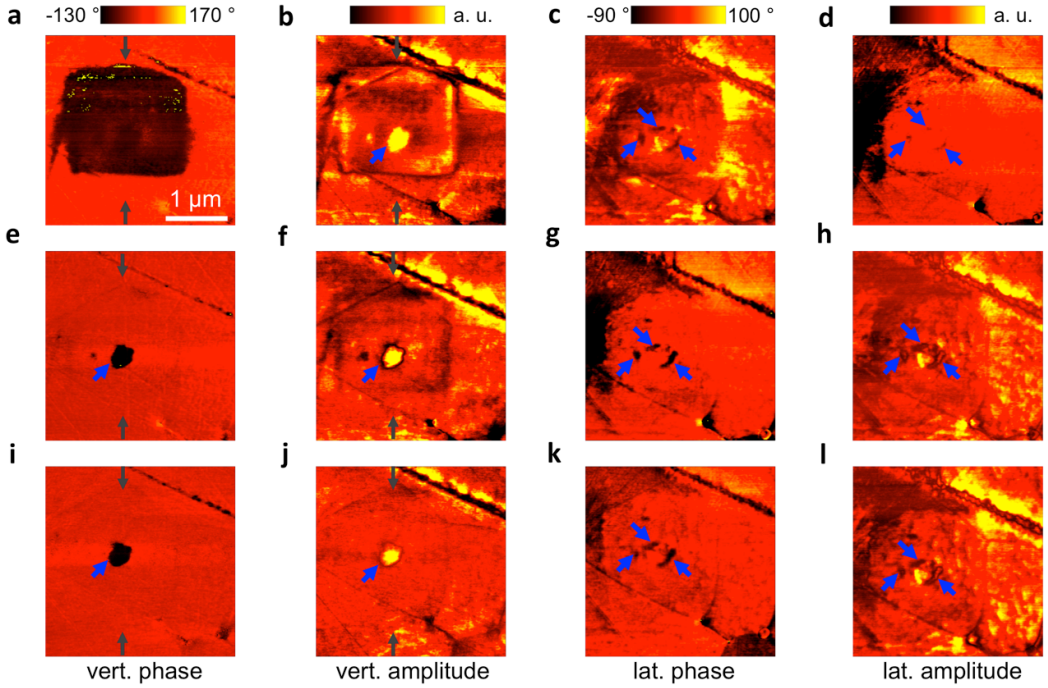


Figure 3.34 Evolution of the polarization after poling the sample in a 1.5 × 1.5 µm$^2$ region of interest, as indicated in Fig. 3.32(m). (**a**–**d**) PFM images captured 15 min, (**e**–**h**) 45 min, and (**i**–**l**) 90 min after the completion of the poling experiment. The PFM data show the (**a**,**e**,**i**) vertical phase and (**b**,**f**,**j**) amplitude, as well as the (**c**,**g**,**k**) lateral phase and (**d**,**h**,**l**) amplitude. The blue arrows highlight core areas; the dark gray arrows indicate the locations where the cross-sectional profiles were drawn in Fig. 3.35**.**

In the vertical amplitude, a circular domain exists inside the poled area (blue arrow, Fig. 3.34(b)). This means that the tip-induced domain in the shell has partially relaxed back within the first 15 min after poling because the vertical amplitude is a measure of the out-of-plane piezoresponse. Moreover, a weak in-plane domain pattern can be observed in the lateral phase (Fig. 3.34(c)) and amplitude (Fig. 3.34(d)) images within the core-shell region. After 45 min, the induced long-range ordered vertical domain shrank down to a distinctive circular area (Fig. 3.34(e) and (f)), which can be identified as the non-ergodic core. The relaxation of the surrounding material can be attributed to the high ergodicity of the shell. The in-plane domain pattern was even more pronounced in the lateral phase and amplitude images 45 min after poling (Fig. 3.34(g) and (h)). After 90 min,

the vertical phase image (Fig. 3.34(i)) did not change further, whereas the vertical amplitude signal in the core (Fig. 3.34(j)) was weaker. In contrast, the lateral phase and amplitude images remained almost unchanged after 45 min (Fig. 3.34(g,h,k,l)).

A detailed study of the evolution of the field-induced vertical domain and the relaxation behavior of the core and the shell, by means of averaged cross-sectional profiles taken in the vertical phase (Fig. 3.32(p), Fig. 3.34(a,e,i)), amplitude (Fig. 3.32(o), Fig. 3.34(b,f,j)) and the respective topography, is presented in Fig. 3.35. From the cross-sectional profiles, the following information can be extracted. The gray box in Fig. 3.35(a) highlights the diameter (approximately 380 nm) of the core, as determined from the topography image. After preparation, the core was initially 0.8 nm deep (red line). However, 15 min after poling, the remaining depth was reduced to 0.2 nm (blue line). Then, the depth increased again to 0.3 nm and 0.5 nm after 45 min (black line) and 90 min (gray line), respectively, whereas the diameter of the structure remained constant. The compositional difference between core and shell also implies a gradual variation in the lattice constant, which can explain the small height variations that were induced by the electric field at the core (Fig. 3.35(a)).[181,182] Before poling, the interfacial region presented an equilibrium stress state that lead to a small depression at the core, which was most likely caused by different ablation rates during polishing. In an external electric field, however, the polarization mismatch causes a stress field at the core-shell interface, which in turn leads to an immediate local volume increase after poling and the subsequent decrease during relaxation. For the virgin state, the vertical phase (red line, Fig. 3.35(b)) is constant across the core-shell region and the corresponding amplitude (red line, Fig. 3.35(c)) exhibits only a very small magnitude, suggesting a weak piezoresponse in the vertical direction. This is in agreement with the data in Fig. 3.33(m–p), where a weak vertical and strong lateral piezoresponsive region was observed in the non-ergodic core area. 15 min after the poling, the phase shift in the poled area was −150° (blue line, Fig. 3.35(b)), indicating that a long-range ferroelectric domain, whose polarization vector points downward, has developed. The poled area is approximately 2 µm large. The corresponding vertical amplitude response (blue line, Fig. 3.35(c)), however, was only affected over a lateral width smaller than 380 nm instead of the fully poled distance of 2 µm. This observation and the evolution of the vertical amplitude in Fig. 3.34 imply that the induced vertical domain in the ergodic shell partially relaxed within the first 15 min. Then, 30 min later (black line, Fig. 3.35(b)), the diameter of the induced vertical domain (characterized by 150° in the phase) decreased from initially 2 µm to 380 nm and then remained stable (gray line in Fig. 3.35(b)), *i.e.*, the poled area shrank down to the core. This means that an irreversible transformation from the non-ergodic relaxor state to the ferroelectric phase can occur in the core, whereas the transformation from the ergodic state to the ferroelectric state is reversible within the shell.[181] It was also observed that the amplitude response of the field-induced domain region further laterally shrank in size, accompanied by the propagation and growth of the in-plane polarization at the core-shell interface.

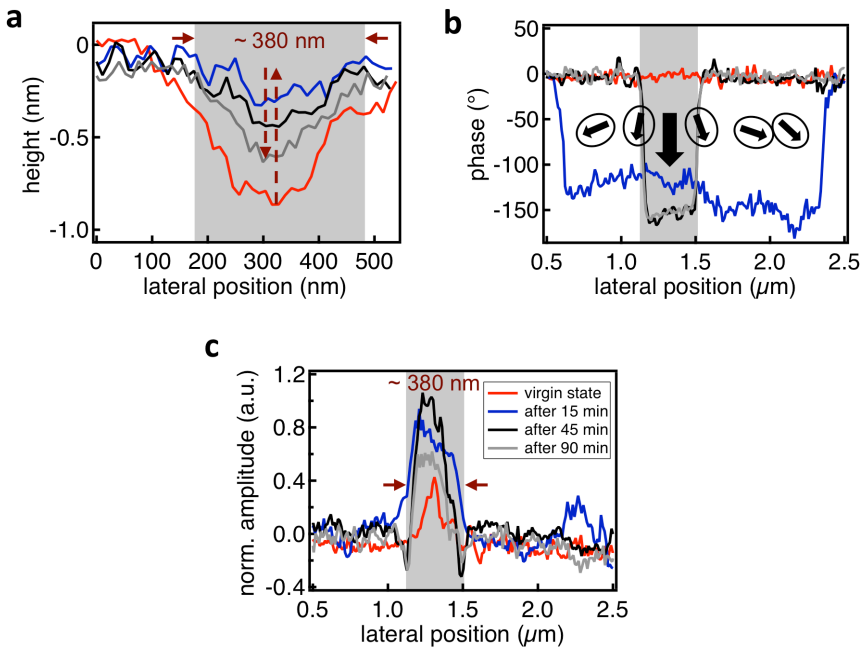


Figure 3.35 Evolution of the field-induced vertical domain and its relaxation behavior, as well as the corresponding topography changes at the core-shell region. (**a**) Cross-sectional profiles of the topography before and after poling, drawn along the arrows in Fig. 3.32(**q**). (**b**) Cross-sectional profiles of the vertical phase before and after poling, drawn along the arrows in Fig. 3.32(**p**) and Fig. 3.34(**a**,**e**,**i**). (**c**) Cross-sectional profiles of vertical amplitude before and after poling, drawn along the arrows in Fig. 3.32(**o**), 3.34(**b**,**f**,**j**). The virgin state in each image is indicated by the red solid line, whereas the blue, black, and gray solid lines indicate the signals 15 min, 45 min and 90 min after poling, respectively. The gray boxes highlight the position of the core, which is approximately 380 nm in width, showing the topographical hollows and polarization states of the tip-induced vertical domain. The red upward and downward arrows (**a**) guide the reader through the evolution of the topography at the core after the poling experiment. Immediately after poling, the hollow nearly disappeared (upward arrow, (**a**)) and grew back with time (downward arrow, (**a**)). The black arrows (**b**) mime the potential domain configuration (polar nanoregions) at the sample surface.

To better illustrate the evolution of the field-induced domain at the core-shell interface, the lateral phase piezoresponse images (Fig. 3.32(n), Fig. 3.34(c,g,k)) are enlarged and shown together in Fig. 3.36. The white lines indicate the interface between the core and its periphery. Figure 3.36(a) shows the virgin domain state, with a strong image contrast in the core but a negligible image contrast within the shell. Figure 3.36(b) reveals that the virgin lateral domain configuration completely disappeared after vertical poling. Moreover, new lateral domains were formed at preferential nucleation spots around the core-shell interface, as indicated by the blue arrows. Remarkably, 45 min after poling (Fig. 3.36(c)), these lateral domains became larger and more pronounced, in contrast to that observed previously, when they remained stable (phase image 90 min after poling, Fig. 3.36(d)). This observation indicates that lateral domains can be induced by the electrical field and start to nucleate at the core-shell interface. These freshly induced domains continue to grow laterally and propagate into the adjacent shell to compensate for the mismatch of stress and polarization between the irreversibly induced ferroelectric state in the core and the ergodic shell, which is the driving force of the lateral domain propagation.

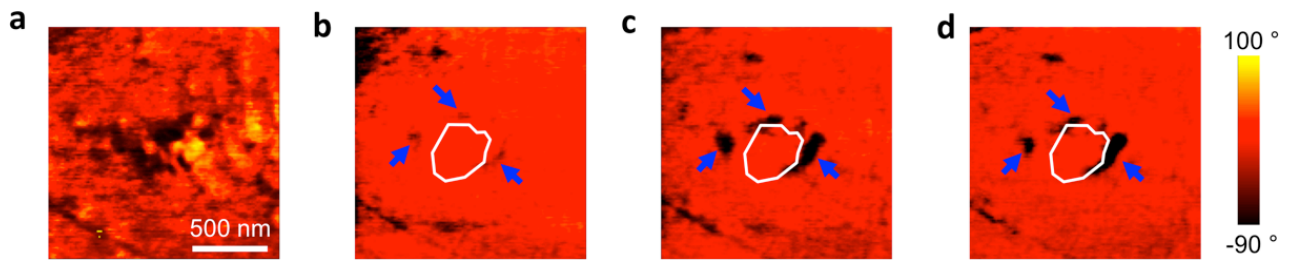


Figure 3.36 Evolution of the lateral domain at the core-shell interface after poling. (**a**) The virgin state of the lateral domain structure. (**b**) The electric field-induced lateral domain phase states 15 min, (**c**) 45 min, (**d**) 90 min after the completion of the poling experiment. The white line denotes the outline of the remanent vertical phase in the core after 45 min (Fig. 3.34(**e**)). The blue arrows highlight the newly formed lateral ferroelectric domain at the core-shell interface. Note: (**a**–**d**) are the enlarged images of the lateral PFM phase data of Fig. 3.32(**n**) and Fig. 3.34(**c**,**g**,**k**).

Under an external field, the entire virgin material can be poled. After removing the field, the core remains poled, whereas the shell reversibly relaxes to the initial state.[23,57] We thus propose a model for the polarization evolution of the core-shell region in the poling experiment (Fig. 3.37). In the virgin state (Fig. 3.37(a)), the core is embedded in a region (azure) where randomly oriented PNRs (encircled black arrows) characterize the material. At this stage, the core (black blue) predominantly exhibits laterally oriented domains (black arrows). To pole the material, an electric field between the AFM tip and the sample was applied. This poling process induced a downward-oriented ferroelectric domain with a long-range order (dark blue area, Fig. 3.37(b)). The AFM induced domain was not stable and shrank to a well-defined core-shell interface (white dashed frame). Then, further relaxation occurred (Fig. 3.37(c)) around the newly formed and electrically induced core-shell interface. Finally, the induced single vertical domain relaxed back to its virgin state (PNRs, encircled black arrows, Fig. 3.37(c)) because there was a high random electrical potential in the ergodic shell. In the non-ergodic core, however, a single vertical domain (dark blue area) that is associated with an irreversible transition to a ferroelectric state was induced. Due to the stress and polarization mismatch at the core-shell interface, a lateral domain nucleated and grew as compensation (brown area represents the lateral domain propagation). The actual spatial domain orientations at the core-shell interfacial area were then a complex mixture of vertical and lateral domain components (Fig. 3.37(d)).

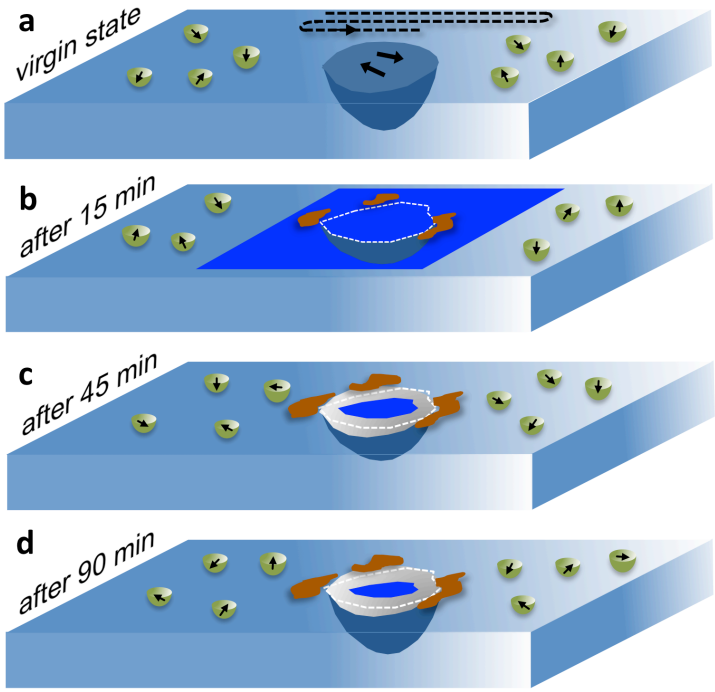


Figure 3.37 Scheme of the proposed model for the relaxation within the core-shell region of an individual grain. (**a**–**d**), Evolution of the vertical and the lateral domain configuration before (**a**) and after 15 min (**b**), 45 min (**c**) and 90 min (**d**) of vertical poling. The light blue planes represent a part of the $Sr^{2+}$-rich shell, with the $Sr^{2+}$-depleted core in the center (dark blue hemisphere). The black arrows indicate the local domain configuration. The white dashed frames separate the tip-induced core from the shell. The dark blue area indicates a vertical downward-oriented domain and the gray area, a mixed vertical and lateral domain. The brownish areas indicate the possible lateral domain propagation from the interface to the shell. The dashed line in (**a**) illustrates the trace of the nanoscale line-by-line poling of an AFM tip.

To gain further insights into the evolution of the domain distribution after poling, a continuum phase field simulation was carried out. The configuration of a core-shell microstructure was included in the model (Fig. 3.38). The initial equilibrium state is shown in Fig. 3.38(a), in which large domains are present in the non-ergodic core and a structure with small-sized domains in the ergodic shell. The corresponding potential distribution (Fig. 3.38(b)) shows a potential with small variations around zero throughout the *x*-*z* plane. The random field distribution caused by the chemical disorder leads to some hot spots with relatively high/low potential.[102] The electric field loading was then applied by a potential difference between the top and bottom boundary. Core and shell regions were fully poled under the peak potential of +10 V (Fig. 3.38(c)), with the polarization pointing downwards. The corresponding distribution of electric potential difference indicates an almost homogeneous gradient (Fig. 3.38(d)). After the external potential is switched off, polarization and potential distribution represent the remanent state (Fig. 3.38(e) and (f)): the poled polarization state in the shell region relaxes to a random state, whereas the field-induced ferroelectric domains within the core region remain poled. The potential distribution also relaxes to zero, except for the bottom of the core-shell interface (red area). The downward polarization of the ferroelectric domain in the non-ergodic core can thus not be compensated for

and leads to the presence of a positive charge beneath the core. As a result, the potential beneath the core is higher (red area) than the one of the rest of the simulated mesh (Fig. 3.38(f)).

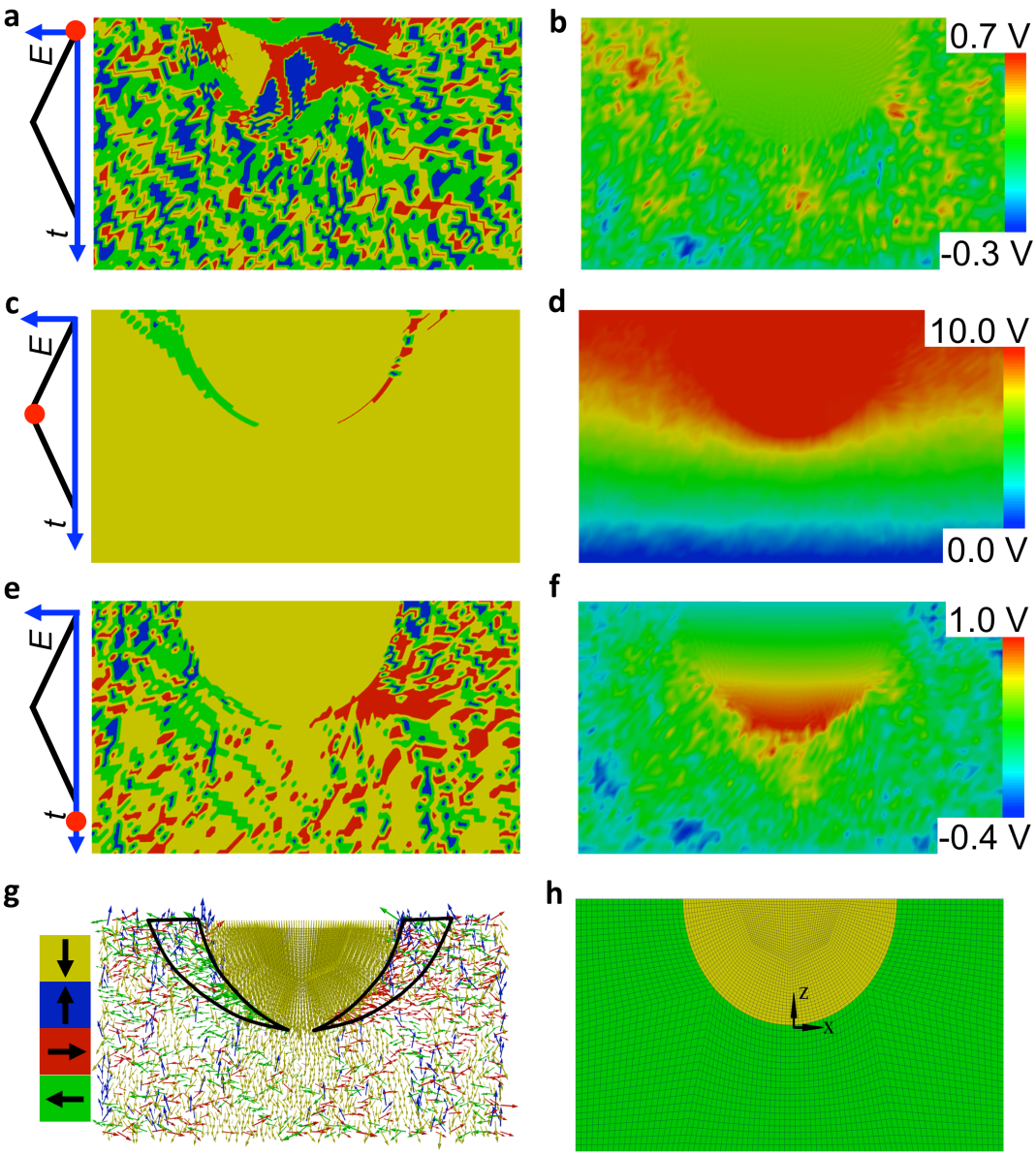


Figure 3.38 Phase field simulation of a formation of the field-induced polarization. (**a**,**c**,**e**,**g**) Domain distribution and respective orientation of the polarization. (**b**,**d**,**f**) Corresponding potential distribution. (**h**) Designed mesh in the *x*-*z* plane through the sample volume miming the geometry of a core-shell structure. The simulation evolves from the initial state (**a**,**b**) over a maximum potential state (**c**,**d**) to the remanent state. (**e**,**f**,**g**) The detailed polarization vector distribution at the remanent state is shown in (**g**). The marked regions (black frames) have a preferential lateral domain orientation. The colors in (**a**,**c**,**e**) and the arrows in (**g**) represent four polarization orientations of the domains: yellow – down; blue – up; green – left; red – right. The length of the arrows indicates the magnitude of the polarization vector. The three upper charts on the left illustrate the different stages of the simulation, in which red dots denote the current applied field and the *y*- and *x*-axis represent the electric potential and the time step, respectively.

The remanent domain configuration is symbolized as polarization vectors (Fig. 3.38(g)), in which black frames enclose regions with predominantly laterally oriented domains (red and green arrows), which is consistent with

the lateral domain phenomenon observed in the PFM experiment (*cf.* Fig. 3.36). The local poling induced a transition from the relaxor states (ergodic – shell, non-ergodic – core) to the ferroelectric state in both regions, which was completely reversible in the shell area but caused the core region to be permanently in the ferroelectric state. These findings and the appearance/growth of a ferroelectric domain with a polarization direction perpendicular to the applied field into the ergodic shell are in good agreement with the results obtained by the phase field simulation based on a core-shell microstructure model. It revealed a strong gradient in the electrical potential at the interfacial area, which causes the nucleation and propagation of an in-plane polarization.

### 3.3.3 Statement of Personal Contribution

[3] Na Liu, Matias Acosta, Shuai Wang, Bai-Xiang Xu, Robert W. Stark and Christian Dietz, "Revealing the core-shell interactions of a giant strain relaxor ferroelectric $0.75Bi_{1/2}Na_{1/2}TiO_3$-$0.25SrTiO_3$", *Scientific Reports*, **6**, 36910 (2016).

The idea behind this work was from myself. All experimental work with respect to the PFM characterizations and the data processing were carried out by myself. The phase field simulation and the relevant writing in the manuscript were done by M.Sc. Shuai Wang and Prof. Dr. Bai-Xiang Xu. The first draft of manuscript related to PFM part was written by myself and later drafts were written and approved together with Dr. Christian Dietz and Prof. Dr. Robert Stark.

# 4 Conclusions and Outlook

## 4.1 Conclusions

Within the scope of this thesis, a nanoscale characterization of $Bi_{1/2}Na_{1/2}TiO_3$ (BNT)-based lead-free relaxor piezoceramics whose relaxor behavior were tailored by different kinds of chemical substitutions was performed at room temperature by using conventional and advanced piezoresponse force microscopy (PFM) techniques. The domain structure with nanometer-sized polar entities (PNRs) is decisive for the macroscopic peculiarities of relaxors, such as the large electric field-induced strain. To enhance the spatial and temporal resolution of PFM for studying PNRs in relaxors, torsional dual *ac* resonance tracking (DART)-PFM and high-speed PFM have been developed. Additionally, a three dimensional quantitative mapping of the local piezoelectric properties has been established based on the damped simple harmonic oscillator (DSHO) model using the DART-PFM data obtained by a vertically and torsionally vibrating cantilever. High-speed PFM using scanning velocities of up to 117 μm/s allowed for an in-depth study of local relaxation processes, which unraveled the distribution of the local degree of ergodicity, the PNRs dynamics, and the nanoscopic relaxation mechanisms at room temperature. Eventually, a core-shell relaxor piezoceramic characterized by a non-ergodic core and an ergodic shell within the individual grains was studied using vector PFM at room temperature. Assisted by phase field simulations, the core-shell interactions triggered by an external electric field was revealed and pivotal points were discovered which reinforced the phase transistion in the ergodic shell triggered by the non-ergodic core.

In the first part, the work was devoted to enhance the lateral resolution of PFM for detecting nanometer-sized polar regions in the lead-free relaxors ceramics BNT-BKT-*x*BMT ($x$ = 0 or 3). A DART-PFM technique utilizing the torsional vibration of the cantilever was realized. Compared to conventional single frequency PFM, the use of torsional DART-PFM enhanced the contrast of the amplitude and phase images and reduced the interference with topographical features. With this technique, the morphology of PNRs on both relaxors was visualized with a higher reliability and signal-to-noise ratio. Notably, fine domain features in the range of a few tens of nanometers were observed in 3BMT, which can be interpreted as PNRs or PNRs clusters. In comparison to 0BMT, these fine domain features observed in 3BMT confirmed its higher degree of ergodicity on the macroscale. On the conventional ferroelectric ceramic PZT, nanoscale features could be resolved as well. By combining torsional DART- and vertical DART-PFM, the spatial orientation of the piezoresponse signal could be obtained. A DSHO model was applied to quantify the tip-sample surface contact mechanics and four tip-sample characteristic parameters were calculated: (1) the true drive phase and (2) amplitude, (3) the instantaneous contact resonance frequency, and (4) the quality factor. A straightforward data representation of the obtained three-dimensional dataset was suggested and showed that the electromechanical response of relaxors remarkably differs between the spatial directions. The three-dimensional DART-PFM enabled the visualization of the actual spatial orientation of PNRs in relaxors. These findings and results from this study were published to the scientific community in publication [1].

In the second part of this thesis, the work was devoted to uncover the mechanisms behind the "coexistence" of ergodic and non-ergodic relaxor states that promote the large recoverable strain functionality in ergodic relaxor systems. The local poling by the tip and subsequent PFM imaging were used to study the local relaxation processes in selective A-site doped $Bi_{1/2}Na_{1/2}TiO_3$-$Bi_{1/2}K_{1/2}TiO_3$ relaxor ferroelectrics with 1 at. % La replacing Na or K abbreviated as BNTNa and BNTK, respectively. At room temperature, macroscopically both samples were characterized as ergodic relaxors due to their freezing temperatures being slightly below. The higher $T_f$ of BNTNa resulted in a comparatively higher degree of ergodicity. The higher recoverable strain in BNTNa is attractive for actuator applications. The different functional properties between the two samples were attributed to small variations in the chemical pressure caused by replacing the A-site cations K or Na with small amounts of La having a different ionic radius.

Initially, we used the conventional single frequency PFM mode to visualize the virgin domain states of both samples. The absence of the domain contrast indicated that the typical PNRs of these relaxor materials could hardly be resolved by this technique due to its limited lateral resolution. To study the reversibility of the ergodic state to the ferroelectric state under an external field, a *dc* voltage of −10 V was vertically applied to the tip to pole a certain area by scanning. Measuring the subsequent amplitude and phase PFM images on a larger area $5 \times 5$ μm$^2$ with a tip velocity of 5 μm/s right after and 60 min after poling, the relaxation processes were studied. The observed partially poled areas directly after poling indicated that the associated field was sufficient to induce ferroelectric domains on both samples. Compared with the relaxation processes observed on the sample of BNTK, the higher degree of ergodicity on the chosen square area of BNTNa sample was reflected by the higher degree of locally induced switching, as well as a faster relaxation at room temperature. Furthermore, local hysteresis loops measured at selected locations in both samples using switching spectroscopy PFM (SS-PFM) revealed a higher piezoresponse at the locations chosen on BNTNa under bias-on and a lower remanent state under bias-off. Theses findings were presented in publication [2].

To provide an in-depth study of the local relaxation processes with respect to PNRs dynamics and the local distribution of ergodicity on different chosen areas of both samples, PFM imaging was improved to achieve tip velocities of up to 117 μm/s (high-speed PFM). The reversible transition from the relaxor state to the ferroelectric state confirmed the averaged ergodic behavior of the four chosen areas regardless of the choice of the sample (BNTNa or BNTK). The different times needed for the completion of this reversible process reflected the difference of the local degree of ergodicity of the chosen areas. The KWW fitting result of the relaxation curves demonstrated a broad distribution of relaxation times on slow relaxing areas, whereas relatively narrow relaxation spectra were found on fast relaxing areas. Comparing the histograms of the relaxation times of individual pixels (proximate to the size of PNRs or PNRs clusters) obtained on all areas, the distribution for the fast relaxing areas exhibited an exponential decay with time, whereas for slow relaxing areas a nearly constant distribution was observed. We suggest that quasi-static and dynamic PNRs originating from local variations of the chemical disorder coexist in ergodic relaxors whose freezing temperatures are close to room temperature. In the virgin state of an area with a high density of dynamic PNRs per unit area (quasi-static

PNRs), the poled domain relaxes fast (slowly). The heterogeneous (homogeneous) distribution of the density of PNRs can broaden (narrow) the distribution of relaxation times. The relative amount and interplay of both types of PNRs provoked the average macroscopic ergodicity of BNT-BKT-based relaxor ferroelectrics. The local relaxation mechanism describing the dissociation processes of the tip-induced ferroelectric domain into small PNRs was summarized as follows. The relaxation preferentially started with a domain wall roughening process triggered by the strong interaction between the tip-induced domain walls and thermally fluctuating dynamic PNRs from the adjacent unpoled area. The curved wall kept moving slowly towards the area that is characterized by a high density of quasi-static PNRs in the virgin state. For areas characterized by a high density of dynamic PNRs, the nucleation of dynamic PNRs occurred triggered by the curved wall. Subsequently, a rapid spreading process around these PNRs due to the high curvature of the interface between poled and relaxed area proceeded.

In the third part of this thesis, the work was devoted to unravel the interfacial interactions between the non-ergodic core and the ergodic shell in a lead-free core-shell material using PFM. A core-shell relaxor ceramic $0.75Bi_{1/2}Na_{1/2}TiO_3$-$0.25SrTiO_3$ (BNT-25ST) was chosen due to its high electromechanical response and reduced hysteresis. Using single frequency vector PFM, a distinctive domain contrast in the core and a weak contrast in the shell were observed, which clearly confirmed the virgin domain structure of the non-ergodic core and the ergodic shell within individual grains. To study the core-shell interactions, we locally poled the core-shell region and subsequently captured vertical and lateral PFM images at different relaxation stages (times). Immediately after poling, a long-range ordered ferroelectric domain orientated downward (normal to the sample surface) was observed. The subsequent reversible transition in the shell and the irreversible one in the core region further confirmed the non-ergodic relaxor state of the core and ergodic relaxor state of the shell at room temperature. Interestingly, after poling tiny laterally oriented domains nucleated at the core-shell interface, and propagated into the adjacent shell. Based on this PFM observation, phase field simulations were carried out and revealed that the evolution of the field-induced lateral domains can be attributed to an emergence of polarization charges at the core-shell interface beneath the sample surface. In the practical application of ergodic relaxor actuators, the electric field-cycling process is executed from the remanent state (relaxed state) to the ferroelectric state and back to the remanent state. Microscopically transferring this cycling to the core-shell region, the relaxed ergodic state in the shell is switched to a ferroelectric state and reversed back (PNRs), whereas in the non-ergodic core, this process is a reversal of the field-induced domain orientations along the polar axis in the remanent ferroelectric state. At the interface, the field-induced lateral domains, which can be considered as pivot points are generated from the residual high potential at the interface beneath the surface. Upon switching on the external field, these “pivot points” at the interface generate domain nuclei and facilitate the alignment of PNRs to the direction of the external electric field. Consequently, the energy barrier for the completion of the phase transition in the shell is reduced. Upon switching off the field, the pivot points reduce the strain mismatch at the interface between the induced ferroelectric core and the ergodic shell. These findings provide an experimental insight into the mechanism behind the macroscopic functionality of core-shell piezoceramics. The results from this study were reported in publication [3].

In short:

- It was often reported that in the lead-free relaxor ceramics the domain contrast visualized by conventional PFM is weak. Our developed torsional DART-PFM could successfully visualize the small PNR clusters that were inaccessible using single frequency PFM.
- The development of high-speed PFM imaging could shed light into the nanoscopic relaxation mechanisms behind lead-free ergodic relaxors. Our work expanded the knowledge of the "coexistence of ergodic and non-ergodic relaxor state"-theory that was conjectured to be responsible for the macroscopic large recoverable strain. In the ergodic relaxor systems, the distribution of the local degree of ergodicity was observed and the coexistence of dynamic PNRs and quasi-static or static (*e.g.* non-ergodic core) PNRs originated from the local chemical heterogeneity was unraveled.
- Combining PFM with phase field simulations, we could reveal the interfacial interactions between the non-ergodic core and ergodic shell under the external electric field. The large recoverable field-induced strain at relatively low electric fields in the core-shell material is because of field-induced domains acting as pivotal points that facilitate the domain orientation in the adjacent shell region. The subsequent field-induced mismatch of the strain and polarization restores the domain pattern to the initial state in the shell upon removal of the external field.
- Associating the coexistence of a non-ergodic core and an ergodic shell to the coexistence of quasi-static and dynamic PNRs, the strain mechanisms of ergodic lead-free relaxors can be derived. The role of quasi-static PNRs in an ergodic relaxor is similar to the role of the non-ergodic core in the cores-shell material. The quasi-static PNRs can be taken as nucleation center. Upon switching, the quasi-static PNRs align and provide a stray field to coalesce the adjacent dynamic PNRs, which thus lower the local energy barrier for aligning dynamic PNRs. During relaxation, the polarization or strain mismatch at the inhomogeneous interfacial area could activate the relaxation of dynamic PNRs.

## 4.2 Outlook

According to our findings, during the dissociation process from a poled long-range ordered domain into small PNRs, the small size of the remaining domains was not resolvable in the phase channel using single frequency high-speed PFM. However, the dissociated nanometer-sized domains increased the density of domain walls per unit area, leading to observable dark areas in the amplitude images. For high-speed imaging, the single frequency PFM is straightforward to realize the fast imaging but is not capable to directly resolve small PNRs. In future, the elaboration of torsional DART-PFM with high-speed imaging in seconds or even milliseconds can facilitate a reliable detection of nanometer-sized PNRs and their depolarization dynamics. Using the DSHO model, the nanoscopic relaxation mechanism might be analyzed in a quantified manner.

The dissociation process of the poled domain into small PNRs indicates that within the selected area or grain, the chemical distribution is inhomogeneous. The increased domain wall energy resulting from the increased

number of PNRs is compensated by the energy gain from the pinning effect.[230] For example, the induced domain relaxed slowly near the grain boundary that serves as the pinning sites to impede the domain wall motion. In Chapter 3.2 it was seen that during the same observation time a slower relaxation was observed by conventional PFM, which is due to existence of grain boundaries within the chosen area. For the future work, the pinning effect of the grain boundaries on the nanoscopic relaxation process can be studied using high-speed PFM.

The coexistence of quasi-static or static PNRs and dynamic PNRs was caused by the mesoscopic heterogeneity of the structure. Due to the chemical inhomogeneity in the relaxor, the freezing temperature $T_f$ locally differs, which leads to different dynamics of PNRs at a fixed temperature.[136] For the future work, the temperature dependent-nanoscopic relaxation behavior can be studied for mapping the distribution of the local activation energy. To transfer the observations on the nanoscale to the macroscale application in future, simultaneously executed field switching and imaging using PFM offer an *in situ* study of the interplay of dynamic PNRs and quasi-static or static PNRs.

## References


[1] K. Uchino, *Piezoelectric actuators and ultrasonic motors*. Kluwer Academic Publishers: Boston, 1997.

[2] R. E. Newnham, *Functional composites for sensors and actuators: smart materials.* The Pennsylvania Academy of Science: Pennsylvania, USA, 1998.

[3] K. Uchino, Ceramic actuators - Principles and applications. *Mrs Bull.* **18**, 42−48 (1993).

[4] B. Sahoo, V. A. Jaleel, P. K. Panda, Development of PZT powders by wet chemical method and fabrication of multilayered stacks/actuators. *Mat. Sci. Eng. B-Solid* **126**, 80−85 (2006).

[5] W. Jo, R. Dittmer, M. Acosta, J. Zang, C. Groh, E. Sapper, K. Wang, J. Rödel, Giant electric-field-induced strains in lead-free ceramics for actuator applications - status and perspective. *J. Electroceram.* **29**, 71−93 (2012).

[6] B. Jaffe, W. R. Cook, H. Jaffe, *Piezoelectric ceramics*. Academic: London, 1971.

[7] J. Rödel, W. Jo, K. T. P. Seifert, E. M. Anton, T. Granzow, D. Damjanovic, Perspective on the development of lead-free piezoceramics. *J. Am. Ceram. Soc.* **92**, 1153−1177 (2009).

[8] S. E. Park, T. R. Shrout, Ultrahigh strain and piezoelectric behavior in relaxor based ferroelectric single crystals. *J. Appl. Phys.* **82**, 1804−1811 (1997).

[9] "EU-Directive 2002/95/EC: Restriction of the use of certain hazardous substances in electrical and electronic equipment (RoHS)." *Off. J. Eur. Union* **L37**, 19 (2002).

[10] "EU-directive 2011/65/EU: Restriction of the use of certain hazardous substances in electrical and electronic equipment (RoHS)." *Off. J. Eur. Union* **L174**, 88 (2011).

[11] "EU-directive 2012/19/EU of the european pariliament and of the council of 4 July 2012 on waste electrical and electronic euipment (WEEE). *Off. J. Eur. Union* **L197**, 38 (2012).

[12] Y. Saito, H. Takao, T. Tani, T. Nonoyama, K. Takatori, T. Homma, T. Nagaya, M. Nakamura, Lead-free piezoceramics. *Nature* **432**, 84 (2004).

[13] T. R. Shrout, S. J. Zhang, Lead-free piezoelectric ceramics: alternatives for PZT? *J. Electroceram.* **19**, 113 (2007).

[14] K. Yoshii, Y. Hiruma, H. Nagata, T. Takenaka, Electrical properties and depolarization temperature of $(Bi_{1/2}Na_{1/2})TiO_3$-$(Bi_{1/2}K_{1/2})TiO_3$ lead-free piezoelectric ceramics. *Jpn. J. Appl. Phys. 1* **45**, 4493−4496 (2006).

[15] R. Dittmer, W. Jo, J. Daniels, S. Schaab, J. Rödel, Relaxor characteristics of morphotropic phase boundary $(Bi_{1/2}Na_{1/2})TiO_3$-$(Bi_{1/2}K_{1/2})TiO_3$ modified with $Bi(Zn_{1/2}Ti_{1/2})O_3$. *J. Am. Ceram. Soc.* **94**, 4283−4290 (2011).

[16] S. C. Zhao, G. R. Li, A. L. Ding, T. B. Wang, Q. R. Yin, Ferroelectric and piezoelectric properties of $(Na, K)_{0.5}Bi_{0.5}TiO_3$ lead free ceramics. *J. Phys. D-Appl. Phys.* **39**, 2277 (2006).

[17] G. A. Smolenskii, Ferroelectric phase transformations in solid solutions of perovskite structure formed in some binary systems. *J. Inorg. Chem.-Ussr* **1**, 296−306 (1956).

[18] G. A. Smolenskii, V. A. Isupov, A. I. Agranovskaya, S. N. Popov, Ferroelectrics with diffuse phase transitions. *Sov. Phys. - Sol. State* **2**, 2584−2594 (1961).

[19] B. Dkhil, J. M. Kiat, G. Calvarin, G. Baldinozzi, S. B. Vakhrushev, E. Suard, Local and long range polar

order in the relaxor-ferroelectric compounds $PbMg_{1/3}Nb_{2/3}O_3$ and $PbMg_{0.3}Nb_{0.6}Ti_{0.1}O_3$. *Phys. Rev. B* **65**, 024104 (2002).

[20] Z. G. Ye, Y. Bing, J. Gao, A. A. Bokov, P. Stephens, B. Noheda, G. Shirane, Development of ferroelectric order in relaxor $(1-x)Pb(Mg_{1/3}Nb_{2/3})O_3$-$xPbTiO_3$ ($0 \leq x \leq 0.15$). *Phys. Rev. B* **67**, 104104 (2003).

[21] S. Wakimoto, C. Stock, R. J. Birgeneau, Z. G. Ye, W. Chen, W. J. L. Buyers, P. M. Gehring, G. Shirane, Ferroelectric ordering in the relaxor $Pb(Mg_{1/3}Nb_{2/3})O_3$ as evidenced by low-temperature phonon anomalies. *Phys. Rev. B* **65**, 172105 (2002).

[22] W. Jo, S. Schaab, E. Sapper, L. A. Schmitt, H.-J. Kleebe, A. J. Bell, J. Rödel, On the phase identity and its thermal evolution of lead free $(Bi_{1/2}Na_{1/2})TiO_3$-6 mol% $BaTiO_3$. *J. Appl. Phys.* **110**, 074106 (2011).

[23] R. Dittmer, D. Gobeljic, W. Jo, V. V. Shvartsman, D. C. Lupascu, J. L. Jones, J. Rödel, Ergodicity reflected in macroscopic and microscopic field-dependent behavior of BNT-based relaxors. *J. Appl. Phys.* **115**, 084111 (2014).

[24] S. Prosandeev, D. Wang, A. R. Akbarzadeh, B. Dkhil, L. Bellaiche, Field-induced percolation of polar nanoregions in relaxor ferroelectrics. *Phys. Rev. Lett.* **110**, 207601 (2013).

[25] R. Dittmer, W. Jo, J. Rödel, S. Kalinin, N. Balke, Nanoscale insight into lead-free BNT-BT-$x$KNN. *Adv. Funct. Mater.* **22**, 4208−4215 (2012).

[26] V. V. Shvartsman, A. L. Kholkin, Domain structure of $0.8Pb(Mg_{1/3}Nb_{2/3})O_3$-$0.2PbTiO_3$ studied by piezoresponse force microscopy. *Phys. Rev. B* **69**, 014102 (2004).

[27] A. Gruverman, O. Auciello, H. Tokumoto, Imaging and control of domain structures in ferroelectric thin films via scanning force microscopy. *Annu. Rev. Mater. Sci.* **28**, 101−123 (1998).

[28] V. Bobnar, Z. Kutnjak, R. Pirc, A. Levstik, Electric-field-temperature phase diagram of the relaxor ferroelectric lanthanum-modified lead zirconate titanate. *Phys. Rev. B* **60**, 6420−6427 (1999).

[29] B. Dkhil, J. M. Kiat, Electric-field-induced polarization in the ergodic and nonergodic states of $PbMg_{1/3}Nb_{2/3}O_3$ relaxor. *J. Appl. Phys.* **90**, 4676 (2001).

[30] D. Viehland, S. J. Jang, L. E. Cross, M. Wuttig, Freezing of the polarization fluctuations in lead magnesium niobate relaxors. *J. Appl. Phys.* **68**, 2916 (1990).

[31] R. Blinc, V. Bobnar, R. Pirc, Coupled spherical pseudospin-phonon model and the pressure-temperature phase diagram of relaxor ferroelectrics. *Phys. Rev. B* **64**, 132103 (2001).

[32] N. Demathan, E. Husson, G. Calvarin, J. R. Gavarri, A. W. Hewat, A. Morell, A structural model for the relaxor $PbMg_{1/3}Nb_{2/3}O_3$ at 5 K. *J. Phys. Condens. Mat.* **3**, 8159−8171 (1991).

[33] P. Bonneau, P. Garnier, G. Calvarin, E. Husson, J. R. Gavarri, A. W. Hewat, A. Morell, X-ray and neutron-diffraction studies of the diffuse phase-transition in $PbMg_{1/3}Nb_{2/3}O_3$ ceramics. *J. Solid State Chem.* **91**, 350−361 (1991).

[34] K. Hirota, S. Wakimoto, D. E. Cox, Neutron and X-ray scattering studies of relaxors. *J. Phys. Soc. Jpn.* **75**, 111006 (2006).

[35] G. Y. Xu, G. Shirane, J. R. D. Copley, P. M. Gehring, Neutron elastic diffuse scattering study of $Pb(Mg_{1/3}Nb_{2/3})O_3$. *Phys. Rev. B* **69**, 064112 (2004).

[36] A. A. Bokov, Z. G. Ye, Recent progress in relaxor ferroelectrics with perovskite structure. *J. Mater. Sci.* **41**, 31−52 (2006).

[37] E. Dul'kin, E. Mojaev, M. Roth, I. P. Raevski, S. A. Prosandeev, Nature of thermally stimulated acoustic emission from $PbMg_{1/3}Nb_{2/3}O_3$-$PbTiO_3$ solid solutions. *Appl. Phys. Lett.* **94**, 252904 (2009).

[38] B. Dkhil, P. Gemeiner, A. Al-Barakaty, L. Bellaiche, E. Dul'kin, E. Mojaev, M. Roth, Intermediate temperature scale $T^*$ in lead-based relaxor systems. *Phys. Rev. B* **80**, 064103 (2009).

[39] D. Viehland, X. H. Dai, J. F. Li, Z. Xu, Effects of quenched disorder on La-modified lead zirconate titanate: Long- and short-range ordered structurally incommensurate phases, and glassy polar clusters. *J. Appl. Phys.* **84**, 458 (1998).

[40] P. M. Vilarinho, Y. Rosenwaks, A. Kingon, *Scanning probe microscopy-characterization, nanofabrication and device application of functional materials*. Kluwer Academic Pbulishers: The Netherlands, 2004.

[41] O. Auciello, A. Gruverman, H. Tokumoto, S. A. Prakash, S. Aggarwal, R. Ramesh, Nanoscale scanning force imaging of polarization phenomena in ferroelectric thin films. *Mrs Bull.* **23**, 33−42 (1998).

[42] M. Alexe, A. Gruverman, *Nanoscale characterization of ferroelectric: Scanning probe microscopy approach*. Springer: Berlin, 2004.

[43] P. Guthner, K. Dransfeld, Local poling of ferroelectric polymers by scanning force microscopy. *Appl. Phys. Lett.* **61**, 1137−1139 (1992).

[44] K. Franke, J. Besold, W. Haessler, C. Seegebarth, Modification and detection of domains on ferroelectric PZT films by scanning force microscopy. *Surf. Sci.* **302**, L283−L288 (1994).

[45] A. Gruverman, O. Auciello, H. Tokumoto, Scanning force microscopy for the study of domain structure in ferroelectric thin films. *J. Vac. Sci. Technol. B* **14**, 602−605 (1996).

[46] A. Gruverman, O. Auciello, H. Tokumoto, Nanoscale investigation of fatigue effects in $Pb(Zr,Ti)O_3$ films. *Appl. Phys. Lett.* **69**, 3191−3193 (1996).

[47] L. M. Eng, H. J. Guntherodt, G. A. Schneider, U. Kopke, J. M. Saldana, Nanoscale reconstruction of surface crystallography from three-dimensional polarization distribution in ferroelectric barium-titanate ceramics. *Appl. Phys. Lett.* **74**, 233−235 (1999).

[48] L. M. Eng, H. J. Guntherodt, G. Rosenman, A. Skliar, M. Oron, M. Katz, D. Eger, Nondestructive imaging and characterization of ferroelectric domains in periodically poled crystals. *J. Appl. Phys.* **83**, 5973−5977 (1998).

[49] M. Abplanalp, L. M. Eng, P. Gunter, Mapping the domain distribution at ferroelectric surfaces by scanning force microscopy. *Appl. Phys. A-Mater.* **66**, S231−S234 (1998).

[50] A. Kholkin, A. Morozovska, D. Kiselev, I. Bdikin, B. Rodriguez, P. P. Wu, A. Bokov, Z. G. Ye, B. Dkhil, L. Q. Chen, M. Kosec, S. V. Kalinin, Surface domain structures and mesoscopic phase transition in relaxor ferroelectrics. *Adv. Funct. Mater.* **21**, 1977 (2011).

[51] P. Lehnen, W. Kleemann, T. Woike, R. Pankrath, Ferroelectric nanodomains in the uniaxial relaxor system $Sr_{0.61-x}Ba_{0.39}Nb_2O_6 : Ce_x^{3+}$. *Phys. Rev. B* **64**, 224109 (2001).

[52] N. Balke, I. Bdikin, S. V. Kalinin, A. L. Kholkin, Electromechanical imaging and spectroscopy of

ferroelectric and piezoelectric materials: state of the art and prospects for the future. *J. Am. Ceram. Soc.* **92**, 1629 (2009).

[53] H. Okino, J. Sakamoto, T. Yamamoto, Contact-resonance piezoresponse force microscope and its application to domain bbservation of $Pb(Mg_{1/3}Nb_{2/3})O_3$-$PbTiO_3$ single crystals. *Jpn. J. Appl. Phys. 1* **42**, 6209 (2003).

[54] V. V. Shvartsman, A. L. Kholkin, A. Orlova, D. Kiselev, A. A. Bogomolov, A. Sternberg, Polar nanodomains and local ferroelectric phenomena in relaxor lead lanthanum zirconate titanate ceramics. *Appl. Phys. Lett.* **86**, 202907 (2005).

[55] M. Hinterstein, M. Knapp, M. Holzel, W. Jo, A. Cervellino, H. Ehrenberg, H. Fuess, Field-induced phase transition in $Bi_{1/2}Na_{1/2}TiO_3$-based lead-free piezoelectric ceramics. *J. Appl. Crystallogr.* **43**, 1314−1321 (2010).

[56] J. Kling, X. L. Tan, W. Jo, H. J. Kleebe, H. Fuess, J. Rödel, In situ transmission electron microscopy of electric field-triggered reversible domain formation in Bi-based lead-free piezoceramics. *J. Am. Ceram. Soc.* **93**, 2452−2455 (2010).

[57] M. Acosta, N. Liu, M. Deluca, S. Heidt, I. Ringl, C. Dietz, R. W. Stark, W. Jo, Tailoring ergodicity through selective A-site doping in the $Bi_{1/2}Na_{1/2}TiO_3$-$Bi_{1/2}K_{1/2}TiO_3$ system. *J. Appl. Phys.* **117**, 134106 (2015).

[58] N. Liu, M. Acosta, S. Wang, B. X. Xu, R. W. Stark, C. Dietz, Revealing the core-shell interactions of a giant strain relaxor ferroelectric $0.75Bi_{1/2}Na_{1/2}TiO_3$-$0.25SrTiO_3$. *Sci. Rep.* **6**, 36910 (2016).

[59] R. Nath, Y.-H. Chu, N. A. Polomoff, R. Ramesh, B. D. Huey, High speed piezoresponse force microscopy: < 1 frame per second nanoscale imaging. *Appl. Phys. Lett.* **93**, 072905 (2008).

[60] N. A. Polomoff, R. N. Premnath, J. L. Bosse, B. D. Huey, Ferroelectric domain switching dynamics with combined 20 nm and 10 ns resolution. *J. Mater. Sci.* **44**, 5189−5196 (2009).

[61] B. D. Huey, R. N. Premnath, S. Lee, N. A. Polomoff, High-speed SPM applied for direct nanoscale mapping of the influence of defects on ferroelectric switching dynamics. *J. Am. Ceram. Soc.* **95**, 1147−1162 (2012).

[62] K. C. Kao, *Dielectric phenomena in solids*. Elsevier Academic Press: 2004.

[63] R. Waser, U. Böttger, S. Tiedke, *Polar oxides - properties, characterization, and imaging*. Wiley-VCH: Weinheim, 2005.

[64] A. J. Moulson, J. M. Herbert, *Electroceramics*. John Wiley & Sons Ltd.: Chichester, 2003.

[65] K. Charles, *Introduction to solid state physics*. John Wiley & Sons, Inc: 2005.

[66] R. E. Newnham, V. Sundar, R. Yimnirun, J. Su, Q. M. Zhang, Electrostriction: nonlinear electromechanical coupling in solid dielectrics. *J. Phys. Chem. B* **101**, 10141−10150 (1997).

[67] G. H. Haertling, Ferroelectric ceramics: History and technology. *J. Am. Ceram. Soc.* **82**, 797−818 (1999).

[68] W. Heywang, K. Lubitz, W. Wersing, *Piezoelectricity - Evolution and future of a technology*. Springer: The Netherlands, 2008.

[69] J. Curie, P. Curie, Development, via compression, of electric polarization in hemihedral crystals with inclined faces. *B. Soc. Mineral. Fr.* **3**, 90−93 (1880).

[70] D. Damjanovic, Ferroelectric, dielectric and piezoelectric properties of ferroelectric thin films and ceramics. *Rep. Prog. Phys.* **61**, 1267−1324 (1998).

[71] K. M. Rabe, C. H. Ahn, J.-M. Triscone, *Physics of ferroelectrics - a modern perspective*. Springer: 2007.

[72] J. F. Scott, C. A. P. Dearaujo, Ferroelectric memories. *Science* **246**, 1400−1405 (1989).

[73] K. Uchino, *Ferroelectric devices*. Second Edition ed.; Taylor & Francis Inc: New York, 2009.

[74] J. Valasek, Piezoelectric and allied phenomena in rochelle salt. *Phys. Rev.* **17**, 475 (1921).

[75] S. Roberts, Dielectric and piezoelectric properties of barium titanate. *Phys. Rev.* **71**, 890−895 (1947).

[76] E. A. Stern, Character of order-disorder and displacive components in barium titanate. *Phys. Rev. Lett.* **93**, 037601 (2004).

[77] H. F. Kay, P. Vousden, Symmetry changes in barium titanate at low temperatures and their relation to its ferroelectric properties. *Philos. Mag.* **40**, 1019−1040 (1949).

[78] R. Landauer, Electrostatic considerations in $BaTiO_3$ domain formation during polarization reversal. *J. Appl. Phys.* **28**, 227−234 (1957).

[79] P. Chandra, P. B. Littlewood, *A landau primer for ferroelectrics: In physics of ferroelectrics, Vol. 105 of topics in Applied Physics.* Springer: Berlin, 2007.

[80] A. F. Devonshire, Theory of ferroelectrics. *Adv. Phys.* **3**, 85−130 (1954).

[81] J. C. Burfoot, W. T. George, *Polar dielectrics and their applications*. Palgrave Macmillan: London, 1979.

[82] G. A. Samara, *Ferroelectricity revisited - advances in materials and physics*, in *Solid State Physics, Vol 56,* Elsevier, 2001.

[83] M. E. Lines, A. M. Glass, *Principles and applications of ferroelectrics and related materials.* Oxford: Clarendon, 1977.

[84] N. Setter, *Piezoelectric materials in devices: extended reviews on current and emerging piezoelectric materials, technology, and applications*. EPFL Swiss Federal Institute of Technology: Lausanne, 2003.

[85] L. Jin, F. Li, S. J. Zhang, Decoding the fingerprint of ferroelectric loops: comprehension of the material properties and structures. *J. Am. Ceram. Soc.* **97**, 1−27 (2014).

[86] D. Damjanovic, Stress and frequency dependence of the direct piezoelectric effect in ferroelectric ceramics. *J. Appl. Phys.* **82**, 1788−1797 (1997).

[87] O. Boser, Statistical-theory of hysteresis in ferroelectric materials. *J. Appl. Phys.* **62**, 1344−1348 (1987).

[88] G. A. Smolenskii, A. I. Agranovskaia, Dielectric polarization and losses of some complex compounds. *Sov. Phys. Tech. Phys.* **3**, 1380−1382 (1958).

[89] L. E. Cross, Relaxor ferroelectrics. *Ferroelectrics* **76**, 241 (1987).

[90] G. A. Samara, The relaxational properties of compositionally disordered $ABO_3$ perovskites. *J. Phys. Condens. Mat.* **15**, R367 (2003).

[91] N. Setter, L. E. Cross, The role of B-site cation disorder in diffuse phase-transition behavior of perovskite ferroelectrics. *J. Appl. Phys.* **51**, 4356−4360 (1980).

[92] R. A. Cowley, S. N. Gvasaliya, S. G. Lushnikov, B. Roessli, G. M. Rotaru, Relaxing with relaxors: a review of relaxor ferroelectrics. *Adv. Phys.* **60**, 229−327 (2011).

[93] G. Burns, F. H. Dacol, Glassy polarization behavior in ferroelectric compounds $Pb(Mg_{1/3}Nb_{2/3})O_3$ and $Pb(Zn_{1/3}Nb_{2/3})O_3$. *Solid State Commun.* **48**, 853−856 (1983).

[94] W. W. Ge, C. P. Devreugd, D. Phelan, Q. H. Zhang, M. Ahart, J. F. Li, H. S. Luo, L. A. Boatner, D. Viehland, P. M. Gehring, Lead-free and lead-based $ABO_3$ perovskite relaxors with mixed-valence A-site and B-site disorder: comparative neutron scattering structural study of $(Na_{1/2}Bi_{1/2})TiO_3$ and $Pb(Mg_{1/3}Nb_{2/3})O_3$. *Phys. Rev. B* **88**, 174115 (2013).

[95] W. Kleemann, The relaxor enigma - charge disorder and random fields in ferroelectrics. *J. Mater. Sci.* **41**, 129−136 (2006).

[96] V. V. Kirillov, V. A. Isupov, Relaxation polarization of $PbMg_{1/3}Nb_{2/3}O_3$ (PMN) - ferroelectric with a diffused phase-transition. *Ferroelectrics* **5**, 3−9 (1973).

[97] V. Westphal, W. Kleemann, M. D. Glinchuk, Diffuse phase-transitions and random-field-induced domain states of the relaxor ferroelectric $PbMg_{1/3}Nb_{2/3}O_3$. *Phys. Rev. Lett.* **68**, 847−850 (1992).

[98] M. A. Akbas, P. K. Davies, Domain growth in $Pb(Mg_{1/3}Ta_{2/3})O_3$ perovskite relaxor ferroelectric oxides. *J. Am. Ceram. Soc.* **80**, 2933−2936 (1997).

[99] R. Pirc, R. Blinc, Spherical random-bond-random-field model of relaxer ferroelectrics. *Phys. Rev. B* **60**, 13470−13478 (1999).

[100] Z. Y. Cheng, R. S. Katiyar, X. Yao, A. Q. Guo, Dielectric behavior of lead magnesium niobate relaxors. *Phys. Rev. B* **55**, 8165−8174 (1997).

[101] R. Blinc, V. V. Laguta, B. Zalar, J. Banys, Polar nanoclusters in relaxors. *J. Mater. Sci.* **41**, 27−30 (2006).

[102] W. Kleemann, Random fields in relaxor ferroelecrtrics - a jubilee review. *J. Adv. Dielectr.* **02**, 1241001 (2012).

[103] A. M. Glass, Investigation of electrical properties of $Sr_{1-x}Ba_xNb_2O_6$ with special reference to pyroelectric detection. *J. Appl. Phys.* **40**, 4699 (1969).

[104] L. Benguigui, K. Bethe, Dffused phase-transitions in $Ba_xSr_{1-x}TiO_3$ single-crystals. *J. Appl. Phys.* **47**, 2787−2791 (1976).

[105] C. G. F. Stenger, F. L. Scholten, A. J. Burggraaf, Ordering and diffuse phase-transitions in $Pb(Sc_{0.5}Ta_{0.5})O_3$ ceramics. *Solid State Commun.* **32**, 989−992 (1979).

[106] N. Setter, L. E. Cross, The contribution of structural disorder to diffuse phase-transitions in ferroelectrics. *J. Mater. Sci.* **15**, 2478−2482 (1980).

[107] C. G. F. Stenger, A. J. Burggraaf, Order-disorder reactions in the ferroelectric perovskites $Pb(Sc_{1/2}Nb_{1/2})O_3$ and $Pb(Sc_{1/2}Ta_{1/2})O_3$. *Phys. Status Solidi. A* **61**, 275−285 (1980).

[108] A. A. Bokov, I. P. Rayevskii, V. G. Smotrakov, O. I. Prokopalo, Kinetics of compositional ordering in $Pb_2B'B''O_6$ crystals. *Phys. Status Solidi. A* **93**, 411−417 (1986).

[109] C. W. Ahn, C. H. Hong, B. Y. Choi, H. P. Kim, H. S. Han, Y. Hwang, W. Jo, K. Wang, J. F. Li, J. S. Lee, I. W. Kim, A brief review on relaxor ferroelectrics and selected issues in lead-free relaxors. *J. Korean Phys. Soc.* **68**, 1481−1494 (2016).

[110] P. K. Davies, M. A. Akbas, Chemical order in PMN-related relaxors: structure, stability, modification, and impact on properties. *J. Phys. Chem. Solids* **61**, 159−166 (2000).

[111] S. B. Vakhrushev, B. E. Kvyatkovsky, A. A. Naberezhnov, N. M. Okuneva, B. P. Toperverg, Glassy phenomena in disordered perovskite-like crystals. *Ferroelectrics* **90**, 173−176 (1989).

[112] A. Naberezhnov, S. Vakhrushev, B. Dorner, D. Strauch, H. Moudden, Inelastic neutron scattering study of the relaxor ferroelectric $PbMg_{1/3}Nb_{2/3}O_3$ at high temperatures. *Eur. Phys. J. B* **11**, 13−20 (1999).

[113] D. La-Orauttapong, J. Toulouse, Z. G. Ye, W. Chen, R. Erwin, J. L. Robertson, Neutron scattering study of the relaxor ferroelectric $(1-x)Pb(Zn_{1/3}Nb_{2/3})O_3$-$xPbTiO_3$. *Phys. Rev. B* **67**, 134110 (2003).

[114] P. M. Gehring, S. E. Park, G. Shirane, Dynamical effects of the nanometer-sized polarized domains in $Pb(Zn_{1/3}Nb_{2/3})O_3$. *Phys. Rev. B* **63**, 224109 (2001).

[115] A. A. Bokov, B. J. Rodriguez, X. H. Zhao, J. H. Ko, S. Jesse, X. F. Long, W. G. Qu, T. H. Kim, J. D. Budai, A. N. Morozovska, S. Kojima, X. L. Tan, S. V. Kalinin, Z. G. Ye, Compositional disorder, polar nanoregions and dipole dynamics in $Pb(Mg_{1/3}Nb_{2/3})O_3$-based relaxor ferroelectrics. *Z. Krist.* **226**, 99−107 (2011).

[116] V. V. Shvartsman, W. Kleemann, J. Dec, Z. K. Xu, S. G. Lu, Diffuse phase transition in $BaTi_{1-x}Sn_xO_3$ ceramics: An intermediate state between ferroelectric and relaxor behavior. *J. Appl. Phys.* **99**, (2006).

[117] M. D. Glinchuk, R. Farhi, A random field theory based model for ferroelectric relaxors. *J. Phys. Condens. Mat.* **8**, 6985−6996 (1996).

[118] W. Kleemann, Relaxor ferroelectrics: cluster glass ground state via random fields and random bonds. *Phys. Status Solidi. B* **251**, 1993−2002 (2014).

[119] V. V. Shvartsman, W. Kleemann, T. Lukasiewicz, J. Dec, Nanopolar structure in $Sr_xBa_{1-x}Nb_2O_6$ single crystals tuned by Sr/Ba ratio and investigated by piezoelectric force microscopy. *Phys. Rev. B* **77**, 054105 (2008).

[120] D. Wang, X. Q. Ke, Y. Z. Wang, J. H. Gao, Y. Wang, L. X. Zhang, S. Yang, X. B. Ren, Phase diagram of polar states in doped ferroelectric systems. *Phys. Rev. B* **86**, 054120 (2012).

[121] Y. J. Guo, Y. Y. Guo, L. Lin, Y. J. Gao, B. B. Jin, L. Kang, J. M. Liu, Mean-field theory of ferroelectricity in $Sr_{1-x}Ca_xTiO_3$ ($0 \leq x \leq 0.4$). *Phys. Rev. B* **86**, 014202 (2012).

[122] A. D. Bruce, R. A. Cowley, Structural phase-transitions III. critical-dynamics and quasi-elastic scattering. *Adv. Phys.* **29**, 219−321 (1980).

[123] L. Boltzmann, On some questions of the kinetic theory of gases. *Wien. Ber.* **96**, 891 (1887).

[124] K. Binder, A. P. Young, Spin-glasses - experimental facts, theoretical concepts, and open questions. *Rev. Mod. Phys.* **58**, 801−976 (1986).

[125] D. Viehland, M. Wuttig, L. E. Cross, The glassy behavior of relaxor ferroelectrics. *Ferroelectrics* **120**, 71−77 (1991).

[126] P. Lehnen, J. Dec, W. Kleemann, T. Woike, R. Pankrath, Relaxor properties of SBN:Ce. *Ferroelectrics* **240**, 1547−1554 (2000).

[127] H. Vogel, *Phys. Z.* **22**, 645 (1921).

[128] G. S. Fulcher, *J. Am. Ceram. Soc.* **8**, 339 (1925).

[129] L. Xie, Y. L. Li, R. Yu, Z. Y. Cheng, X. Y. Wei, X. Yao, C. L. Jia, K. Urban, A. A. Bokov, Z. G. Ye, J.

Zhu, Static and dynamic polar nanoregions in relaxor ferroelectric $Ba(Ti_{1-x}Sn_x)O_3$ system at high temperature. *Phys. Rev. B* **85**, 014118 (2012).

[130] R. Blinc, V. Laguta, B. Zalar, Field cooled and zero field cooled $^{207}Pb$ NMR and the local structure of relaxor $PbMg_{1/3}Nb_{2/3}O_3$. *Phys. Rev. Lett.* **91**, 247601 (2003).

[131] F. H. Schader, Z. Y. Wang, M. Hinterstein, J. E. Daniels, K. G. Webber, Stress-modulated relaxor-to-ferroelectric transition in lead-free $(Na_{1/2}Bi_{1/2})TiO_3$-$BaTiO_3$ ferroelectrics. *Phys. Rev. B* **93**, 134111 (2016).

[132] D. Gobeljic, R. Dittmer, J. Rödel, V. V. Shvartsman, D. C. Lupascu, Macroscopic and nanoscopic polarization relaxation kinetics in lead-free relaxors $Bi_{1/2}Na_{1/2}TiO_3$-$Bi_{1/2}K_{1/2}TiO_3$-$BiZn_{1/2}Ti_{1/2}O_3$. *J. Am. Ceram. Soc.* **97**, 3904−3912 (2014).

[133] S. V. Kalinin, B. J. Rodriguez, J. D. Budai, S. Jesse, A. N. Morozovska, A. A. Bokov, Z. G. Ye, Direct evidence of mesoscopic dynamic heterogeneities at the surfaces of ergodic ferroelectric relaxors. *Phys. Rev. B* **81**, 064107 (2010).

[134] C. Stock, L. Van Eijck, P. Fouquet, M. Maccarini, P. M. Gehring, G. Y. Xu, H. Luo, X. Zhao, J. F. Li, D. Viehland, Interplay between static and dynamic polar correlations in relaxor $Pb(Mg_{1/3}Nb_{2/3})O_3$. *Phys. Rev. B* **81**, 144127 (2010).

[135] H. S. Han, W. Jo, J. Rödel, I. K. Hong, W. P. Tai, J. S. Lee, Coexistence of ergodicity and nonergodicity in $LaFeO_3$-modified $Bi_{1/2}(Na_{0.78}K_{0.22})_{1/2}TiO_3$ relaxors. *J. Phys. Condens. Mat.* **24**, 365901 (2012).

[136] S. V. Kalinin, B. J. Rodriguez, S. Jesse, A. N. Morozovska, A. A. Bokov, Z. G. Ye, Spatial distribution of relaxation behavior on the surface of a ferroelectric relaxor in the ergodic phase. *Appl. Phys. Lett.* **95**, 142902 (2009).

[137] B. P. Burton, E. Cockayne, U. V. Waghmare, Correlations between nanoscale chemical and polar order in relaxor ferroelectrics and the lengthscale for polar nanoregions. *Phys. Rev. B* **72**, 064113 (2005).

[138] R. Sommer, N. K. Yushin, J. J. Vanderklink, Polar metastability and an electric-field-induced phase-transition in the disordered perovskite $Pb(Mg_{1/3}Nb_{2/3})O_3$. *Phys. Rev. B* **48**, 13230−13237 (1993).

[139] O. Bidault, M. Licheron, E. Husson, A. Morell, The onset of an electric field-induced ferroelectric-like phase in the perovskite $Pb(Mg_{1/3}Nb_{2/3})O_3$. *J. Phys. Condens. Mat.* **8**, 8017−8026 (1996).

[140] E. Sapper, N. Novak, W. Jo, T. Granzow, J. Rödel, Electric-field-temperature phase diagram of the ferroelectric relaxor system $(1-x)Bi_{1/2}Na_{1/2}TiO_3$-$xBaTiO_3$ doped with manganese. *J. Appl. Phys.* **115**, 194104 (2014).

[141] M. Chabin, M. Malki, E. Husson, A. Morell, dielectric-properties of electric-field-induced ferroelectric transition in $PbMg_{1/3}Nb_{2/3}O_3$ (PMN) ceramics. *J. Phys. III* **4**, 1151−1163 (1994).

[142] J. Rödel, K. G. Webber, R. Dittmer, W. Jo, M. Kimura, D. Damjanovic, Transferring lead-free piezoelectric ceramics into application. *J. Eur. Ceram. Soc.* **35**, 1659−1681 (2015).

[143] S. T. Zhang, A. B. Kounga, E. Aulbach, H. Ehrenberg, J. Rödel, Giant strain in lead-free piezoceramics $Bi_{0.5}Na_{0.5}TiO_3$-$BaTiO_3$-$K_{0.5}Na_{0.5}NbO_3$ system. *Appl. Phys. Lett.* **91**, 112906 (2007).

[144] G. A. Smolenskii, V. A. Isupov, A. I. Agranovskaya, N. N. Krainik, New ferroelectrics of complex composition. *Sov. Phys.-Sol. State* **2**, 2651−2654 (1961).

[145] A. Herabut, A. Safari, Processing and electromechanical properties of $(Bi_{0.5}Na_{0.5})_{(1-1.5x)}La_xTiO_3$ ceramics. *J. Am. Ceram. Soc.* **80**, 2954−2958 (1997).

[146] J. Suchanicz, K. Roleder, A. Kania, J. Handerek, Electrostrictive strain and pyroeffect in the region of phase coexistence in $Na_{0.5}Bi_{0.5}TiO_3$. *Ferroelectrics* **77**, 107−110 (1988).

[147] J. A. Zvirgzds, P. P. Kapostins, J. V. Zvirgzde, T. V. Kruzina, X-ray study of phase-transitions in ferroelectric $Na_{0.5}Bi_{0.5}TiO_3$. *Ferroelectrics* **40**, 75−77 (1982).

[148] I. G. Siny, C. S. Tu, V. H. Schmidt, Critical acoustic behavior of the relaxor ferroelectric $Na_{1/2}Bi_{1/2}TiO_3$ in the intertransition region. *Phys. Rev. B* **51**, 5659−5665 (1995).

[149] G. O. Jones, P. A. Thomas, The tetragonal phase of $Na_{0.5}Bi_{0.5}TiO_3$ - a new variant of the perovskite structure. *Acta. Crystallogr. B* **56**, 426−430 (2000).

[150] G. O. Jones, P. A. Thomas, Investigation of the structure and phase transitions in the novel A-site substituted distorted perovskite compound $Na_{0.5}Bi_{0.5}TiO_3$. *Acta. Crystallogr. B* **58**, 168−178 (2002).

[151] S. B. Vakhrushev, V. A. Isupov, B. E. Kvyatkovsky, N. M. Okuneva, I. P. Pronin, G. A. Smolensky, P. P. Syrnikov, Phase-transitions and soft modes in sodium bismuth titanate. *Ferroelectrics* **63**, 153−160 (1985).

[152] V. Dorcet, G. Trolliard, P. Boullay, Reinvestigation of phase transitions in $Na_{0.5}Bi_{0.5}TiO_3$ by TEM. Part I: first order rhombohedral to orthorhombic phase transition. *Chem. Mater.* **20**, 5061−5073 (2008).

[153] M. Gröting, I. Kornev, B. Dkhil, K. Albe, Pressure-induced phase transitions and structure of chemically ordered nanoregions in the lead-free relaxor ferroelectric $Na_{1/2}Bi_{1/2}TiO_3$. *Phys. Rev. B* **86**, 134118 (2012).

[154] T. Takenaka, K. Maruyama, K. Sakata, $(Bi_{1/2}Na_{1/2})TiO_3$-$BaTiO_3$ system for lead-free piezoelectric ceramics. *Jpn. J. Appl. Phys. 1* **30**, 2236−2239 (1991).

[155] M. Acosta, W. Jo, J. Rödel, Temperature- and frequency-dependent properties of the $0.75Bi_{1/2}Na_{1/2}TiO_3$-$0.25SrTiO_3$ lead-free incipient piezoceramic. *J. Am. Ceram. Soc.* **97**, 1937−1943 (2014).

[156] M. Ehmke, J. Glaum, W. Jo, T. Granzow, J. Rödel, Stabilization of the fatigue-resistant phase by CuO addition in $(Bi_{1/2}Na_{1/2})TiO_3$-$BaTiO_3$. *J. Am. Ceram. Soc.* **94**, 2473−2478 (2011).

[157] J. Glaum, M. Zakhozheva, M. Acosta, E. Aksel, H. J. Kleebe, M. Hoffman, L. A. Schmitt, Influence of B-site disorder on the properties of unpoled $Bi_{1/2}Na_{1/2}TiO_3$-$0.06Ba(Zr_xTi_{1-x})O_3$ piezoceramics. *J. Am. Ceram. Soc.* **99**, 2801−2808 (2016).

[158] W. Jo, E. Erdem, R. A. Eichel, J. Glaum, T. Granzow, D. Damjanovic, J. Rödel, Effect of Nb-donor and Fe-acceptor dopants in $(Bi_{1/2}Na_{1/2})TiO_3$-$BaTiO_3$-$(K_{1/2}Na_{1/2})NbO_3$ lead-free piezoceramics. *J. Appl. Phys.* **108**, 014110 (2010).

[159] C. Groh, D. J. Franzbach, W. Jo, K. G. Webber, J. Kling, L. A. Schmitt, H. J. Kleebe, S. J. Jeong, J. S. Lee, J. Rödel, Relaxor/ferroelectric composites: A solution in the quest for practically viable lead-free incipient piezoceramics. *Adv. Funct. Mater.* **24**, 356−362 (2014).

[160] W. Jo, R. Dittmer, M. Acosta, J. D. Zang, C. Groh, E. Sapper, K. Wang, J. Rödel, Giant electric-field-induced strains in lead-free ceramics for actuator applications - status and perspective. *J. Electroceram.* **29**, 71−93 (2012).

[161] W. Jo, T. Granzow, E. Aulbach, J. Rödel, D. Damjanovic, Origin of the large strain response in $(K_{0.5}Na_{0.5})NbO_3$-modified $(Bi_{0.5}Na_{0.5})TiO_3$-$BaTiO_3$ lead-free piezoceramics. *J. Appl. Phys.* **105**, 094102 (2009).

[162] J. Wei-Jing, C. Yan-Bin, Z. Shan-Tao, Y. Bin, Z. Xiao-Ning, W. Qian-Jin, Microstructure and electric properties of lead-free $0.8Bi_{1/2}Na_{1/2}TiO_3$-$0.2Bi_{1/2}K_{1/2}TiO_3$ ceramics. *Ceram. Int.* **38**, 1683−1686 (2012).

[163] F. F. Wang, C. M. Leung, Y. X. Tang, T. Wang, W. Z. Shi, Composition induced structure evolution and large strain response in ternary $Bi_{0.5}Na_{0.5}TiO_3$-$Bi_{0.5}K_{0.5}TiO_3$-$SrTiO_3$ solid solution. *J. Appl. Phys.* **114**, 164105 (2013).

[164] A. Sasaki, T. Chiba, T. Mamiya, E. Otsuki, Dielectric and piezoelectric properties of $(Bi_{0.5}Na_{0.5})TiO_3$-$(Bi_{0.5}K_{0.5})TiO_3$ systems. *Jap. J. Appl. Phys.* **38**, 5564−5567 (1999).

[165] Y. Hiruma, K. Yoshii, H. Nagata, T. Takenaka, Phase transition temperature and electrical properties of $(Bi_{1/2}Na_{1/2})TiO_3$–$(Bi_{1/2}A_{1/2})TiO_3$ (A = Li and K) lead-free ferroelectric ceramics. *J. Appl. Phys.* **103**, 084121 (2008).

[166] N.-B. Do, H.-B. Lee, C.-H. Yoon, J.-K. Kang, J.-S. Lee, I.-W. Kim, Effect of Ta-substitution on the ferroelectric and piezoelectric properties of $Bi_{0.5}(Na_{0.82}K_{0.18})_{0.5}TiO_3$ ceramics. *Trans. Electr. Electron. Mater.* **12**, 64−67 (2011).

[167] A. Hussain, C. W. Ahn, A. Ullah, J. S. Lee, I. W. Kim, Effects of hafnium substitution on dielectric and electromechanical properties of lead-free $Bi_{0.5}(Na_{0.78}K_{0.22})_{0.5}(Ti_{1-x}Hf_x)O_3$ ceramics. *Jap. J. Appl. Phys.* **49**, 041504 (2010).

[168] A. Hussain, C. W. Ahn, J. S. Lee, A. Ullah, I. W. Kim, Large electric-field-induced strain in Zr-modified lead-free $Bi_{0.5}(Na_{0.78}K_{0.22})_{0.5}TiO_3$ piezoelectric ceramics. *Sensor. Actuat. A-Phys.* **158**, 84−89 (2010).

[169] A. Ullah, C. W. Ahn, A. Hussain, S. Y. Lee, I. W. Kim, Phase transition, electrical properties, and temperature-insensitive large strain in $BiAlO_3$-modified $Bi_{0.5}(Na_{0.75}K_{0.25})_{0.5}TiO_3$ lead-free piezoelectric ceramics. *J. Am. Ceram. Soc.* **94**, 3915−3921 (2011).

[170] A. Ullah, C. W. Ahn, A. Hussain, S. Y. Lee, H. J. Lee, I. W. Kim, Phase transitions and large electric field-induced strain in $BiAlO_3$-modified $Bi_{0.5}(Na, K)_{0.5}TiO_3$ lead-free piezoelectric ceramics. *Curr. Appl. Phys.* **10**, 1174−1181 (2010).

[171] N. Kumar, T. Y. Ansell, D. P. Cann, Role of point defects in bipolar fatigue behavior of $Bi(Mg_{1/2}Ti_{1/2})O_3$ modified $(Bi_{1/2}K_{1/2})TiO_3$-$(Bi_{1/2}Na_{1/2})TiO_3$ relaxor ceramics. *J. Appl. Phys.* **115**, 154104 (2014).

[172] A. Ullah, C. W. Ahn, A. Ullah, I. W. Kim, Large strain under a low electric field in lead-free bismuth-based piezoelectrics. *Appl. Phys. Lett.* **103**, 022906 (2013).

[173] E. A. Patterson, D. P. Cann, Bipolar piezoelectric fatigue of $Bi(Zn_{0.5}Ti_{0.5})O_3$-$(Bi_{0.5}K_{0.5})TiO_3$-$(Bi_{0.5}Na_{0.5})TiO_3$ Pb-free ceramics. *Appl. Phys. Lett.* **101**, 042905 (2012).

[174] N. Kumar, D. P. Cann, Electromechanical strain and bipolar fatigue in $Bi(Mg_{1/2}Ti_{1/2})O_3$-$(Bi_{1/2}K_{1/2})TiO_3$-$(Bi_{1/2}Na_{1/2})TiO_3$ ceramics. *J. Appl. Phys.* **114**, 054102 (2013).

[175] H. Dinh, H.-Y. Lee, C.-H. Yoon, R. A. Malik, Y.-M. Kong, J.-S. Lee, Effect of lanthanum doping on the structural, ferroelectric, and strain properties of $Bi_{1/2}(Na_{0.82}K_{0.18})_{1/2}TiO_3$ lead-free ceramics. *J. Korean Phys. Soc.* **62**, 1004−1008 (2013).

[176] J. Yoo, J. Hong, H. Lee, Y. Jeong, B. Lee, H. Song, J. Kwon, Piezoelectric and dielectric properties of $La_2O_3$ added Bi(Na, K)$TiO_3$-$SrTiO_3$ ceramics for pressure sensor application. *Sensor. Actuat. A-Phys.* **126**, 41−47 (2006).

[177] B. Wang, L. Luo, F. Ni, P. Du, W. Li, H. Chen, Piezoelectric and ferroelectric properties of $(Bi_{1-x}Na_{0.8}K_{0.2}La_x)_{0.5}TiO_3$ lead-free ceramics. *J. Alloys Compd.* **526**, 7984 (2012).

[178] Q. Zheng, C. Xu, D. Lin, D. Gao, K. W. Kwok, Piezoelectric and ferroelectric properties of $(Bi_{0.94-x}La_xNa_{0.94})_{0.5}Ba_{0.06}TiO_3$ lead-free ceramics. *J. Phys. D: Appl. Phys.* **41**, 125411 (2008).

[179] X. Dai, Z. Xu, D. Viehland, The spontaneous relaxor to normal ferroelectric transformation in La-modified lead zirconate titanate. *Phil. Mag. B* **70**, 33−48 (1994).

[180] J.-K. Lee, J. Y. Yi, K. S. Hong, Dependence of incommensurate phase formation on vacancy type in La-doped $(Na_{1/2}Ba_{1/2})TiO_3$. *J. Appl. Phys.* **96**, 1174 (2004).

[181] M. Acosta, L. A. Schmitt, L. Molina-Luna, M. C. Scherrer, M. Brilz, K. G. Webber, M. Deluca, H.-J. Kleebe, J. Rödel, W. Donner, Core-shell lead-free piezoelectric ceramics: current satus and advanced characterization of the $Bi_{1/2}Na_{1/2}TiO_3$-$SrTiO_3$ system. *J. Am. Ceram. Soc.* **98**, 3405−3422 (2015).

[182] J. Koruza, V. Rojas, L. Molina-Luna, U. Kunz, M. Duerrschnabel, H.-J. Kleebe, M. Acosta, Formation of the core-shell microstructure in lead-free $Bi_{1/2}Na_{1/2}TiO_3$-$SrTiO_3$ piezoceramics and its influence on the electromechanical properties. *J. Eur. Ceram. Soc.* **36**, 1009−1016 (2016).

[183] Z. Kutnjak, J. Petzelt, R. Blinc, The giant electromechanical response in ferroelectric relaxors as a critical phenomenon. *Nature* **441**, 956−959 (2006).

[184] M. Anoufa, J. M. Kiat, I. Kornev, C. Bogicevic, Vortices of polarization in $BaTiO_3$ core-shell nanoceramics: calculations based on ab initio derived hamiltonian versus landau theory. *Phys. Rev. B* **88**, 144106 (2013).

[185] M. Acosta. *Strain mechanism in lead-free ferroelectrics for actuators*. Technische Universität Darmstadt, Darmstadt, Germany, 2015.

[186] W. Krauss, D. Schutz, F. A. Mautner, A. Feteira, K. Reichmann, Piezoelectric properties and phase transition temperatures of the solid solution of $(1-x)(Bi_{0.5}Na_{0.5})TiO_3$-$xSrTiO_3$. *J. Eur. Ceram. Soc.* **30**, 1827−1832 (2010).

[187] Y. Hiruma, Y. Imai, Y. Watanabe, H. Nagata, T. Takenaka, Large electrostrain near the phase transition temperature of $Bi_{0.5}Na_{0.5}TiO_3$-$SrTiO_3$ ferroelectric ceramics. *Appl. Phys. Lett.* **92**, 262904 (2008).

[188] I. Fujii, S. Shimizu, K. Yamashita, K. Nakashima, N. Kumada, C. Moriyoshi, Y. Kuroiwa, Y. Fujikawa, D. Tanaka, M. Furukawa, S. Wada, Enhanced piezoelectric response of $BaTiO_3$-$KNbO_3$ composites. *Appl. Phys. Lett.* **99**, 202902 (2011).

[189] S.-Y. Choi, S.-J. Jeong, D.-S. Lee, M.-S. Kim, J.-S. Lee, J. H. Cho, B. I. Kim, Y. Ikuhara, Gigantic electrostrain in duplex structured alkaline niobates. *Chem. Mater.* **24**, 3363−3369 (2012).

[190] J. F. Ihlefeld, B. M. Foley, D. A. Scrymgeour, J. R. Michael, B. B. McKenzie, D. L. Medlin, M. Wallace, S. Trolier-McKinstry, P. E. Hopkins, Room-temperature voltage tunable phonon thermal conductivity via reconfigurable interfaces in ferroelectric thin films. *Nano Lett.* **15**, 1791−1795 (2015).

[191] G. Y. Kim, K. D. Sung, Y. Rhyim, S. Y. Yoon, M. S. Kim, S. J. Jeong, K. H. Kim, J. Ryu, S. D. Kim, S.

Y. Choi, Enhanced polarization by coherent heterophase interface between polar and nonpolar phase. *Nanoscale* **8**, 7443−7448 (2016).

[192] D. Liu, C. Tian, C. Ma, L. Luo, Y. Tang, T. Wang, W. Shi, D. Sun, F. Wang, Composition, electric-field and temperature induced domain evolution in lead-free $Bi_{0.5}Na_{0.5}TiO_3$-$BaTiO_3$-$SrTiO_3$ solid solutions by piezoresponse force microscopy. *Scripta Mater.* **123**, 64−68 (2016).

[193] A. Gruverman, O. Auciello, J. Hatano, H. Tokumoto, Scanning force microscopy as a tool for nanoscale study of ferroelectric domains. *Ferroelectrics* **184**, 1120 (1996).

[194] A. Gruverman, O. Kolosov, J. Hatano, K. Takahashi, H. Tokumoto, Domain-structure and polarization reversal in ferroelectrics studied by atomic force microscopy. *J. Vac. Sci. Technol. B* **13**, 1095−1099 (1995).

[195] A. Gruverman, S. V. Kalinin, Piezoresponse force microscopy and recent advances in nanoscale studies of ferroelectrics. *J. Mater. Sci.* **41**, 107−116 (2006).

[196] S. V. Kalinin, D. A. Bonnell, Imaging mechanism of piezoresponse force microscopy of ferroelectric surfaces. *Phys. Rev. B* **65**, 125408 (2002).

[197] T. M. T. Hidaka, M. Saitoh, N. Mikoshiba, M. Shimizu *et al*., Formation and observation of 50 nm polarized domains in $PbZr_{1-x}Ti_xO_3$ thin film using scanning probe microscope. *Appl. Phys. Lett.* **68**, (1996).

[198] S. Jesse, B. Mirman, S. V. Kalinin, Resonance enhancement in piezoresponse force microscopy: mapping electromechanical activity, contact stiffness, and *Q* factor. *Appl. Phys. Lett.* **89**, 022906 (2006).

[199] S. V. Kalinin, A. Rar, S. Jesse, A decade of piezoresponse force microscopy: progress, challenges, and opportunities. *IEEE T. Ultrason. Ferr.* **53**, 2226 (2006).

[200] U. Rabe, S. Amelio, E. Kester, V. Scherer, S. Hirsekorn, W. Arnold, Quantitative determination of contact stiffness using atomic force acoustic microscopy. *Ultrasonics* **38**, 430 (2000).

[201] R. Garcia, E. T. Herruzo, The emergence of multifrequency force microscopy. *Nat. Nanotechnol.* **7**, 217−226 (2012).

[202] B. J. Rodriguez, C. Callahan, S. V. Kalinin, R. Proksch, Dual-frequency resonance-tracking atomic force microscopy. *Nanotechnology* **18**, 475504 (2007).

[203] A. Gannepalli, D. G. Yablon, A. H. Tsou, R. Proksch, Mapping nanoscale elasticity and dissipation using dual frequency contact resonance AFM. *Nanotechnology* **22**, 355705 (2011).

[204] N. Liu, R. Dittmer, R. W. Stark, C. Dietz, Visualization of polar nanoregions in lead-free relaxors via piezoresponse force microscopy in torsional dual *AC* resonance tracking mode. *Nanoscale* **7**, 11787−11796 (2015).

[205] S. Jesse, H. N. Lee, S. V. Kalinin, Quantitative mapping of switching behavior in piezoresponse force microscopy. *Rev. Sci. Instrum.* **77**, 073702 (2006).

[206] S. Jesse, A. P. Baddorf, S. V. Kalinin, Switching spectroscopy piezoresponse force microscopy of ferroelectric materials. *Appl. Phys. Lett.* **88**, 062908 (2006).

[207] S. V. Kalinin, A. Gruverman, D. A. Bonnell, Quantitative analysis of nanoscale switching in $SrBi_2Ta_2O_9$ thin films by piezoresponse force microscopy. *Appl. Phys. Lett.* **85**, 795−797 (2004).

[208] M. Molotskii, A. Agronin, P. Urenski, M. Shvebelman, G. Rosenman, Y. Rosenwaks, Ferroelectric domain breakdown. *Phys. Rev. Lett.* **90**, 107601 (2003).

[209] R. Dittmer, W. Jo, E. Aulbach, T. Granzow, J. Rödel, Frequency-dependence of large-signal properties in lead-free piezoceramics. *J. Appl. Phys.* **112**, 014101 (2012).

[210] S. V. Kalinin, A. N. Morozovska, L. Q. Chen, B. J. Rodriguez, Local polarization dynamics in ferroelectric materials. *Rep. Prog. Phys.* **73**, 056502 (2010).

[211] T. Jungk, Á. Hoffmann, E. Soergel, *New insights into ferroelectric domain imaging with piezoresponse force microscopy: in ferroelectric crystals for photonic applications.* Springer Berlin Heidelberg: 2009.

[212] J. P. Killgore, D. G. Yablon, A. H. Tsou, A. Gannepalli, P. A. Yuya, J. A. Turner, R. Proksch, D. C. Hurley, Viscoelastic property mapping with contact resonance force microscopy. *Langmuir* **27**, 13983 (2011).

[213] P. A. Yuya, D. C. Hurley, J. A. Turner, Contact-resonance atomic force microscopy for viscoelasticity. *J. Appl. Phys.* **104**, 074916 (2008).

[214] A. Gannepalli, D. G. Yablon, A. H. Tsou, R. Proksch, Mapping nanoscale elasticity and dissipation using dual frequency contact resonance AFM (**22**, 355705 (2011)). *Nanotechnology* **24**, 159501 (2013).

[215] V. V. Shvartsman, W. Kleemann, R. Haumont, J. Kreisel, Large bulk polarization and regular domain structure in ceramic $BiFeO_3$. *Appl. Phys. Lett.* **90**, 172115 (2007).

[216] K. Yamanaka, S. Nakano, Quantitative elasticity evaluation by contact resonance in an atomic force microscope. *Appl. Phys. A-Mater.* **66**, S313 (1998).

[217] S. V. Kalinin, B. J. Rodriguez, S. Jesse, J. Shin, A. P. Baddorf, P. Gupta, H. Jain, D. B. Williams, A. Gruverman, Vector piezoresponse force microscopy. *Microsc. Microanal.* **12**, 206 (2006).

[218] A. P. Nievergelt, B. W. Erickson, N. Hosseini, J. D. Adams, G. E. Fantner, Studying biological membranes with extended range high-speed atomic force microscopy. *Sci. Rep.* **5**, 11987 (2015).

[219] D. C. Lupascu, S. Fedosov, C. Verdier, J. Rodel, H. von Seggern, Stretched exponential relaxation in perovskite ferroelectrics after cyclic loading. *J. Appl. Phys.* **95**, 1386−1390 (2004).

[220] V. V. Shvartsman, A. L. Kholkin, Spontaneous and induced surface piezoresponse in $PbMg_{1/3}Nb_{2/3}O_3$ single crystals. *Z. Kristallogr.* **226**, 108−112 (2011).

[221] C. S. Ganpule, V. Nagarajan, S. B. Ogale, A. L. Roytburd, E. D. Williams, R. Ramesh, Domain nucleation and relaxation kinetics in ferroelectric thin films. *Appl. Phys. Lett.* **77**, 3275−3277 (2000).

[222] C. S. Ganpule, A. L. Roytburd, V. Nagarajan, B. K. Hill, S. B. Ogale, E. D. Williams, R. Ramesh, J. F. Scott, Polarization relaxation kinetics and 180 degrees domain wall dynamics in ferroelectric thin films. *Phys. Rev. B* **65**, 014101 (2002).

[223] V. A. Stephanovich, M. D. Glinchuk, B. Hilczer, E. V. Kirichenko, Physical mechanisms responsible for the relaxation time distribution in disordered dielectrics. *Phys. Solid State* **44**, 946−952 (2002).

[224] D. Schrade, R. Mueller, B. Xu, D. Gross, Domain evolution in ferroelectric materials: a continuum phase field model and finite element implementation. *Comput. Method. Appl. M.* **196**, 4365−4374 (2007).

[225] B.-X. Xu, D. Schrade, R. Mueller, D. Gross, T. Granzow, J. Roedel, Phase field simulation and experimental investigation of the electro-mechanical behavior of ferroelectrics. *ZAMM-Z. Angew. Math. Me.* **90**, 623−632 (2010).

[226] P. Gao, J. Britson, J. R. Jokisaari, C. T. Nelson, S.-H. Baek, Y. Wang, C.-B. Eom, L.-Q. Chen, X. Pan, Atomic-scale mechanisms of ferroelastic domain-wall-mediated ferroelectric switching. *Nat. Commun.* **4**, 2791 (2013).

[227] S. Wang, M. Yi, B.-X. Xu, A phase-field model of relaxor ferroelectrics based on random field theory. *Int. J. Solids Struct.* **83**, 142−153 (2016).

[228] R. L. Taylor, *FEAP-finite element analysis program*, University of California, Berkeley 2014.

[229] K. Uchino, *Advanced piezoelectric materials*. USA, 2010.

[230] A. L. Kholkin, I. K. Bdikin, D. A. Kiselev, V. V. Shvartsman, S. H. Kim, Nanoscale characterization of polycrystalline ferroelectric materials for piezoelectric applications. *J. Electroceram.* **19**, 83−96 (2007).

# Cumulative Publications

Nanoscale

PAPER

View Article Online
View Journal | View Issue



Cite this: *Nanoscale*, 2015, **7**, 11787

# Visualization of polar nanoregions in lead-free relaxors *via* piezoresponse force microscopy in torsional dual AC resonance tracking mode†

Na Liu,[a,b] Robert Dittmer,[c] Robert W. Stark*[a,b] and Christian Dietz*[a,b]

Received 27th February 2015,
Accepted 15th June 2015

DOI: 10.1039/c5nr01326g

www.rsc.org/nanoscale

Polar nanoregions (PNRs) play a key role in the functionality of relaxor ferroelectrics; however, visualizing them in lead-free relaxor ferroelectrics with high lateral resolution is still challenging. Thus, we studied herein the local ferroelectric domain distribution of the lead-free bismuth-based $(1-x)(Bi_{1/2}Na_{1/2}TiO_3$–$Bi_{1/2}K_{1/2}TiO_3) - x(Bi_{1/2}Mg_{1/2}TiO_3)$ piezoceramics which show a relaxor behavior using dual AC resonance tracking (DART) piezoresponse force microscopy (PFM). By using excitation frequencies at either side of the contact resonance peak of the torsional cantilever vibration, an enhanced contrast in the amplitude and phase images of the piezoresponse can be achieved. Additionally, this tracking technique reduces the topographical crosstalk while mapping the local electromechanical properties. The true drive amplitude, drive phase, contact resonant frequency and quality factor can be estimated from DART-PFM data obtained with vertically or torsionally vibrating cantilevers. This procedure yields a three-dimensional quantitative map of the local piezoelectric properties of the relaxor ferroelectric samples. With this approach, torsional DART allowed for the visualization of fine substructures within the monodomains, suggesting the existence of PNRs in relaxor ferroelectrics. The domain structures of the PNRs were visualized with high precision, and the local electromechanical characteristics of the lead-free relaxor ferroelectrics were quantitatively mapped.

## Introduction

Piezoelectric ceramics are widely used in sensors, actuators, transducers and generators because of their excellent conversion efficiency.[1–3] Today, lead-zirconate-titanate ($Pb(Zr_xTi_{1-x})O_3$ or PZT) is the predominantly used piezoelectric ceramic,[1,3,4] however, lead oxide contaminates the environment and is harmful for human and animal health in general.[4] As enforced by European RoHS/WEEE regulations,[5–7] materials scientists have thus focused on the development of lead-free piezoceramics.[4,8,9] In particular, $Bi_{1/2}Na_{1/2}TiO_3$ (BNT)–$Bi_{1/2}K_{1/2}TiO_3$ (BKT)-based relaxor ferroelectrics have become promising candidates for replacing the PZT family because of their large macroscopic electric field-induced strain response.[4,10–12] The relaxor behavior of ferroelectrics is closely related to their nanoscale structural arrangement (polar nanoregions),[13] the characterization of which remains a challenge. To better understand the relationship between functionality and nanostructure, it is essential to functionally characterize the material with high lateral resolution in real space. To this end, we have developed an approach based on the dual ac resonance tracking (DART) mode[14] of piezoresponse force microscopy (PFM). By analyzing the torsional cantilever vibrations,[15,16] the reliability of the image of PFM can be enhanced, thus allowing for visualization of the local ferroelectric domain distribution of lead-free bismuth-based $(1-x)$(BNT–BKT) $- x(Bi_{1/2}Mg_{1/2}TiO_3)$ relaxor piezoceramics on the nanoscale.

In ferroelectrics, relaxor behavior features a strong frequency dispersion and a broad maximum in the temperature dependence of the dielectric permittivity and is thus characterized by a strong deviation from the Curie–Weiss law.[17,18] It was previously demonstrated that the macroscopically constitutive large-signal behavior of lead-free solid solutions, such as BNT–0.2BKT, could be greatly enhanced by the addition of a ternary compound.[4,19,20] For example, the incorporation of 2 mol% $BiZn_{1/2}Ti_{1/2}O_3$ (BZT) resulted in a high normalized strain of up to 500 pm $V^{-1}$.[11] It was hypothesized that the introduction of the mixed B-site was the underlying cause for the enhanced

[a]*Institute of Materials Science, Physics of Surfaces, Technische Universität Darmstadt, Alarich-Weiss-Str. 2, 64287 Darmstadt, Germany*
[b]*Center of Smart Interfaces, Technische Universität Darmstadt, Alarich-Weiss-Str. 10, 64287 Darmstadt, Germany. E-mail: stark@csi.tu-darmstadt.de, dietz@csi.tu-darmstadt.de*
[c]*Institute of Materials Science, Nichtmetallische-Anorganische Werkstoffe, Technische Universität Darmstadt, Alarich-Weiss-Str. 2, 64287 Darmstadt, Germany*
†Electronic supplementary information (ESI) available. See DOI: 10.1039/c5nr01326g

strain as a result of an improvement of the properties of relaxor ferroelectrics.[11] Introducing $Mg^{2+}$ ions into the lattice of BNT–BKT allowed for further study of the effect of mixed B-site occupation.[19,20] The origin of this large electromechanical response can be attributed to the phase transformation of this ceramic system from the relaxor to the ferroelectric state upon the application of a sufficiently large external electrical field.[1,21] By modifying the BNT–BKT system through solid solutions, either an ergodic relaxor state with a reversible electric field-induced phase transition at low temperatures or a non-ergodic relaxor state characterized by an irreversible phase transformation could be generated.[22–24] The presence and dynamics of short-range ordered polar nanoregions (PNRs)[22,25,26] with an estimated size of 5–10 nm[23,27] are claimed to be responsible for the extraordinary dielectric properties of relaxors, particularly their large strain response. The size, morphology, and dynamic response to an external electric stimulus of the PNRs in BNT–BKT-based relaxors systems, however, are still unclear and need to be studied in detail to understand their peculiar relaxor behavior.

PNRs can be analyzed by different experimental methods, *e.g.*, X-ray diffraction,[25] diffuse neutron scattering,[28,29] dielectric spectroscopy,[30,31] acoustic emission[32,33] and high resolution transmission electron microscopy.[34] However, these techniques do not provide a direct observation or the local identification of the virgin state of PNRs. In contrast, PFM can be applied to directly study the fundamental mechanisms behind the functionalities of relaxors at the micro- and nanometer scales.[23,27,35] The advantages of PFM over other techniques include high spatial resolution (few tens of nanometers), high sensitivity to the local polarization as a result of the direct tip-surface interaction mechanism, non-destructive character, and straightforward operation.[36–39] To successfully image the domain structure with PFM, an alternating electrical field (AC field) generated by the tip that is high enough to obtain a detectable response of the local ferroelectric domains but sufficiently low to avoid tip-induced local switching effects has been suggested.[38,39] The mechanical response to an electrical stimulus of the PNRs in lead-free relaxor ferroelectrics, however, is close to or below the detection limit of the PFM system.[23] The contact resonance technique using excitation frequencies at or close to the contact resonant frequency between the cantilever-tip ensemble and the sample surface has been developed to considerably improve the signal-to-noise ratio (SNR) of the amplitude and phase signals during imaging.[14,40–42] This approach allows for the detection of very small piezoresponse signals of lead-free relaxors as they originate, for example, from PNRs. Additionally, the local mechanical properties obtained *via* the contact resonance technique can also be studied quantitatively.[42–47]

The contact resonant frequency of the system strongly depends on the tip-surface contact mechanics, *i.e.*, rough samples and inhomogeneity of the mechanical properties of the sample surface can induce large variations.[39,40,42,43] As a consequence, the excitation frequency is far from the resonance and an enhanced SNR is not guaranteed. This crosstalk can be avoided by permanently tracking the instantaneous contact resonance between the tip and the sample surface. Based on this idea, the DART methodology, a multifrequency application,[48] has been developed to minimize crosstalk between the topography and the electromechanical signals.[49] In DART-PFM, a superposition of two oscillating signals at frequencies slightly below and slightly above the contact resonance is applied to the conductive cantilever. The cantilever response caused by the sample deformation is then detected. Two lock-in amplifiers analyze the respective oscillations and provide amplitude and phase signals with respect to each excitation signal. Maintaining the difference between the amplitudes at low and high frequencies through an additional feedback loop allows for tracking the instantaneous contact resonance at each tip position during scanning.

DART can improve the sensitivity of the measured piezoresponse signal and extract the local electromechanical properties more accurately with respect to the vertical vibration of the cantilever compared to the single frequency (SF) contact resonance mode in PFM.[14] The DART methodology can also be applied to detect the torsional vibration of the cantilever when in-plane polarizations cause a lateral movement of the tip. By combining the DART mode applied to the vertical cantilever vibration with the torsional oscillation in two orthogonal in-plane directions, complete three-dimensional information of the orientation polarization vector on a ferroelectric surface can be visualized with very high resolution and minimal topographical and mechanical crosstalk between the tip and the sample surface.

In this study, we developed a torsional DART-PFM (TDART) mode for detecting the in-plane components of the polarization of relaxor ferroelectric samples and compared the respective piezoresponse signals (amplitude and phase) with those obtained in the single frequency excitation mode. We demonstrated a higher SNR and reliability of the image of this technique for visualizing the domain features of relaxor ferroelectrics. The damped simple harmonic oscillator model (DSHO) facilitated the quantitative mapping of the local electromechanical properties of the relaxor ferroelectric in three dimensions.

## Experimental section

### PFM imaging

Measurements were performed in the single frequency and DART-PFM modes with a Cypher atomic force microscope (Asylum Research, Santa Barbara, USA). Conductive cantilevers, ASYELEC-02 and AC240TM (Asylum Research), with tip-coatings of Ti/Ir (5/20) and Ti/Pt (5/20) were used. The nominal spring constants for both types of cantilevers were 42 N $m^{-1}$ and 2 N $m^{-1}$ with a fundamental resonance frequency of the free tip-vibration (non-contact resonance) of approximately 300 kHz and 70 kHz, respectively. The contact resonant frequencies for the torsional motion of the tip were in the range of 1.8–2.0 MHz for the stiff and 630–650 kHz for the soft cantilever. The exact values depended on the local

 

tip-sample contact stiffness and the cantilever-tip properties. For the single frequency PFM measurements, a driving frequency approximately 4 kHz below the contact resonant frequency was chosen. To collect the data for the quantitative piezoresponse properties of the sample by DART-PFM in three dimensions, the vertical and torsional components were measured. After acquiring the image for the flexural vibration of the cantilever and the torsional vibration in one direction ($x$-direction), a subsequent physical 90° rotation around the $z$-axis of the sample was performed and the orthogonal component ($y$-direction) was recorded by rescanning the same area of interest. All of the PFM images were taken with a lateral resolution of 256 × 256 pixel. AC driving voltages of 2 V for the comparison experiments between single frequency and TDART-PFM modes and 2.5 V for the quantitative mapping experiments were applied to the tip while scanning perpendicular to the length of the cantilever with a tip velocity of 2.5 μm $s^{-1}$. All amplitude values are given in arbitrary units and normalized by the maximum amplitude range found within the cross-sectional profiles. For the DART-PFM measurements, the contact resonance ${f_0}^t$ was determined and the difference between the two excitation frequencies $f_{1,2}$ was set to $\Delta f$ = 8 kHz ($f_{1,2} = {f_0}^t \pm 4$ kHz). The frequency feedback loop thus tracked a constant amplitude difference. The frequency difference of 8 kHz was in the range of the imaging bandwidth, which is typically in the order of several kilohertz.[14] The P and I gains for the topography feedback loop and the scanning speed were optimized for a maximum overlap of the trace and retrace curves and to avoid ringing. To keep the measurements obtained in TDART method comparable to those in single frequency mode, we chose the same parameters for the topography feedback. The filter bandwidth of each lock-in amplifier was set to 5 kHz. The minimum detectable amplitude change of the lock-in amplifier can be roughly estimated to 60 μV for a 5 kHz bandwidth (see ESI, Fig. S1†). From the inverse slope (${S_1}^{-1} = \mathrm{d}f_1/\mathrm{d}A_1 \approx 2890$ Hz $mV^{-1}$) of the resonance peak of an ASYELEC-02 cantilever on the 3BMT sample surface at the detection point (point 1, see ESI, Fig. S2†), a minimum detectable frequency shift of $\mathrm{d}f_1 \approx$ 170 Hz was estimated. The same limit applies for the single frequency technique because the drive frequency was set to the same point of the resonance. The frequency sensitivity could be optimized further ($\mathrm{d}f_2 \approx 30$ Hz) by choosing the point with the largest slope (smallest inverse sensitivity, point 2, see ESI, Fig. S2†) at the expense of a less robust frequency feedback. The imaging resolution of PFM can be estimated from the width of the domain wall.[50] The domain wall width $W$ was estimated using the fitting formula[51]

$$X(x) = A\ \tanh(x/W) + B\ \arctan(x/W) \quad (1)$$

to the phase shift data obtained at the domain boundary using the analysis software Igor Pro v6.36 (WaveMetrics Inc., Lake Oswego, USA). Here, $A$ and $B$ are fitting parameters setting the height of the phase range. The topography images were first-order flattened to remove the tilt of the sample surface.

### Sample preparation

To demonstrate the imaging capability of this mode and quantitatively map the local three-dimensional piezoelectric properties, we used two compositions of lead-free piezoceramic samples, $0.81Bi_{1/2}Na_{1/2}TiO_3$–$0.19Bi_{1/2}K_{1/2}TiO_3$ and $0.97(0.81Bi_{1/2}Na_{1/2}TiO_3$–$0.19Bi_{1/2}K_{1/2}TiO_3)$–$0.03BiMg_{1/2}Ti_{1/2}O_3$, which are hereafter referred to as 0BMT and 3BMT, respectively. Both samples were classified as relaxors because of their macroscopic properties (see ESI, Fig. S3 and S4†). To produce these two samples following the mixed oxide route, oxides and carbonates of the respective elements (all from Alfa Aesar GmbH & Co. KG, Karlsruhe, Germany) were used to synthesize the abovementioned compositions. The reagent grade raw materials MgO (99.0%), $Bi_2O_3$ (99.975%), $Na_2CO_3$ (99.5%), $TiO_2$ (99.9%) and $K_2CO_3$ (99.0%) were mixed according to the stoichiometric formula and milled with zirconia balls in ethanol for 24 h at 250 rpm using a planetary mill (Fritsch Pulverisette 5, Idar-Oberstein, Germany). Subsequently, the slurry was dried at 100 °C and the resulting powder was calcined for 3 h at 900 °C in covered alumina crucibles. After another milling step of 24 h, the pestled and sieved powders were shaped by manual uniaxial pressing into pellets of 10 mm in diameter. Then, the green bodies were further compacted by hydrostatic pressure of 300 MPa. Sintering was performed with a ramp rate of 10 K $min^{-1}$ at 1100 °C for 3 h in covered alumina crucibles. To minimize the loss of volatile elements, samples were covered with an atmospheric powder of the same composition. For the PFM observations, the sintered samples were ground down to approximately 250 μm and subsequently polished using polycrystalline diamond paste with abrasive particles of 15 μm, 6 μm, 3 μm, 1 μm and 0.25 μm (DP-Paste P by Struers A/S, Ballerup, Denmark) for 1 h each. The finishing was performed in a final polishing step of 15 min with a colloidal silica polishing suspension (Buehler Mastermet by Buehler GmbH, Düsseldorf, Germany). The ferroelectric standard PIC 151 (lead-zirconate-titanate, PZT) was purchased from PI Ceramic GmbH (Lederhose, Germany) and was measured as is, *i.e.* in the initial state of the ferroelectric domain structure.

### Macroscopic measurements and sample characterization

For the electrical measurements, the sintered pellets were ground, polished and painted with silver paste, which was burned in at 400 °C. The temperature-dependent relative permittivity, $\varepsilon_r$, and loss factor, $\tan\delta$, were determined with an LCR-meter HP 4284A (Hewlett-Packard Co., Palo Alto, CA, USA) at a heating rate of 2 K $min^{-1}$ at 0.1 kHz, 1 kHz, 10 kHz, 100 kHz and 1000 kHz using a Nabertherm LE4/11/R6 box furnace (Nabertherm GmbH, Lilienthal, Germany) with a custom-made sample holder. The permittivity was obtained for samples that were previously poled for 1 min under an electric field of 6 kV $mm^{-1}$ at room temperature. Samples for the X-ray diffraction (XRD) studies were poled at room temperature under an electric field of 6 kV $mm^{-1}$. The XRD measurements were performed in theta-2-theta geometry using a Bruker D8 (Bruker Corp., Billerica, MA, USA). The XRD patterns con-

firmed a perovskite structure for both materials (see ESI, Fig. S3†). There are no indications of an undesirable non-perovskite phase. It is apparent from the asymmetry of the $\{111\}_c$ and the $\{200\}_c$ reflections that both compositions possess a significant non-cubic distortion in their poled states. In this respect, the materials share similarities with BNT–BKT–BZT, which is pseudocubic in the virgin state but develops a tetragonal and rhombohedral phase mixture upon application of a sufficiently large electric field.[11] The dielectric properties were measured as a function of temperature at frequencies of 0.1 kHz, 1 kHz, 10 kHz, 100 kHz and 1000 kHz for both materials in their poled states (see ESI, Fig. S4†). Both compositions exhibit remarkable frequency dispersion characteristics of the permittivity and loss tangent factor, tan $\delta$, with temperature. This result indicates that both compositions have a strong relaxor character. It is apparent from the peak in the temperature dependency of the loss tangent factor that 0BMT has a comparably high depolarization temperature, $T_d$, of approximately 100 °C. By contrast, 3BMT does not provide any indication of a peak, *i.e.*, no depolarization in the examined temperature range from room temperature to 400 °C. It was demonstrated that the introduction of aliovalent B-site ions significantly lowered the $T_d$ of the various BNT-based solid solutions.[52] This evolution is often rationalized by the enhancement of the quenched random fields that impede the formation of a stable long-range order upon poling.

## Methodology

**Dual AC resonance tracking in the torsional vibration mode.** The basic principle of dual AC resonance tracking (DART)[14] piezoresponse force microscopy (PFM) is illustrated in Fig. 1a. A dual frequency electrical signal with two sinusoidal waves of frequencies $f_1$ and $f_2$ close to each other is applied to a conductive cantilever that is brought into contact with the ferroelectric sample surface. The resulting cantilever deflection caused by the electromechanical coupling between the tip and the piezoelectric sample surface is recorded by a photoelectric diode through a laser reflected on the backside of the cantilever. The generated signal is analyzed by two lock-in amplifiers, providing the amplitudes $A_1$ and $A_2$ and the phase shifts $\varphi_1$ and $\varphi_2$ at the two excitation frequencies, respectively. To track the instantaneous contact resonant frequency during scanning, the difference between the two amplitude responses, $\Delta A = A_1 - A_2$, is taken as an error signal for the feedback loop. The principle of the contact resonance tracking is illustrated in Fig. 1b. The two excitation frequencies, $f_1$ and $f_2$, are chosen on either side of the tip-sample contact resonant frequency, $f_0$, with the corresponding initial amplitudes, $A_1(f_1)$ and $A_2(f_2)$, resulting in a constant difference of $\Delta A = A_1(f_1) - A_2(f_2)$. When the contact resonance shifts during imaging from $f_0$ (solid line) to a smaller value $f_0'$ (dashed line) because of a change in the mechanical coupling between the tip and sample surface, the amplitude $A_1$ increases to $A_1'$, whereas the amplitude $A_2$ decreases to $A_2'$. In the case of a positive shift of the contact resonant frequency, the change of the amplitudes is reversed. Tracking of the contact resonance by a feedback loop is realized by maintaining the amplitude difference $\Delta A$ at a constant value, through variation of the driving frequencies, $f_1$ and $f_2$. Thus far, the DART-PFM mode has been reported in the literature for flexural vibrations of the cantilever.[14,49] We herein suggest applying this method to torsional vibrations of the cantilever as well. This torsional DART-PFM mode can be used to characterize domains with an in-plane polarization complementary to conventional DART.

**Damped simple harmonic oscillator (DSHO) model.** The tip-sample contact mechanics can be modeled as decoupled damped simple harmonic oscillators as shown in Fig. 2, where a Newtonian damper and a Hookean elastic spring are connected in parallel. The sample surface motion, induced by the dual AC excitation, is characterized by the drive amplitude ($A_{dr,i}$) and drive phase ($\varphi_{dr,i}$) in each direction $i \in \{x, y, z\}$. Each direction features a contact resonant frequency, $f_{0,i}$, as a result of the elastic energy and a quality factor, $Q_i$, representing the energy loss of the respective system. This sample motion in turn drives the tip-cantilever system and results in the measured amplitudes $A_{1,i}$ and $A_{2,i}$ and the phase shifts $\varphi_{1,i}$ and $\varphi_{2,i}$ at the excitation frequencies $f_{1,i}$ and $f_{2,i}$, respectively. The four unknown parameters, $A_{dr,i}$, $\varphi_{dr,i}$, $f_{0,i}$ and $Q_i$, described by the DSHO model contain complete information regarding the local piezoelectric coefficient of the ferroelectric sample, the local polarization orientation, and the conservative and dissipative nature of the tip-sample contact. Calculating these parameters in the *x*-, *y*- and *z*-directions from the corresponding amplitudes $A_{1,i}$, $A_{2,i}$ and phase $\varphi_{1,i}$, $\varphi_{2,i}$ allows for the quantitative mapping of the local electromechanical properties of the ferroelectric material.[14,45,53]

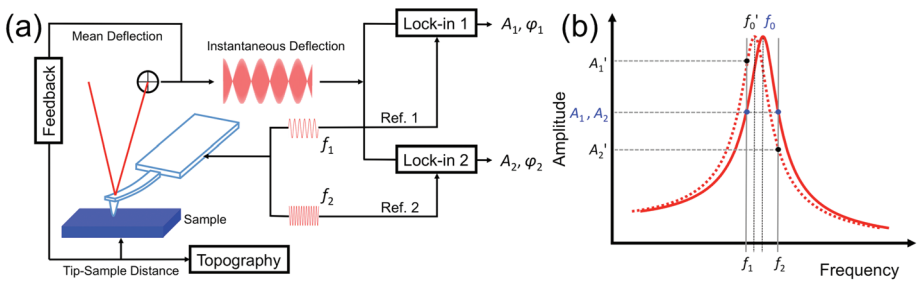


**Fig. 1** Principle of dual AC resonance tracking piezoresponse force microscopy. (a) Scheme and (b) contact resonant frequency tracking principle.

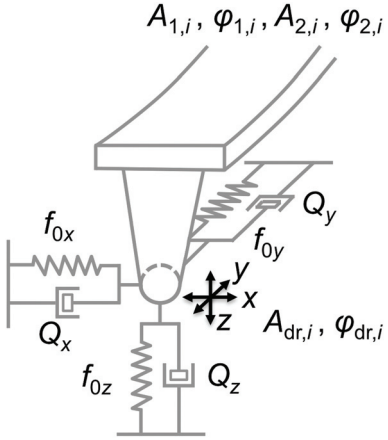


Fig. 2 Simplified model of the cantilever tip-sample contact mechanics as independent damped simple harmonic oscillators in three dimensions. In the scheme, "*i*" represents the space direction in either *x*, *y* or *z*.

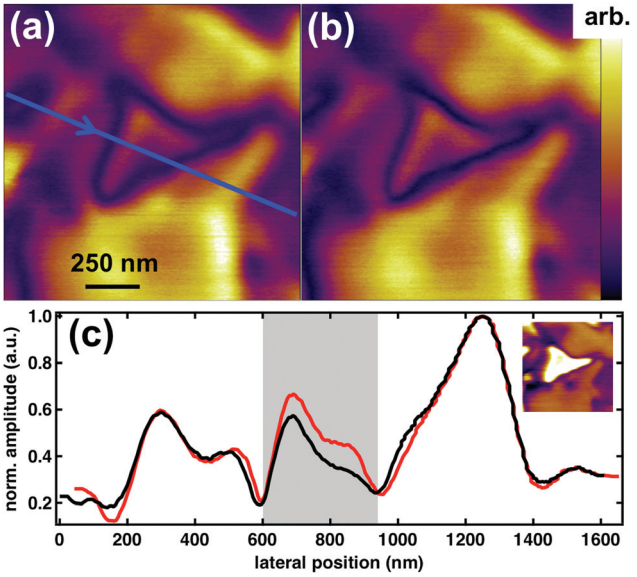


Fig. 3 Comparison of the piezoresponse amplitude images of the relaxor, 0BMT, measured by (a) SF-PFM and (b) TDART-PFM. (c) Cross-sectional profiles drawn along the blue line in (a). The black and red lines correspond to the normalized amplitude response measured by SF- and TDART-PFM, respectively. The region highlighted in gray indicates the extension of the center domain in this particular direction. The inset shows the corresponding contact resonant frequency image (color bar: 637–640 kHz).

**Calculation of the DSHO model parameters: $A_{dr,i}$, $\varphi_{dr,i}$, $f_{0,i}$ and $Q_i$.** The four parameters, $A_{dr,i}$, $\varphi_{dr,i}$, $f_{0,i}$ and $Q_i$, in the *x*-, *y*- and *z*-directions need to be calculated to fully describe the DSHO model. These parameters can be expressed by:[14,54]

$$f_{0,i} = \sqrt{f_{1,i} f_{2,i} \frac{f_{2,i}X_{1,i} - f_{1,i}X_{2,i}}{f_{1,i}X_{1,i} - f_{2,i}X_{2,i}}}, \quad (2)$$

$$Q_i = \frac{\sqrt{f_{1,i} f_{2,i} (f_{2,i}X_{1,i} - f_{1,i}X_{2,i})(f_{1,i}X_{1,i} - f_{2,i}X_{2,i})}}{{f_{2,i}}^2 - {f_{1,i}}^2}, \quad (3)$$

$$A_{dr,i} = A_{1,i} \frac{\sqrt{\left({f_{0,i}}^2 - {f_{1,i}}^2\right)^2 + \left(f_{0,i} f_{1,i}/Q_i\right)^2}}{{f_{0,i}}^2}, \quad (4)$$

$$\varphi_{dr,i} = \varphi_{1,i} - \tan^{-1}\left(\frac{f_{0,i} f_{1,i}}{Q_i\left({f_{0,i}}^2 - {f_{1,i}}^2\right)}\right), \quad (5)$$

with $X_{j,i} \equiv Q_i({f_{0,i}}^2 - {f_{j,i}}^2)/f_{0,i} f_{j,i}$. The amplitudes ($A_{1,i}$, $A_{2,i}$) and phases ($\varphi_{1,i}$, $\varphi_{2,i}$) at the corresponding driving frequencies $f_{1,i}$ and $f_{2,i}$ can be obtained by DART-PFM in the vertical (*z*-direction) and torsional vibration (*x*- and *y*-directions) of the cantilever to calculate the parameters of the DSHO model. Because the difference between the two excited frequencies, $\Delta f_i = f_{2,i} - f_{1,i}$, is always constant, only one frequency (typically $f_{1,i}$) is needed. To obtain the precise results, a restricted condition of $\varphi_{2,i} > \varphi_{1,i}$ is required for $f_{2,i} > f_{1,i}$.[45]

## Results and discussion

### Increased reliability of the image and reduced topographical crosstalk by TDART-PFM

We compared the single frequency mode in the lateral vibration of the cantilever with the TDART-PFM mode on the relaxor ferroelectric sample, 0BMT, with respect to the amplitude (Fig. 3) and phase piezoresponse (see ESI, Fig. S5†). The amplitude image is a measure of the magnitude of the local electromechanical response, whereas the phase image provides a map of the domain orientation below the tip in the corresponding sample direction. A clear lateral domain contrast is visible by the two PFM modes in these figures. Fig. 3 shows the piezoresponse amplitude signals measured by SF- (a) and TDART- (b) PFM, both depicting a triangle-shaped domain in the center of the images. By drawing the cross-sectional profiles (Fig. 3c) at the position as indicated by the blue line in Fig. 3a, the different domains, including the domain walls, become visible and a comparison between the two modes can be made. Remarkably, the cross-sectional profile of the amplitude response within the triangle-shaped domain region, highlighted in gray, shows an amplitude value for the TDART mode (red line) approximately 24%, on average, higher than that of the SF technique (black line), though both profiles coincide in the outer regions. Additionally, at the domain walls, the slope of the red curve obtained by TDART-PFM is greater than that of the black line (SF-PFM). The higher amplitude value determined in the central domain is a consequence of the increase of the contact resonant frequency (change from 638 kHz to 641 kHz, see inset Fig. 3c), which leads to a smaller amplitude at the corresponding excitation frequency in the SF mode. The TDART technique, however, tracks the instantaneous contact resonance, hence, always amplifies the piezoresponse signal by the same amount giving a better reliability of the image. The reduced width of the domain wall itself implies a greater

lateral resolution obtained by TDART-PFM compared to the SF-PFM technique. To quantify the lateral resolution for both modes, we used an approach suggested by Jungk *et al.*[51] We fitted eqn (1) to the cross-sectional phase profiles in order to extract the full width at half maximum $W$ as a measure for the domain wall width (right side of the peaks, see ESI, Fig. S5†). We obtained a domain wall width of (38 ± 3) nm for the TDART-PFM and (42 ± 2) nm for the SF technique, corroborating the above-mentioned assumption. Additionally, TDART-PFM clearly reduces crosstalk originated by topographical features when a bump or hollow causes a major shift in the contact resonant frequency (blue highlighted regions, see ESI, Fig. S5†). TDART-PFM performed on a piezoelectric standard PIC 151 (PZT) revealed small features in the amplitude image that could not be resolved by the SF-PFM (*cf.* ESI, Fig. S6†) whereas the corresponding phase images exhibited the same lateral distribution of ferroelectric in-plane domains.

### Quantitative mechanical surface properties and three-dimensional visualization

The combination of TDART and vertical DART (VDART) enables three-dimensional visualization of the local piezoresponse of the 3BMT sample. Gannepalli *et al.* developed a routine to transfer the observables provided by DART-PFM into quantitative information of the local mechanical sample properties.[14,54] We applied eqn (2)–(5) to calculate the DSHO model parameters for the tip-sample contact based on the experimental results of the VDART and TDART for the 3BMT sample, leading to the local mechanical and piezoresponse properties in all three spatial directions (Fig. 4). Fig. 4a shows the topographical image of the sample surface. The sample exhibits holes on the surface that are 150–200 nm in diameter and several nanometers (1–4 nm) in depth. Maps of the calculated DSHO model parameters for the drive amplitude, drive phase, quality factor and contact resonant frequency in the $z$-, $x$- and $y$-directions are given in Fig. 4(b)–(e) for $A_{\mathrm{dr},z}$, $\varphi_{\mathrm{dr},z}$, $Q_z$, and $f_{0,z}$; Fig. 4(f)–(i) for $A_{\mathrm{dr},x}$, $\varphi_{\mathrm{dr},x}$, $Q_x$, and $f_{0,x}$; and Fig. 4(j)–(m) for $A_{\mathrm{dr},y}$, $\varphi_{\mathrm{dr},y}$, $Q_y$, and $f_{0,y}$. Dashed lines highlight the potential domain walls at the sample surface where the associated strength of the piezoresponse signal is weak in these areas. In most portions of the imaged area, however, the requirements of the DSHO model are fulfilled. The true drive phases $\varphi_{\mathrm{dr},x}$ and $\varphi_{\mathrm{dr},y}$ of the 3BMT sample reveal a clear phase contrast between the ferroelectric domains in both $x$- and $y$-torsional components, suggesting differently orientated domains (Fig. 4(g) and (k)), whereas a weak vertical polarization is apparent in Fig. 4c. This implies that the out-of-plane component of the piezoresponse is less pronounced than the associated in-plane components of the same domains.

The images of the drive amplitudes $A_{\mathrm{dr},x}$ and $A_{\mathrm{dr},y}$ (Fig. 4(f) and (j)) represent the local lateral piezoresponse coefficients. In particular, the $A_{\mathrm{dr},x}$ image taken in the $x$-direction reveals extremely fine domain features compared to the vertical amplitude response (Fig. 4b). This observation can be ascribed to two contributions: (1) the strong and permanent mechanical contact between the tip and sample that is better for lateral

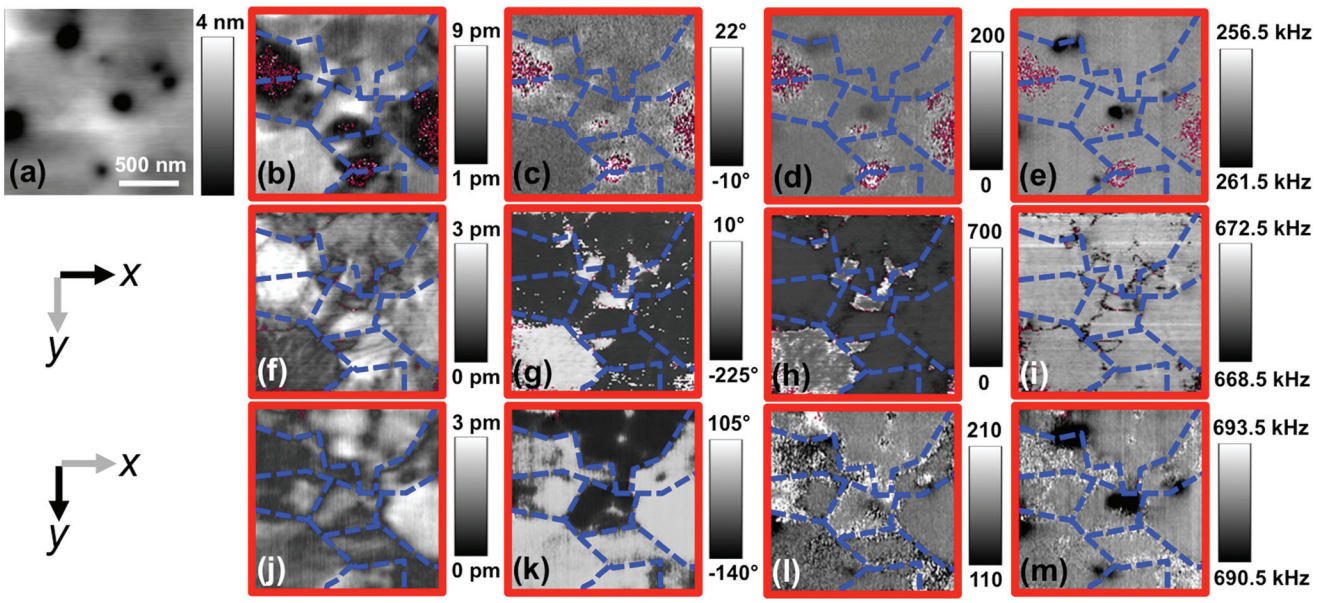


**Fig. 4** Mechanical sample properties quantified by the decoupled damped simple harmonic oscillator model in three dimensions. (a) Topography and (b–m) calculated DSHO model parameters in the $x$-, $y$- and $z$-directions calculated by transforming the data obtained by vertical and torsional dual AC resonance tracking. (b), (c), (d), and (e) represent the drive amplitude ($A_{\mathrm{dr},z}$), drive phase ($\varphi_{\mathrm{dr},z}$), the quality factor ($Q_z$) and contact resonant frequency ($f_{0,z}$) in the $z$-direction, respectively. Accordingly, (f), (g), (h), (i) represent $A_{\mathrm{dr},x}$, $\varphi_{\mathrm{dr},x}$, $Q_x$, $f_{0,x}$, in the $x$-direction and (j), (k), (l), (m) correspond to $A_{\mathrm{dr},y}$, $\varphi_{\mathrm{dr},y}$, $Q_y$, $f_{0,y}$ in the $y$-direction. Dashed lines indicate the domain walls for better comparison of the images. The red dots indicate invalid pixels where the model assumption $\varphi_{2,i} > \varphi_{1,i}$ was not fulfilled.[14]

 

rather than vertical vibrations; and (2) the large in-plane piezoelectric coefficients of the sample.[55] The true local contact resonant frequencies, $f_{0,i}$, that mainly depend on the tip-surface contact stiffness,[14,47,54] are visualized in the maps of Fig. 4(e), (i) and (m) for the *z*-, *x*- and *y*-directions, respectively. The resonant frequencies $f_{0,y}$ and $f_{0,z}$ show the structures that are related to the topography, whereas $f_{0,x}$ exhibits features that are connected to those obtained in the driving amplitude image (Fig. 4f) in the sample direction.

We also observed a difference in the contact resonant frequency between the *x*- and *y*-torsional directions of approximately 20 kHz (*cp.* Fig. 4(i) and (m)). Differences in the tip-sample contact mechanics because of discrepancies in the sample coupling conditions in the three spatial directions cause this deviation. In addition, Fig. 4(d), (h) and (l) map the calculated *Q*-factor in the *z*-, *x*- and *y*-directions, respectively, as the damping of the tip-sample system. The damping in the *z*- and *y*-directions is uniform ($Q_z \approx 100$ and $Q_y \approx 150$), whereas in the *x*-direction a clear contrast is observed ($Q_x \approx$ 170–400). This result is another indication that the mechanical coupling between the tip and the sample and/or the mechanical surface properties itself varies in the distinctive sample directions; therefore, a three-dimensional characterization technique is necessary to fully describe the local electromechanical properties of the sample surface.

The quantified data obtained in all three dimensions can be represented in single maps (Fig. 5) using a similar approach as Kalinin *et al.*[56] Fig. 5a shows the local distribution of the true drive amplitude, $A_{\mathrm{dr},i}$; Fig. 5b shows the drive phase, $\varphi_{\mathrm{dr},i}$; Fig. 5c shows the quality factor, $Q_i$; and Fig. 5d shows the contact resonant frequency, $f_{0,i}$, in the vertical direction. The blue dashed lines in the images highlight differently oriented domains. Arrows pointing to the left and up refer to negative drive phase values in the *x*- and *y*-directions. The strength of the respective signal for the *x*- and *y*-directions is encoded in the gray scale color inside the arrows. The color-coded arrows provide the complimentary information for the three-dimensional visualization of the quantitative sample properties. This data representation allows the observer to conveniently get an overview of the electromechanical properties in three dimensions at a glance, avoiding the necessity of elaborate three-dimensional visualization.

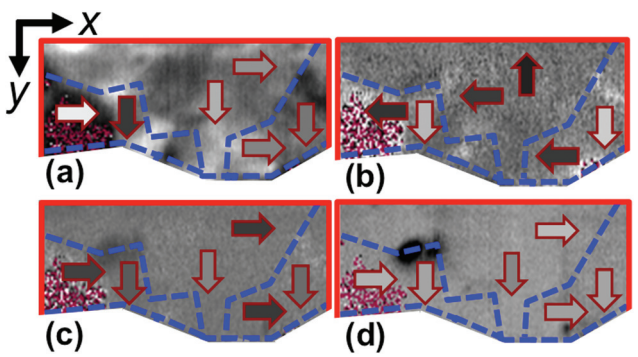


**Fig. 5** Visualization of the calculated DSHO model parameters obtained by DART accomplished in three spatial directions. (a) Drive amplitude ($A_{\mathrm{dr},i}$), (b) drive phase ($\varphi_{\mathrm{dr},i}$), (c) quality factor ($Q_i$), and (d) contact resonant frequency ($f_{0,i}$) based on the data of Fig. 4 (upper portion). Dashed lines indicate the domain walls of the different ferroelectric domains. The arrows point out the orientation of the respective parameter of each domain and the gray scale value encodes the strength for the *x*- and *y*-directions. The color bar is the same as in Fig. 4. The red dots in these images indicate invalid pixels.

## Detection of polar nanoregions

Using TDART-PFM, we also observed an improved lateral resolution of the in-plane orientation of the ferroelectric domains on different relaxors, *e.g.*, 3BMT that possesses a higher electric field-induced strain compared to 0BMT. Fig. 6 shows the topographical image (Fig. 6a) and the local distribution of the in-plane domain orientation at the sample surface measured by SF-PFM (Fig. 6(b) and (c)) and TDART-PFM (Fig. 6(e) and (f)), as well as a map of the driving frequency $f_1$ (Fig. 6d). The amplitude (Fig. 6(b) and (e)) and phase images (Fig. 6(c) and (f)) reveal the absence of a long-range ordered ferroelectric domain structure that would be typical for classical ferroelectric systems. Instead, polar clusters with a minimum size of a few tens of nanometers were detected. Comparing the phase images of both techniques, we observed an enhanced phase contrast in the case of TDART-PFM (Fig. 6f) compared to the SF-PFM technique (Fig. 6c). The phase image measured using the TDART technique shows a clear distribution of the ferroelectric domains with a sharp transition at the interphase between different domain orientations. The image contrast reveals that the phase signal appropriately follows the domain distribution with a constant phase value for each state, hence, it can be reliably considered for visualizing solely the domain orientation. In contrast, the phase image obtained by SF-PFM exhibits features within single domains most probably generated by crosstalk between the amplitude and phase channels, caused by noise or topography. This effect becomes particularly apparent as the white dots in Fig. 6(c).

Additionally, we found more distinctive features in the TDART-PFM amplitude signal with sharply defined boundary. This observation becomes highly apparent when focusing on the blue-framed area in Fig. 6. A magnified area of this region is displayed for both SF-PFM (Fig. 7a) and TDART-PFM (Fig. 7b). Only the TDART-PFM technique reveals features that are considerably smaller than hundreds of nanometers. Fig. 7c compares the cross-sectional profiles obtained using both techniques (SF-PFM – black line; TDART-PFM – red line) for the entire distance drawn along the gray line indicated in Fig. 6b. The two profiles depict similar tendencies except in the region of the enlarged area highlighted by the gray box. In this region, the profile measured by TDART-PFM shows peaks invisible in the black line obtained by SF-PFM, which corroborates the visual impression of a higher contrast apparent in Fig. 7b. In principle, noise and feedback lagging or ringing might cause very tiny features in the amplitude and phase images that can be misinterpreted as PNRs. To corroborate the

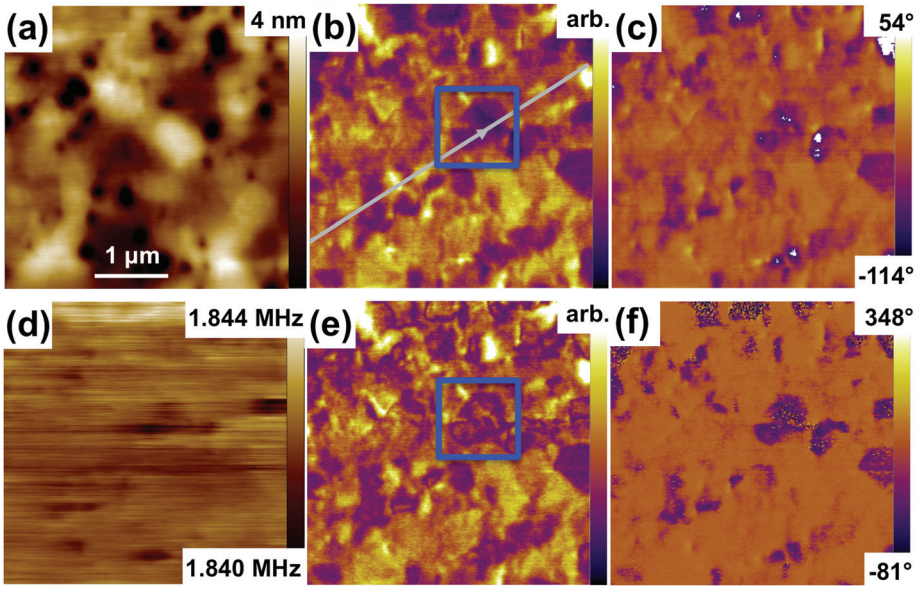


**Fig. 6** Comparison between the piezoresponse amplitude and phase images of a 3BMT ferroelectric sample measured by SF-PFM (upper row) and TDART-PFM (lower row). (a) Respective sample topography. (b) Amplitude and (c) phase response images obtained by SF-PFM. (e) Amplitude and (f) phase response measured by TDART-PFM. (d) Map of the driving frequency $f_1$ (below the contact resonance) in TDART-PFM. (e) The area within the blue rectangular frame exhibits a fine domain structure for TDART-PFM with additional features visible compared to the single frequency technique (b). This fine structure can be explained by polar nanoregions.

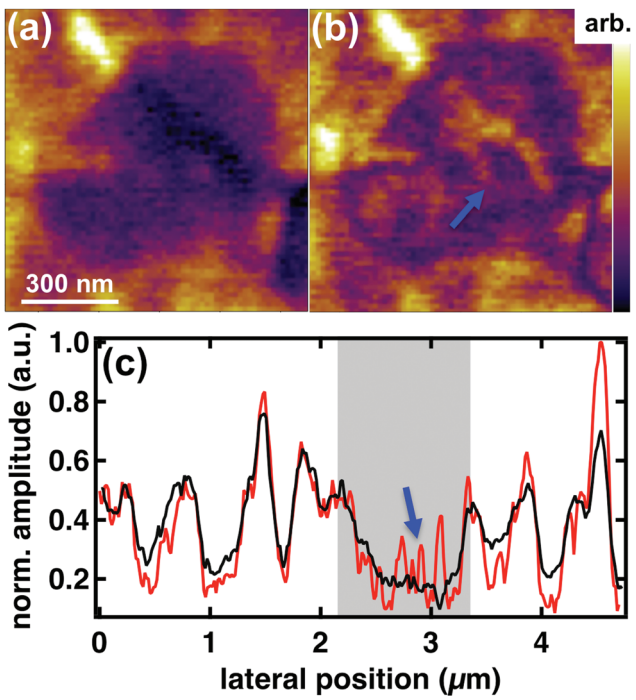


**Fig. 7** Visualization of polar nanoregions. Enlarged areas of the region marked with a blue frame in the amplitude images of Fig. 6 for (a) SF-PFM and (b) TDART-PFM. (c) Respective cross-sectional profiles along the gray line indicated in Fig. 6 for SF-PFM (black line) and TDART-PFM (red line). The gray box highlights the nanostructured region (arrow) in (b), which can be interpreted as the signature of polar nanoregions. The size of these regions is approximately 50 nm.

detectability of PNRs by TDART, we focused on nanoscale features prevailing in the amplitude images. These features were repeatedly scanned at scan angles parallel and perpendicular to the cantilever axis (see ESI, Fig. S7†). The shape and structure of the same nanoscale features irrespective of the scan direction and their existence after repeated scans demonstrate that noise or feedback induced artifacts as origin of such features can be excluded. Furthermore, the similar trends of the cross-sectional profiles in Fig. 7c outside the region highlighted in gray indicate that the noise level was similar for both imaging techniques. Analyzing the width of the peaks within the gray area in the profile through the full width at half maximum, we measured a domain size of approximately 50 nm (marked by a blue arrow). We thus interpreted these tiny structures as the signatures of PNRs, which are difficult to visualize with other microscopic techniques.

## Conclusions

In summary, we applied a DART technique to the torsional contact resonance of the cantilever. Piezoresponse imaging in this mode resulted in an enhanced contrast of the piezoresponse amplitude and phase signals as well as a reduced interference with topographical features. For DART, we exerted a superimposed electrical driving field to the piezoelectric domains with two distinctive frequencies close to the contact resonance (one below and one above), allowing for instantaneous tracking of the true contact resonant frequency. Fine domain features in the range of a few tens of nanometers were observed by TDART, which can be interpreted as the PNRs of

the lead-free relaxor ferroelectric. These PNRs are correlated to the macroscopic peculiarities of relaxors, such as the large electric field-induced strain. Hence, TDART can contribute to a better understanding of the complex interplay between the macroscopic functionality and the nanoscopic piezoelectric properties of lead-free relaxors. To acquire the local electromechanical properties of the relaxor ferroelectric in three dimensions, we first measured the piezoresponse of the sample in the *x*-direction, rotated it by 90° to obtain the data in the *y*-direction and subsequently imaged the out-of-plane component at the same spot on the surface. Simplifying the tip-sample surface contact mechanics with a decoupled, damped simple harmonic oscillator model, we calculated four important tip-sample characteristic parameters, such as the true drive phase and amplitude, the instantaneous contact resonant frequency and the quality factor representative for the damping of the tip-sample system. We suggested a straightforward data representation of the obtained three-dimensional dataset where we combine all values into one single gray-scale image (*z*-direction) for each parameter by including two arrows with the distinctive color for the *x*- and *y*-directions within each domain. The results showed that the electromechanical sample properties differ remarkably between the spatial directions. The three-dimensional DART-PFM enabled the visualization of the spatial orientation of PNRs in the relaxor ferroelectric.

## Acknowledgements

The authors gratefully acknowledge Florian Johann from Asylum Research (Oxford Instruments GmbH) for fruitful discussions. We also thank the Center of Smart Interfaces for financial support. Robert Dittmer thanks the SFB 595 for financial support.

## References

1 W. Jo, R. Dittmer, M. Acosta, J. D. Zang, C. Groh, E. Sapper, K. Wang and J. Rodel, *J. Electroceram.*, 2012, **29**, 71–93.
2 B. Jaffe, W. R. Cook and H. Jaffe, *Piezoelectric Ceramics*, Academic, London, 1971.
3 J. M. Herbert, *Ferroelectric Transducers and Sensors*, Gordon and Breach Science, New York, 1982.
4 J. Rodel, W. Jo, K. T. P. Seifert, E. M. Anton, T. Granzow and D. Damjanovic, *J. Am. Ceram. Soc.*, 2009, **92**, 1153.
5 "Eu-Directive 2002/95/Ec: Restriction of the use of certain hazardous sbustances in electrical and electronic equipment (RoHS)," *Off. J. Eur. Union*, 2003, L37, 19–23.
6 "Eu-Directive 2011/65/Eu: Restriction of the use of certain hazardous substances in electrical and electronic equipment (RoHS)," *Off. J. Eur. Union*, 2011, L174, 88–110.
7 "Directive 2012/19/EU of the european pariliament and of the council of 4 July 2012 on waste electrical and electronic euipment (WEEE)," *Off. J. Eur. Union*, 2012, L197, 38–71.
8 Y. Saito, H. Takao, T. Tani, T. Nonoyama, K. Takatori, T. Homma, T. Nagaya and M. Nakamura, *Nature*, 2004, **432**, 84.
9 T. R. Shrout and S. J. Zhang, *J. Electroceram.*, 2007, **19**, 113.
10 K. Yoshii, Y. Hiruma, H. Nagata and T. Takenaka, *Jpn. J. Appl. Phys., Part 1*, 2006, **45**, 4493.
11 R. Dittmer, W. Jo, J. Daniels, S. Schaab and J. Rodel, *J. Am. Ceram. Soc.*, 2011, **94**, 4283.
12 S. C. Zhao, G. R. Li, A. L. Ding, T. B. Wang and Q. R. Yin, *J. Phys. D: Appl. Phys.*, 2006, **39**, 2277.
13 W. W. Ge, C. T. Luo, C. P. Devreugd, Q. H. Zhang, Y. Ren, J. F. Li, H. S. Luo and D. Viehland, *Appl. Phys. Lett.*, 2013, **103**, 241914.
14 A. Gannepalli, D. G. Yablon, A. H. Tsou and R. Proksch, *Nanotechnology*, 2011, **22**, 355705.
15 O. Sahin, S. Magonov, C. Su, C. F. Quate and O. Solgaard, *Nat. Nanotechnol.*, 2007, **2**, 507–514.
16 A. Yurtsever, A. M. Gigler, C. Dietz and R. W. Stark, *Appl. Phys. Lett.*, 2008, **92**, 143103.
17 L. E. Cross, *Ferroelectrics*, 1987, **76**, 241.
18 G. A. Samara, *J. Phys.: Condens. Matter*, 2003, **15**, R367.
19 N. Kumar, T. Y. Ansell and D. P. Cann, *J. Appl. Phys.*, 2014, **115**, 154104.
20 A. Ullah, C. W. Ahn, A. Ullah and I. W. Kim, *Appl. Phys. Lett.*, 2013, **103**, 022906.
21 W. Jo, T. Granzow, E. Aulbach, J. Roedel and D. Damjanovic, *J. Appl. Phys.*, 2009, **105**, 094102.
22 R. Dittmer, D. Gobeljic, W. Jo, V. V. Shvartsman, D. C. Lupascu, J. L. Jones and J. Roedel, *J. Appl. Phys.*, 2014, **115**, 084111.
23 R. Dittmer, W. Jo, J. Rodel, S. Kalinin and N. Balke, *Adv. Funct. Mater.*, 2012, **22**, 4208.
24 B. Dkhil and J. M. Kiat, *J. Appl. Phys.*, 2001, **90**, 4676.
25 W. Jo, S. Schaab, E. Sapper, L. A. Schmitt, H.-J. Kleebe, A. J. Bell and J. Roedel, *J. Appl. Phys.*, 2011, **110**, 074106.
26 S. Prosandeev, D. Wang, A. R. Akbarzadeh, B. Dkhil and L. Bellaiche, *Phys. Rev. Lett.*, 2013, **110**, 207601.
27 V. V. Shvartsman and A. L. Kholkin, *Phys. Rev. B: Condens. Matter*, 2004, **69**, 014102.
28 K. Hirota, S. Wakimoto and D. E. Cox, *J. Phys. Soc. Jpn.*, 2006, **75**, 111006.
29 G. Y. Xu, G. Shirane, J. R. D. Copley and P. M. Gehring, *Phys. Rev. B: Condens. Matter*, 2004, **69**, 064112.
30 A. A. Bokov and Z. G. Ye, *J. Mater. Sci.*, 2006, **41**, 31–52.
31 D. Viehland, S. J. Jang, L. E. Cross and M. Wuttig, *J. Appl. Phys.*, 1990, **68**, 2916.
32 E. Dul'kin, E. Mojaev, M. Roth, I. P. Raevski and S. A. Prosandeev, *Appl. Phys. Lett.*, 2009, **94**, 252904.
33 B. Dkhil, P. Gemeiner, A. Al-Barakaty, L. Bellaiche, E. Dul'kin, E. Mojaev and M. Roth, *Phys. Rev. B: Condens. Matter*, 2009, **80**, 064103.
34 D. Viehland, X. H. Dai, J. F. Li and Z. Xu, *J. Appl. Phys.*, 1998, **84**, 458.
35 S. V. Kalinin, B. J. Rodriguez, J. D. Budai, S. Jesse, A. N. Morozovska, A. A. Bokov and Z. G. Ye, *Phys. Rev. B: Condens. Matter*, 2010, **81**, 064107.

36 A. Kholkin, A. Morozovska, D. Kiselev, I. Bdikin, B. Rodriguez, P. P. Wu, A. Bokov, Z. G. Ye, B. Dkhil, L. Q. Chen, M. Kosec and S. V. Kalinin, *Adv. Funct. Mater.*, 2011, **21**, 1977.
37 P. Lehnen, W. Kleemann, T. Woike and R. Pankrath, *Phys. Rev. B: Condens. Matter*, 2001, **64**, 224109.
38 N. Balke, I. Bdikin, S. V. Kalinin and A. L. Kholkin, *J. Am. Ceram. Soc.*, 2009, **92**, 1629.
39 H. Okino, J. Sakamoto and T. Yamamoto, *Jpn. J. Appl. Phys., Part 1*, 2003, **42**, 6209.
40 S. V. Kalinin, A. Rar and S. Jesse, *IEEE Trans. Ultrason. Ferr.*, 2006, **53**, 2226.
41 C. Harnagea, M. Alexe, D. Hesse and A. Pignolet, *Appl. Phys. Lett.*, 2003, **83**, 338.
42 S. Jesse, B. Mirman and S. V. Kalinin, *Appl. Phys. Lett.*, 2006, **89**, 022906.
43 U. Rabe, S. Amelio, E. Kester, V. Scherer, S. Hirsekorn and W. Arnold, *Ultrasonics*, 2000, **38**, 430.
44 S. Jesse, S. V. Kalinin, R. Proksch, A. P. Baddorf and B. J. Rodriguez, *Nanotechnology*, 2007, **18**, 435503.
45 J. P. Killgore, D. G. Yablon, A. H. Tsou, A. Gannepalli, P. A. Yuya, J. A. Turner, R. Proksch and D. C. Hurley, *Langmuir*, 2011, **27**, 13983.
46 A. B. Kos and D. C. Hurley, *Meas. Sci. Technol.*, 2008, **19**, 015504.
47 K. Yamanaka and S. Nakano, *Appl. Phys. A*, 1998, **66**, S313.
48 R. Garcia and E. T. Herruzo, *Nat. Nanotechnol.*, 2012, **7**, 217–226.
49 B. J. Rodriguez, C. Callahan, S. V. Kalinin and R. Proksch, *Nanotechnology*, 2007, **18**, 475504.
50 S. V. Kalinin, A. N. Morozovska, L. Q. Chen and B. J. Rodriguez, *Rep. Prog. Phys.*, 2010, 73.
51 T. Jungk, Á. Hoffmann and E. Soergel, in *Ferroelectric crystals for photonic applications*, ed. P. Ferraro, S. Grilli and P. De Natale, Springer, Berlin, Heidelberg, 2009, pp. 209–228, DOI: 10.1007/978-3-540-77965-0_8.
52 R. Dittmer, W. Jo, E. Aulbach, T. Granzow and J. Roedel, *J. Appl. Phys.*, 2012, **112**, 014101.
53 P. A. Yuya, D. C. Hurley and J. A. Turner, *J. Appl. Phys.*, 2008, **104**, 074916.
54 A. Gannepalli, D. G. Yablon, A. H. Tsou and R. Proksch, *Nanotechnology*, 2013, **24**, 159501.
55 V. V. Shvartsman, W. Kleemann, R. Haumont and J. Kreisel, *Appl. Phys. Lett.*, 2007, **90**, 172115.
56 S. V. Kalinin, B. J. Rodriguez, S. Jesse, J. Shin, A. P. Baddorf, P. Gupta, H. Jain, D. B. Williams and A. Gruverman, *Microsc. Microanal. Microstruct.*, 2006, **12**, 206.

Electronic Supplementary Information (ESI) for Nanoscale.
This journal is © The Royal Society of Chemistry

Supporting Information

# Visualization of polar nanoregions in lead-free relaxors via piezoresponse force microscopy in torsional dual AC resonance tracking mode

Na Liu,[a,b] Robert Dittmer,[c] Robert W. Stark[*a,b] and Christian Dietz[*a,b]

[a]*Institute of Materials Science, Physics of Surfaces, Alarich-Weiss-Str. 2, 64287 Darmstadt, Germany*

[b]*Center of Smart Interfaces, Technische Universität Darmstadt, Alarich-Weiss-Str. 10, 64287 Darmstadt, Germany*

[c]*Institute of Materials Science, Nichtmetallische-Anorganische Werkstoffe, Technische Universität Darmstadt, Alarich-Weiss-Str. 2, 64287 Darmstadt, Germany*

**Resonance tune in torsional dual AC resonance tracking mode.**

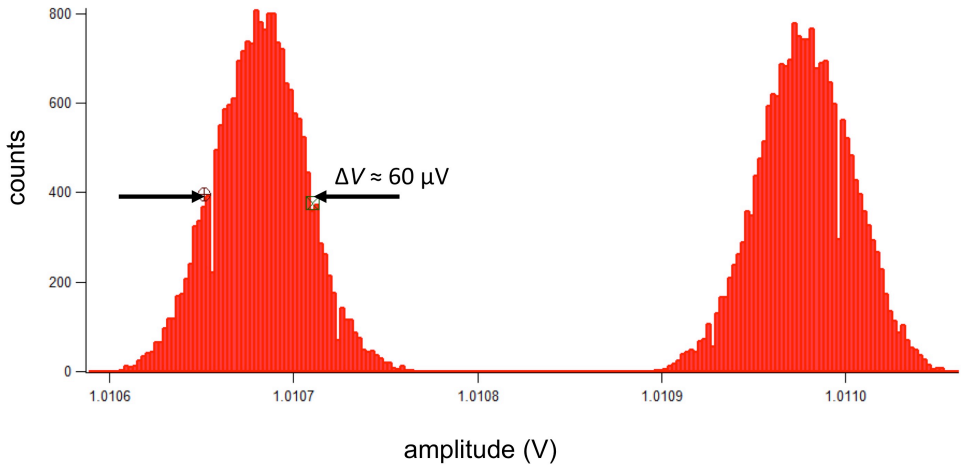


Fig. S1 Estimation of the amplitude resolution. To estimate the amplitude resolution the drive amplitude was stepped between two values. The output of the lock-in amplifier (measured amplitude) is shown as a histogram. The histogram shows a bimodal distribution around both driving amplitude values. The full width at half maximum of the peaks (~ 60 µV) is mainly determined by noise, digitalization and the transient response of the circuitry. It thus provides a rough estimate for the minimum detectable amplitude difference (the bandwidth filter was set to 5 kHz).

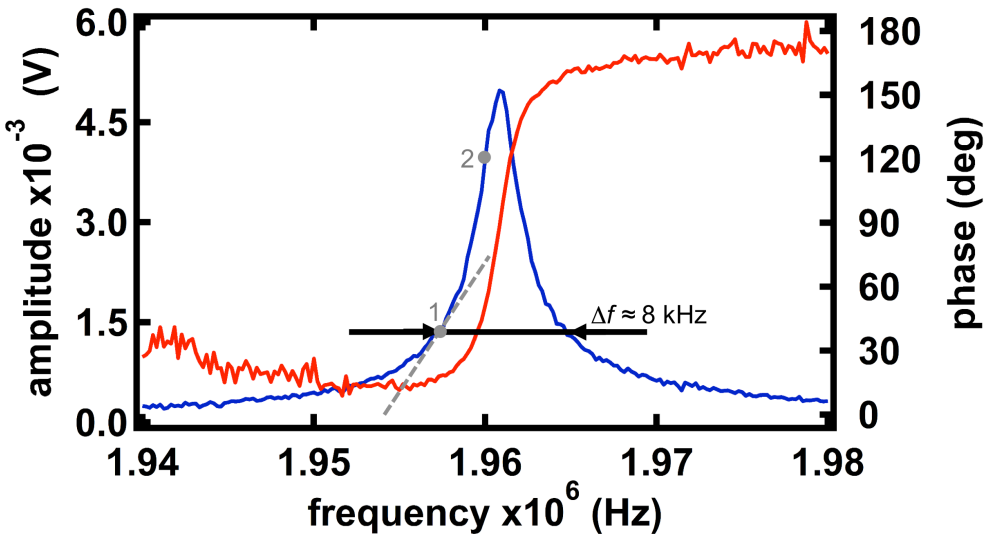


Fig. S2 Amplitude (blue, left axis) and phase (red, right axis) versus excitation frequency of the torsional vibration of an ASYELEC-02 (Asylum Research, Santa Barbara, USA) cantilever on a 3BMT sample surface applying an AC voltage 3 V to the tip. The frequency range for the frequency feedback loop is indicated by the arrows. Point 1 marks the detection point for the amplitude at $f_1$. The inverse slope ($S_1^{-1} = \mathrm{d}f_1/\mathrm{d}A_1 \approx 2890$ Hz/mV) is marked by the gray dashed line determining the minimum detectable frequency shift. The maximum slope (minimum inverse slope) of the resonance curve can be found at point 2 ($S_2^{-1} = \mathrm{d}f_2/\mathrm{d}A_2 \approx 465$ Hz/mV)

**Macroscopic characteristics of $0.81Bi_{1/2}Na_{1/2}TiO_3$-$0.19Bi_{1/2}K_{1/2}TiO_3$ (0BMT) and $0.97(0.81Bi_{1/2}Na_{1/2}TiO_3$-$0.19Bi_{1/2}K_{1/2}TiO_3)$-$0.03BiMg_{1/2}Ti_{1/2}O_3$ (3BMT).**

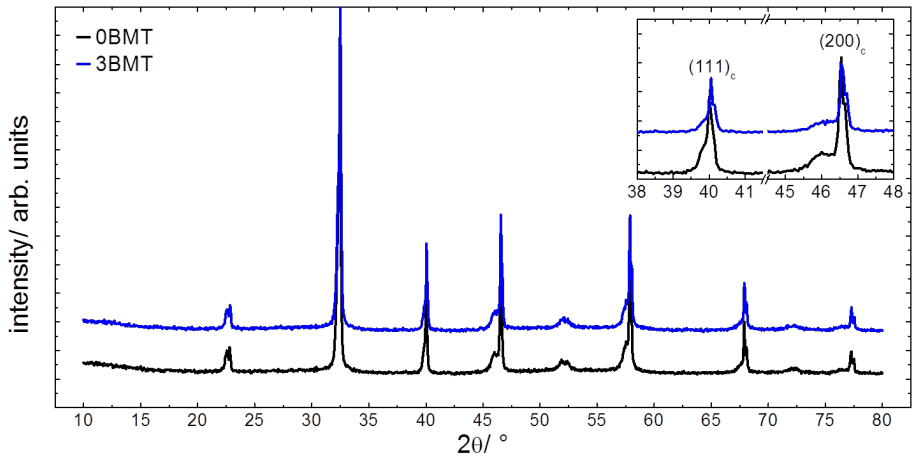


**Fig. S3** X-ray diffraction pattern for 0BMT and 3BMT poled at 6 kV/mm. The inset shows the $\{111\}_c$ and the $\{200\}_c$ reflection of both materials.

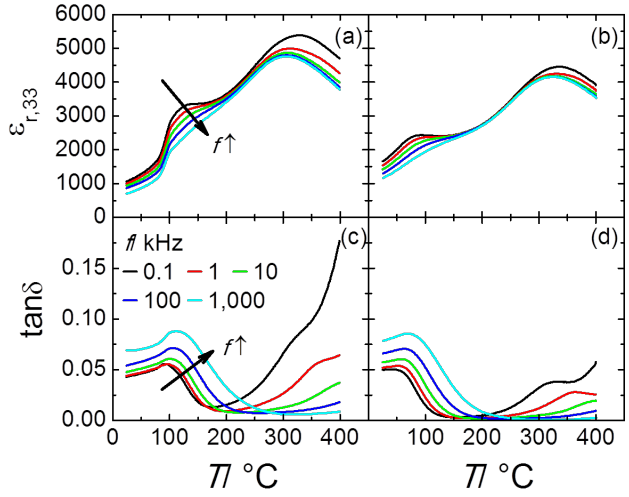


**Fig. S4** Relative dielectric permittivity (top row) and loss tangent *tan δ* (bottom row) at various frequencies for 0BMT (a and c) and 3BMT (b and d) in the poled state from room temperature up to 400 °C.

**Increased reliability of the image and reduced topographical crosstalk of dual AC resonance tracking in the cantilever's torsional vibration mode.**

The Fig. S5 shows the phase response of the same area measured by SF- (a) and TDART-(b) PFM, as well as the respective cross-sectional profiles (c). Both images feature two dominant phase values that can be attributed to the two possible domain orientations in the particular direction of the observation. A bright dot (encircled by the blue circle) directly below the central domain is visible in the SF-PFM image. Highlighted by the blue ellipse and the arrows in the cross-section, the phase profile measured by SF-PFM clearly deviates from the profile obtained by TDART with a bump/hollow combination rather than a flat area at the same position. The associated topography image (see inset of Fig. S5(c)) exhibits a hole approximately 500 pm in depth at this exact position. For clarity, we added the topographical profile into the cross-section, which indicates the correlation between the height and phase. In the case of the SF-PFM technique, this artifact was caused by topographical crosstalk induced by the feedback loop keeping the mean deflection signal constant during scanning. At the falling edge, the deflection of the cantilever changes to lower values, forcing the *z*-piezo to move the tip towards the sample surface to trace the topography. A sloped topography, however, can only be tracked with residual error. As a consequence, the contact resonance shifts to lower frequencies and hence the phase shifts to larger values compared to the contact resonance corresponding to the given deflection set point (note that the phase data shown in Fig S5 corresponds to the retrace curve, *i.e.*, the scan direction was from right to left). At the rising edge, the topography error has the opposite sign; thus, the contact resonant frequency shifts to higher values and smaller phase shifts. These variations lead to a wave-like shape of the phase shift profile in SF-PFM as shown in Fig. S5(a). In TDART mode, however, this artifact is corrected by the additional feedback loop tracking the instantaneous contact resonance. In addition, the slope derived from the phase profile obtained by TDART (red) is higher than that measured by the SF technique at the right domain wall between the central

and outer domains, corroborating the higher lateral resolution for the TDART mode previously confirmed by the amplitude signal. The fit of the experimental phase data resulted in a domain wall width of (38 ± 3) nm for the TDART mode and (42 ± 2) nm for the SF technique (see main article for details).

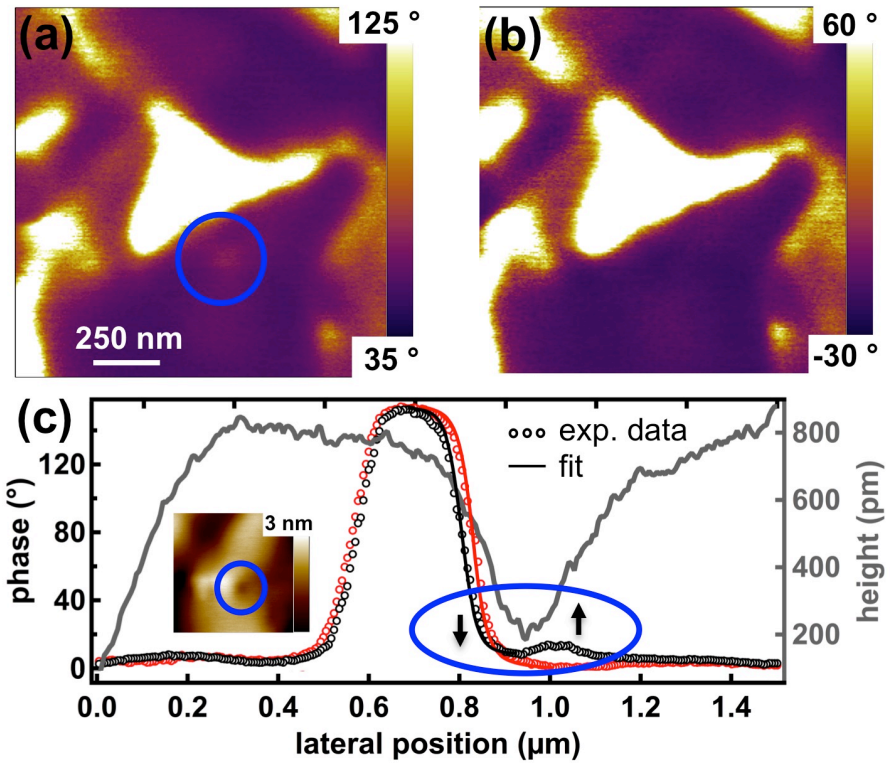


**Fig. S5** Comparison between the phase signals of the 0BMT sample surface measured by (a) SF- and (b) TDART-PFM modes. (c) Cross-sectional profiles of the SF-PFM (black dots) and TDART-PFM (red dots) phase signals. The gray line corresponds to the respective topographical profile. The inset in (c) shows the topographical image, in which the encircled area is the position of the hollow in the profile. Upward and downward arrows show the falling and rising edges of the hole, which had to be compensated by the feedback loop, leading to imaging artifacts. The black and red solid lines correspond to the fit data for the phase values at the right domain wall (phase data was shifted for the fit).

**Resolution of nanoscale features**

In principle, noise and feedback lagging or ringing might cause very tiny features in the amplitude and phase images that can be misinterpreted as PNRs. To corroborate the detectability of PNRs by TDART, we focused on nanoscale features prevailing in the amplitude images. These features were repeatedly scanned at scan angles parallel and perpendicular to the cantilever axis. Figure S7 shows the topography (top row), amplitude (middle row) and phase images (bottom row) of a 3BMT sample measured by SF-PFM (left two columns) and TDART-PFM (right two columns). The left column for each mode was obtained by scanning at an angle of $\alpha_{scan} = 0°$, *i.e*. with the fast scan axis in the same direction as the long axis of the cantilever, whereas the right column was scanned perpendicular to the cantilever axis. The features indicated by the arrows appear in both images irrespective of the scan direction. This clearly indicates that the nanoscale features are not caused by the noise or feedback induced artifacts. Furthermore, these nanoscale features are hardly visible in the amplitude image obtained by the SF-PFM mode. Notably, the orientation of some features apparent in the phase images measured by SF-PFM strongly depends on the scan direction as indicated by the encircled area (left two images, bottom row).

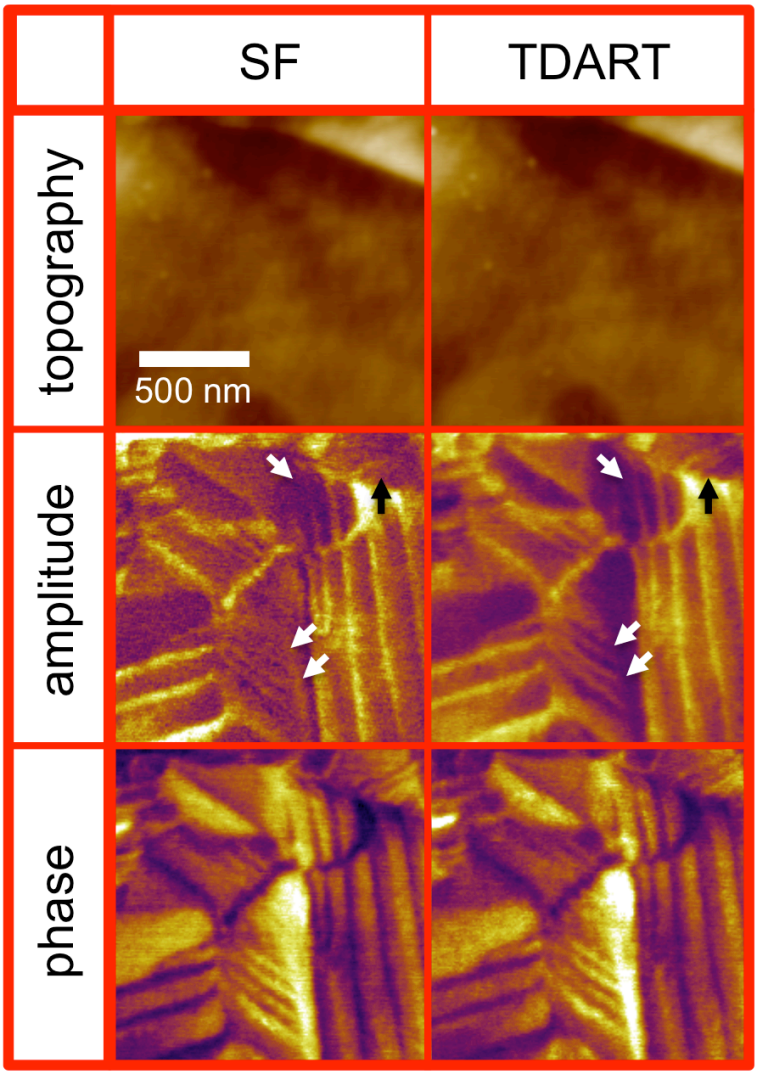


Fig. S6. Comparison between the SF-PFM (left column) and the TDART techniques (right column). Shown are the topography (top row), amplitude (middle row) and phase (bottom row) images obtained on piezoelectric standard material PIC 151 (lead-zirconate-titanate, PZT). The TDART amplitude image clearly reveals a riffled structure that could not be resolved by SF-PFM (see locations indicated by the arrows). The corresponding phase images exhibit the same lateral distribution of ferroelectric in-plane domains.

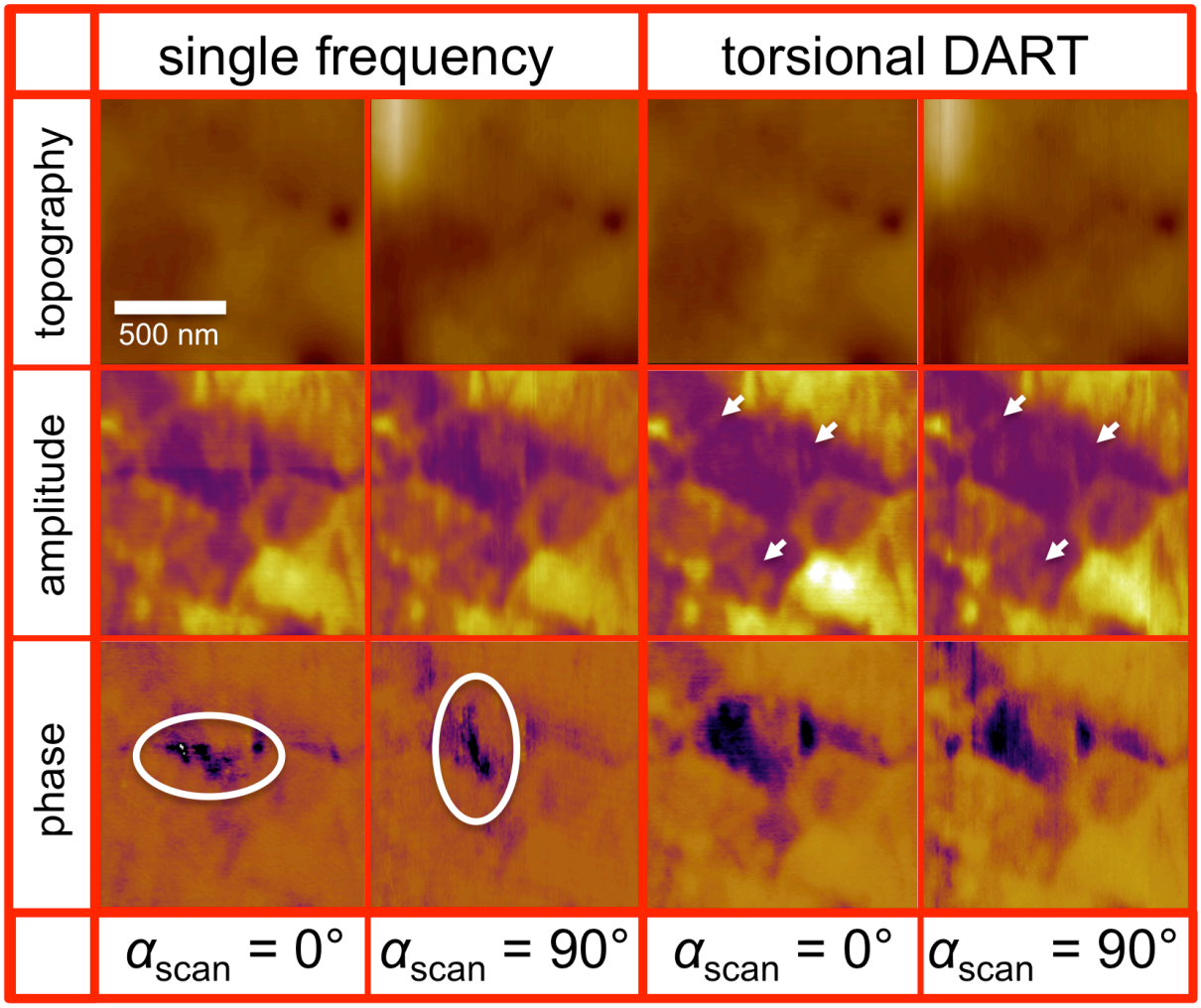


**Fig. S7** Comparison between the SF-PFM mode (left two columns) and the TDART technique (right two colums). Topography (top row), amplitude (middle) and phase (bottom) images of a 3BMT sample. The images were measured in different scan directions as noted at the bottom. Arrows indicate similar features that are independent of the scan direction with respect to the sample, whereas the encircled areas highlight a region showing a domain orientation that indeed depends on the scan direction. Color bars: topography 0–8 nm, amplitude arbitrary, phase -19–58 °, -16–54 °, 53–233 °, 48–228 ° (from left to right).

# Tailoring ergodicity through selective A-site doping in the $Bi_{1/2}Na_{1/2}TiO_3$–$Bi_{1/2}K_{1/2}TiO_3$ system

Matias Acosta' , Na Liu, Marco Deluca, Sabrina Heidt, Ines Ringl, Christian Dietz, Robert W. Stark, and Wook Jo

Citation: Journal of Applied Physics **117**, 134106 (2015); doi: 10.1063/1.4916719
View online: http://dx.doi.org/10.1063/1.4916719
View Table of Contents: http://aip.scitation.org/toc/jap/117/13
Published by the American Institute of Physics



# Tailoring ergodicity through selective A-site doping in the $Bi_{1/2}Na_{1/2}TiO_3$–$Bi_{1/2}K_{1/2}TiO_3$ system

Matias Acosta,[1,a)] Na Liu,[2] Marco Deluca,[3,4] Sabrina Heidt,[1] Ines Ringl,[3,4] Christian Dietz,[2] Robert W. Stark,[2] and Wook Jo[1,5]
[1]*Department of Materials Science, Technische Universität Darmstadt, Alarich-Weiss-Strasse 2, 64287 Darmstadt, Germany*
[2]*Department of Materials Science and Center of Smart Interfaces, Technische Universität Darmstadt, Alarich-Weiss- Strasse 10, 64287 Darmstadt, Germany*
[3]*Materials Center Leoben Forschung GmbH, Roseggerstraße 12, Leoben A-8700, Austria*
[4]*Institut für Struktur-und Funktionskeramik, Montanuniversitaet Leoben, Peter Tunner Straße 5, Leoben A-8700, Austria*
[5]*School of Materials Science and Engineering, Ulsan National Institute of Science and Technology, 689-798 Ulsan, South Korea*

(Received 27 October 2014; accepted 21 March 2015; published online 6 April 2015)

The morphotropic phase boundary composition $Bi_{1/2}Na_{1/2}TiO_3$-20 mol. % $Bi_{1/2}K_{1/2}TiO_3$ was chosen as initial material to do selective A-site aliovalent doping replacing Na and K by 1 at. % La, respectively. The materials were studied macroscopically by measuring dielectric and electromechanical properties. The Na-replaced material has a lower freezing temperature $T_{fr}$, lower remanent polarization and remanent strain, and thus a higher degree of ergodicity than the K-replaced material. These results are contrasted with local poling experiments and hysteresis loops obtained from piezoresponse force microscopy. The faster relaxation of the tip-induced local polarization and the lower remanent state in bias-on and -off loops confirm the higher degree of ergodicity of the Na-replaced material. The difference in functional properties is attributed to small variations in chemical pressure achieved through selective doping. Raman results support this working hypothesis. © *2015 AIP Publishing LLC*. [http://dx.doi.org/10.1063/1.4916719]

## I. INTRODUCTION

Currently, new lead-free piezoelectric ceramics for actuators applications are widely studied.[1,2] These efforts are driven by concerns regarding lead toxicity[3,4] and environmental hazards.[5] Therefore, there has been a continuous effort to replace $Pb(Zr,Ti)O_3$ (PZT) ceramics in commercial devices such as actuators.[1,2] Various solid solutions in the families of bismuth-alkali-based and alkali-niobium-based systems have been investigated so far.[1] Among these materials, the $Bi_{1/2}Na_{1/2}TiO_3$ (BNT)–$Bi_{1/2}K_{1/2}TiO_3$ (BKT) is a good candidate for technical applications because its properties can be engineered through proper chemical modifications.[2] Although La was used to modify the electrical properties of perovskite materials, its potential as dopant in BNT–BKT is not yet fully explored.

The binary solid solution BNT–BKT presents a morphotropic phase boundary (MPB) at about 18–22 mol. % BKT.[6,7] Several reports have focused on modifying the system through solid solutions achieving promising large signal strain properties, namely, $d_{33}$* above 500 pm/V at 6 kV/mm.[8–12] Other studies focused on either A- and/or B-site doping to improve small and large signal electromechanical properties.[13–16] It was proved that either replacing Bi on the A-site[16] or all A-site cations are effective approaches.[13] Compositional modifications with iso- and aliovalent dopants are technologically relevant because small doping amounts can modify considerably electrical properties due to cation vacancy formation and chemical pressure. Specifically, La was widely used in several archetypal perovskite materials such as $Pb(Zr,Ti)O_3$, and $Ba_{1/2}Na_{1/2}TiO_3$.[16–18] Isovalent La-doping was shown to be a viable approach to tailor the dielectric and electromechanical properties of the BNT–BKT system.[13,16] Nevertheless, aliovalent doping was not yet used as a strategy, neither selective doping.

Changes in degree of ergodicity, vacancies, and chemical pressure were shown to be critical in determining relaxor features.[2,17–22] The ergodicity term was first implemented in statistical mechanics. An ergodic property is such when the time average characteristic of it is indistinguishable from the ensemble average for the distribution of all accessible points in the phase space of the system. In other words, in an ergodic system an arbitrary function can be defined in a certain mathematical space within the phase space of the whole system, in which its characteristic becomes indistinguishable from the ensemble over all accessible points.[23] Expressing a higher degree of ergodicity can be understood as increasing the fraction of phase space in which its property time average characteristic becomes indistinguishable from the ensemble average for the distribution of all accessible points in the phase space of the system. Expressing a degree of non-ergodicity is therefore not a proper term but a consequence of the degree of ergodicity. However, we use this term throughout the manuscript to distinguish considerable changes in the degree of ergodicity. Considering that there has been reports demonstrating only a certain degree of

a)Email: acosta@ceramics.tu-darmstadt.de. Telephone: +49 (0)6151 16-6312.

 

ergodicity,[24] understanding the properties and structure locally and macroscopically is key for assessing a complete physical view.

Piezoresponse force microscopy (PFM) and Raman scattering have proven to be powerful experimental techniques to elucidate microscopic piezoelectric properties and resolve the local structure in lead-free piezoceramics.[25–29] PFM has been widely applied to study ferroelectric domains on the nanoscale.[27,30] As other scanning probe microscopy techniques, PFM allows for a lateral resolution of a few tens of nanometers and is characterized by its sensitivity to the local polarization when an external electrical field is applied to a conductive tip. This facilitates the potential to investigate local phenomena behind the functionality of relaxors on the nanoscale such as the existence of polar nanoregions (PNRs).[31] Additionally, local hysteresis loops and local poling experiments can be performed on particular positions of the sample[26] allowing to obtain information about the local remnant polarization and relaxation behavior.[25] In contrast, Raman spectroscopy is very useful to study the structural changes occurring on a short range owing to its coherence length down to the nanometer scale. Therefore, it offers the ability to combine the results with the nanoscale functional properties obtained by PFM.[28] The gathered information with these techniques is of particular importance for BNT-based materials, which are characterized by a high degree of structural disorder.[32] Raman spectroscopy can visualize phase transitions or short-range structural rearrangements as a function of composition,[33–35] temperature,[36] or applied electric-field.[29] Nevertheless, a distinction between chemically ordered regions and PNRs is not feasible solely by Raman spectroscopy. Hence, both techniques allow for observation of complementary information about local microstructural features.

In this study, the A-site doping replacing Na and K by 1 at. % La on the BNT–20BKT system is reported. The effects of the selective aliovalent doping are investigated by means of macroscopic dielectric and electromechanical properties. The dielectric properties indicate that the Na-replaced material presents a lower freezing temperature and thus a higher degree of ergodicity at room temperature. This result is corroborated by a lower macroscopic remanent polarization and local features such as faster tip-induced poling relaxation and lower remanent state in bias-off experiments. It is suggested that the different dielectric and electromechanical properties of both materials are due to small differences in chemical pressure in the Na-replaced as suggested by Raman spectroscopy and in qualitative agreement with hydrostatic measurements in archetypal relaxors. Therefore, a correlation between local techniques such as PFM and Raman spectroscopy and macroscopic functional properties is obtained. It is shown that selective aliovalent doping can be used to modify relaxor features locally, thus giving the possibility of engineering macroscopic lead-free relaxor piezoceramics.

## II. EXPERIMENTAL

The MPB of the $0.8Bi_{1/2}N_{1/2}TiO_3$–$0.2Bi_{1/2}K_{1/2}TiO_3$ (BNKT) system[6,7] was chosen as initial material. Two variants were designed replacing Na and K by 1 and 3 at. % La, leading to the stoichiometric formulas $Bi_{0.5}Na_{0.39}K_{0.1}La_{0.01}TiO_3$ (BN0.39KLT) and $Bi_{0.5}Na_{0.4}K_{0.09}La_{0.01}TiO_3$ (BNK0.09LT), respectively. The materials were prepared by a conventional solid state route using $Bi_2O_3$ (99.975%), $Na_2CO_3$ (99.5%), $K_2CO_3$ (99.0%), and $La_2O_3$ (99.9%) as raw materials (Alfa Aesar GmbH & Co., Germany). Calcination was done at 850 °C for 3 h and sintering at 1150 °C for 2 h. Further details on the processing route can be found elsewhere.[37] In order to highlight the importance of selective acceptor doping, functional properties in the 1 at. %-doped compositions will be presented. Nevertheless, the reader should be aware that results of the selective doping remain valid for 3 at. %-doped compositions.

The densities were measured by the classical Archimedes method. For the microstructure investigation, sintered samples were polished in a semi-automatic machine (Jean Wirtz, Phoenix 4000, Germany). Afterwards, the samples were thermally etched at 940 °C for 30 min with a heating rate of 10 °C/min. To ensure conductive surfaces, all samples were sputtered with silver (Gwent Electronic Materials, Ltd., C60704D8, United Kingdom). Imaging was performed in a scanning electron microscope (SEM) (Philips, XL 30 FEG, Netherlands). The average grain size was obtained by the mean intercept length method with a numerical multiplication factor of 1.56.[38]

A commercial impedance analyzer (Novocontrol Technologies, Impedance analyzer Alpha-A, Germany) equipped with a cryostat was used for the temperature- and frequency-dependent real relative permittivity $\varepsilon_r'$ of the unpoled samples during cooling. Frequencies ranging from $10^{-1}$ to $10^6$ Hz with amplitude of 1 V in the temperature range from −150 to 250 °C and a cooling rate of 1 K/min were employed.

For the polarization and strain measurements, virgin samples were used. A function generator (Agilent Corporation, 33220A, U.S.) supplied an input bipolar signal to a voltage amplifier (Trek, High Voltage Amplifier 20/20 C, U.S.) for the macroscopic electrical characterization of the specimens. This resulted in an electric-field strength of 6 kV/mm and 1 Hz. The polarization at room temperature was measured with a standard Sawyer-Tower circuit with a measuring capacitor of 10 $\mu$F. At the same setup, strain was measured by an optical sensor (Philtec, D63, U.S.).

A Cypher atomic force microscope with Ti/Ir (5/20) coated conductive cantilevers ASYELEC-01 (both from Asylum Research, U.S.) was used for the PFM study. The nominal spring constant of this type of cantilevers was $k = 2$ N/m with a nominal fundamental resonance frequency $f_0 = 70$ kHz. All PFM images were acquired on mirror-polished sample surfaces (polishing down to $^1/_4$ $\mu$m) using the dual alternating current resonance tracking (DART) mode provided by the microscope manufacturer. Using the contact resonance imaging technique, the recorded amplitudes indicated the magnitude of the local effective piezoelectric constant $d_{33}$ beneath the tip whereas the phase shift between the mechanical oscillation and the electrical stimulus was used to determine the orientation of the polarization of the sample with respect to the applied electric-field. PFM images with a resolution of (256 × 256) pixel using a constant loading force of approximately $F = 120$ nN were

acquired. A peak-to-peak driving voltage of 6 V was applied to the tip while scanning perpendicular to the length axis of the cantilever with a velocity of 5 $\mu$m/s. Local areas of $(1 \times 1)\,\mu m^2$ were poled by scanning the sample surface line-wise with a tip velocity of 5 $\mu$m/s and simultaneously applying a direct voltage of −10 V.

Local hysteresis loops on the sample surface were acquired by the switching spectroscopy PFM method in DART mode.[39] An alternating current voltage (2 V peak-to-peak) was superimposed to a bias voltage. The bias served for the local poling of the sample at specific locations. The alternating current was used for the simultaneous read-out of the piezoresponse. In the DART mode, this alternating current signal is a combination of two frequencies, one below and one above the contact resonance frequency that is constantly tracked by an additional feedback loop. The bias describes a sinusoidal-like function (16 V peak-to-peak) starting from initially 0 V with a stepwise increasing/decreasing rectangular pulse including an off-state after each poling step. The oscillation amplitude/phase during the bias-on and bias-off states was read out to measure the piezoelectric response of the surface. A pulse time of 25 ms in 100 steps was chosen for each oscillation cycle with a bias-off time equal to the pulse time. The scan direction was from top to bottom, and the acquisition time for one image was approximately 8 min. The bias-on and bias-off hysteresis loops both can be read out by SS-PFM. The bias-off hysteresis loops are related to the remanent piezoresponse signal measured between the consecutive dc bias steps with the dc bias switched off. The bias-on hysteresis loops, however, are influenced by the electrostatic interactions generated by the electrical field beneath the tip.[39] This leads to a substantially lower coercive voltage,[40] a higher slope and response compared to the off-state including an inversion of the loops.[40] The on- and off-state loops were obtained at the same sample positions. As a result, the electrostatic influence of the applied electrical field on the piezoresponse signal can be extracted. Furthermore, the hysteresis loops obtained on the different samples were recorded under same experimental conditions; hence, they are relatively comparable to each other.

Topography images were first-order flattened, all other images were leveled by a line-wise offset subtraction. For the hysteresis loops, a total number of seven cycles per position were averaged to achieve the final hysteresis loops representative for each sample. An estimate for the effective piezoelectric coefficient $d_{33}$ was calculated, as given in the below equation

$$d_{33} = A\cos(\phi)/V_{ac}, \tag{1}$$

where A is the amplitude of the cantilever oscillation, $\phi$ is the respective phase shift between the mechanical oscillation and the electrical excitation of the cantilever when the tip interacts with the sample surface, and $V_{ac}$ is the applied alternating voltage to the tip.

Raman measurements were performed on a LabRAM spectrometer (Horiba Jobin Yvon, France) with 532 nm (frequency doubled Nd:YAG) laser excitation. Laser power was kept below 5 mW to avoid substantial heating on the sample. The laser was focused on the surface of the samples by means of a long-working distance objective with 100× magnification and a numerical aperture of 0.8. Spectral resolution was 1.5 $cm^{-1}$/pixel (numerical grating 1800 g/mm). The acquired spectra were averaged on a minimum of 5 repetitions in order to improve the signal-to-noise ratio. Each spectrum was measured three times with an integration time of 0.5 s. Consequently, spectra were smoothed and normalized using a commercial software (Labspec 6, Horiba Jobin Yvon, France).

## III. RESULTS AND DISCUSSION

### A. Effect of chemical substitution on microstructure

Density and grain size analysis did not show differences between BN0.39KLT and BNK0.09LT. Both materials presented relative densities above 97% and grain sizes of approximately 1.3 $\mu$m. Similar densities were reported in other La-doped materials and were related to the presence of La-cation complex defects aiding the sintering process.[41,42]

The X-ray diffraction patterns of both materials showed a single pseudocubic perovskite structure. This is consistent with the results found in the literature in similar lead-free materials with little non-cubic distortions.[43] This measurement reveals the representative macroscopic average structure. Nevertheless, the detection of a Raman spectrum in such materials is a proof that the structure at the unit cell scale is not centrosymmetric,[33] as will be presented in Section III D. Average structure of BNKT also resembles that of La-modified BNKT. Non-cubic distortions are hardly distinguishable because they are very low[43] and thus below the resolution limit of our setup. A detailed structural investigation of these materials is out of the scope of the present paper, but it will be considered for future investigations.

Since La diffused into the lattice, either formation of cation vacancies, reduced concentration of oxygen vacancies or free electrons should develop during the incorporation process[42] to compensate the charge of the aliovalent doping. Previous reports in La-doped perovskites showed that $La^{3+}$ is exclusively incorporated on the A-site.[42,44,45] In the case of BNT–BKT, there are different A-site cation replacement possibilities. *A priori*, it can be thought that $La^{3+}$ would replace $Bi^{3+}$ cations on the A-site taking into account oxidation state, similar radii ($Bi^{3+} \sim 1.32$, $Na^{+} \sim 1.39$, $K^{+} \sim 1.64$, and $La^{3+} \sim 1.36$ Å (Ref. 46)), and the non-negligible volatilization of $Bi^{3+}$ during calcination and sintering.[47] Nevertheless, the macroscopic properties of BNT–BKT system with $La^{3+}$ entering into Bi-sites differ considerably from the materials presented here.[15] Therefore, we presume that $La^{3+}$ entered into the lattice in the chosen deficient sites of $Na^{+}$ and $K^{+}$ for the BN0.39KLT and BNK0.09LT, respectively. The most feasible charge compensation is thus by the creation of $K^{+}$ and $Na^{+}$ cation vacancies,[18,42] as given in the below equation

$$La_2O_3 \rightarrow 2La^{\cdot\cdot}_{Bi,K,Na} + 4V'_{Bi,K,Na} + \uparrow 3O_2. \tag{2}$$

The presented reaction is expected taking into account that alkali cations tend to volatilize during sintering, and their non-stoichiometry is encountered in many lead-free systems.[41,47,48] Although we already discarded the possibility of

exclusive $Bi^{3+}$ replacement by $La^{3+}$, we cannot neglect the compensation of pairs of ($Bi^{3+}$,$Na^{+}$) and ($Bi^{3+}$,$K^{+}$) for BN0.39KLT and BNK0.09LT, nor electronic compensation, nor a decrease in oxygen vacancy concentration. As it will be seen in Section III B, there have not been clear differences in the conductivity of BN0.39KLT and BNK0.09LT, and thus, cation compensation seems to be responsible for charge compensation. However, there is no driving force for different charge compensation mechanisms in BN0.39KLT and BNK0.09LT. Further inquiries on defect stoichiometry are out of the scope of the present paper and left for future work. Nevertheless, clear differences in macroscopic physical features of both materials are observed leading to the conclusion that changes in electromechanical are related to the presence of La in the system entering into different lattice sites.

### B. Dielectric and electromechanical properties

Fig. 1 introduces the $\varepsilon_r'$ values as function of temperature and frequency. A frequency dependent anomaly at approximately 345 K and 355 K is observed for BN0.39KLT (a) and BNK0.09LT (b), respectively. This anomaly shifts to higher temperatures and decreases its magnitude with increasing frequency, which indicates relaxor properties in both materials.[49] This behavior is also common to other lead-free materials[37,50,51] and was associated with the relaxation of PNRs fluctuations, i.e., a dynamic slowing down of PNRs thermally activated fluctuations.[50] Therefore, with further temperature decrease either a spontaneous transformation into a long-range ferroelectric order (non-canonic relaxor) or freezing of the PNRs fluctuations (canonic relaxor) can be expected.[52] There is no indication of a transformation into a long-range order ferroelectric state, and thus, we classify these materials as canonic relaxors. It was proposed that the freezing of PNRs can be rationalized by the Vogel–Fulcher[53,54] relationship.[55] Fig. 2 presents the freezing temperatures ($T_{fr}$) of both materials calculated from the local maxima $\varepsilon_r'$ values fitted with the Vogel–Fulcher[53,54] relationship. The $T_{fr}$ for BN0.39KLT is (253 ± 12) K, while for BNK0.09LT, it is (283 ± 9) K. Because in both cases $T_{fr}$ is close to room temperature, ergodic and non-ergodic states may coexist in these material. We stress here that we refer to a difference in the local degree of ergodicity and not necessarily to two different macroscopic phases with different relaxor states. Different degree of ergodicity was already found in similar lead-free materials both macroscopically[24,51] and microscopically.[56] Given the difference in freezing temperatures, BN0.39KLT should present a higher degree

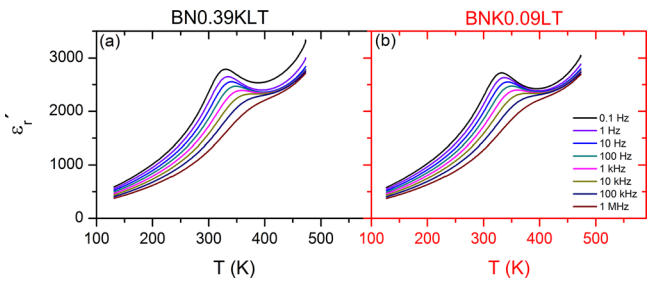


FIG. 1. Real part of the relative permittivity of (a) BN0.39KLT (black) and (b) BNK0.09LT (red).

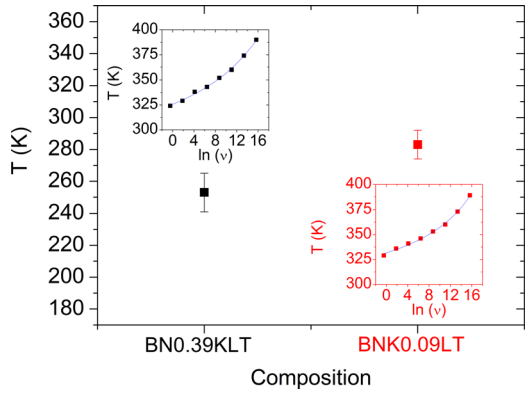


FIG. 2. Freezing temperature obtained from Vogel–Fulcher fitting for BN0.39KLT (black) and BNK0.09LT (red). Insets display the fitting curves utilized to determine $T_{fr}$.

of ergodicity at room temperature in comparison to BNK0.09LT. Pure BNKT at its MPB presents a $T_{fr}$ corresponding to (315 ± 5) K (not shown). Therefore, the pure MPB material is expected to present the lowest degree of ergodicity at room temperature.

Macroscopically bipolar polarization and strain loops obtained on virgin specimens are presented in Fig. 3 together with pure BNKT for comparison. Pure BNKT presents a remanent polarization $P_r = 0.26\,C/m^2$ and maximum polarization at 6 kV/mm is $P_{max} = 0.36\,C/m^2$. For BN0.39KLT, the remanent polarization is $P_r = 0.17\,C/m^2$ and the maximum polarization at 6 kV/mm is, $P_{max} = 0.35\,C/m^2$. For BNK0.09LT, a $P_r = 0.24\,C/m^2$ and $P_{max} = 0.36\,C/m^2$ were measured. The $P_r$ of BN0.39KLT is ∼35% lower than in BNKT and ∼30% lower than in BNK0.09LT. In all materials $P_{max}$ values are within 5% difference. The lowest $P_r$ in the BN0.39KLT material results from the more pronounced pinching of the polarization loop.

The strain curves indicate that BNKT presents a remanent strain of $S_r = 0.26\%$, an irreversible strain of $S_{irr} = 0.13\%$, and a maximum strain of $S_{max} = 0.44\%$ at 6 kV/mm. The BN0.39KLT presents a remanent strain of $S_r = 0.13\%$, an irreversible strain of $S_{irr} = 0.02\%$, and a maximum strain of $S_{max} = 0.4\%$ at 6 kV/mm. The BNK0.09LT presents $S_r = 0.22\%$, $S_{irr} = 0.1\%$, and $S_{max} = 0.41\%$. $S_{max}$ is similar in both materials doped materials and slightly larger in BNKT, which is consistent with polarization measurements. However, the BN0.39KLT presents a decrease of 40% in $S_r$ and 20% in $S_{irr}$ in comparision to BNK0.09LT. Moreover, if compared to pure BNKT, BNK0.09LT presents ∼15% in $S_r$ and $S_{irr}$. Reduced $P_r$, $S_r$, and $S_{irr}$ are common features observed in lead-free materials with increased ergodicity.[2] Therefore, the BN0.39KLT presents the highest

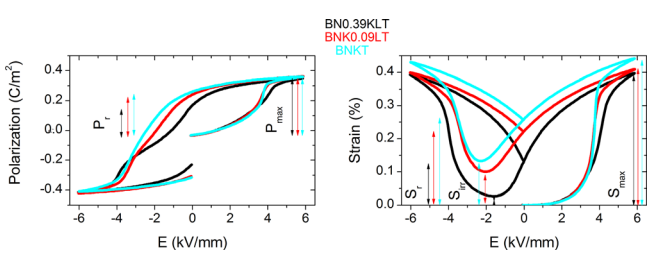


FIG. 3. (a) Polarization and (b) strain curves on a virgin state for BN0.39KLT (black) and BNK0.09LT (red).

degree of ergodicity, followed by BNK0.09LT and BNKT. This observation is in agreement with the calculated $T_{fr}$ of all the materials. Interestingly, for large signal electromechanical applications, BN0.39KLT presents one of the highest strain responses reported so far resulting in an exemplary candidate for actuator applications.[2]

Since we expect similar defect chemistry in both materials (Eq. (2)), the difference in ergodicity may result from local chemical pressure changes[20] exerted by the difference in the A-site cation radii upon doping. In $BaTiO_3$, it was experimentally shown that a similar qualitative shift of $T_c$ was obtained by modifying the system with Sr-doping or applying an hydrostatic pressure, indicating similarities between chemical and hydrostatic pressure.[57] Theoretical calculations showed that hydrostatic pressure mostly modifies bond lengths and slightly affects tilting angles, suggesting that these microstructural rearrangements are responsible of the functional properties modification.[21,22] However, in archetypal relaxors, it was also shown experimentally that tilting angles change at sufficient high pressures[58] and lead to oxygen anisotropic displacements.[59] These structural changes were also reflected in the change of dielectric and electromechanical properties under hydrostatic pressure in relaxors, as reported in several works by Samara *et al.*[60–65] Specifically, it was shown that with the increase in hydrostatic pressure, the thermal relaxation of PNRs occurred gradually at lower temperatures.[60,66,67] This behavior indicates a qualitative correlation with the chemical pressure exerted in this work due to selective La-doping and hydrostatic pressure in archetypal relaxors. We hypothesize that the BNT–BKT reduces its chemical pressure locally when $K^+$ is replaced due to its larger ionic radius in comparison to the similar radii of $Bi^{3+}$, $Na^+$, and $La^{3+}$. In other words, BN0.49KLT presents a higher local chemical pressure, and thus, its dielectric thermal relaxation, rationalized with $T_{fr}$, is expected at lower temperatures (Fig. 2). The changes in the local chemical pressure should be small because the maximum values of the dielectric properties (Fig. 1) remain similar, which is in agreement with low hydrostatic pressures.[60] This result indicates that the functional properties of the MPB of BNT–BKT should be quite sensitive to hydrostatic pressures. In order to probe locally the physical features of doped materials, PFM and Raman spectroscopy are presented subsequently. It should be pointed out that the concepts related to degree of ergodicity in Sections III C and III D could be extrapolated to the pure BNKT based on the presented macroscopic results. However, to the authors' knowledge, a detailed microscopic study of the MPB of the BNKT system is missing in literature and remains as future work.

### C. Piezoresponse force microscopy

Fig. 4 shows piezoresponse images $(5 \times 5)\,\mu m^2$ of the virgin domain state of BN0.39KLT (a)–(c) and BNK0.09LT (d)–(f), respectively. The averaged root mean squared roughness (calculated from three images of each sample) was approximately $(1.5 \pm 0.5)$ nm and $(1.6 \pm 0.3)$ nm for the BN0.39KLT and BNK0.09LT, respectively. The relatively low surface roughness for both samples suggests a minor

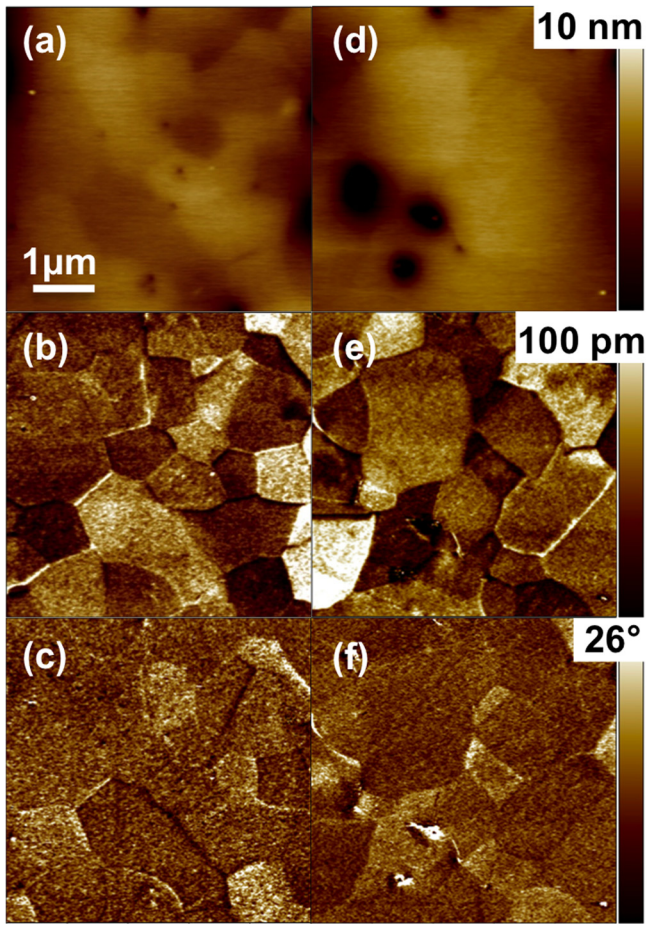


FIG. 4. (a) and (d) Topography, amplitude images ((b) and (e)) and phase response ((c) and (f)) of the initial domain state of a BN0.39KLT ((a)–(c)) and BNK0.09LT sample ((d)–(f)) measured by PFM in the DART mode.

crosstalk between topography and amplitude/phase channels. Figs. 4(b) and 4(e) correspond to the amplitude and Figs. 4(c) and 4(f) to the phase responses of the BN0.39KLT and BNK0.09LT, respectively. The amplitude response images of the initial state (Figs. 4(b) and 4(e)) depict regions with distinctive amplitude values on the size of a few micrometers for both samples. The phase response images of the initial state (Figs. 4(c) and 4(f)), however, do not show the clear contrast. The absence of the contrast and the associated phase alignment is typical for relaxors and was previously shown in similar lead-free systems.[25] The typical PNRs of these relaxor materials can hardly be resolved by the conductive AFM tip.[68]

To pole a certain area $(1 \times 1)\,\mu m^2$, we applied an input dc voltage of $-10$ V while line-wise scanning the sample surface in the contact mode. The associated electric-field was sufficient to partially induce ferroelectric domains with an orientation perpendicular to the sample surface. Figs. 5(a)–5(d) (BN0.39KLT) and Figs. 5(e)–5(h) (BNK0.09LT) show an image series of the local relaxation process with the amplitude ((a) and (e)) and phase response ((b) and (f)) captured immediately after the poling and the respective amplitude/phase response ("(c) and (g)" and "(d) and (h)") captured 60 min after poling. Immediately after the poling, approximately 80% of the poled area in the phase response

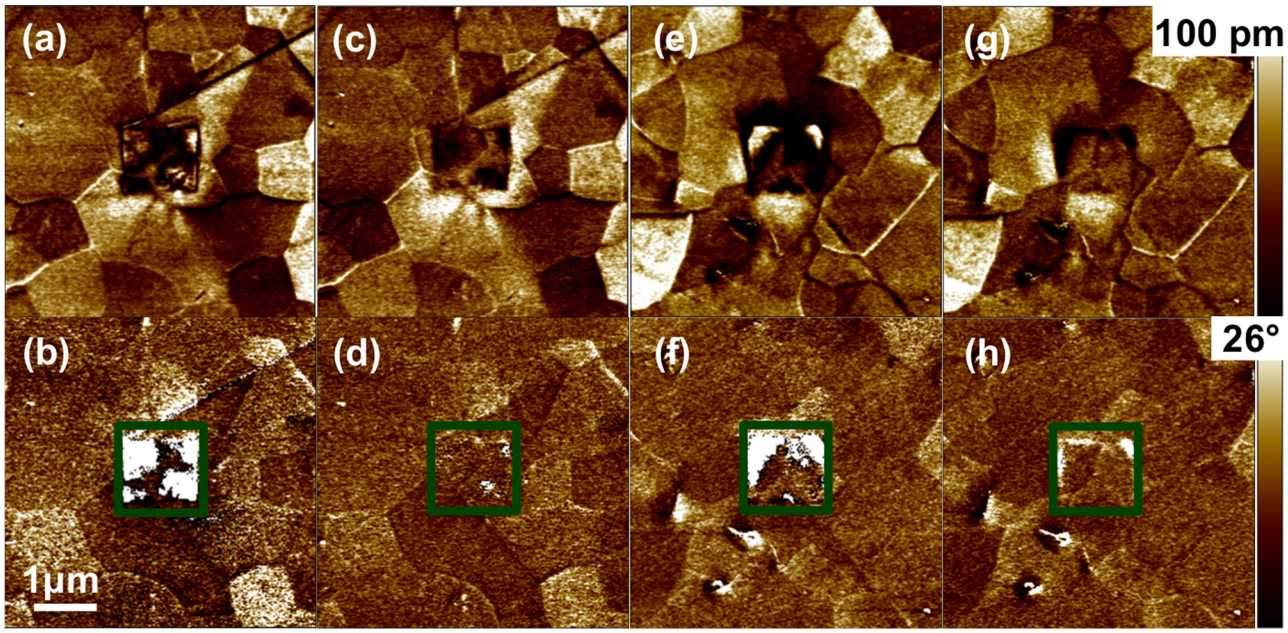


FIG. 5. Relaxation process of BN0.39KLT ((a)–(d)) and BNK0.09LT ((e)–(h)) after a local poling experiment measured by PFM in the DART mode. (a) and (e) Amplitude and (b)–(f) phase response subsequently imaged after poling a $(1 \times 1)\,\mu m^2$ region in the center (enclosed by the green frame); (c) and (g) amplitude and (d) and (h) phase response imaged 60 min after poling, respectively. For a better visibility of the piezoresponse, the color bar of the phase images was set to a range smaller than the total recorded phase shift. The values of the white area within the green frames of the phase images (b), (d), (f), and (h) correspond to approximately 180°.

of the BN0.39KLT sample (Fig. 5(b)) changed to 180°. In contrast, only 50% of the framed area (Fig. 5(f)) of the BNK0.09LT sample could be poled. The majority of the poled areas of both samples relaxed back to the initial domain state as detected 60 min after subsequent PFM imaging ("Figs. 5(c) and 5(d)" and "Figs. 5(g) and 5(h)"). Compared to the BN0.39KLT sample, a larger region at the upper side of the poling area of the remaining tip-induced domain was observed for the BNK0.09LT sample. The results demonstrate that ferroelectric domains could be induced in both samples. However, the tip-induced ferroelectric domains of both samples were unstable with time. A faster relaxation was observed for the BN0.39KLT sample and a larger long-range ordered domain could be initially induced compared to the BNK0.09LT sample. These results are attributed to the higher ergodicity of BN0.39KLT. It was already shown that

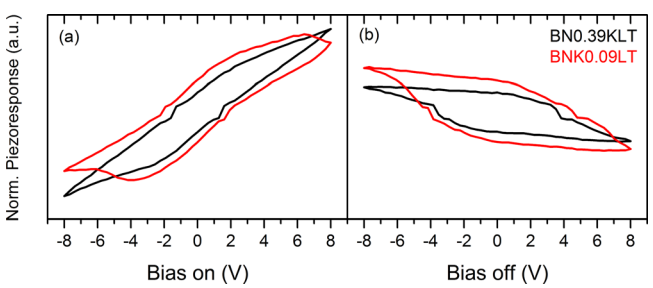


FIG. 6. Local hysteresis loops acquired on single spots applying the switching spectroscopy PFM mode with (a) bias-on and (b) bias-off for BN0.39KLT (black) and BNK0.09LT (red). Each loop is an average of 7 single loops taken at the same spot on the sample surface. The normalized piezoresponse (Norm. Piezoresponse, proportional to the effective piezoelectric coefficient $d_{33}$) was calculated from the product of the amplitude and the sine of the phase shift divided by the ac driving voltage. It was normalized by the maximum piezoresponse obtained on BN0.39LKT (bias-on). Scales in (a) and (b) are comparable to each other.

materials with a high degree of ergodicity present incipient features and high-electromechanical response.[2,51,69]

Fig. 6 shows the averaged local hysteresis loops obtained on BN0.39KLT and BNK0.09LT samples with bias switched on (a) and off (b). The bias-on hysteresis loops reveal that the maximum local strain value of the BN0.39KLT is higher than that of the BNK0.09LT, consistent with macroscopic measurements (Fig. 3). The bias-off, i.e., the remnant piezoresponse signal, results gave the opposite tendency. In both graphs, we found a larger remanent polarization for the BNK0.09LT sample. This phenomenon is also consistent with the macroscopic large signal measurements, indicating that because of the lower ergodicity of BNK0.09LT, the remanent polarization and strain are macroscopically and microscopically retained in this material.

The reason for the discrepancy between bias-off and bias-on hysteresis loops can be explained by the increased tendency to back-switch domains in case of the BN0.39KLT compared with the BNK0.09LT, as observed in the poling experiment in Fig. 3. This finding, together with the larger remnant polarization, corroborates the higher ergodicity of the BN0.39KLT. By analyzing $T_{fr}$ of both materials, it was also revealed a higher ergodicity in BN0.39KLT as well. These results are in good agreement with the nanoscopic observations. The relaxation behavior of both samples demonstrates that a high electric-field can induce macroscopic ferroelectric domains in both relaxor surfaces.

### D. Raman scattering

Room-temperature Raman spectra of BN0.39KLT and BNK0.09LT are shown in Fig. 7. The spectral signature was consistent with that of BNT-based materials, and was

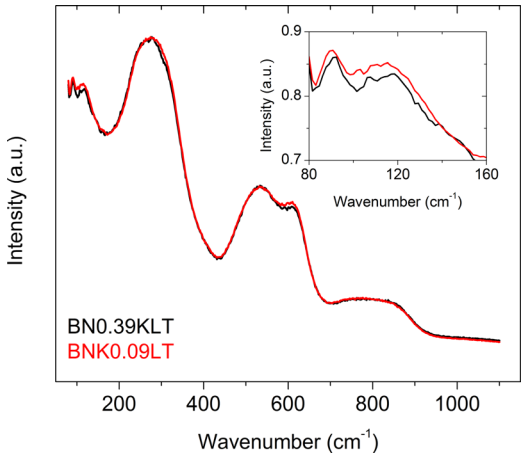


FIG. 7. Room-temperature Raman spectra of BN0.39LKT (black) and BNK0.09LT (red). In the inset the mode at ~135 $cm^{-1}$ related to A-site Na/K-O vibrations is shown. The mode at ~270 $cm^{-1}$ is ascribed to Ti–O vibrations, whereas above 400 $cm^{-1}$, $BO_6$ polyhedral vibrational modes are located. The overall broad spectral signature is an indication of intrinsic translational disorder.

dominated by translational disorder, visible by the overall broad spectral appearance.[28,29,70] The peak at ~135 $cm^{-1}$ (shown in the inset of Fig. 7) is ascribed to a two-mode behavior of Na- and K-based chemical clusters,[28] and thus is influenced by A-site doping. Experimental confirmation of chemical clusters in ferroelectrics was performed very recently,[71] in agreement with the described two-mode behavior. Also, the Ti–O mode at ~270 $cm^{-1}$ and the higher wavenumber (oxygen-related) modes can be influenced by chemical substitution, because replacement of a cation with different size at the A-site produces distortion of the unit cell.[28] Nevertheless, no clear differences could be observed between the spectra of both specimens. We interpreted this as due to the small substituent amount. The width of Raman modes is a distinctive trait of the short-range order/disorder state of a material.[72] Higher doping contents are needed to produce changes that can be distinguished from the overall broad spectrum on which they are superposed due to intrinsic disorder.[33] Only slight changes in the spectra of BN0.39KLT and BNK0.09LT were observed. A slight shifting of the mode at 135 $cm^{-1}$ and the mode at 270 $cm^{-1}$ was observed. This may be attributed to a small degree of chemical pressure, which would be consistent with the low chemical pressure depicted from dielectric measurements (Fig. 1). Nevertheless, it must be highlighted that changes in Raman spectra are rather small. Further investigations are being conducted to quantify the chemical pressure and their influence in the physical features of the system. However, it should be emphasized that the exerted chemical pressure was high enough to modify considerably the microscopic and macroscopic functional properties of the BNKT system.

## IV. CONCLUSIONS

The functional properties of BNT–BKT change drastically through selective A-site doping. Replacing Na by 1 at. % La resulted in an attractive material for actuator applications with a high recoverable strain that is attributed to its high degree of ergodicity. In contrast, replacing K by 1 at. % La resulted in a material with a higher freezing temperature and thus higher degree of non-ergodicity and remanent state. The macroscopic properties are corroborated by local measurements obtained from piezoresponse force microscopy. The higher degree of ergodicity of the Na-replaced material is reflected in a higher degree of locally induced switching, as well as a faster relaxation at room temperature. Furthermore, measuring the local hysteresis loops revealed a higher piezoresponse in the Na-replaced material under bias-on and a lower remanent state under bias-off. The different functional properties are attributed to small variations of the chemical pressure. We hypothesize that the chemical pressure of the K-replaced material is reduced due to the lower amount of $K^+$ that presents the highest cation radius.

Our results indicate that not only the concentration and cation used for iso- or aliovalent doping has to be considered but also the crystallographic site chosen for the dopant may be critical in future investigations. This approach gives an extra degree of freedom for engineering functional properties of complex A- and B-site lead-free piezoceramics.

## ACKNOWLEDGMENTS

This work was supported by the Deutsche Forschungsgemeinschaft through the Sonderforschungsbereich 595/D6 “Electrical Fatigue in Functional Materials” and the AdRIA Hesse state center for Adaptronics.

[1]J. Rödel, W. Jo, K. T. P. Seifert, E.-M. Anton, T. Granzow, and D. Damjanovic, J. Am. Ceram. Soc. **92**, 1153 (2009).
[2]W. Jo, R. Dittmer, M. Acosta, J. Zang, C. Groh, E. Sapper, K. Wang, and J. Rödel, J. Electroceram. **29**, 71 (2012).
[3]P. N. D. Lyn, Altern. Med. Rev. **11**, 2 (2006).
[4]W. J. Foster, J. K. Meen, and D. A. Fox, Cutaneous Ocul. Toxicol. **32**, 18 (2013).
[5]Off. J. Eur. Union: Legis. **174**, 88 (2011).
[6]A. Sasaki, T. Chiba, T. Mamiya, and E. Otsuki, Jpn. J. Appl. Phys. **38**, 5564 (1999).
[7]Y. Hiruma, K. Yoshii, H. Nagata, and T. Takenaka, J. Appl. Phys. **103**, 084121 (2008).
[8]N.-B. Do, H.-B. Lee, C.-H. Yoon, J.-K. Kang, J.-S. Lee, and I.-W. Kim, Trans. Electr. Electron. Mater. **12**, 64 (2011).
[9]A. Hussain, C. W. Ahn, A. Ullah, J. S. Lee, and I. W. Kim, Jpn. J. Appl. Phys. **49**, 041504 (2010).
[10]A. Hussain, C. W. Ahn, J. S. Lee, A. Ullah, and I. W. Kim, Sens. Actuators, A **158**, 84 (2010).
[11]A. Ullah, C. W. Ahn, A. Hussain, S. Y. Lee, and I. W. Kim, J. Am. Ceram. Soc. **94**, 3915 (2011).
[12]A. Ullah, C. W. Ahn, A. Hussain, S. Y. Lee, H. J. Lee, and I. W. Kim, Curr. Appl. Phys. **10**, 1174 (2010).
[13]T. H. Dinh, H.-Y. Lee, C.-H. Yoon, R. A. Malik, Y.-M. Kong, and J.-S. Lee, J. Korean Phys. Soc. **62**, 1004 (2013).
[14]J. Yoo, J. Hong, H. Lee, Y. Jeong, B. Lee, H. Song, and J. Kwon, Sens. Actuators, A **126**, 41 (2006).
[15]B. Wang, L. Luo, F. Ni, P. Du, W. Li, and H. Chen, J. Alloys Compd. **526**, 79 (2012).
[16]Q. Zheng, C. Xu, D. Lin, D. Gao, and K. W. Kwok, J. Phys. D: Appl. Phys. **41**, 125411 (2008).
[17]X. Dai, Z. Xu, and D. Viehland, Philos. Mag. B **70**, 33 (1994).
[18]J.-K. Lee, J. Y. Yi, and K. S. Hong, J. Appl. Phys. **96**, 1174 (2004).
[19]F. Chu, N. Setter, and A. K. Tagantsev, J. Appl. Phys. **74**, 5129 (1993).
[20]D. C. Fredrickson, J. Am. Chem. Soc. **134**, 5991 (2012).
[21]H. J. Zhao, W. Ren, Y. Yang, X. M. Chen, and L. Bellaiche, J. Phys.: Condens. Matter **25**, 466002 (2013).

[22]H. J. Zhao, W. Ren, X. M. Chen, and L. Bellaiche, J. Phys.: Condens. Matter **25**, 385604 (2013).
[23]T. Komatsuzaki, A. Baba, S. Kawai, M. Toda, J. E. Straub, and R. S. Berry, *Advancing Theory for Kinetics and Dynamics of Complex, Many-Dimensional Systems: Clusters and Proteins* (John Wiley & Sons, Inc., 2011), p. 171.
[24]H. S. Han, W. Jo, J. Rödel, I. K. Hong, W. P. Tai, and J. S. Lee, J. Phys.: Condens. Matter **24**, 365901 (2012).
[25]R. Dittmer, W. Jo, J. Rödel, S. Kalinin, and N. Balke, Adv. Funct. Mater. **22**, 4208 (2012).
[26]S. V. Kalinin, B. J. Rodriguez, S. Jesse, P. Maksymovych, K. Seal, M. Nikiforov, A. P. Baddorf, A. L. Kholkin, and R. Proksch, Mater. Today **11**, 16 (2008).
[27]A. Kholkin, A. Morozovska, D. Kiselev, I. Bdikin, B. Rodriguez, P. Wu, A. Bokov, Z.-G. Ye, B. Dkhil, L.-Q. Chen, M. Kosec, and S. V. Kalinin, Adv. Funct. Mater. **21**, 1977 (2011).
[28]J. Kreisel, A. M. Glazer, G. Jones, P. A. Thomas, L. Abello, and G. Lucazeau, J. Phys.: Condens. Matter. **12**, 3267 (2000).
[29]D. Schütz, M. Deluca, W. Krauss, A. Feteira, T. Jackson, and K. Reichmann, Adv. Funct. Mater. **22**, 2285 (2012).
[30]N. Balke, I. Bdikin, S. V. Kalinin, and A. L. Kholkin, J. Am. Ceram. Soc. **92**, 1629 (2009).
[31]G. Burns and F. H. Dacol, Solid State Commun. **48**, 853 (1983).
[32]V. V. Shvartsman and D. C. Lupascu, J. Am. Ceram. Soc. **95**, 1 (2012).
[33]B. Wylie-van Eerd, D. Damjanovic, N. Klein, N. Setter, and J. Trodahl, Phys. Rev. B **82**, 104112 (2010).
[34]L. Luo, W. Ge, J. Li, D. Viehland, C. Farley, R. Bodnar, Q. Zhang, and H. Luo, J. Appl. Phys. **109**, 113507 (2011).
[35]H. Foronda, M. Deluca, E. Aksel, J. S. Forrester, and J. L. Jones, Mater. Lett. **115**, 132 (2014).
[36]E. Aksel, J. S. Forrester, B. Kowalski, M. Deluca, D. Damjanovic, and J. L. Jones, Phys. Rev. B **85**, 024121 (2012).
[37]M. Acosta, J. Zang, W. Jo, and J. Rödel, J. Eur. Ceram. Soc. **32**, 4327 (2012).
[38]M. I. Mendelson, J. Am. Ceram. Soc. **52**, 443 (1969).
[39]S. Jesse, H. N. Lee, and S. V. Kalinin, Rev. Sci. Instrum. **77**, 073702 (2006).
[40]Y. Liu, Y. Zhang, M.-J. Chow, Q. N. Chen, and J. Li, Phys. Rev. Lett. **108**, 078103 (2012).
[41]H. Zhang, S. Jiang, K. Kajiyoshi, and J. Xiao, J. Am. Ceram. Soc. **93**, 750 (2010).
[42]J. Y. Yi, J.-K. Lee, and K.-S. Hong, J. Am. Ceram. Soc. **85**, 3004 (2002).
[43]M. Hinterstein, M. Knapp, M. Hölzel, W. Jo, A. Cervellino, H. Ehrenberg, and H. Fuess, J. Appl. Crystallogr. **43**, 1314 (2010).
[44]D. Hennings and K. H. Hardtl, Phys. Status Solidi A **3**, 465 (1970).
[45]D. Makovec, Z. Samardzija, U. Delalut, and D. Kolar, J. Am. Ceram. Soc. **78**, 2193 (1995).
[46]R. Shannon, Acta Crystallogr. A **32**, 751 (1976).
[47]A. Popovič, L. Bencze, J. Koruza, B. Malič, and M. Kosec, Int. J. Mass Spectrom. **309**, 70 (2012).
[48]J. König, M. Spreitzer, B. Jančar, D. Suvorov, Z. Samardžija, and A. Popovič, J. Eur. Ceram. Soc. **29**, 1695 (2009).
[49]L. E. Cross, Ferroelectrics **76**, 241 (1987).
[50]W. Jo, S. Schaab, E. Sapper, L. A. Schmitt, H. J. Kleebe, A. J. Bell, and J. Rödel, J. Appl. Phys. **110**, 074106 (2011).
[51]M. Acosta, W. Jo, and J. Rödel, J. Am. Ceram. Soc. **97**, 1937 (2014).
[52]A. A. Bokov and Z. G. Ye, J. Mater. Sci. **41**, 31 (2006).
[53]H. Vogel, Phys. Z. **22**, 645 (1921).
[54]G. S. Fulcher, J. Am. Ceram. Soc. **8**, 339 (1925).
[55]D. Viehland, S. J. Jang, L. E. Cross, and M. Wuttig, J. Appl. Phys. **68**, 2916 (1990).
[56]S. V. Kalinin, B. J. Rodriguez, S. Jesse, A. N. Morozovska, A. A. Bokov, and Z. G. Ye, Appl. Phys. Lett. **95**, 142902 (2009).
[57]W. J. Merz, Phys. Rev. **78**, 52 (1950).
[58]J. Kreisel, A. M. Glazer, P. Bouvier, and G. Lucazeau, Phys. Rev. B **63**, 174106 (2001).
[59]G. M. Rotaru, S. N. Gvasaliya, V. Pomjakushin, B. Roessli, T. Strässle, S. G. Lushnikov, T. A. Shaplygina, and P. Günter, J. Phys.: Condens. Matter **20**, 104235 (2008).
[60]G. A. Samara and E. L. Venturini, Phase Transfer **79**, 21 (2006).
[61]G. A. Samara and L. A. Boatner, Phys. Rev. B **61**, 3889 (2000).
[62]G. A. Samara, Ferroelectrics **274**, 183 (2002).
[63]G. A. Samara, J. Appl. Phys. **84**, 2538 (1998).
[64]G. A. Samara, Phys. Rev. Lett. **77**, 314 (1996).
[65]G. A. Samara, Ferroelectrics **117**, 347 (1991).
[66]J. Gao, Z. Xu, C. Zhang, and X. Yao, Ferroelectrics **401**, 86 (2010).
[67]J. Rouquette, V. Bornand, J. Haines, M. Pintard, and P. Papet, Ferroelectrics **288**, 147 (2003).
[68]S. V. Kalinin, B. J. Rodriguez, J. D. Budai, S. Jesse, A. N. Morozovska, A. A. Bokov, and Z. G. Ye, Phys. Rev. B **81**, 064107 (2010).
[69]Y. Hiruma, Y. Imai, Y. Watanabe, H. Nagata, and T. Takenaka, Appl. Phys. Lett. **92**, 262904 (2008).
[70]J. Petzelt, S. Kamba, J. Fabry, D. Noujni, V. Porokhonskyy, A. Pashkin, I. Franke, K. Roleder, J. Suchanicz, and R. Klein, J. Phys.: Condens. Matter **16**, 2719 (2004).
[71]R. Kirchhofer, D. R. Diercks, B. P. Gorman, J. F. Ihlefeld, P. G. Kotula, C. T. Shelton, G. L. Brennecka, and D. J. Green, J. Am. Ceram. Soc. **97**, 2677 (2014).
[72]E. Husson, Key Eng. Mater. **155–156**, 1 (1998).

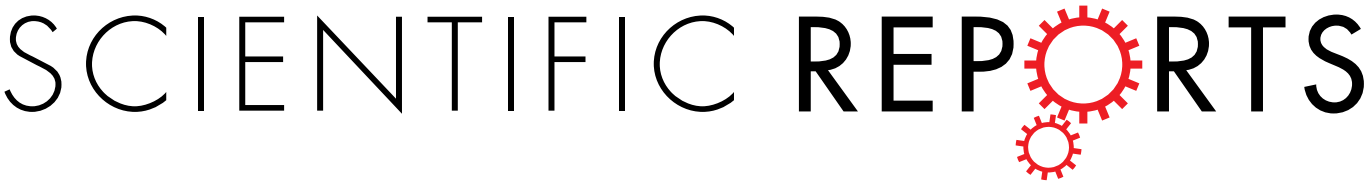

OPEN

# Revealing the core-shell interactions of a giant strain relaxor ferroelectric $0.75Bi_{1/2}Na_{1/2}TiO_3$-$0.25SrTiO_3$

Received: 22 July 2016
Accepted: 21 October 2016
Published: 14 November 2016

Na Liu[1], Matias Acosta[2], Shuai Wang[3], Bai-Xiang Xu[3], Robert W. Stark[1] & Christian Dietz[1]

**Lead-free relaxor ferroelectrics that feature a core-shell microstructure provide an excellent electromechanical response. They even have the potential to replace the environmentally hazardous lead-zirconia-titanate (PZT) in large strain actuation applications. Although the dielectric properties of core-shell ceramics have been extensively investigated, their piezoelectric properties are not yet well understood. To unravel the interfacial core-shell interaction, we studied the relaxation behaviour of field-induced ferroelectric domains in $0.75Bi_{1/2}Na_{1/2}TiO_3$-$0.25SrTiO_3$ (BNT-25ST), as a typical core-shell bulk material, using a piezoresponse force microscope. We found that after poling, lateral domains emerged at the core-shell interface and propagated to the shell region. Phase field simulations showed that the increased electrical potential beneath the core is responsible for the in-plane domain evolution. Our results imply that the field-induced domains act as pivotal points at the coherent heterophase core-shell interface, reinforcing the phase transition in the non-polar shell and thus promoting the giant strain.**

Concerns about the harmful effects of lead-containing piezoelectrics on the environment as well as human and animal health drive the development of lead-free relaxor ferroelectrics (relaxors)[1–7]. Three perovskite systems based on $BaTiO_3$, $(K,Na)NbO_3$ and $Bi_{1/2}Na_{1/2}TiO_3$ have been identified as competitive materials that feature an electric field-induced giant strain akin to or even surpassing the strain of PZT-based materials[8–11]. Generally, their large strain response is associated with a reversible field-induced phase transition from a macroscopic ergodic relaxor state to a ferroelectric state with a long-range order[12,13], as recently demonstrated by piezoresponse force microscopy (PFM)[14]. Nevertheless, the technological use of these materials thus far remains limited, mainly because of their large hysteresis and the large electric fields required to trigger the phase transition[10,15]. Current research activities have, however, led to novel systems with increasingly large strains albeit at too large electric fields[16–18]. Liu and Tan[17] demonstrated that in a complex Bi-based system $((Bi_{1/2}(Na_{0.84}K_{0.16})_{1/2})_{0.96}Sr_{0.04})(Ti_{1-x}Nb_x)O_3$, it was feasible to obtain an electrostrain under unipolar fields as large as 0.65% at 5 kV/mm, corresponding to a piezoelectric coefficient $d_{33}^* = 1300$ pm/V. The high strain was attributed to the phase transitions between an ergodic relaxor state with coexisting rhombohedral and tetragonal phases a ferroelectric rhombohedral phase. In addition to these advancements, it has been shown that the strain mechanisms behind large electrostrain materials can be highly complex, and not only piezoelectricity but also rotostriction might play a crucial role[19]. Recent studies highlighted that the strain state[20] and intergranular constraints could greatly influence the phase transitions leading to a giant strain, thus paving the way to new potential developmental routes[19,21].

The synthesis of a bulk core-shell material has been one of the recent approaches for improving the electromechanical response while reducing the hysteresis[1]. In BNT-25ST, which is a typical representative for a relaxor core-shell material, the formation of a core-shell structure is driven by the low diffusion rate of Sr during the sintering process, which leads to nanometre-sized, $Sr^{2+}$ depleted regions that eventually turn into rhombohedral

[1]Institute of Materials Science and Center of Smart Interfaces, Physics of Surfaces, Technische Universität Darmstadt, Alarich-Weiss-Str. 10, 64287 Darmstadt, Germany. [2]Insititute of Materials Science, Nichtmetallische-Anorganische Werkstoffe, Technische Universität Darmstadt, Alarich-Weiss-Str. 2, 64287 Darmstadt, Germany. [3]Insititute of Materials Science, Mechanik funktionaler Materialien, Technische Universität Darmstadt, Jovanka-Bontschits-Str. 2, 64287 Darmstadt, Germany. Correspondence and requests for materials should be addressed to R.W.S. (email: stark@pos.tu-darmstadt.de) or C.D. (email: dietz@pos.tu-darmstadt.de)

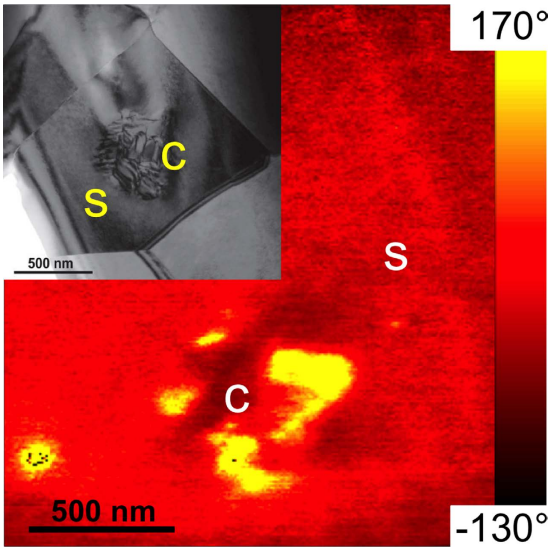


**Figure 1. Core-shell structure of individual grains.** PFM vertical phase image exhibiting distinct contrast in the core region. Inset: Typical TEM micrograph showing the core-shell microstructure (different location). The cores and the shells are marked with the letters C and S, respectively. Note that the contour of the grain is noticeable. TEM image reproduced with permission from ref. 1, © 2015 Wiley.

core regions. The core-shell structure is a non-equilibrium metastable state that can be removed gradually by extending the sintering time. Thus, the core density and average grain size can be engineered. Both parameters are crucial factors for the macroscopic electromechanical performance of the material[3]. The core-shell interface between the coherent heterophases also has a considerable effect on the macroscopic properties under an electrical stimulus[12,22–24]. Nevertheless, the physical mechanism of the domain evolution at the core-shell interface and the respective structure-property relationship remain unexplored for both dielectric and piezoelectric materials.

Piezoresponse force microscopy is a well-established tool for directly and nondestructively mapping the domain structure and evolution of field-induced polarisations on the surfaces of ferroelectrics, with nanometre precision[25,26]. Both the in-plane and out-of-plane polarisation can be mapped on the sample surface[25,27]. The domain distribution and evolution strongly depend on the variability of the polarisation beneath the surface. Here, phase field simulations have emerged as attractive computational tools for predicting the evolution mechanisms of induced domains in bulk ferroelectrics[28–30]. Based on the random field theory, a generic phase field model[31], implemented by a finite element calculation, was recently developed for the simulation of the temporal and spatial evolution of the polarisation in relaxors. Thus, theoretical predictions of the domain evolution in the bulk can be combined with experimental observations on the sample surface. Here we propose a model for the local core-shell configuration of BNT-25ST. At room temperature, BNT-25ST features a large normalized strain $d_{33}^{*} > 600$ pm/V under an electric field of 4 kV/mm[2,3,32]. The virgin domain structure, as well as its field-induced switching and subsequent domain evolution, is investigated by means of PFM. The different relaxor states between core and shell are confirmed. A responsive phase-electric field relaxor model well reflects the experimental observation of the formation of lateral domains and their evolution at the core-shell interface.

Transmission electron microscopy (TEM), X-ray diffraction (XRD) and macroscopic characterisation showed that BNT-25ST has a core-shell structure with $Sr^{2+}$-depleted cores[1,32]. A typical TEM image of the microstructure of BNT-25ST exhibiting the non-ergodic core (C) and the ergodic shell (S) within an individual grain in the virgin state at room temperature is shown as inset in Fig. 1. To identify surface regions with a distinct piezoresponse in the virgin state, we first investigated an untreated sample of BNT-25ST with vector PFM. A representative core-shell structure of an individual grain is captured by the vertical phase channel (Fig. 1, note that TEM and PFM images do not show the same grain). This individual grain exhibits distinctive domain contrasts in the core (C), whereas there is only a weak contrast in the surrounding areas (S). The observation of two distinct relaxor states within the material is in good agreement with the TEM images[1]. See the Supplementary Information for different grains and their respective vector orientations of the polarisation (Supplementary Fig. S1).

In the next step, the response of the material to an external electric field (local poling) and the subsequent relaxation of the tip-induced polarisation were investigated. A surface area of $1.5 \times 1.5\,\mu m^2$ was poled within the region of interest (Supplementary Fig. S1m, dashed square). Then, the same region was analyzed 15, 45 and 90 min later. Figure 2 shows the corresponding time series of PFM images. In each row, the PFM data of one time step is summarized. The vertical phase and amplitude signals (Fig. 2a,b) indicate that a long-range ordered and downward-oriented ferroelectric domain (Fig. 2a, dark area) was successfully induced by the +10 V biased-tip 15 min after poling. However, this domain was slightly larger ($\sim 2.0 \times 2.0\,\mu m^2$) than the area that was scanned during the poling procedure ($1.5 \times 1.5\,\mu m^2$). The sidewall of the tip cone around the tip apex can additionally contribute to the effective area of the electric field[33]. The tail-shaped trace at the left edge of the poled area was caused by residual charges on the tip as the tip moved away after poling.

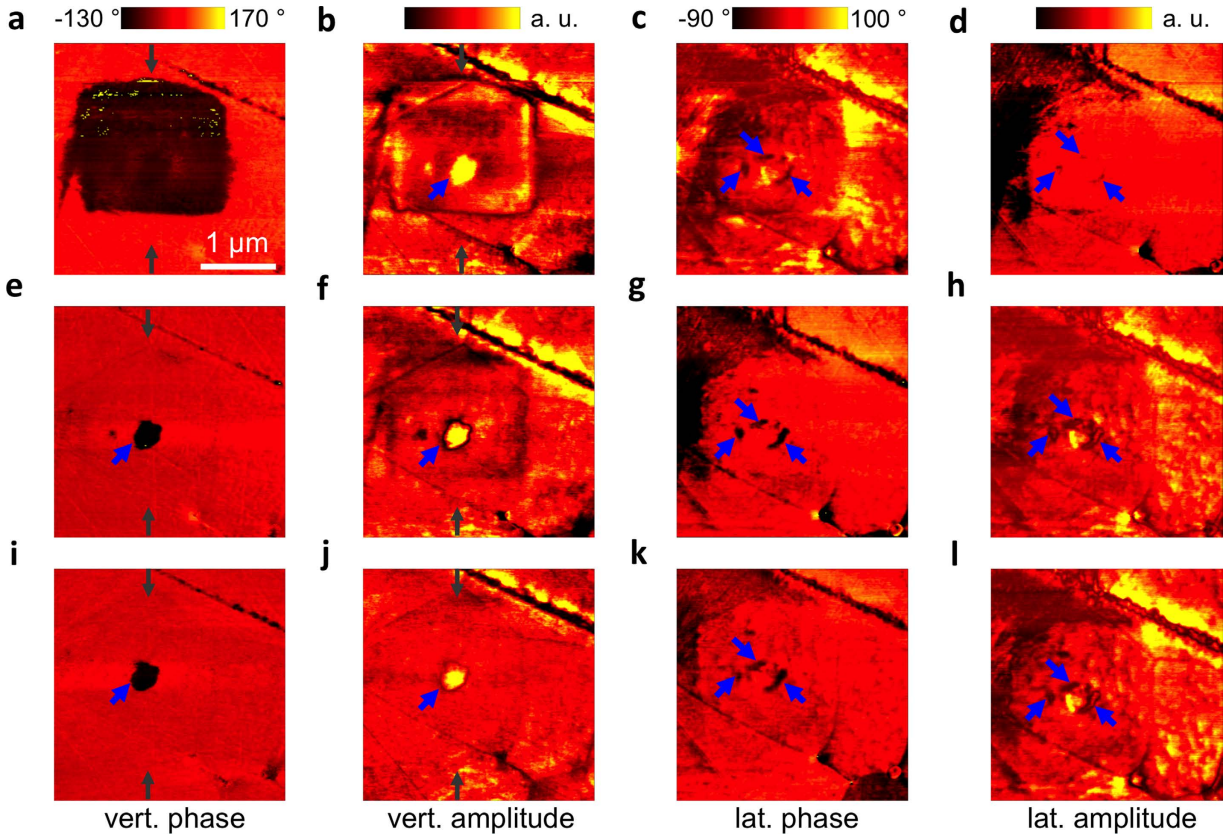


**Figure 2. Evolution of the polarisation after poling the sample in a 1.5 × 1.5 µm² region of interest, as indicated in Fig. S2m (Supplementary Information).** (**a**–**d**) PFM images captured 15 min, (**e**–**h**) 45 min, and (**i**–**l**) 90 min after the completion of the poling experiment. The PFM data show the (**a**,**e**,**i**) vertical phase and (**b**,**f**,**j**) amplitude, as well as the (**c**,**g**,**k**) lateral phase and (**d**,**h**,**l**) amplitude. The blue arrows highlight core areas; the dark grey arrows indicate the locations where the cross-sectional profiles were drawn in Fig. S1 (Supplementary Information).

In the vertical amplitude, a circular domain exists inside the poled area (Fig. 2b, blue arrow). This means that the tip-induced domain in the shell has partially relaxed back within the first 15 min after poling because the vertical amplitude is a measure of the out-of-plane piezoresponse. Moreover, a weak in-plane domain pattern can be observed in the lateral phase (Fig. 2c) and amplitude (Fig. 2d) images within the core-shell region. After 45 min, the induced long-range ordered vertical domain shrank down to a distinctive circular area (Fig. 2e,f), which can be identified as the non-ergodic core. The relaxation of the surrounding material can be attributed to the high ergodicity of the shell. The in-plane domain pattern was even more pronounced in the lateral phase and amplitude images 45 min after poling (Fig. 2g,h). After 90 min, the vertical phase image (Fig. 2i) did not change further, whereas the vertical amplitude signal in the core (Fig. 2j) was weaker. In contrast, the lateral phase and amplitude images remained almost unchanged after 45 min (Fig. 2g,h,k,l). A detailed study of the evolution of the field-induced vertical domain and the relaxation behaviour of the core and the shell, by means of averaged cross-sectional profiles taken in the vertical phase (Fig. 2a,e,i and Supplementary Fig. S1p), amplitude (Fig. 2b,f,j and Supplementary Fig. S1o) and the respective topography, is presented in the Supplementary Information (Supplementary Fig. S2). The compositional difference between core and shell[1,3] also implies a gradual variation in the lattice constant, which can explain the small height variations that were induced by the electric field at the core (Supplementary Fig. S2a). Before poling, the interfacial region presented an equilibrium stress state that lead to a small depression at the core, which was most likely caused by different ablation rates during polishing. In an external electric field, however, the polarisation mismatch causes a stress field at the core-shell interface, which in turn leads to an immediate local volume increase after poling and the subsequent decrease during relaxation.

To better illustrate the evolution of the field-induced domain at the core-shell interface, the lateral phase piezoresponse images (Fig. 2c,g,k and Supplementary Fig. S1n) are enlarged and shown together in Fig. 3. The white lines indicate the interface between the core and its periphery. Figure 3a shows the virgin domain state, with a strong image contrast in the core but a negligible image contrast within the shell. Figure 3b reveals that the virgin lateral domain configuration completely disappeared after vertical poling. Moreover, new lateral domains were formed at preferential nucleation spots around the core-shell interface, as indicated by the blue arrows. Remarkably, 45 min after poling (Fig. 3c), these lateral domains became larger and more pronounced, in contrast to that observed previously, when they remained stable (Fig. 3d, phase image 90 min after poling). This observation indicates that lateral domains can be induced by the electrical field and start to nucleate at the core-shell interface. These freshly induced domains continue to grow laterally and propagate into the adjacent shell to

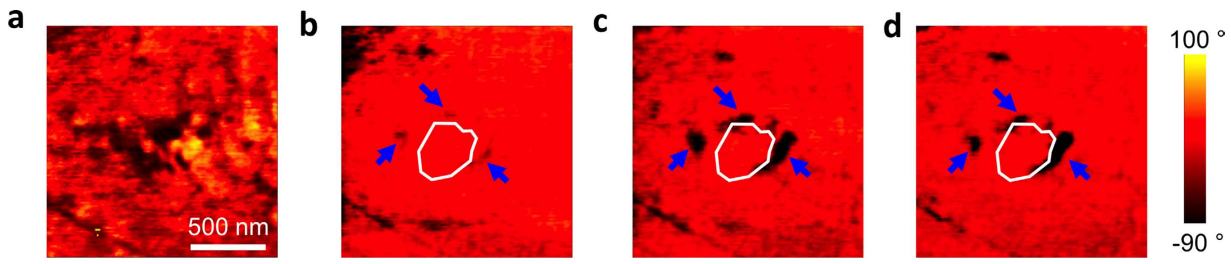


**Figure 3. Evolution of the lateral domain at the core-shell interface after poling.** (**a**) The virgin state of the lateral domain structure. (**b**) The electric field-induced lateral domain phase states 15 min, (**c**) 45 min, (**d**) 90 min after the completion of the poling experiment. The white line denotes the outline of the remanent vertical phase in the core after 45 min (Fig. 2e). The blue arrows highlight the newly formed lateral ferroelectric domain at the core-shell interface. Note: (**a–d**) are the enlarged images of the lateral PFM phase data from Fig. 2c,g,k and Supplementary Fig. S1n.

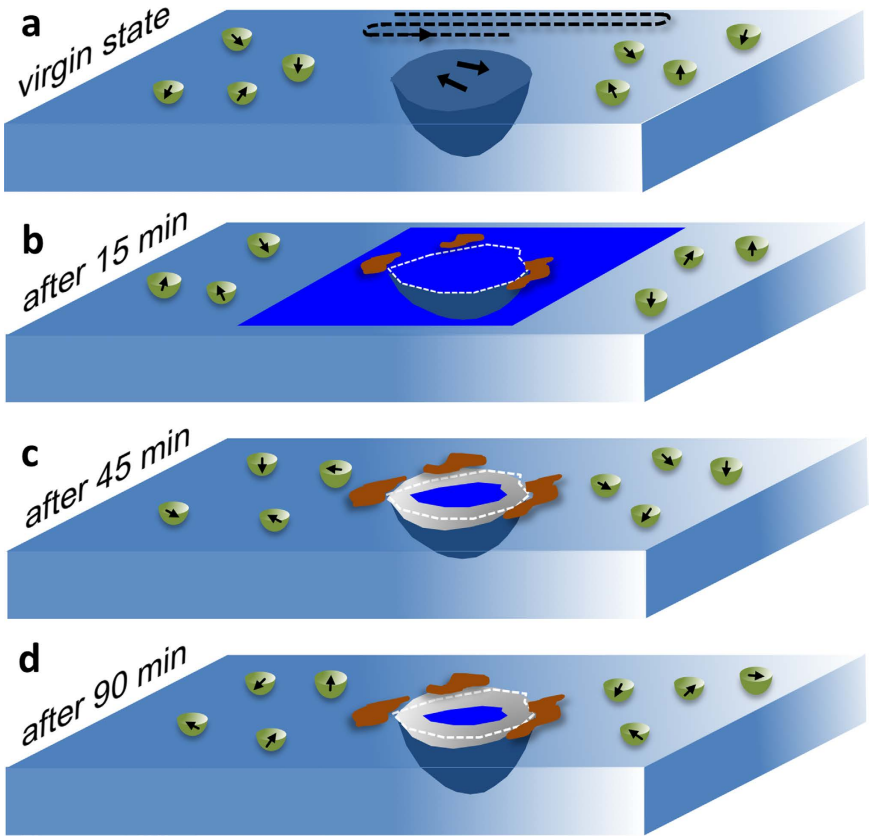


**Figure 4. Scheme of the proposed model for the relaxation within the core-shell region of an individual grain.** (**a–d**) Evolution of the vertical and the lateral domain configuration before (**a**) and after 15 min (**b**), 45 min (**c**) and 90 min (**d**) of vertical poling. The light blue planes represent a part of the $Sr^{2+}$-rich shell, with the $Sr^{2+}$-depleted core in the centre (dark blue hemisphere). The black arrows indicate the local domain configuration (polar nanoregions). The white dashed frames separate the tip-induced core from the shell. The dark blue area indicates a vertical downward-oriented domain and the grey area, a mixed vertical and lateral domain. The brownish areas indicate the possible lateral domain propagation from the interface to the shell. The dashed line in (**a**) illustrates the trace of the nanoscale line-by-line poling of an AFM tip.

compensate for the mismatch of stress and polarisation between the irreversibly induced ferroelectric state in the core and the ergodic shell, which is the driving force of the lateral domain propagation.

Under an external field, the entire virgin material can be poled. After removing the field, the core remains poled, whereas the shell reversibly relaxes to the initial state[27,34]. We thus propose a model for the polarisation evolution of the core-shell region in the poling experiment (Fig. 4). In the virgin state (Fig. 4a), the core is embedded in a region (azure) where randomly oriented polar nanoregions (PNRs) (encircled black arrows) characterize the material. At this stage, the core (black blue) predominantly exhibits laterally oriented domains (black arrows).

To pole the material, an electric field between the AFM tip and the sample was applied. This poling process induced a downward-oriented ferroelectric domain with a long-range order (Fig. 4b, dark blue area). The AFM induced domain was not stable and shrank to a well-defined core-shell interface (white dashed frame). Then, further relaxation occurred (Fig. 4c) around the newly formed and electrically induced core-shell interface. Finally, the induced single vertical domain relaxed back to its virgin state (PNRs, encircled black arrows, Fig. 4c) because there was a random electrical potential in the ergodic shell. In the non-ergodic core, however, a single vertical domain (dark blue area) that is associated with an irreversible transition to a ferroelectric state was induced. Due to the stress and polarisation mismatch at the core-shell interface, a lateral domain nucleated and grew as compensation (brown area represents the lateral domain propagation). The actual spatial domain orientations at the core-shell interfacial area were then a complex mixture of vertical and lateral domain components (Fig. 4d).

To gain further insights into the evolution of the domain distribution after poling, a continuum phase field simulation was carried out. The configuration of a core-shell microstructure was included in the model (Fig. 5). The initial equilibrium state is shown in Fig. 5a, in which large domains are present in the non-ergodic core and a structure with small-sized domains in the ergodic shell. The corresponding potential distribution (Fig. 5b) shows a potential with small variations around zero throughout the *x*-*z* plane. The random field distribution caused by the chemical disorder leads to some hot spots with relatively high/low potential[35]. The electric field loading was then applied by a potential difference between the top and bottom boundary. Core and shell regions were fully poled under the peak potential of +10 V (Fig. 5c), with the polarisation pointing downwards. The corresponding distribution of electric potential difference indicates an almost homogeneous gradient (Fig. 5d). After the external potential is switched off, polarisation and potential distribution represent the remanent state (Fig. 5e,f): the poled polarisation state in the shell region relaxes to a random state, whereas the field-induced ferroelectric domains within the core region remain poled. The potential distribution also relaxes to zero, except for the bottom of the core-shell interface (red area). The downward polarisation of the ferroelectric domain in the non-ergodic core can thus not be compensated for and leads to the presence of a positive charge beneath the core. As a result, the potential beneath the core is higher (red area) than the one of the rest of the simulated mesh (Fig. 5f). The remanent domain configuration is symbolized as polarisation vectors (Fig. 5g), in which black frames enclose regions with predominantly laterally oriented domains (red and green arrows), which is consistent with the lateral domain phenomenon observed in the PFM experiment (*cf*. Fig. 3). The local poling induced a transition from the relaxor states (ergodic – shell, non-ergodic – core) to the ferroelectric state in both regions, which was completely reversible in the shell area but caused the core region to be permanently in the ferroelectric state. These findings and the appearance/growth of a ferroelectric domain with a polarisation direction perpendicular to the applied field into the ergodic shell are in good agreement with the results obtained by the phase field simulation based on a core-shell microstructure model. It revealed a strong gradient in the electrical potential at the interfacial area, which causes the nucleation and propagation of an in-plane polarisation.

The phase field simulation demonstrated that the observed evolution of field-induced lateral domains via PFM is due to a compensation of polarisation charges at the core-shell interface beneath the sample surface. Transferring these local observations within an individual grain to the macroscopic scale offers new insights into the performance and functionality of actuators: actuator applications require materials with large, recoverable, electric field-induced strain outputs executed at low fields[13]. Macroscopically, an actuator based on a relaxor runs from the remanent state (generally negligible) to a state where the entire material is held at the ferroelectric state by a sufficiently strong external electric field and returns back to the remanent state. Interpreting this cycle microscopically implies that the relaxed ergodic state of each shell is switched to a ferroelectric state and back. The core, in contrast, permanently remains in the ferroelectric state. Upon switching on the external field, the alignment of the "pivot points" at the interface from a polarisation direction perpendicular to the applied field to a parallel configuration facilitates the domain orientation in the shell. These pivot points originate from the residual high potential at the interface and generate domain nuclei at the adjacent shell. These nuclei aggregate, and the surrounding PNRs align with the external electric field. Consequently, the energy barrier for the completion of the phase transition in the shell is reduced. Conversely, upon switching off the external field, the pivot points reduce the mechanical stress at the interface that was established during the relaxation process between the polarised core and the arbitrarily distributed shell polarisation. The formation of the lateral polarisation thus plays the central role in the compensation of the polarisation and strain mismatches between the core and the shell during the poling and relaxation processes.

In summary, our findings provide an experimental and theoretical insight into the mechanism behind the macroscopic functionality of core-shell piezoceramics. The fact that the coherent heterophase core-shell interface plays such a crucial role in enhancing the polarisation under an electric field lets us conclude that tailoring the core-shell configuration with regard to shape, relative size, or the interface between core and shell can lead to more efficient materials as they are needed for technical applications.

## Methods

**Sample preparation.** BNT-25ST was synthesized via a mixed oxide route employing $Bi_2O_3$ (99.975%), $Na_2CO_3$ (99.5%), $TiO_2$ (99.9%), and $SrCO_3$ (99%) (Alfa Aesar GmbH, Karlsruhe, Germany) as reagent-grade oxides and carbonates. The powders were mixed according to the $0.75Bi_{1/2}Na_{1/2}TiO_3$-$0.25SrTiO_3$ stoichiometric formula. Complete processing details of this material can be found elsewhere[32]. The sample preparation processing for PFM measurements followed a protocol reported elsewhere[27].

**Piezoresponse force microscopy.** The PFM measurements were performed using a Cypher atomic force microscope (Asylum Research, Santa Barbara, CA). Ti/Ir- (5/20) and Ti/Pt- (5/20) coated conductive cantilevers ASYELEC-02 and AC240TM (both from Asylum Research, Santa Barbara, CA) were used. The nominal spring constants and fundamental resonance frequencies were $k = 40$ N/m and $f = 300$ kHz for the ASYELEC-02

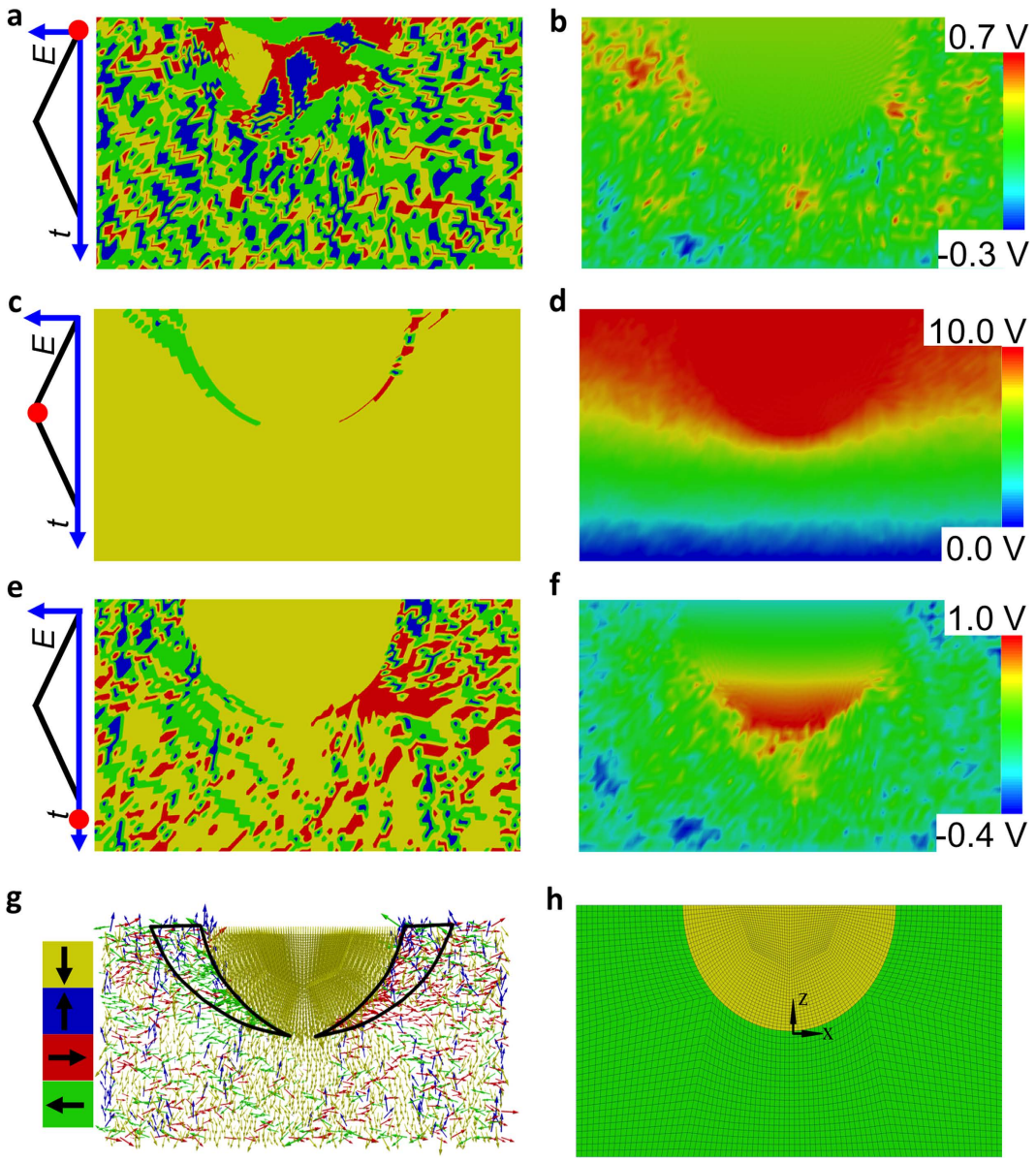


**Figure 5. Phase field simulation of a formation of the field-induced polarisation.** (**a,c,e,g**) Domain distribution and respective orientation of the polarisation. (**b,d,f**) Corresponding potential distribution. (**h**) Designed mesh in the *x*-*z* plane through the sample volume miming the geometry of a core-shell structure. The simulation evolves from the initial state (**a,b**) over a maximum potential state (**c,d**) to the remanent state (**e,f,g**). The detailed polarisation vector distribution at the remanent state is shown in (**g**). The marked regions (black frames) have a preferential lateral domain orientation. The colours in (**a,c,e**) and the arrows in (**g**) represent four polarisation orientations of the domains: yellow – down; blue – up; green – left; red – right. The length of the arrows indicates the magnitude of the polarisation vector. The three upper charts on the left illustrate the different stages of the simulation, in which red dots denote the current applied field and the *y*- and *x*-axis represent the electric potential and the time step, respectively.

cantilevers and $k = 2$ N/m and $f = 70$ kHz for AC240TM. For PFM imaging, the driving frequencies were set slightly below the respective contact resonance frequencies. Images were taken with a lateral resolution of $256 \times 256$ pixels; the tip was scanned perpendicular to the cantilever's length axis. To perform the vertical domain poling, a $+10$ V *dc* voltage was applied to the tip while it scanned line-wise an area of $1.5 \times 1.5\,\mu m^2$ with a velocity of 1.1 μm/s. The tip-induced domain patterns were successively characterized, with a scan area of $3.0 \times 3.0\,\mu m^2$, after 15 min, 45 min and 90 min. The detailed vector PFM imaging parameters are listed in Table 1. Note that the actual contact resonance frequencies can shift due to changes of the tip-surface contact mechanics; hence, the measuring parameters (amplitude, frequency of the driving signal) needed to be frequently adjusted to keep the driving signals in the vicinity of the contact resonance frequency. Topographic images were processed using first-order line flattening to remove the effect of the surface tilt and thermal drift within the fast and slow scan directions. Cross-sectional profiles were averaged over 5 scan lines.

| Cantilever | ASYELEC-02 | | AC240TM | |
|---|---|---|---|---|
| Direction | Vertical | Lateral | Vertical | Lateral |
| Driving amplitude (V) | 3.0 | 2.5 | 3.5 | 3.5 |
| Driving frequency (kHz) | 926 | 1886 | 268 | 736 |
| Scanning speed (μm/s) | 3.1 | | 2.3 | |

**Table 1. PFM imaging experimental parameters.**

**Phase field simulation.** The finite element phase field simulations for the domain evolution in the non-ergodic core (taken as a classical ferroelectric for simulation) and ergodic shell relaxor state were based on the models presented by Wang *et al.*[31]. In the simulations, the spontaneous polarisation and the electric potential were treated as degrees of freedom. In an ergodic relaxor, the phase field potential $H$ included three terms: the electrostatic energy $H^{ele}$, the Landau energy $H^{lan}$ and the gradient energy $H^{grad}$. The phase field potential $H$ for the simulation was

$$H = H^{ele} + H^{lan} + H^{grad}. \tag{1}$$

In the 2-dimensional case,

$$H^{ele} = -\frac{1}{2}k_{ij}(E_i + E_i^{random})\left(E_j + E_j^{random}\right) - P_iE_i - P_iE_i^{random}, \tag{2}$$

$$H^{lan} = \beta_1(a_1 + a_2(P_1^2 + P_2^2) + a_3(P_1^4 + P_2^4) + a_4P_1^2P_2^2 + a_5(P_1^6 + P_2^6)), \tag{3}$$

$$H^{grad} = \beta_2P_{i,j}P_{i,j}, \tag{4}$$

where $k_{ij}$ is the dielectric tensor and $\beta_1$ and $\beta_2$ are the calibration coefficients, which depend on the domain wall energy and the domain wall width, respectively. In this expression, the Einstein notation was implied, in which the indices $i$ and $j$ ranged between 1 and 2. The Landau term $H^{lan}$ contains an incomplete Taylor expansion up to the sixth order, and the parameters $a_1$ to $a_5$ are based on those used by Cross *et al.*[36]. The random field $E_i^{random}$ was assumed as Gaussian distribution miming the chemical disorder[37]; its strength was controlled by the variance of this distribution. Here, a moderate value of 8 kV/mm was adopted to insure that the random field was neither too strong to allow local domain switching nor too weak to show relaxor properties. The evolution of the order parameter P is determined by

$$\frac{\delta P_i}{\delta t} = -M\left[\frac{\partial H}{\partial P_i} - \left(\frac{\partial H}{\partial P_{i,j}}\right)_j\right], \tag{5}$$

where $M$ is a mobility parameter. For the simulation of the non-ergodic core, a model analogous to that used for the ergodic shell relaxors was used, but the random electric field was excluded. Thus, the potential could be written as

$$H_{ergodic} = -k_{ij}E_iE_j - P_iE_i + H^{lan} + H^{grad}. \tag{6}$$

These models were implemented in the software FEAP[38] using the finite element method. Based on the measured geometric dimensions of the core-shell microstructure and assuming that the region deeper than 500 nm from the surface was not affected by the biased-tip, a non-ergodic spherical core of radius 250 nm surrounded by an ergodic matrix of size 500 nm × 1,000 nm (depth × width) was simulated. A coherent interface was assumed between the core and the shell. Due to the rotational symmetry, the system could be reduced to a 2-dimensional configuration on the *x-z* plane for the simulation. The size of the finite elements should be fine enough to resolve the domain structure and to guarantee the precision of the results. Moreover, symmetric boundary conditions were set on the left and right edges of the box to ensure that the simulation represents a periodic case without the boundary effect. The reference potential at the bottom boundary was set to zero, and the electric field was assumed to undergo a linear potential decrease with distance between the top and bottom boundaries. The simulations revealed not only the polarisation state of the sample surface but also the domain configuration beneath the surface. For vertical poling, a +10 V *dc* voltage difference was applied, similar to the PFM experiment. A triangular potential *vs*. time distribution was employed for simulating the increase and the subsequent decrease of the electric field. The quasi-static simulation was performed with a potential increment of 0.1 V. Before poling, the equilibrium polarisation distribution in the non-ergodic core and the ergodic shell was awaited.

## References

1. Acosta, M. *et al.* Core-shell lead-free piezoelectric ceramics: Current status and advanced characterization of the $Bi_{1/2}Na_{1/2}TiO_3$-$SrTiO_3$ system. *J. Am. Ceram. Soc.* **98,** 3405–3422 (2015).
2. Groh, C. *et al.* Relaxor/ferroelectric composites: A solution in the quest for practically viable lead-free incipient piezoceramics. *Adv. Funct. Mater.* **24,** 356–362 (2014).

3. Koruza, J. *et al.* Formation of the core-shell microstructure in lead-free $Bi_{1/2}Na_{1/2}TiO_3$-$SrTiO_3$ piezoceramics and its influence on the electromechanical properties. *J. Eur. Ceram. Soc.* **36,** 1009–1016 (2016).
4. Kutnjak, Z., Petzelt, J. & Blinc, R. The giant electromechanical response in ferroelectric relaxors as a critical phenomenon. *Nature* **441,** 956–959 (2006).
5. Anoufa, M., Kiat, J. M., Kornev, I. & Bogicevic, C. Vortices of polarization in $BaTiO_3$ core-shell nanoceramics: Calculations based on ab initio derived hamiltonian versus landau theory. *Phys. Rev. B* **88,** 144106 (2013).
6. Saito, Y. *et al.* Lead-free piezoceramics. *Nature* **432,** 84–87 (2004).
7. Cross, E. Materials science - lead-free at last. *Nature* **432,** 24–25 (2004).
8. Dittmer, R., Jo, W., Daniels, J., Schaab, S. & Rödel, J. Relaxor characteristics of morphotropic phase boundary $(Bi_{1/2}Na_{1/2})TiO_3$-$(Bi_{1/2}K_{1/2})TiO_3$ modified with $Bi(Zn_{1/2}Ti_{1/2})O_3$. *J. Am. Ceram. Soc.* **94,** 4283–4290 (2011).
9. Rödel, J. *et al.* Transferring lead-free piezoelectric ceramics into application. *J. Eur. Ceram. Soc.* **35,** 1659–1681 (2015).
10. Rödel, J. *et al.* Perspective on the development of lead-free piezoceramics. *J. Am. Ceram. Soc.* **92,** 1153–1177 (2009).
11. Zhang, S. T., Kounga, A. B., Aulbach, E., Ehrenberg, H. & Rödel, J. Giant strain in lead-free piezoceramics $Bi_{0.5}Na_{0.5}TiO_3$-$BaTiO_3$-$K_{0.5}Na_{0.5}NbO_3$ system. *Appl. Phys. Lett.* **91,** 112906 (2007).
12. Choi, S.-Y. *et al.* Gigantic electrostrain in duplex structured alkaline niobates. *Chem. Mater.* **24,** 3363–3369 (2012).
13. Jo, W. *et al.* Giant electric-field-induced strains in lead-free ceramics for actuator applications – status and perspective. *J. Electroceram.* **29,** 71–93 (2012).
14. Liu, D. *et al.* Composition, electric-field and temperature induced domain evolution in lead-free $Bi_{0.5}Na_{0.5}TiO_3$-$BaTiO_3$-$SrTiO_3$ solid solutions by piezoresponse force microscopy. *Scripta Mater.* **123,** 64–68 (2016).
15. Dittmer, R., Jo, W., Rödel, J., Kalinin, S. & Balke, N. Nanoscale insight into lead-free BNT-BT-*x*KNN. *Adv. Funct. Mater.* **22,** 4208–4215 (2012).
16. Li, L., Hao, J., Xu, Z., Li, W. & Chu, R. 0.46% unipolar strain in lead-free BNT-BT system modified with Al and Sb. *Mater. Lett.* **184,** 152–156 (2016).
17. Liu, X. & Tan, X. Giant strains in non-textured $(Bi_{1/2}Na_{1/2})TiO_3$-based lead-free ceramics. *Adv. Mater.* **28,** 574–578 (2016).
18. Bai, W. *et al.* Phase evolution and correlation between tolerance factor and electromechanical properties in BNT-based ternary perovskite compounds with calculated end-member $Bi(Me_{0.5}Ti_{0.5})O_3$ (Me = Zn, Mg, Ni, Co). *Dalton Trans.* **45**, 14141–14153 (2016).
19. Acosta, M. *et al.* Piezoelectricity and rotostriction through polar and non-polar coupled instabilities in bismuth-based piezoceramics. *Sci. Rep.* **6,** 28742 (2016).
20. Schader, F. H., Wang, Z. Y., Hinterstein, M., Daniels, J. E. & Webber, K. G. Stress-modulated relaxor-to-ferroelectric transition in lead-free $(Na_{1/2}Bi_{1/2})$ $TiO_3$-$BaTiO_3$ ferroelectrics. *Phys. Rev. B* **93,** 134111 (2016).
21. Hossain, M. J. *et al.* The effect of inter-granular constraints on the response of polycrystalline piezoelectric ceramics at the surface and in the bulk. *Appl. Phys. Lett.* **109,** 092905 (2016).
22. Fujii, I. *et al.* Enhanced piezoelectric response of $BaTiO_3$-$KNbO_3$ composites. *Appl. Phys. Lett.* **99,** 202902 (2011).
23. Ihlefeld, J. F. *et al.* Room-temperature voltage tunable phonon thermal conductivity via reconfigurable interfaces in ferroelectric thin films. *Nano Lett.* **15,** 1791–1795 (2015).
24. Kim, G. Y. *et al.* Enhanced polarization by coherent heterophase interface between polar and nonpolar phase. *Nanoscale* **8,** 7443–7448 (2016).
25. Liu, N., Dittmer, R., Stark, R. W. & Dietz, C. Visualization of polar nanoregions in lead-free relaxors via piezoresponse force microscopy in torsional dual ac resonance tracking mode. *Nanoscale* **7,** 11787–11796 (2015).
26. Kalinin, S. V., Morozovska, A. N., Chen, L. Q. & Rodriguez, B. J. Local polarization dynamics in ferroelectric materials. *Rep. Prog. Phys.* **73,** 056502 (2010).
27. Acosta, M. *et al.* Tailoring ergodicity through selective A-site doping in the $Bi_{1/2}Na_{1/2}TiO_3$-$Bi_{1/2}K_{1/2}TiO_3$ system. *J. Appl. Phys.* **117,** 134106 (2015).
28. Schrade, D., Mueller, R., Xu, B. & Gross, D. Domain evolution in ferroelectric materials: A continuum phase field model and finite element implementation. *Comput. Method. Appl. M.* **196,** 4365–4374 (2007).
29. Xu, B.-X. *et al.* Phase field simulation and experimental investigation of the electro-mechanical behavior of ferroelectrics. *ZAMM-Z. Angew. Math. Me.* **90,** 623–632 (2010).
30. Gao, P. *et al.* Atomic-scale mechanisms of ferroelastic domain-wall-mediated ferroelectric switching. *Nat. Commun.* **4,** 2791 (2013).
31. Wang, S., Yi, M. & Xu, B.-X. A phase-field model of relaxor ferroelectrics based on random field theory. *Int. J. Solids Struct.* **83,** 142–153 (2016).
32. Acosta, M., Jo, W. & Rödel, J. Temperature- and frequency-dependent properties of the $0.75Bi_{1/2}Na_{1/2}TiO_3$-$0.25SrTiO_3$ lead-free incipient piezoceramic. *J. Am. Ceram. Soc.* **97,** 1937–1943 (2014).
33. Gruverman, A. & Kalinin, S. V. Piezoresponse force microscopy and recent advances in nanoscale studies of ferroelectrics. *J. Mater. Sci.* **41,** 107–116 (2006).
34. Dittmer, R. *et al.* Ergodicity reflected in macroscopic and microscopic field-dependent behavior of BNT-based relaxors. *J. Appl. Phys.* **115,** 084111 (2014).
35. Kleemann, W. Random fields in relaxor ferroelecrtrics – a jubilee review. *J. Adv. Dielectr.* **02,** 1241001 (2012).
36. Cross, L. E. Relaxor ferroelectrics. *Ferroelectrics* **76,** 241 (1987).
37. Westphal, V., Kleemann, W. & Glinchuk, M. D. Diffuse phase-transitions and random-field-induced domain states of the relaxor ferroelectric $PbMg_{1/3}Nb_{2/3}O_3$. *Phys. Rev. Lett.* **68,** 847–850 (1992).
38. Taylor, R. L. *FEAP: A finite element analysis program*. University of California, Berkeley, USA URL: http://www.ce.berkeley.edu/projects/feap/ (2013).


## Acknowledgements

N.L., R.W.S. and C.D. thank the Center of Smart Interfaces for their financial support. M.A. thanks the Deutsche Forschungsgemeinschaft through the Sonderforschungsbereich 595/D6 "Electrical Fatigue in Functional Materials". S.W. and B.X.X. appreciate the financial support from the 'Excellence Initiative' of the German Federal and State Governments and the Graduate School of Computational Engineering at Technische Universität Darmstadt.

## Author Contributions

N.L., C.D., M.A. and R.W.S. conceived and designed the experiments. N.L. conducted the experiments. M.A. synthesized the sample. S.W. and B.X.X. conceived and carried out the phase field simulation and drafted the corresponding simulation section in the manuscript. N.L., M.A., R.W.S. and C.D. discussed and interpreted the experimental results. N.L., C.D. and R.W.S. drafted the manuscript. All authors were involved in the final preparation of the manuscript.

## Additional Information

**Supplementary information** accompanies this paper at http://www.nature.com/srep

**Competing financial interests:** The authors declare no competing financial interests.

**How to cite this article**: Liu, N. *et al.* Revealing the core-shell interactions of a giant strain relaxor ferroelectric $0.75Bi_{1/2}Na_{1/2}TiO_3$-$0.25SrTiO_3$. *Sci. Rep.* **6**, 36910; doi: 10.1038/srep36910 (2016).

**Publisher's note:** Springer Nature remains neutral with regard to jurisdictional claims in published maps and institutional affiliations.

# Supplementary Information

# Revealing the core-shell interactions of a giant strain relaxor ferroelectric $0.75Bi_{1/2}Na_{1/2}TiO_3$-$0.25SrTiO_3$

*Na Liu[1], Matias Acosta[2], Shuai Wang[3], Bai-Xiang Xu[3], Robert W. Stark[1*], and Christian Dietz[1*]*

[1]*Institute of Materials Science and Center of Smart Interfaces, Physics of Surfaces, Technische Universität Darmstadt, Alarich-Weiss-Str. 10, 64287 Darmstadt, Germany*

[2]*Insititute of Materials Science, Nichtmetallische-Anorganische Werkstoffe, Technische Universität Darmstadt, Alarich-Weiss-Str. 2, 64287 Darmstadt, Germany*

[3]*Insititute of Materials Science, Mechanik funktionaler Materialien, Technische Universität Darmstadt, Jovanka-Bontschits-Str. 2, 64287 Darmstadt, Germany*

*Corresponding authors email addresses: stark@csi.tu-darmstadt.de, dietz@csi.tu-darmstadt.de.

**Virgin state of the core-shell structure of $0.75Bi_{1/2}Na_{1/2}TiO_3$-$0.25SrTiO_3$**

To identify surface regions with a distinct piezoresponse in the virgin state, we first investigated an untreated sample of $0.75Bi_{1/2}Na_{1/2}TiO_3$-$0.25SrTiO_3$ (abbreviated BNT-25ST) using vector piezoresponse force microscopy (PFM). Three different regions of interest (roi) were investigated (Fig. S1): roi 1: upper row Fig. S1a-f, roi 2: middle row Fig. S1g-l, and roi 3: bottom row Fig. S1m-r. In PFM, the amplitude and phase signals locally represent the magnitude of the electromechanical response and the domain orientation beneath the tip, respectively. It can be clearly seen from the lateral and vertical amplitude and phase signals (Fig. S1a-d, Fig. S1g-j and Fig. S1m-p) that these individual grains exhibit distinctive domain contrasts (blue arrows), whereas there is only a weak contrast in the surrounding areas. The presence of central and outer regions indicates the coexistence of two types of domain states. These states can be ascribed to the core-shell microstructure[1,2], which is related to the non-ergodic and ergodic relaxor states[3]. The observation of two distinct relaxor states within individual grains is in good agreement with transmission electron microscopy (TEM) study carried out on the same material[1]. The core in the topography images has a circular shape, whereas the outline in the lateral amplitude/phase images is asymmetric. Nevertheless, considering the outline to be an ellipse-like structure, the average size of the long and short axes from the three examples can be estimated to be 760 nm and 340 nm, respectively (Fig. S1). However, the core diameter of BNT-25ST, as estimated from the TEM results[3], was, on average, only 180 − 360 nm. There does not seem to be a sharp interface between the core and the shell[2], but the authors discussed a possible polarisation or stress mismatch at the interface[3,4]. Thus, the different sizes observed by TEM and PFM may be well explained by the different measurement and setup conditions (ambient conditions *vs*. vacuum, geometrical tip/surface convolution[5] *vs*. electron impact/distribution, electric field distribution from tip to sample *vs*. beam diameter).

The piezoresponse signal showed a stronger contrast in the lateral channels than in the vertical ones (*cf*. top and bottom row, Fig. S1). The domain configurations in the three regions of interest substantially differ. These differences can be attributed to individual grain orientations relative to the global coordinate system in the polycrystalline ceramic[6]. Hence, the ferroelectric domain orientation depends on the grain orientation and on the crystallographically allowed directions, in which the

crystal structure of the BNT-25ST is spontaneously polarized. The corresponding topography images of the three different regions of interest are shown in Fig. S1e, k and q. Interestingly, tiny hollows are detected in the core of all three locations. The hollows at roi 1, 2 and 3 are characterized by depths of approximately 1.2 nm, 0.8 nm and 0.9 nm, respectively (cross-section profiles drawn along the direction indicated by the grey arrows). The lateral dimensions of these hollows are 400 − 700 nm. The occurrence of the tiny hollows in the core is most likely caused by the macroscopic surface polishing or grinding. We speculate that the different chemical compositions of core and shell cause a distinct critical shear strength in both constituents, leading to selectively polishing-induced topographical hollows in the softer material[3]. Thus, the picture of the core embedded in the non-ergodic shell describes the situation well (Fig. 1a).

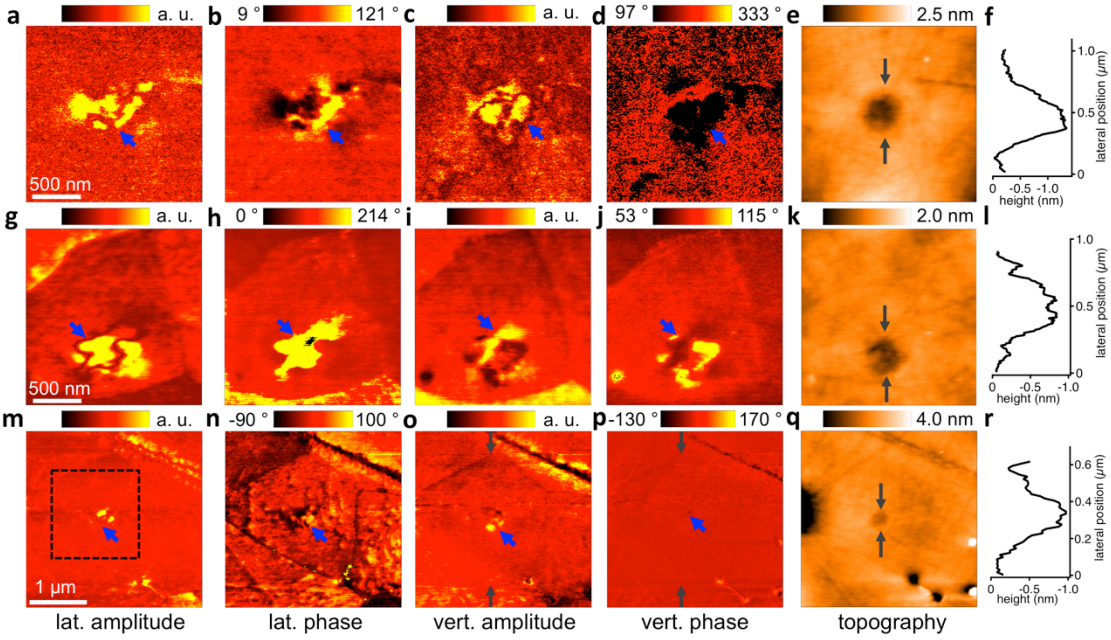


Figure S1. Visualisation of virgin domain states of core-shell microstructures at three different regions of interest. a-f, Region of interest 1. g-l, Region of interest 2. m-r, Region of interest 3. Each column shows the same PFM channel for the three regions of interest: (a,g,m) lateral amplitude and (b,h,n) phase, (c,i,o) vertical amplitude and (d,j,p) phase. The respective topography is shown in (e,k,q). The distinct domain structures in the core are revealed (blue arrows). At all three locations, the core is correlated with a depression in the topography, as illustrated in the cross-sectional

profiles (f,l,r) drawn along the dark grey arrows. The dashed black frame in (m) marks the 1.5 × 1.5 $\mu m^2$ that was poled (Fig. 2).

**Evolution of the field-induced domain, as analyzed using cross-sectional profiles**

To study the evolution of the field-induced domain and the relaxation behaviour in the core-shell region, averaged cross-sectional profiles taken in the vertical phase (Fig. S1p, Fig. 2a,e,i), amplitude (Fig. S1o, Fig. 2b,f,j) and the respective topography are displayed in Fig. S2. The grey box in Fig. S2a highlights the diameter (approx. 380 nm) of the core, as determined from the topography image. After preparation, the core was initially 0.8 nm deep (red line). However, 15 min after poling, the remaining depth was reduced to 0.2 nm (blue line). Then, the depth increased again to 0.3 nm and 0.5 nm after 45 min (black line) and 90 min (grey line), respectively, whereas the diameter of the structure remained constant. From the cross-sectional profiles, the following information can be extracted. For the virgin state, the vertical phase (Fig. S2b, red line) is constant across the core-shell region and the corresponding amplitude (Fig. S2c, red line) exhibits only a very small magnitude, suggesting a weak piezoresponse in the vertical direction. This is in agreement with the data in Fig. S1m-p, where a weak vertical and strong lateral piezoresponsive region was observed in the non-ergodic core area. 15 min after the poling, the phase shift in the poled area was –150° (Fig. S2b, blue line), indicating that a long-range ferroelectric domain, whose polarization vector points downward, has developed. The poled area is approx. 2 µm large. The corresponding vertical amplitude response (Fig. S2c, blue line), however, was only affected over a lateral width smaller than 380 nm instead of the fully poled distance of 2 µm. This observation and the evolution of the vertical amplitude (Fig. 2) imply that the induced vertical domain in the ergodic shell partially relaxed within the first 15 min. Then, 30 min later (Fig. S2b, black line), the diameter of the induced vertical domain (characterized by 150° in the phase) decreased from initially 2 µm to 380 nm and then remained stable (Fig. S2b, grey line), *i.e.*, the poled area shrank down to the core. This means that an irreversible transformation from the non-ergodic relaxor state to the ferroelectric state can occur in the core, whereas the transformation from the ergodic state to the ferroelectric state is reversible within the shell[3]. We also observed that the amplitude response of the field-induced domain

region further laterally shrank in size, accompanied by the propagation and growth of the in-plane polarization at the core-shell interface.

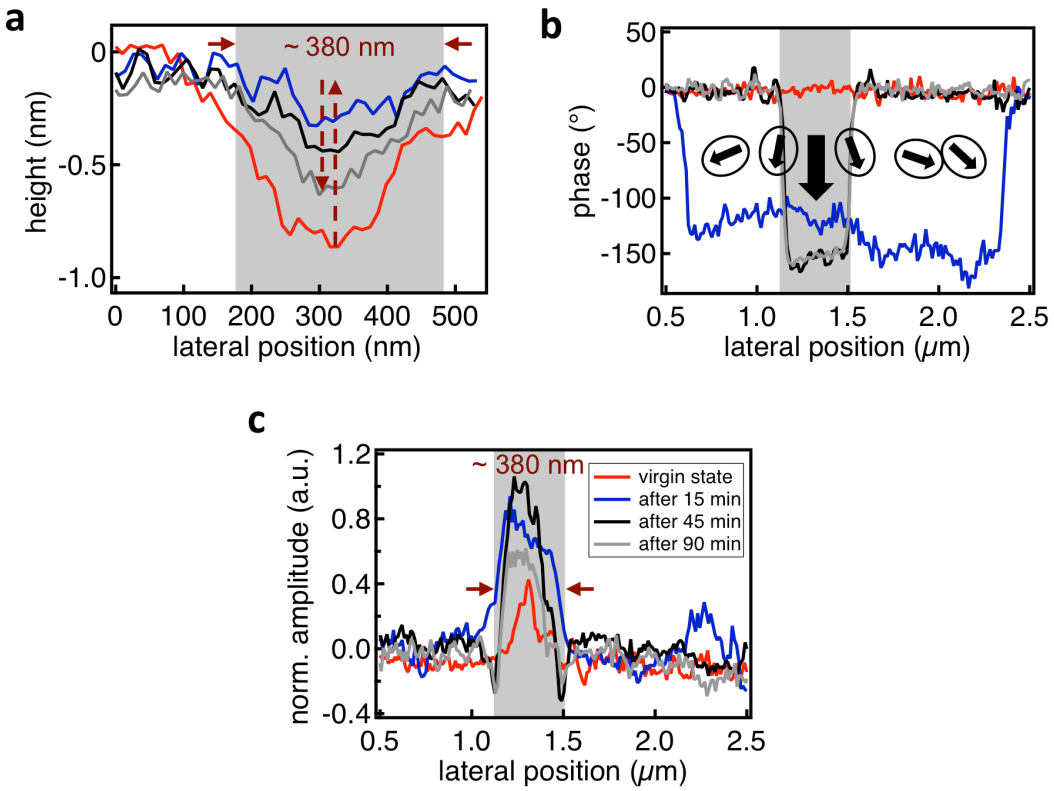


Figure S2. Evolution of the field-induced vertical domain and its relaxation behaviour, as well as the corresponding topography changes at the core-shell region. a, Cross-sectional profiles of the topography before and after poling, drawn along the arrows in Fig. S1q. b, Cross-sectional profiles of the vertical phase before and after poling, drawn along the arrows in Fig. S1p, and Fig. 2a,e,i from the main article. c, Cross-sectional profiles of vertical amplitude before and after poling, drawn along the arrows in Fig. S1o and Fig. 2b,f,j from the main article. The virgin state in each image is indicated by the red solid line, whereas the blue, black, and grey solid lines indicate the signals 15 min, 45 min and 90 min after poling, respectively. The grey boxes highlight the position of the core, which is ~ 380 nm in width, showing the topographical hollows and polarization states of the tip-induced vertical domain. The red upward and downward arrows (a) guide the reader through the evolution of the topography at the core after the poling experiment. Immediately after poling, the hollow nearly disappeared (upward arrow, a) and grew back with time (downward arrow, a). The black arrows (b) mime the potential domain configuration (polar nanoregions) at the sample surface.

## References


1. Acosta, M., Jo, W. & Rodel, J. Temperature- and frequency-dependent properties of the $0.75Bi_{1/2}Na_{1/2}TiO_3$-$0.25SrTiO_3$ lead-free incipient piezoceramic. *J. Am. Ceram. Soc.* **97,** 1937–1943 (2014).

2. Koruza, J., Rojas, V., Molina-Luna, L., Kunz, U., Duerrschnabel, M., *et al.* Formation of the core-shell microstructure in lead-free $Bi_{1/2}Na_{1/2}TiO_3$-$SrTiO_3$ piezoceramics and its influence on the electromechanical properties. *J. Eur. Ceram. Soc.* **36,** 1009–1016 (2016).

3. Acosta, M., Schmitt, L. A., Molina-Luna, L., Scherrer, M. C., Brilz, M., *et al.* Core-shell lead-free piezoelectric ceramics: Current status and advanced characterization of the $Bi_{1/2}Na_{1/2}TiO_3$-$SrTiO_3$ system. *J. Am. Ceram. Soc.* **98,** 3405–3422 (2015).

4. Park, Y., Kim, Y. H. & Kim, H. G. The effect of grain size on dielectric behavior of $BaTiO_3$ based X7R materials. *Mater. Lett.* **28,** 101–106 (1996).

5. Villarrubia, J. S. Algorithms for scanned probe microscope image simulation, surface reconstruction, and tip estimation. *J. Res. Natl. Inst. Stan.* **102,** 425–454 (1997).

6. Uchino, K. *Advanced piezoelectric materials* (USA, 2010).

## Acknowledgements

With this PhD dissertation, I would like to give my sincere acknowledgements to the following people who supported and helped me during my PhD period at TU Darmstadt:

- First, I would like to deeply and foremost thank my doctor father Prof. Robert Stark, who gave me the opportunity and continuous financial support to work in his group, Physics of Surfaces, as a PhD student. His effective advices provided the inspiration for my PhD research and will also inspire me in my future scientific career.
- Secondly, I want to give my special and heartfelt thanks to my wonderful supervisor Dr. Christian Dietz. He always motivated and supported me to think openly and creatively, hence we could successfully develop the TDART and High-speed PFM modes. He was always patient to answer my questions, provide me the effective opinions, revise and polish the paper manuscripts that were always drafted with a lot of pages by me. I was always amazed and inspired by his outstanding scientific knowledge, unique physical thinking and strong problems-solving capabilities. The scientific discussions and conversations with him sparked my scientific creativity and innovation and will be always inspiring me in my future scientific career. I am so much grateful for the effort and time he has spent on me. He created a lot of chances for me, *e.g.* giving my first-time 90-min lecture in Materials Science, and cooperating with different groups with respect to different projects by using conductive AFM or Kelvin probe force microscopy AFM modes. He is more than a supervisor, colleague and officemate to me. He was always honest, faithful, and considerate to me in our friendship, and his sense of humor could always amuse the serious scientific life. I will always remember the time when we played the basketball, you explained me the German culture and showed me the nice songs. I have learnt a lot of things from him. Thank you so much, Christian, for always believing in my research skills, being proud of me and taking care of me during my stay in Darmstadt.
- I would like to thank Prof. Robert Stark, Prof. Baixiang Xu, Prof. Wolfgang Ensinger and Prof. Helmut F. Schlaak for spending time and effort on reviewing my thesis and being my committee members. Thank you Prof. Ralf Riedel for supportively chairing my PhD defense.
- Deeply thanks to Dr. Matias Acosta and Dr. Robert Dittmer from Nnichtmetallisch-Anorganische werkstoffe (NAW) group at TU Darmstadt for providing me lead-free relaxor samples and the fruitful discussions we had, which helped me to efficiently gain the basic and important knowledge about relaxor ferroelectrics. Thank you for inviting me to the dinner events, coffee break you organized and let me quickly get familiar with the SFB595 project and the corresponding members.
- Next thanks goes to my colleague M.Sc. Marcus Schulze who was always listening with full patience. Whenever I asked for help from him, he was always willing to help me out with patience and passion. He encouraged me to give a 90-min lecture in materials science. I will always remember the nice events we went together with the group, indoor climbing, kletterwald adventure, movie-dinner events. Thank you so much.
- Thanks a lot Christian Dietz, Marcus Schulze, Xijie Jiang, Lukas Stühn and Alena Bell for your opinions and suggestions about my PhD defense talk.

▪ Heartfelt thanks to Christian Rust for his excellent bachelor work on realizing our idea about High-speed PFM on relaxors. The effective discussions and results we had motivated me for the further supervising.

▪ I would like to thank Dr. Lars-Oliver Heim from Center Smart of Interfaces for his technical support about MFP-3D AFM with a lot of patience and passion.

▪ Many thanks to Dr. Florian Johann from Asylum Research for the technical support about TDART-PFM and problems solving on the Cypher AFM with many patience.

▪ I would like to thank M.Sc. Shuai Wang and Prof. Dr. Baixiang Xu for the corroboration regarding to the phase field simulation and the effective discussions.

▪ Deep thanks to my former colleague Dr. Simon Schiwek for the help of solving the computer problems and being a thoughtful, helpful, and honest friend.

▪ I want to give many thanks to my former colleague Dr. Marek Janko for his introduction about Raman microscopy and his care, attention and understanding about me. And I want to thank Dr. Kim Phuong Lieu for her enthusiastic help at the beginning of my PhD period to help me quickly to adapt to the group. Many thanks to my friend Julia Auernhammer for all her thoughtful supports. She was always proud of introducing me to her friends and shared nice stories. I will always remember our dumpling and hot-port parties.

▪ I want to give my thanks to all the members and colleagues from Physics of Surfaces for the support and great time we spent together.

▪ Sincere thanks to my friends M.Sc. Pan Hu and Dr. Xin Zhao for supporting and encouraging me. I will always remember our fantastic dinner and party time with a lot of heart-to-heart talks. Thanks my friend M.Sc. Wenjuan Hu for the nice time we spent together. Because of you I got to know climbing and bodybuilding. Our beautiful dancing memory will be nicely recalled. Thank you girls.

▪ I want to express my deep thanks to my friends Dr. Jia Yuan, Dr. Yingwei Zhao, Dr. Qingbo Wen for their help and support during my PhD period/defense.

▪ Deep gratitude to my friend/colleague/flatmate M.Sc. Xijie Jiang for her constant support and help with full patience and tenderness. I will always remember all the nice times we spent together. Thank you so much.

▪ I want to give my deep thanks to my friend Dr. Hairui Liu, who spent the time and effort on checking the "introduction-relaxor ferroelectrics" of my thesis and gave me some crucial opinions. And thank you for all the motivation you brought to me.

▪ I want to give my heartfelt gratitude to my best friend Dr. Ying Liu for her constant motivation and encouragement during my PhD period. Your family-like company eased my tension before the defense. Remember, we will be always there for each other and be the better "I-self" to meet the future "you and me". Thank you so much, Ying.

▪ I want to give my heartfelt appreciation to all my friends in Darmstadt for your help, support, motivation and encouragement during my stay in Darmstadt. Thank you M.Sc. Shasha Tao, Dr. Cong Zhou, Dr. Yan Gao, M.Sc. Hongguang Wang, M.Sc. Ye Sun, Dr. Donghang Lu, M.Sc. Nan Cai, M.Sc. Chen Shen, Dr. Jian Cui, Dr. Zing Zhao, M.Sc. Jiangbin Fan, Prof. Haibo Zhang and Prof. Ke Wang, Dr. Qi Zhang, Dr. Jiquan Liu, M.Sc.

Ying Xu… Thank you the girls whom I met and trained together with in the gym: Dr. Ying Liu, M.Sc. Lu Yu, M.Sc. Sha Liu, Tian Zhang, M.Sc. Huaxin Dong, M.Sc. Jie Zheng…

- I want to express my appreciation to my beloved parents, sister and family for their constant support and encouragement.
- I want to give my most important gratitude to my beloved husband Dr. Wenjie Li for always believing in me and being there for me!

## List of Publications

1. N. Liu, M. Acosta, S. Wang, B.-X. Xu, R. W. Stark and C. Dietz, Revealing the core-shell interactions of a giant strain relaxor ferroelectric $0.75Bi_{1/2}Na_{1/2}TiO_3$-$0.25SrTiO_3$. *Scientific Reports*, **6**, 54 (2016).
2. N. Liu, R. Dittmer, R. W. Stark, and C. Dietz, Visualization of polar nanoregions in lead-free relaxors via piezoresponse force microscopy in torsional dual AC resonance tracking mode. *Nanoscale*, **7**, 11787 (2015).
3. L. Riemer, L. K. Venkataraman, X. Jiang, N. Liu, C. Dietz, R. Stark, P. B. Groszewicz, G. Buntkowsky, J. Chen, S.-T. Zhang, J. Rödel, and J. Koruza, "Stress-induced phase transition in lead-free relaxor ferroelectric composites", *Acta Materialia*. (in revision)
4. S. Vowinkel, C. G. Schäfer, G. Cherkashinin, C. Fasel, F. Roth, N. Liu, C. Dietz, E. Ionescu, and M. Gallei, 3D-ordered carbon materials by melt-shear organization for tailor-made hybrid core-shell polymer particle architectures. *Journal of Materials Chemistry C*, **4**, 3976 (2016).
5. C. Rüttiger, S. Mehlhase, S. Vowinkel, G. Cherkashinin, N. Liu, C. Dietz, R. W. Stark, M.Biesalski, M. Gallei, Redox-mediated flux control in functional paper. *Polymer*, **98**, 429 (2016)
6. V. Rojas, J. Koruza, E. Patterson, M. Acosta, X. Jiang, N. Liu, C. Dietz, and J. Rödel, "Influence of composition on the unipolar electric fatigue of $Ba(Zr_{0.2}Ti_{0.8})O_3$-$(Ba_{0.7}Ca_{0.3})TiO_3$ lead-free piezoceramics", *Journal of the American Ceramic Society*. (accepted on 1st of June in 2017, doi: 10.1111/jace.15013)
7. M. F. Bekheet, I. Svoboda, N. Liu, L. Bayarjargal, E. Irran, C. Dietz, R. W. Stark, R. Riedel, and A. Gurlo, Ferroelectric $InMnO_3$: growth of single crystals, structure and high-temperature phase transitions. *Journal of Solid State Chemistry*, **241**, 54 (2016).
8. M. Acosta, N. Liu, M. Deluca, S. Heidt, I. Ringl, C. Dietz, R. W. Stark, and W. Jo, Tailoring ergodicity through selective A-site doping in the $Bi_{1/2}Na_{1/2}TiO_3$–$Bi_{1/2}K_{1/2}TiO_3$ system. *Journal of Applied Physics*, **117**, 134106 (2015).
9. C. Rust,* N. Liu,* C. Riesch, J. Schultheiß, M. Acosta, R. W. Stark, and C. Dietz, "Relaxation behavior and ergodicity in La-doped $Bi_{0.5}Na_{0.5}TiO_3$-$Bi_{0.5}K_{0.5}TiO_3$ Relaxor ferroelectrics studied by high-speed piezoresponse force microscopy". (to be submitted)

10. N. Liu, Y. Wang, X. Jing, M. Zhou, Y. Wang, Y. Cui, and Y. Jin, 2 μm femtosecond-laser pulse damage of the wavelength separation multilayer. *Chinese Journal of Lasers*, **38**, 0107003 (2011). (in Chinese) DOI: 10.3788/CJL201138.0107003.
11. N. Liu, Y.-J. Wang, M. Zhou, X.-F. Jing, Y.-Z. Wang, Y. Cui, and Y.-X. Jin, Laser resistance of $Ta_2O_5/SiO_2$ and $ZrO_2/SiO_2$ optical coatings under 2 μm femtosecond pulsed irradiation. *Chinese Physics Letters*, **27**, 074215 (2010).
12. W. Li, S.-M. Zhou, H. Lin, H. Teng, N. Liu, Y. Li, X. Hou, and T. Jia, Controlling of grain size with different additives in $Tm^{3+}$:$Y_2O_3$ transparent ceramics. *Journal of the American Ceramic Society*, **93**, 3819 (2010).
13. W.-J. Li, S.-M. Zhou, N. Liu, H. Lin, H. Teng, Y.-K. Li, X.-R. Hou, and T.-T. Jia, Synthesis and spectral

properties of $Yb^{3+}/Ho^{3+}$ co-doped yttria 2 μm transparent ceramics. *Materials Letters*, **64**, 1344 (2010).

14. W. Li, S.-M. Zhou, N. Liu, H. Lin, H. Teng, Y. Li, X. Hou, and T. Jia, Effect of additives on optical characteristic of thulium doped yttria transparent ceramics. *Optical Materials*, **32**, 971 (2010).
15. W. Li, H. Lin, H. Teng, N. Liu, Y. Li, X. Hou, T. Jia, and S.-M. Zhou, Synthesis and optical properties of $Yb^{3+}$，$Ho^{3+}$ Co-doped Yttria transparent ceramics, *Chinese Journal of Inorganic Chemistry*, **26**, 687 (2010) (In Chinese).

# Curriculum Vitae

## Personal Data


Name: Na Liu
Place of Birth: Shenyang, Liaoning, China
Nationality: Chinese
E-mail: lntqyi@gmail.com
Address: Nieder-Ramstädter-Str. 11, 64283 Darmstadt, Germany


## Education

- *Sep 2012 – Jun 2017* **Ph.D Student,** Physics of Surfaces, Materials Science, Technische Universität Darmstadt, Germany
  Thesis: Characterization of the domain structure and the relaxation dynamics of BNT-based lead-free piezoceramics via piezoresponse force microscopy
  Advisor: Prof. Robert W. Stark

- *Dec 2010 – Dec 2011* **Research Fellow**, Institute of Glass and Ceramics, Department of Materials Science and Engineering, Friedrich-Alexander Universität Erlangen-Nürnberg, Germany
  Research Topic: Improvement of the mechanical properties of glasses by surface nitridation
  Advisor: Prof. Lothar Wondraczek

- *Sep 2008 – Jun 2010* **Master Student (postgraduate without entrance exams)**, Key Laboratory of Materials for High Power Laser, Shanghai Institute of Optics and Fine Mechanics, Chinese Academic of Science, Shanghai, China
  Thesis: Preperation and laser-induced damage of 2 μm wavelength optical coatings
  Advisor: Prof. Yingjian Wang

- *Sep 2007 – Jun 2008* **Master Student**, studying master curriculum in Materials Science, University of Science and Technology of China, Hefei, China
  GPA: 3.76/4.0

- *Sep 2003 – Jul 2007* **Bachelor Student**, Inorganic Non-metallic Materials Engineering, Department of Minerals Processing and Bioengineering, Central South University, Changsha, China
  Thesis: Study the dispersion and stability properties for γ-alumina/ceria nanocomposite materials
  GPA: 3.61/4.0 (rank 1/64)
  Advisor: Prof. Xiaolan Song

## Awards and Honors

- *Jun 2014*: award to the 2nd Prize for the Poster Presentation, *5th the Multifrequency AFM Conference 2014, Madrid, Spain.*

- *2004 –2007:* In Central South University, won National Scholarship, Top Prize and First Prize Scholarships; awarded as Excellent Student (twice), Excellent Student Carde, Excellent Graduate

## Languages

- **Chinese**: Native； **English**: Fluent； **German**: Basic

## Conference Oral Contributions and Posters

- N. Liu, C. Rust, S. Wang, M. Acosta, Bai-Xiang Xu, R. W. Stark and C. Dietz, "Visualization of the domain structure and quantification of the relaxation behavior via piezoresponse force microscopy in lead-free relaxor ferroelectric characterized by different degree of ergodicity", 2016 Joint ISAF/ECAPD/PFM, August 21–25, 2016 Darmstadt, Germany. (**Oral presentation**)

- N. Liu, M. Acosta, W. Jo, C. Dietz, and R. W. Stark, "investigating core-shell domain structure of lead-free incipient piezoceramics by piezoresponse force microscopy", International Symposium SFB 595, September 15–17, 2014 Sellin, Rügen Island, Germany. (**Oral presentation**)

- N. Liu, R. W. Stark, and C. Dietz, "piezoresponse force microscopy of relaxors using torsional dual AC resonance tracking mode", 5th Multifrequency AFM Conference, June 17–19, 2014 Madrid, Spain. (**Poster**)

- N. Liu, M. Acosta, S. Heidt, W. Jo, R. W. Stark, and C. Dietz, "nanoscale investigation of lead-free relaxors by piezoresponse force microscopy", 4th Euro AFM Forum, March 17–19, 2014 Göttingen, Germany. (**Poster**)